POLITECNICO DI MILANO

Department of Civil and Environmental Engineering
Doctoral School in Structural, Earthquake and Geotechnical Engineering
XXV cycle

BEHAVIOUR OF COUPLING BEAMS RETROFITTED WITH ADVANCED CEMENTITIOUS COMPOSITES: EXPERIMENTS AND MODELLING

Doctoral Dissertation of:
Milot MUHAXHERI

Supervisors:
Prof. Marco di PRISCO
Prof. Liberato FERRARA

The Chair of the Doctoral Program:
Prof. Roberto PAOLUCCI

March 2014

Milot Muhaxheri 754203
Behaviour of Coupling Beams Retrofitted with Advanced Cementitious Composites: Experiments and Modelling
© March 2014

e-mail:
milot.muhaxheri@polimi.it

BEHAVIOUR OF COUPLING BEAMS RETROFITTED WITH ADVANCED CEMENTITIOUS COMPOSITES: EXPERIMENTS AND MODELLING

A Thesis
Presented to
The Academic Faculty

by

Milot MUHAXHERI

In Partial Fulfilment
Of the Requirements for the degree
Doctor of Philosophy
in
Structural, Earthquake and Geotechnical Engineering

March 2014

Doctoral School in Structural, Earthquake and Geotechnical Engineering
Department of Civil and Environmental Engineering
Politecnico di Milano
XXV Cycle

BOARD COMMITTEE:
Prof. Raffele Ardito
Prof. Fabio Biondini
Prof. Gabriella Bolzon
Prof. Claudia Comi
Prof. Alberto Corigliano
Prof. Dario Coronelli
Prof. Marco di Prisco
Prof. Claudio di Prisco
Prof. Liberato Ferrara
Prof. Attilio Frangi
Prof. Elsa Garavaglia
Prof. Cristina Jommi
Prof. Pier Giorgio Malerba
Prof. Anna Pandolfi
Prof. Roberto Paolucci
Prof. Umberto Perego
Prof. Federico Perotti
Prof. Lorenza Petrini
Prof. Gianpaolo Rosati
Prof. Luigi Zanzi

To my dear Nita and Gyler

PREFACE

Fibre reinforced cement based composites due to their enhanced mechanical performance, mainly for their peculiar tensile behaviour, in recent decades have attracted a great attention among research and engineers community as a replacement of conventional concrete or as strengthening/retrofitting solution in existing r/c structures. Usually the lateral resistance of medium and high rise buildings relies on r/c concrete core, which due to architectural restraints such as door or window opening results in structural division of core walls into singular shafts which usually are connected with deep beams by so called coupling beams. In order to provide a good transfer of forces between the shafts these beams should be properly designed, which requires a dense and complicated reinforcement arrangement. In this thesis the use of fibre reinforced cement based composites is explored as upgrading/retrofitting solution for the poorly designed coupling beams, namely the High Performance Cementitious Composite (HPFRCC) and Textile Reinforced Cementitious Composite (TRCC). This has involved a "multi-scale" studies which started from material characterization and moved up to structural element and to the structural level.

In order to design the experimental test specimens reference has been made to the case of a shear wall containing a typical door opening 900 mm wide (equal to the length of the coupling beam) and 2.1 m high; this resulted (assuming the inter-storey height equal to 2.7 m) in a depth of coupling beam equal to 600 mm and hence in a span to depth ratio of 1.5. The coupling beam was perceived to be a "poorly designed" element; just satisfying the minimum reinforcement requirement prescribed by design codes for non-seismic design situations. Previously calibrated numerical approach based on multi-fibre Timoshenko beam element was used for estimation of load bearing capacity of coupling beams with different strengthening typologies. The experimental campaign performed involved tests on "non-retrofitted" coupling beam specimens, through which it was possible to study the influence of the different resisting contributions (concrete tensile strength, longitudinal and transverse reinforcement), as well tests on retrofitted ones. Two retrofitting choices were pursued: with HPFRCC (6 specimens) and TRCC (2 specimens), tested both under monotonic and reversed cyclic displacements. In total 14 specimens were tested.

In order to have an insight into the results of the experimental results at member level a through characterization of the retrofitting material had also to be performed. A newly conceived test method known as Double Edge Wedge Splitting for the identification of material tensile behaviour of HPFRCC has been employed. Moreover the fracture toughness parameters were related to fibre density and orientation assessed both through non-destructive and destructive testing technique. Depending on the fibre orientation either a strain hardening or softening behaviour can be obtained. Constitutive laws were proposed in tension for both cases and have been implemented in "crush-crack" damage model.

The same numerical model used for modelling DEWS specimens, has been then applied to model the behaviour of HPFRCC coupling beams under monotonic loading, making reference to the experimental campaign performed at University of Michigan on 4 individual coupling beams, cast with either conventional reinforced concrete or HPFRCCs and with different reinforcement arrangements.

As a further step, an alternative modelling technique was explored using a multi-fibre Timoshenko beam element, which incorporates reliable description of unilateral effects of concrete cyclic behaviour, in which suitable assumptions resulting from the previous modelling phase were also incorporated. This approach has been then adopted to predict the cyclic behaviour of coupling beams made of or retrofitted with HPFRCCs and provided reliable description.

Finally, the results performed were employed to numerically asses the efficacy of coupling beams retrofitting on the structural performance of a shear wall. The efficiency of the HPFRCC retrofitting of a poorly designed coupling beam in recovering the same coupling action as a correctly designed one has been highlighted. The possibility of retrofitting coupling beam at selected locations along the wall height with equal structural performance was also addressed through a numerical parametric study.

«Lorsqu'un théoricien trouve un résultat nouveau personne n'y croit, sauf lui! lorsqu'un expérimentateur trouve un résultat nouveau tout le monde y croit, sauf lui! »

J. Lemaitre and J. L.Chaboche

ACNOWLEGEMENTS

This research was jointly supervised by Prof. Marco di Prisco and Prof. Liberato Ferrara, to whom I am grateful for making this research possible through their efforts of finding the financial support to carry out the experiments and partially a year of my PhD studies. The fund was obtained from The Italian Department of Emergency Management in the framework of the ReLUIS project: "Development of new materials for seismic retrofitting", which is gratefully acknowledged.
I am deeply indebted to both of them: to Prof. di Prisco for offering crucial suggestions to better develop this research and to Prof. Ferrara, not only for his advising excellence to tackle the rising problems throughout this research, but also for following and keeping me motivated and optimistic during all the PhD studies.

I owe a great debt of gratitude to the fundamental help and patience of Marco Lamperti who guided and taught me throughout these years to perform all the experiments, at Department of Structural Engineering of Politecnico di Milano. Indeed, I would like to thank also Tonino, Paolo, Giovanni, Andrea, Marco and Massimo the technicians of the Laboratory for Materials and Structures testing of Politecnico di Milano.

I also thank the students who accompanied me during experiments as a part of their degree fulfilment, Stefano Bufalino (BSc) at material level and Alessandro Spini (MSc) at structural level.

I would thank my colleagues at department, who provided a pleasant working and friendly environment.

Finally, I am beholden also to my family not only for their relentless love support, but also that could provide me the rest of financial maintenance to carry out the PhD studies.

Milot Muhaxheri

TABLE OF CONTENTS

LIST OF FIGURES

LIST OF TABLES

1

1 Introduction

Progressive deterioration of existing reinforced concrete structures is highlighting an urgent need for repairing and strengthening structural elements in order to make the structure to perform as intended or even anticipated or simply to make it complying with updated and, not seldom, more rigorous and stringent design provisions. In this framework, the use of advanced cement based materials has become an attractive solution within the research community, particularly for rehabilitation of slender beams and columns e.g. [Meda, et al., 2007; Martinola, et al., 2010; Shin et al., 2011], as these materials are highly damage tolerant and can hence provide the required performance and ease of application. In this thesis the use has been investigated of advanced cement based materials specifically i.e. High Performance Cementitious Composites (HPFRCC) and Textile Reinforced Cementitious Composites (TRCC) as a upgrading/repairing for coupling beams in order to improve, as obviously, the performance of damaged and/or poorly designed coupling beams in terms of strength, ductility and energy dissipation capacity but also to recover, as possible, the "coupling effect" on the behaviour of the shafts. It is worth remarking, as peculiar features of the use of these materials, that they do not require a minimum cover in order to comply with durability constraints. Moreover, it is possible to align in the case of HPFRCCs the fibres along the expected loading direction by controlling the fresh state performance and casting process and in case of TRCCs by placing the textile fabric according to the desired direction.

1.1 Thesis outline

This thesis is structured in eight chapters, starting with the current chapter describing the organisation of the research work.

Chapter two is mainly concerned with engineering motivation based on literature review that stands behind this research, with reference to the historical background of coupling beams up to now, and highlighting the importance of upgrading such elements.

Chapter three deals with the choice of fibre reinforced cementitious composite as upgrading/retrofitting solution, with attention on tensile characterization using a novel indirect technique known as "Double Edge Wedge Splitting" test. It is explored the effectiveness of using both non-destructive and destructive techniques to correlate the fibre

related parameters to the tensile behaviour. The robustness of "crush-crack" damage model with reference on modelling the fibre reinforced cementitious composites is emphasized.

Chapter four is dedicated on modelling the coupling beams with reference to experimental results chosen from the literature review, consisting either from conventional reinforced concrete or high performance fibre reinforced cementitious composites. To this purpose is employed the crush "crack damage" model which would allow a very detailed analyses of the structural element. As well a simpler modelling approach based on multi-fiber Timoshenko beam element is assessed.

Chapter five is mainly concerned on design of the experimental campaign for testing with reference to coupling beams which involved the preparation of the specimens and the application of both retrofitting techniques either HPFRCC or TRCC. To this purpose a detailed description of the testing rig is also provided.

Chapter six presents the experimental investigations of coupling beam tests that were either non upgraded/retrofitted or upgraded/retrofitted. It is assessed the use of HPFRCC and TRCC as beneficial solution on upgrading/retrofitting coupling beams under monotonic and reversed cyclic displacements. Design equations are evaluated provided by strut and tie method and [*fib* Model Code 2010] provisions with reference to experimental tests. And last it is employed the fibre Timoshenko beam to model a couple of cases of coupling beams at issue.

Chapter seven highlights the importance of upgrading the coupling beams on the overall behaviour of the shear wall, through numerical analysis.

Chapter eight provides the main conclusions of this research work and finally remarks the future perspective needs.

2

2 Literature Review

2.1 Coupling beams

Coupling beams as interconnection of shear walls in earthquake-resistant structures have to be designed with the purpose of transmitting the lateral forces resulting from earthquake excitation between the different shafts the wall consists of. Moreover, since the shear walls, could be subjected as well to strong lateral load produced by winds or differential downward settlement of soils (Figure 2.1) the coupling beams must be able also to resist stresses arising from the aforementioned situations while undergoing the resulting deformations. The coupling beams as force transfer elements between shafts play a crucial role on global wall performance. This capacity of transferring forces has to be guaranteed up to high levels of deformations, to allow for the development of plastic hinge at the base of the wall. In practice, achieving a realistic transfer of force, as most of design codes are promoting, requires careful arrangement of the reinforcement, which may result in details difficult to be executed. It is vital that coupling beams must be able to undergo large inelastic deformation under load reversals without a significant reduction on stiffness, load bearing and energy dissipation capacity. When walls are subjected to lateral load, the shear transfer in coupling beam result in tension in one wall, and in compression in the other wall. This coupling effect provides additional moment resistance for the entire wall system, with respect to uncoupled systems as illustrated in (Figure 2.2), because of increased lever arm between the resultants of tensile and compressive stresses which can take profit of the entire length of the wall cross-section.

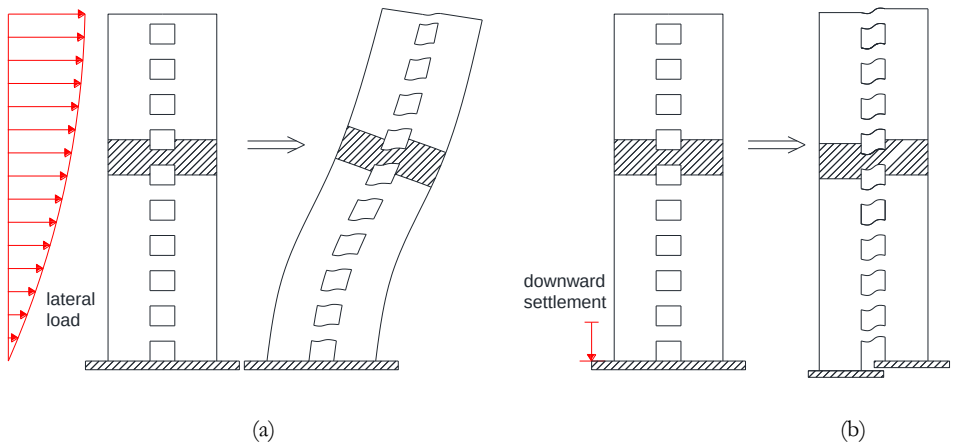

Figure 2.1 – Wall behaviour (a) under lateral load and (b) soil settlements

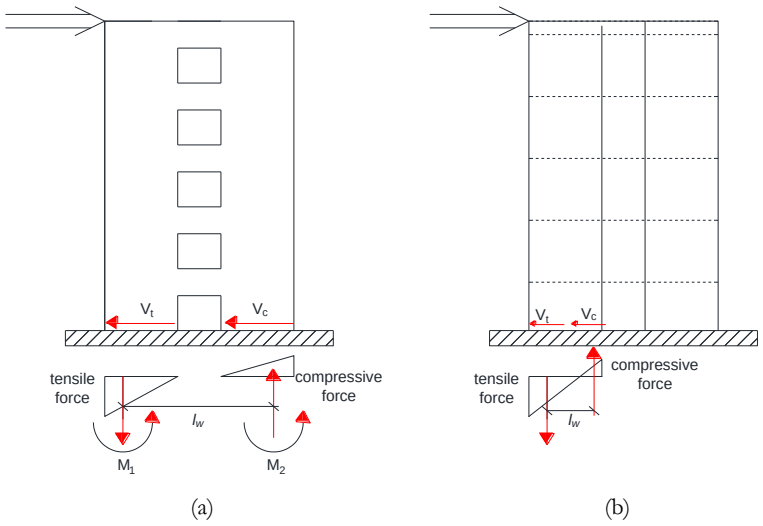

Figure 2.2 – Resisting mechanism of (a) coupled and (b) uncoupled wall systems

$$M_R = M_1 + M_2 + T(\text{or } C)l_w \tag{2.1}$$

$$V_R = V_c + V_t \tag{2.2}$$

The observed brittle failure of coupling beams of Mt. McKinley apartments after the 1964 Alaska earthquake, confirmed that coupling beams should be carefully designed to provide effective link between the walls. Since then, many studies have been carried out to enhance the ductile behaviour of coupling beams considering the geometrical constraints. It has been indicated that traditional principles for the beam design are not appropriate for deep coupling beams. The very first and the most innovative reinforcement arrangement for the coupling beam to avoid brittle failure was proposed by Paulay in 70's. It consisted of diagonal reinforcement to improve the diagonal tensile failure under cyclic loading, as suggested by crack patterns. Lateral confinement of diagonal bars by stirrups was also recommended to avoid buckling under large lateral loads.

Figure 2.3 – Failure of coupling beams due to earthquake Alaska (Alaska Digital Archive)

Other researches in later studies [Taassios et al., 1996; Galano et al., 2000; Fortney et al., 2008] tested coupling beams with different aspect ratios (equal to 1 and 0.75 respectively) in

order to assess the effectiveness of reinforcement layouts other than bi-diagonal. The proposed and tested reinforcement arrangements are sketched in (Figure 2.4); (a) conventional; (b) bi-diagonal; (c) rhombic; (d) short dowels and (e) long dowels. It has been reconfirmed the overall superior performance of diagonally reinforced coupling beams among all layouts. However, it has been observed that also rhombic layout would be an interesting alternative to be considered due to its simplicity in detailing, since it exhibited less stiffness degradation than conventional layout.

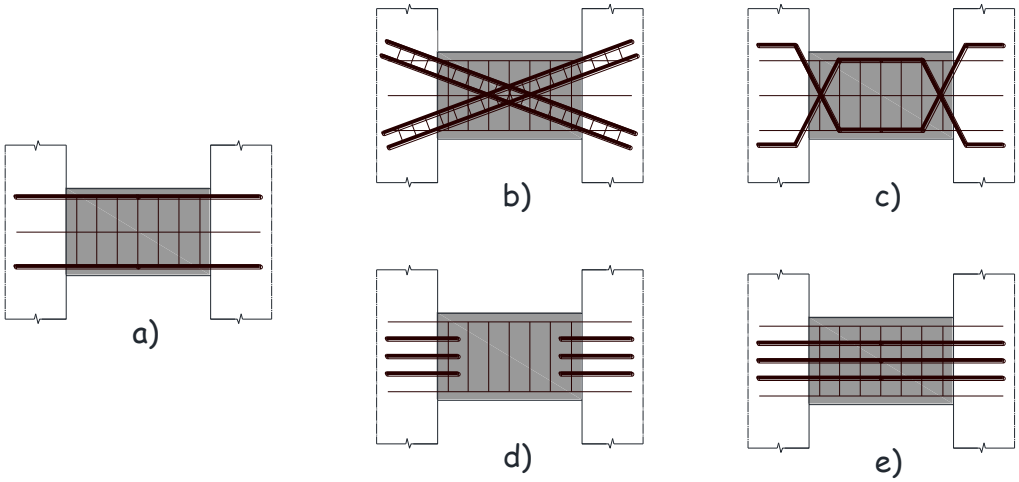

Figure 2.4 – Various reinforcing configurations for coupling beams

During the last decade several promising studies have been conducted aimed at improving the structural behaviour of coupling beams using embedded structural element such as I-beams, plates and tubes [Harries, 1995; Lam et al., 2004; Gong et al., 2001]. Recently HPFRCC has been suggested as an alternative replacement of the traditional concrete, allowing the reinforcement reduction and a simplified detailing. Such an alternative has also been shown to dramatically improve energy dissipation capacity, besides highlighting a simpler constructability [Canbolat et al., 2005; Lequesne et al., 2011; Park et al., 2011]. The experimental investigations by [Canbolat et al., 2005] are taken as reference for model calibration in forthcoming chapters of this thesis.

[ACI 318-08] has "relaxed" the strict provisions of [ACI 318-05], which required diagonal bars confined with transverse ties, and has allowed the full section confinement and the elimination of the diagonal reinforcement. Experimental tests by [Naish et. al 2009; 2013] have in fact shown that full transverse section confinement would provide even better performance of the longitudinally reinforced coupling beams in terms of strength and ductility compared to the diagonally reinforced ones. Moreover, it has been demonstrated by experiments that also lateral restraint that could be attributed to slabs would provide slight improvement on performance of coupling beams.

To have efficient performance of the coupled shear wall systems, it is important to guarantee a well balanced degree interaction between coupling beams and wall units, since over coupling would induce large axial forces and bending moments in wall shafts and would be characterized by highly stressed compression corners. Hence, coupling beams should be designed to yield prior to the shear walls in order to benefit from their ductility, which under severe earthquakes would dissipate large amount of energy.

While designing coupled shear walls, four basic failure mechanisms should be considered for coupling beams:

- Flexural failure (common for beams with span-to-depth ratio >4);
- Diagonal shear failure in tension or compression (common for beams with span-to-depth ratio <4);
- Shear sliding;
- Strong coupling.

Most of the surveyed studies suggest that the common failure mode of coupling beams is characterized by brittle failure in shear rather than in bending, due to their relatively low span to depth ratio (<3) caused by inescapable geometrical constraints.

2.1.1 Steel/composite coupling beams

Other approaches have been proposed to overcome the difficulty of execution of concrete coupling beams. In an early study [Paparoni, 1972] reported on reinforced coupling beams containing encased structural "I" steel profiles. The results suggested that this type of coupling beams can exhibit intermediate ductility between conventionally reinforced and diagonally reinforced member. Another alternative has been also studied [Harries, 1995], consisting of the embedment of the steel "I" profile into concrete shear wall. From these investigations it has been shown that proper embedment of the relatively shallow-depth wide-flange steel profiles could provide significant improvement of the cyclic reversed response of the coupling beams. A combination of two preceding techniques studied by [Gong et al., 2001] is another alternative proposed, which would provide additional capacity. Regardless that these type of coupling beams provide an excellent performance, the main obstacle that have been faced in practice and put in stand such type of beams is that the embedment of steel profile into either the coupling beam or the wall interferes with conventional reinforcement detailing, and consequently increases the labour cost.

2.1.2 HPFRCC coupling beams

[Yun et al., 2008] investigated the cyclic behaviour of short coupling beams. Three beams were tested with two different variables considered, the reinforcing arrangements and the mortar composition. All the beams have same geometry with length 600 mm, height 600 mm and width 200 mm (span-to-depth ratio equal to 1), and are transversally reinforced with stirrups ϕ6 spaced at 150 mm with yield strength 291 N/mm^2. The first coupling beam was reference one (CB1) made of conventional concrete and reinforced with rhombic and longitudinal reinforcement, the second case (CB2) was identical to the previous one as illustrated in (Figure 2.5), but instead of conventional concrete, high performance fibre reinforced cementitious composite (HPFRCC) was used. The last beam (CB3) had the same matrix as (CB2) but did not have any rhombic reinforcement, being solely reinforced longitudinally with 2ϕ16 with yield strength equal to 474 N/mm^2. The employed HFRCC was composed by hybrid fibre reinforcement consisting of 0.75% by volume ultra-high molecular weight polyethylene (PE) fibres (with length equal to 12 mm and diameter equal to 0.012 mm), and 0.75% twisted steel fibres by volume (with length equal to 32 mm and diameter equal to 0.4 mm) [Yun et al., 2007]. The reported compressive and tensile strength were between 44 to 57 N/mm^2, and 3.02 to 3.53 N/mm^2 respectively, with strain capacity up to 3%. The beam was connected with two stiff blocks: one serves to apply the load and the other to maintain the specimen fixed. Two jacks were used to maintain the upper block

planar to the lower one, and one actuator was used to apply cyclic loading. The test setup is illustrated in more details in (Figure 2.6).

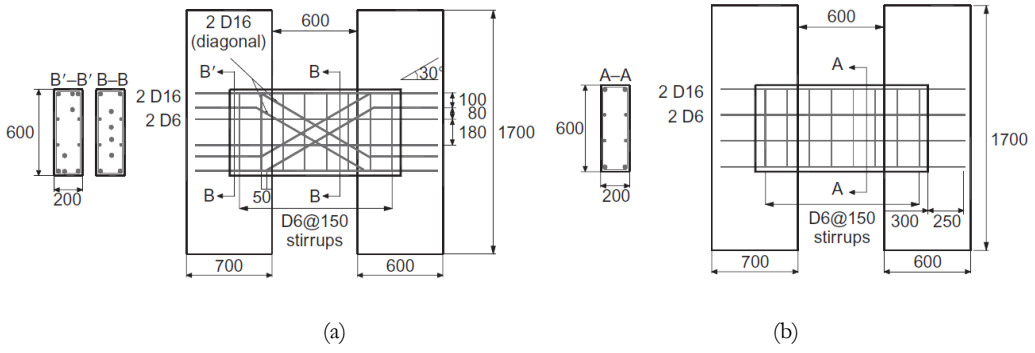

(a) (b)

Figure 2.5 – Specimen geometries and reinforcement details (unit mm): (a) (CB1) and (CB2) specimens; and (b) (CB3) specimen [Yun et al., 2008]

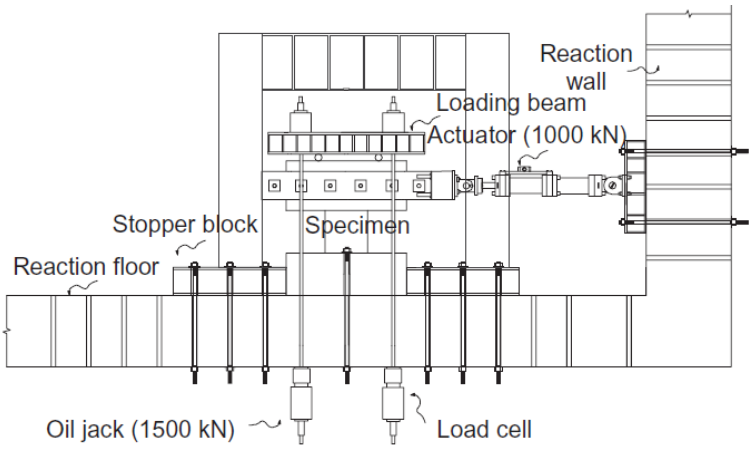

Figure 2.6 – Test setup [Yun et al., 2008]

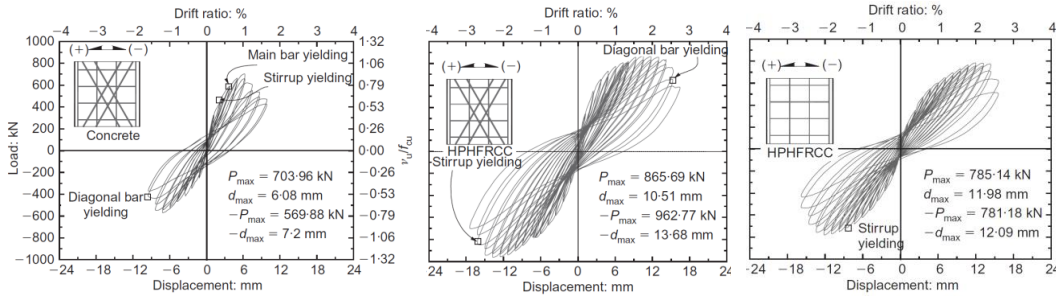

(a) (b) (c)

Figure 2.7 – Cyclic behaviour of specimen: (a) (CB1); (b) (CB2); and (c) (CB3) [Yun et al., 2008]

From the hysteretic response of beams (CB1) and (CB2) the significance has been highlighted of using HPFRCC by observing increase in strength from 704 kN to 865 kN, and significant increase on deformability which was associated with multiple crack observed on the specimens. Instead the (CB3) confirms that using HPFRCC would allow simplified reinforcement arrangement while still providing better behaviour with respect to beam (CB1).

A wide experimental campaign has been performed in the last decade on the behaviour of coupling beams and shear walls at University of Michigan [Canbolat et al., 2005; Hung, 2010;

Athanasopoulou, 2010; Lequesne, 2011]. Several variables have been considered to have better understanding of the behaviour of the coupling beams. Moreover, the use has been explored of a new generation of cementitious composites with moderate volume fraction of fibres up to 2%. In the following the work will be presented performed by [Canbolat et al., 2005], which highlights the significance of using HPFRCC to provide a reduced labour work for reinforcement detailing while guaranteeing a better structural performance. The geometry of the beam was the same for all specimens, with span-to-depth ratio of 1 (600x600 mm), and width of 200 mm or 150 mm. The specimen consists of two stiff blocks connected by the coupling beams, which would serve for fixing of the specimen to the base floor and connection of the actuator to apply the quasi static load at mid-span of the beam, as illustrated in (Figure 2.8).

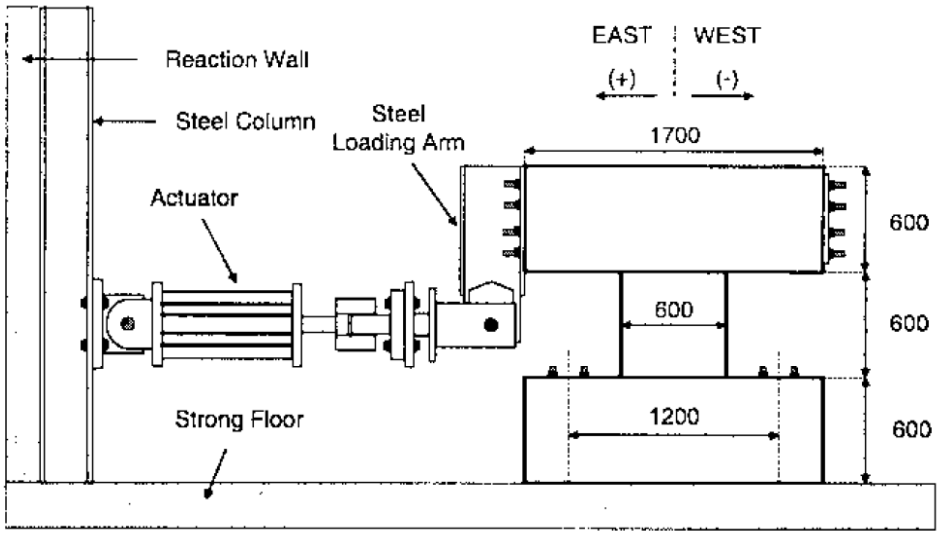

Figure 2.8 – Test setup employed [Canbolat et al., 2005]

The first specimen was a r/c control specimen, designed and detailed accordingly to ACI building code, suggesting diagonally reinforcement; each diagonal has 4ϕ13 bars confined with stirrups ϕ6 spaced at 120 mm, steel yield strength was 450 N/mm² and concrete compressive strength at test day was 41 N/mm². The second specimen was made of HPFRCC with ultra-high molecular weight polyethylene (PE) fibres at 2% volume fraction (with length equal to 13 mm and diameter equal to 0.038 mm), and reinforced only with longitudinal 3ϕ15 bars and stirrups ϕ6 spaced at 150 mm in order to evaluate the effectiveness of addition of fibres. The third specimen was made with the same HPFRCC as the second one but the diagonal reinforcement was simplified adopting only 2ϕ16 bars for each diagonal with no transverse stirrup. The fourth specimen had rhombic reinforcement arrangement to provide easier handling, and was made of FRCC with twisted steel fibres at 1.5% volume fraction (with length equal to 30 mm and diameter equal to 0.3 mm). On the

testing day the compressive strength was between 57 and 63 N/mm², and tensile strength equal to 3.1 and 5.5 N/mm² up to 0.5% strain capacity, for the HPFRCC with PE and twisted steel fibres respectively.

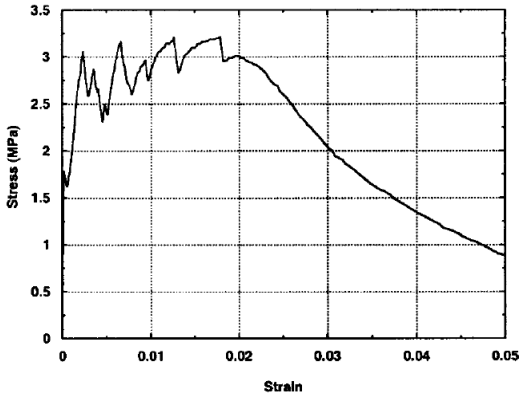

Figure 2.9 – Uniaxial tensile response of specimen with polyethylene

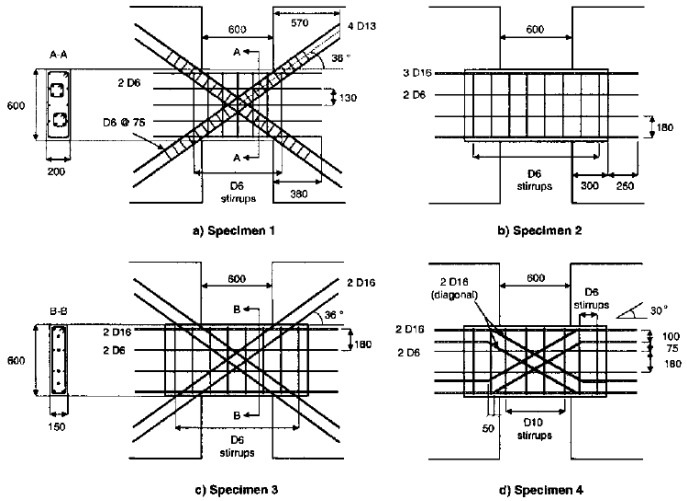

Figure 2.10 – Geometries and the different reinforcement details [Canbolat et al., 2005]

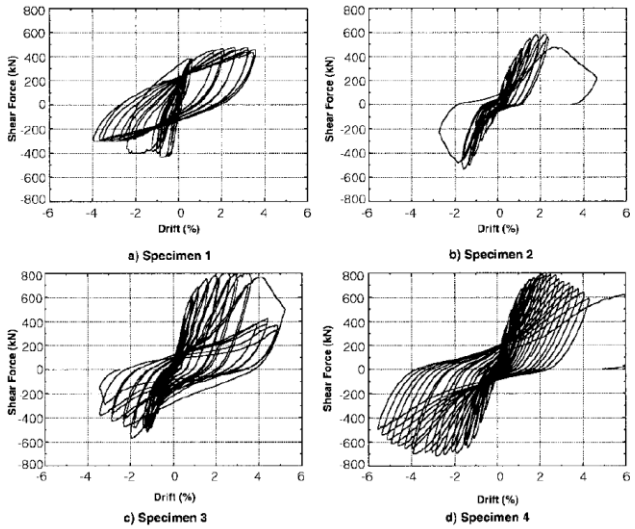

Figure 2.11 – Cyclic behaviour of various specimens [Canbolat et al., 2005]

From the experimental results shown in (Figure 2.11) it has been highlighted that using PE fibres would allow to remove the diagonal bars and have better performance in load bearing capacity, which increased from 470 kN to 600 kN. Nevertheless, the drift capacity was strongly reduced from 4% to 1.8% with a simplified arrangement. Which indicated a lower energy dissipation. Alternatively the addition of diagonal bars in the specimen with PE fibres, even with simplified arrangement up to 800 kN achieved at 2.5% of drift also guaranteed the same level to be maintained up to 4% drift. Anyway a strong asymmetric behaviour was measured on reversed loading due to compressive buckling of bars. The fourth specimen, using the bent diagonal bars and twisted steel fibres showed a very stable energy dissipation and the same strength capacity as specimen 3. In the following chapter four these experimental evidences have been used as reference on design and modelling coupling beams

2.2 Design and modelling of the coupling beams

When designing coupling beams whose geometry is of such that they feature a low (<3) span-to-depth ratio; the beam model that section remain plane cannot evidently be held true.

As shown by theoretical studies on the failure behaviour of the coupling beams, after cracking the beam behaves as a truss. This suggests the strut and tie approach to be adopted for designing the elements at issue. The first one equation has been proposed by [Park et al., 1975] to predict the maximum capacity of diagonally reinforced coupling beams with aspect ratio less than 2. The proposed approach could well predict the test results; that it strictly assumes the failure is governed by diagonal steel yielding and it does not take into account the contribution of concrete or transverse reinforcement. Where α is the inclination angle of the diagonal bars.

$$V=2A_{sd}f_{y}\sin\alpha \tag{2.3}$$

[Subedi, 1991] did a step further by proposing a mathematical model to assess the ultimate load capacity by distinguishing between two different failure modes, flexural and shear. Nowadays, several different models are proposed, based on the same approach by considering different combinations of strut and tie mechanisms depending on the reinforcing configurations [Jang et al., 2004], yet the main obscurity remain the definition of the strut cracking angle requiring engineering intuition. Most of the equations would serve to calculate the maximum shear capacity of the coupling beams related to different failure modes, but would not give any information about the deformation capacity, which is of the equal importance, since coupling beams are required and expected to dissipate a large amount of energy under large lateral loadings prior to failure.

A sound method has been developed [Baczkowski, 2007] to predict the load-deflection behaviour for both r/c and steel fibre reinforced concrete (SFRC) deep coupling beams based on experimental tests. In this method are combined the strut and tie model, fracture mechanics and energy principles, the latter one being used for determination of the cracking angle in order to guarantee physical soundness. However, from comparisons between the model and experiments a good prediction of maximum load bearing capacity was observed but the loading paths were not described equally well.

From some of the aforementioned issues highlighted above, the whole (nonlinear) behaviour is hence of interest and not only the maximum load bearing capacity. Since its introduction,

performance based design has become a common tool for structural engineers to evaluate the nonlinear behaviour (Force-displacement or Moment-rotation) for a given structure. In this technique it is necessary to introduce the nonlinear response for each member by force-displacement envelopes, known as backbone curves, in specific zones to evaluate the global structural response. This modelling technique has been adopted [Brena et al., 2009 and Lequesene, 2011] to describe the behaviour of r/c and HPFRCC coupling beams, and it provided realistic description. However, since the definition of a force component at corresponding displacement is required, this approach becomes cumbersome to be used in everyday practice. Evidently the calibration of these approaches requires a huge number of experimental tests and that is obvious with observations in the literature on increased experimental database. However, this data should be consistent with real behaviour of the coupling beams which in experiments may be not well captured, as for instance, with reference to the clear definition of boundary conditions, interaction of different contributions as shear, flexural and axial deformation etc..

Indeed finite element method is widely used for modelling different structural members, and some attempts have been performed very recently by few authors to model coupling beams. However, the simplified assumptions are still necessary to be made, and require calibration of parameters to relevant experimental evidences.

[Zhao et al., 2004] In a recent study four r/c specimens scaled at 1:2 were tested under monotonic loading with different aspect ratios namely (MCB1, l/h=1.17), (MCB2, l/h=1.4), (MCB3, l/h=1.75) and (MCB4, l/h=2.0). All the beams were similarly reinforced both with longitudinal and transverse reinforcement ratio, equal to 0.5% and 1.07% respectively. Below in (Figure 2.12) the specimen geometry and tests setup are shown. They used FE to model the nonlinear behaviour of coupling beams under monotonic loading, providing relatively good agreement between experimental investigations and numerical approach adopted (Figure 2.13).

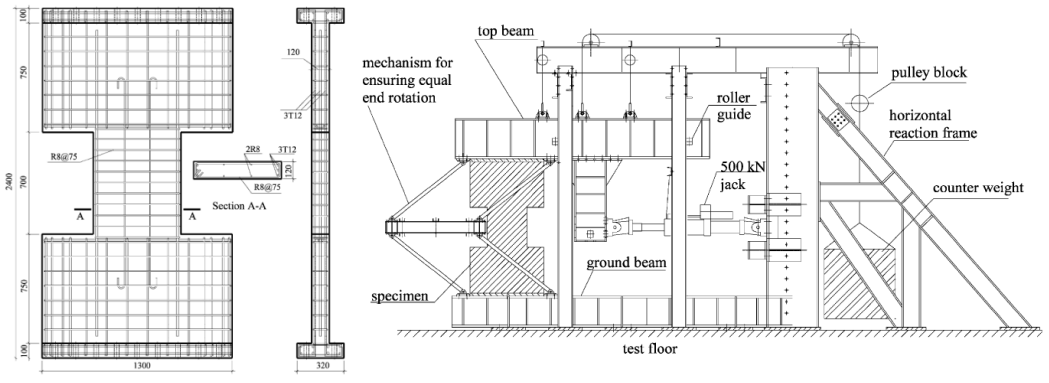

(a) (b)

Figure 2.12 – (a) Specimen (MCB1) and (b) test setup

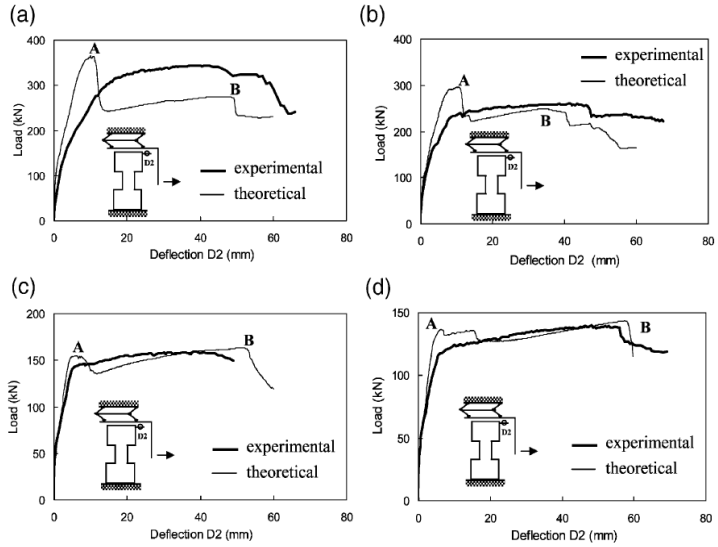

Figure 2.13 – Comparison between experimental investigation and numerical results: (a) (MCB1); (b) (MCB2); (c) (MCB3) and (d) (MCB4)

They also performed a parametric study on the effects of boundary conditions on the nonlinear behaviour, highlighting the great importance of the degree of axial constraint since it contributes on increase of strength and ductility (Figure 2.14).

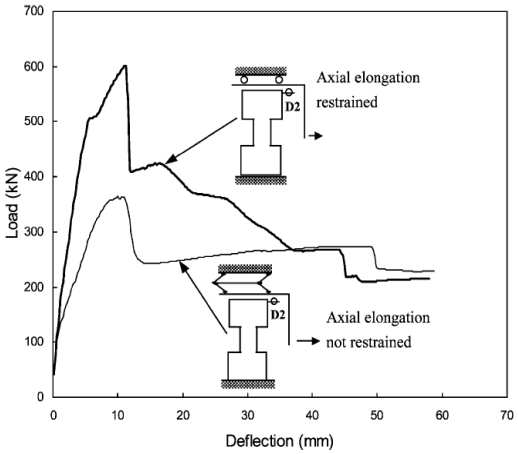

Figure 2.14 – Effects of axial restraining on specimen (MCB1) numerically assessed

2.3 Retrofitting/strengthening of structural elements

Progressive deterioration of existing r/c structures is highlighting the urgent need of retrofitting and strengthening structural elements in order to make the structure to perform as intended or anticipated or simply to make it complying with updated and, not seldom, more rigorous and stringent design provisions. Because of this, upgrading or retrofitting of existing structures is becoming an important field of study both from economical and environmental aspects. Several viable retrofitting/strengthening techniques are available nowadays, as listed below.

The most conventional method is by jacketing existing structural element with an additional reinforced concrete layer; due to durability constraints these technique requires sectional enlargement between 60-70 mm due to presence of steel reinforcement [*fib* Bulletin 24, 2003].

Another technique is using steel plates bonded either with epoxy based adhesives to the existing element. The main problem concerning these techniques is due to differences in stiffness and plastic deformations between substrate and adhesive materials which can cause stress concentration.

Epoxy bonded Fibre Reinforced Polymer (FRP) sheets has gained increased popularity, due to numerous attractive features [Triantafillou et al., 2005] (i.e. high specific strength, corrosion resistance, speed of application and very low thickness). However several drawbacks are also observed such as high cost of resins, hazard for the manual worker due to their toxic solvent content, non-applicability on wet or moist surface and at temperatures lower than 10°C, lack of vapour permeability which may lead to durability problems [Emmons et al., 1994] and incompatibility between adherent and organic binders which do not suit the poor concrete surfaces and could cause debonding of FRP laminates. As consequence of high bond achieved by inorganic binders, high shear stresses at interfaces between the old concrete and the composite are developed, which may cause the loss of repair action and may induce an essential damage to the element.

To overcome these drawbacks, cement based materials have attracted a great attention; the main concept is to substitute the FRP sheet with a textile mesh and to use instead of resins, an inorganic binder to penetrate it.

The reinforcement mechanism is changed as the organic binders are more ductile than carbon or glass fibres. Instead for cement matrix the failure strain in tension is lower (Figure 2.15) making the interaction between fabric and composite to become more effective due to crack bridging and allows the redistribution of forces to other sections [Peled, 2003]. The bond between the cementitious composite and substrate is lower than the one achieved with organic binders. These two features, the crack formation and lower bond, would lead to reduced interface stress concentrations.

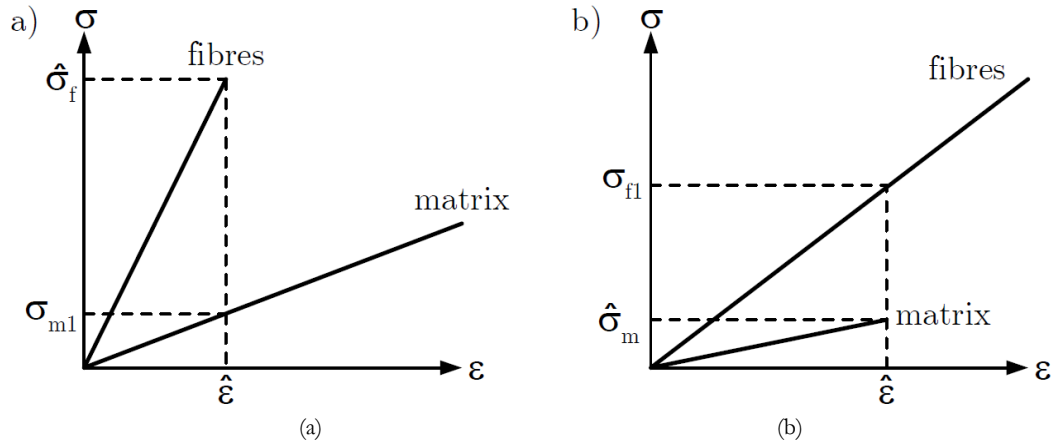

Figure 2.15 – Categories of Textile reinforced composites (a) failure of fibres and (b) failure of matrix [Wiberg, 2003]

2.4 HPFRCC as strengthening material

2.4.1 Flexural strengthening

The use of High Performance Fibre Reinforced Cementitious Composites (HPFRCCs) has become an attractive solution within the research community, particularly for rehabilitation

of slender beams and columns [Martinola et al., 2010; Meda et al., 2007; 2009]. Four point bending true scale testing have been performed on 4.55 m long, and 0.5 m deep beams to study both retrofitting and strengthening using tensile strain hardening material [Martinola et al., 2010]. Before applying the jacket the surfaces were sandblasted, and then a 40 mm thin HPFRCC layer was applied. The employed HPFRCC contained 2.5% by volume steel micro-fibres having a length of 12 mm and a diameter of 0.18 mm, and exhibited an almost elastic plastic behaviour in tension with 11.8 N/mm² tensile strength and strain capacity equal to 0.47%. Four cases were considered, a reference beam with 2ϕ16 longitudinal reinforcement and ϕ8 spaced at 150 mm stirrups to avoid shear failure; two beams having the same reinforcement arrangement but the one upgraded and the other was pre-damaged up to longitudinal reinforcement yielding, and was retrofitted with HPFRCC. The final beam had no reinforcement (neither longitudinal nor transverse reinforcement) but was strengthened with HPFRCC.

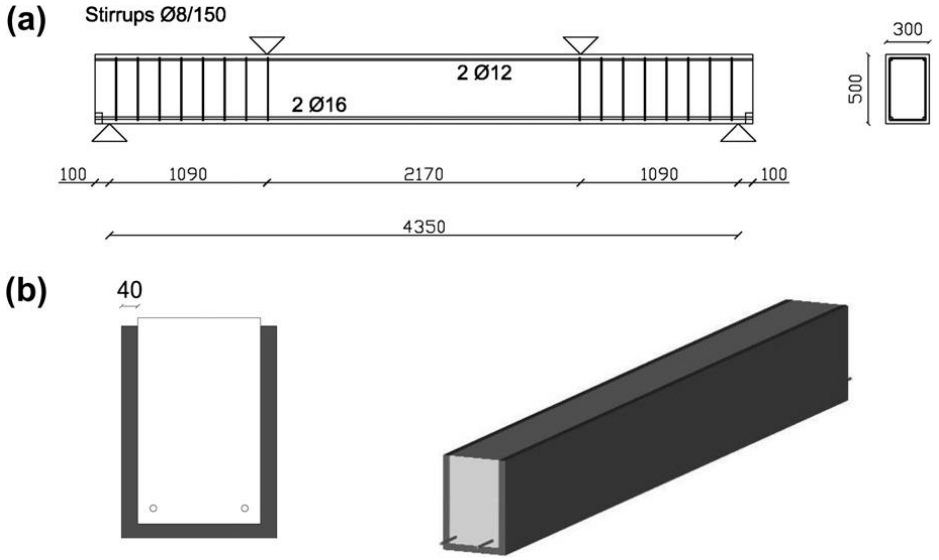

Figure 2.16 – (a) Geometry and loading of the specimen and (b) jacketing with HPFRCC [Martinola et al., 2010]

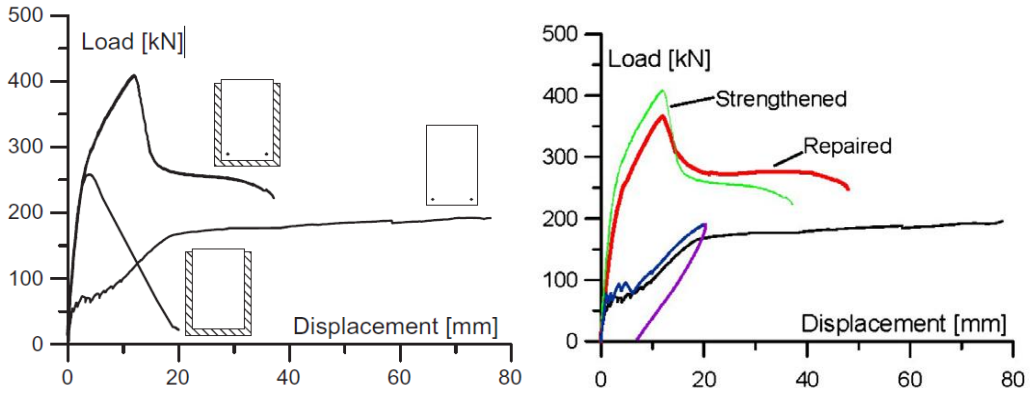

Figure 2.17 – Behaviour of the tested beams [Martinola et al., 2010]

From the experimental results it has been observed (Figure 2.17) that the retrofitted and strengthened beam has exhibited a load bearing capacity as higher as twice the one of the reference beam. Moreover an increase of stiffness was also evident, that could be due to the section enlargement.

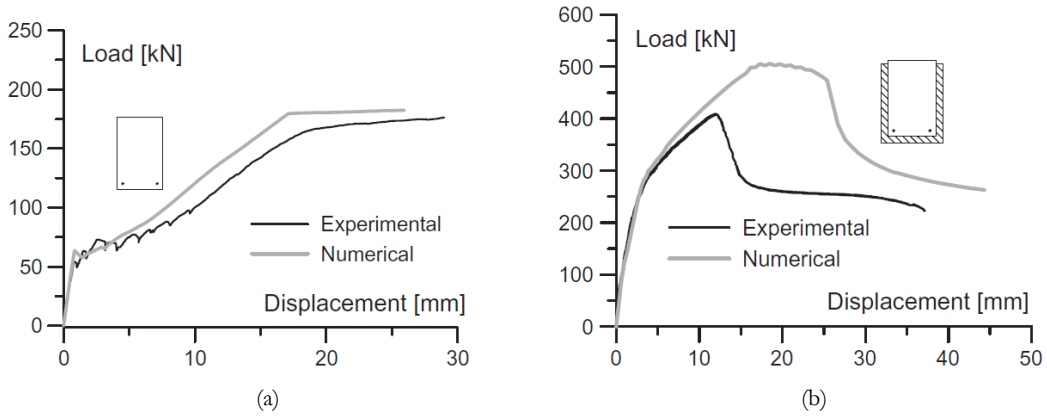

Figure 2.18 – Numerical results of the beam: (a) without jacketing and (b) with HPFRCC jacketing [Martinola et al., 2010]

From nonlinear FEM analysis it is evident that the behaviour of conventional r/c beam could well predict the experimental investigations, while regarding the r/c beam strengthened with HPFRCC the analysis has shown an overestimation on overall performance of the beam (Figure 2.18). That could be related to question of tensile identification tests on small specimens representative to the behaviour in the retrofit layer. Not only, in the analysis was considered perfect bond between the HPFRCC layer and concrete substrate which in reality could undergo some debonding, which entail identification of interface interaction between the two different materials .

Regarding numerical models, as a matter of fact reliable approaches to predict the behaviour of HPFRCC coupling beams and transfer the garnered knowledge into reliable design prescriptions are so far lacking, also because of this still ongoing evolution of code prescriptions concerning structural applications of Fibre Reinforced Concrete.

2.4.2 Shear strengthening

[Maringoni et al., 2011] investigated the use of different high strength jackets with or without combination of steel meshes to provide shear strengthening for slender beams. Four beams with effective span of 2.5 m and the height of 450 mm were tested in 4 point bending test (Figure 2.19). Three of them were upgraded with different configurations as sketched in (Figure 2.20). To provide a good bond between existing substrate and new composite layer, the surface was sandblasted to provide an average roughness of about 1 mm. The great potential of using advanced cement based for upgrading was demonstrated with about double increase in strength and stiffness, by using a jacket with thickness 50 mm. To this purpose two different typologies of HPFRCC were used, one was self levelling matrix that could be casted directly in the formwork, the other was thixotropic that could be applied directly on the surface. In this work the beam was made with concrete class C20/25; the bars had a yield strength of 518 N/mm², whereas the HPFRCC contained 3.9% fibres by volume content (with length 15 mm and diameter 0.175 mm) and tensile strength equal to 6 N/mm² and 5 N/mm², for self levelling and thixotropic HPFRCC; a steel wire mesh of ϕ2 spaced at 25 mm with yield strength 550 N/mm² was also used. The beam (B) was strengthened with self levelling HPFRCC jacket 50 mm thick, and inside it has been inserted the U shaped stainless steel mesh. The other two beams (D) and (E) at the intrados were upgraded with self levelling HPFRCC and on the lateral surface with thixotropic HPFRCC. Also in these

cases were placed the U shaped stainless steel mesh, in beam (D) for sake simplicity on application the U shaped mesh was applied up to a height of 20 cm on lateral surfaces.

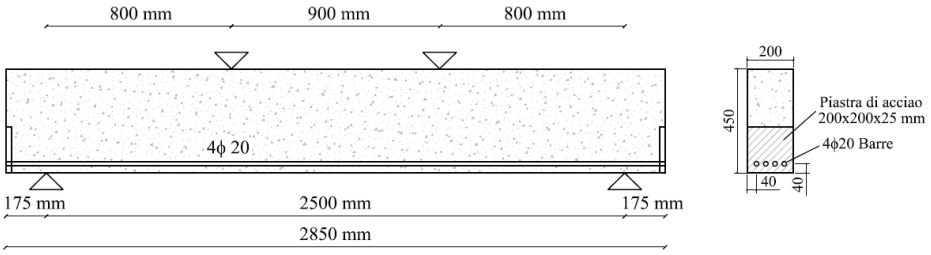

Figure 2.19 – Geometry and testing of the beam [Maringoni et al., 2011]

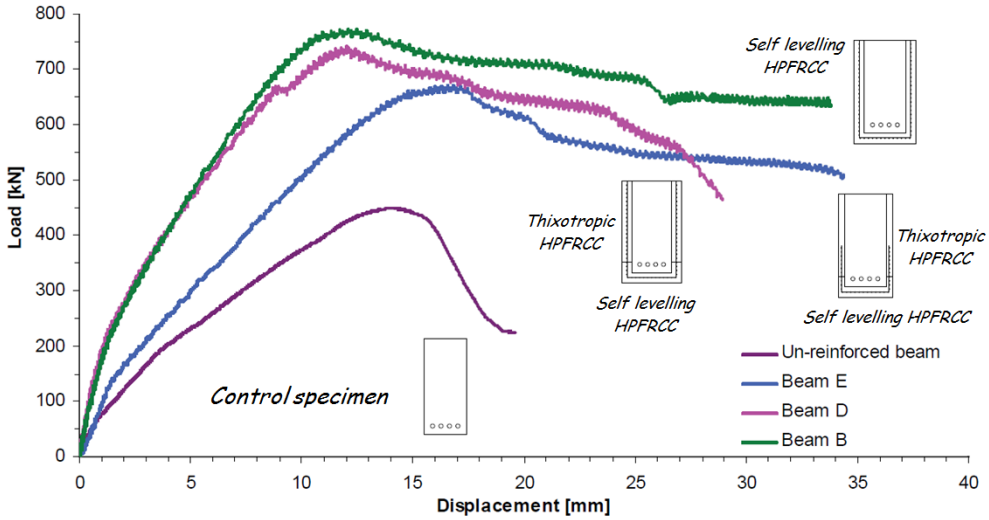

Figure 2.20 – Performance of strengthened beam with different configurations [Maringoni et al., 2011]

2.5 Textile reinforced cementitious composites TRCC as retrofitting/strengthening material

2.5.1 Shear strengthening

Several studies have confirmed the effectives of using the Textile Reinforced Cementitious Composites (TRCC) systems applied to concrete structural elements in order to improve their capacities such as flexural behaviour of beams and slabs [Larrinaga, 2010; Weiland et al., 2006], behaviour of columns under axial loading [Al-Jamous et al., 2006]. [Triantafillou et al., 2005] tested in four point bending 6 beams, with length of 2.5 m and section 15x30 cm, as illustrated in (Figure 2.21a-b). The beams were poorly designed in shear. Four beams were tested in monotonic and two in cyclic loadings. The concrete strength was reported to be 30.5 N/mm², and average yield strength of longitudinal and transverse reinforcement equal to 575 N/mm² and 275 N/mm² respectively. For jacketing unwoven carbon textile was used with mass 168 gr/m² and with nominal thickness of each layer 0.047 mm. In both directions the textile provides strength of 3350 N/mm² and elastic modulus 225 GPa.

The four specimens that were tested monotonically: specimens were denoted as follows (C) was a control specimen without any strengthening, (M2) beam was strengthened with two layers of mortar based jacketing over shear span, (R2) beam has same strengthening instead but instead of mortar a resin was used, and (M2-s) has spirally applied strips in (Figure

2.21c). Two further specimens were tested under cyclic loading; a reference specimen (R1) identical to (R2) and (M1) identical to (M2).

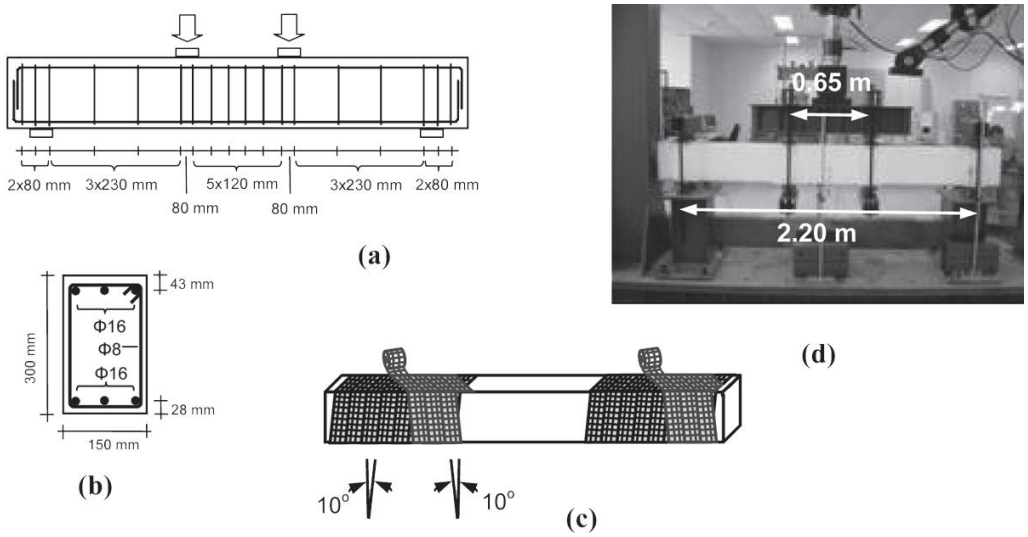

Figure 2.21 – Geometry and loading of the beam reinforced with TRCC [Triantafillou et al., 2005]

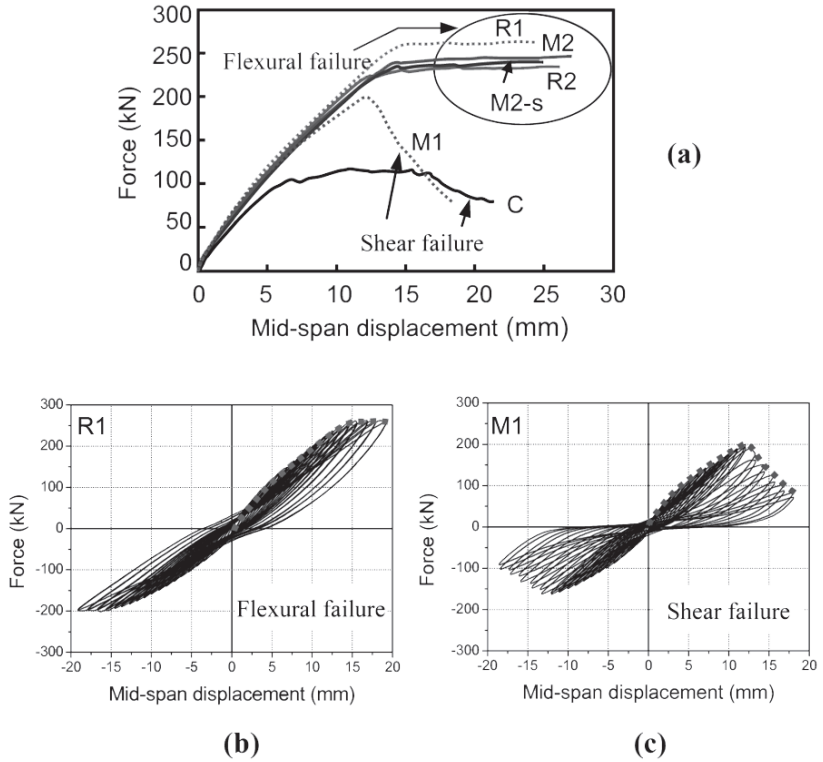

Figure 2.22 – Behaviour of beams under monotonic and cyclic loading with different configurations of TRCC [Triantafillou et al., 2005]

From the results it is evident (Figure 2.22) that in strengthened beams (M2), (R2), (R1) and (M2-s), the failure mechanism was changed from shear to flexural with respect to reference beam. The results of cyclic tests indicated anyway that for beam (M1) shear strength increased but failure mode did not change.

2.6 Coupling beam strengthening techniques

[Tudor et al., 1990 and Mihaescu et al., 1990] provided/performed the earliest studies found in the literature concerning the retrofitting and strengthening of coupling beams. Their research was motivated by damages observed during the site investigations after the Vrancea earthquake in Romania (March 4th, 1977). It was in fact reported that coupled reinforced concrete walls had undergone damages under seismic action with highest damage degree in coupling beams.

In this experimental campaign two different variables were explored depending on damage level quantified by crack openings and the expected failure either in bending (RM) or shear (RT). The specimens were at scale 1:2, with height equal to 300 mm, length 450 mm and width 200 mm (length to depth ratio equal to 1.5). The specimens (RM) were longitudinally reinforced with 8 bars of diameter 8 mm, and stirrups were provided ϕ6 spaced at 100 mm. The other specimens (RT) contained 4 bars of diameter 8 mm as longitudinal reinforcement, and stirrups were provided ϕ6 spaced at 50 mm.

Depending on the damage level observed through experiments the repair and strengthening technique was chosen. For bending cracks of maximum widths 1.5 mm, (respectively in shear 1.0 mm width), epoxy resin injection in the cracks was proposed. As for wider cracks of maximum widths 5.0 mm in bending, correspondingly 2.5 mm in shear it was proposed that the coupling beams could be strengthened by reinforced concrete jacketing. The employed jacket strengthening was 30 mm thick for each face and for (RT) specimen should contain longitudinal reinforcement 4ϕ6 and transverse reinforcement ϕ6 spaced at 90 mm, on each side. Whereas, for the (RM) jacket thickness was the same but the longitudinal reinforcement ratio was increased to 4ϕ8 and the transverse reinforcement ratio was decreased to ϕ6 spaced at 112 mm. This strengthening method has been reported to re-establish the bearing capacity, stiffness and post-elastic features.

The fact that jacketing of slender coupling beams requires to be at least at thickness of 6-7 cm, to satisfy the durability condition of the welded wire fabrics, makes this technique not very feasible to be applied in everyday practices.

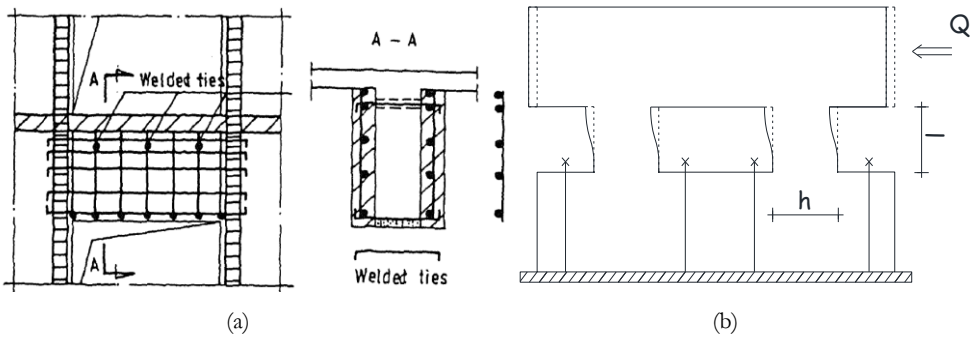

Figure 2.23 – (a) Strengthening and repair of coupling beams with r/c jacketing and (b) testing setup [Tudor et al., 1990]

[Su et al., 2005] conducted testing on three full scale r/c coupling beams; all specimens had the same dimensions (length 750 mm, height 300 mm and width 180 mm) (span-to-depth ratio equal to 2.5). All the specimens were identically reinforced with 4ϕ20 mm longitudinal

bars and stirrups ϕ8 spaced at 110 mm. The compressive strength of concrete employed has been about 50 N/mm².

Besides the reference specimen (CB1), the other two specimens were strengthened by bolting external steel plates with two different plate thickness, 3 and 6 mm namely (CB2) and (CB3) illustrated in (Figure 2.24), with yielding strength reported between 342 and 354 N/mm². All the specimens were subjected to cyclic loading. This method has shown to considerably enhance the strength and deformation capacity of coupling beams under cyclic loading as shown from the envelopes in (Figure 2.25).

However this technique remains unpractical as it requires prior knowledge of reinforcement position to provide sufficient bond by bolts between concrete and steel plate. Moreover, the bolting might cause the impairment of structural elements due to drilling of holes, and furthermore is associated with increased labour cost.

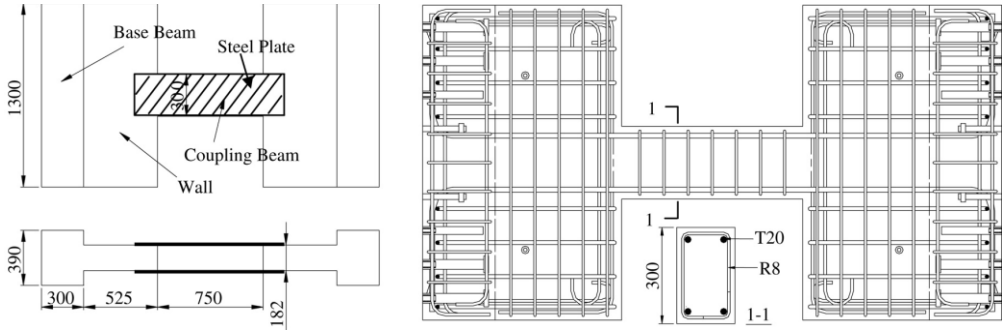

Figure 2.24 – Strengthening of coupling beams with steel plate [Su et al., 2005]

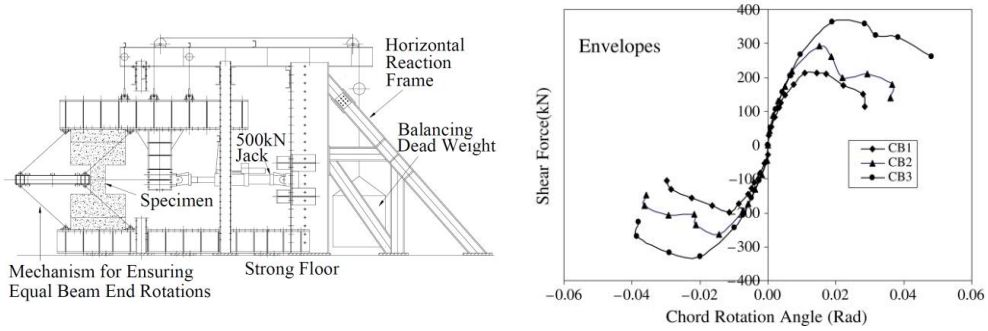

(a) (b)

Figure 2.25 – Coupling beams: (a) loading setup and (b) performance strengthened with steel plate with respect to non strengthened beam [Su et al., 2005]

[Riyaz, et al., 2007] studied the effect of Carbon Fibre Reinforced Polymers (CFRP) sheets of thickness 0.176 mm to rehabilitate coupling beams with and without axial constraint. The beam length was 600 mm and with sectional height of 500 mm and width 150 mm, (span-to-depth ratio equal to 1.2). The specimens (P1) and (P3) had similar longitudinal 4ϕ16 and transverse ϕ6 spaced at 70 mm, but (P3) was axially constrained whereas (P1) was free to deform along that direction. The pre-damaged coupling beams (P1 and P3) up to 60 mm and

37 mm drift respectively, strengthened with CFRP sheets could recover the initial strength (P1-RE) or in the other case exceed it (P3-RE), due to positive effect axial restraining.

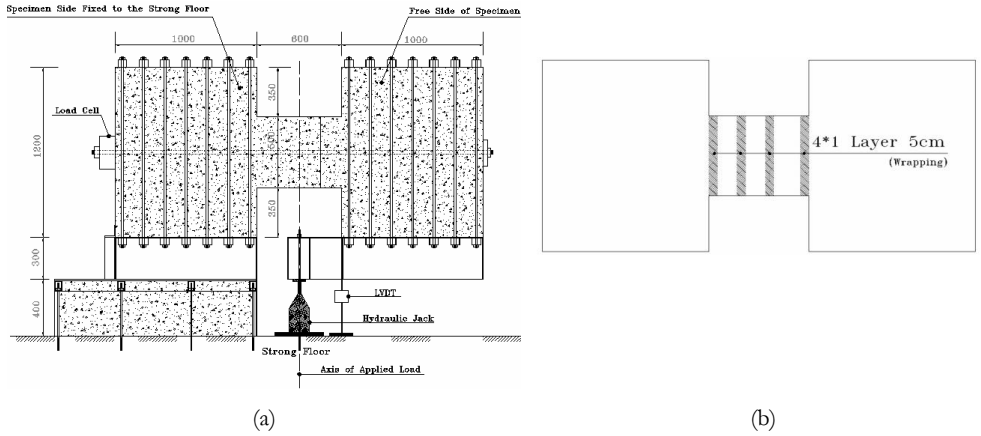

Figure 2.26 – Coupling beam: (a) testing setup and geometry and (b) repair with CFRP [Riyaz et al., 2007]

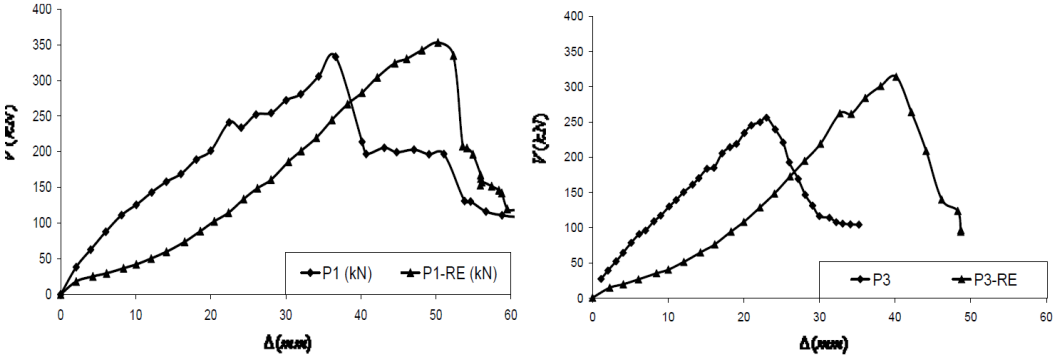

Figure 2.27 – Coupling beam performance before and after repair with CFRP [Riyaz et al., 2007]

2.7 Effect of coupling beam upgrade on structural behaviour

The upgrading of coupling beams becomes an important factor when the walls are partially or not effective in flexure. As a matter of fact, the coupling would provide a larger lever arm than if the wall shafts were separated, thus resulting into a reduction of axial stresses on the walls. The optimal position of upgrading is of crucial importance to give maximum lateral stiffness, thus higher fundamental natural frequency [Moudarres, et al., 1986; Chan et al., 1989].

The applicability of the efficiency for upgrading a partially coupled wall has been illustrated by [Nollet, et al., 2002] providing charts to be used by practicing engineers, in order to reduce lateral deflection under uniformly distributed load. It has been introduced an efficiency coefficient based on the ability of the upgraded coupling beams to reduce the overall drift. Uncoupled shaft generally gives maximum overall drift d_{max}, providing efficiency equal to 0. If the wall is fully coupled the wall behaves as unity with maximum efficiency factor equal to 1, associated with overall drift at minimum d_{min}. Thus, efficiency

coefficient can vary between 0 and 1, by relating the relative value of its drift d, with respect to d_{min} and d_{max}.

They considered as an example of 20 storeys building subjected to lateral loading, with two uniform linked shear walls that are connected with stiffening beams. Based on this concept, it has been shown that the increasing the stiffness of just one beam at mid of building (10th storeys) resulted in efficacy factor of η=83% by comparing the overall drifts of fully coupled and uncoupled wall systems, and showed a reduction on top lateral deflection of 14%. Indeed, the upgrading of a higher number of beams across the same level height position further did not give any significant improvement on reduction of the displacement, but would result in obvious higher cost.

$$\eta = \frac{d_{max} - d}{d_{max} - d_{min}} \tag{2.4}$$

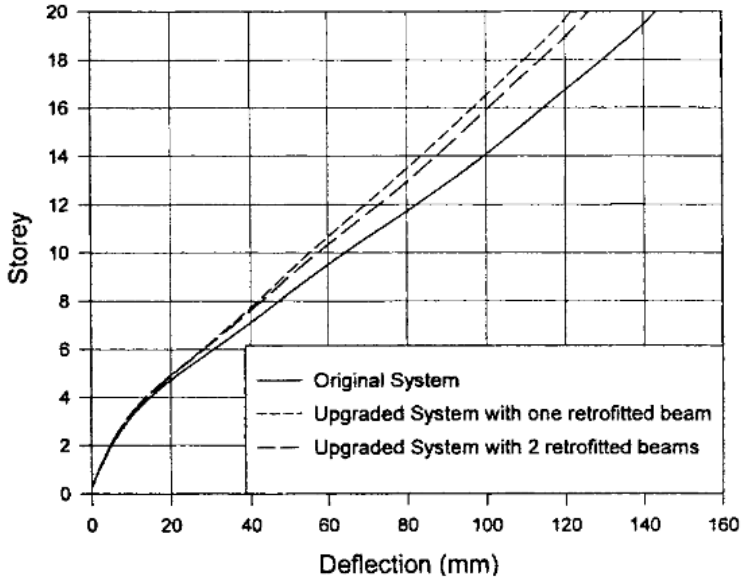

Figure 2.28 – Effectiveness of upgrading coupling beams

2.8 Fibre reinforced cementitious composites (FRCC)

The use of randomly distributed short fibres throughout a brittle matrix acting as crack arrestors can be traced on evidences dating as back to ancient Egypt and Babylonia. However, in 1960s, initiated by the pioneer studies of [Romualdi et al., 1964], it was attracted a great attention to increase the knowledge about the behaviour of fibre reinforcing mechanism in cementitious composites, primarily with the use of short steel fibres. Following studies as by [Shah et al., 1971] indicated substantially higher fracture toughness, which also results in a more "damage tolerant" material, rather than increase in the tensile strength. These developments paved the way for fibre reinforced cementitious composites to be used for a wide variety of non-structural applications, where cracking may not be induced by mechanical loadings, e.g., slabs on grade, industrial floors, pavements, overlays, decks, shotcrete linings, as well as for enhancement of fire resistance, repairing and strengthening works [ACI-544, 1982].

[Naaman et al., 2006; *fib* Model Code 2010; CNR-DT 204] proposed fibre reinforced cementitious composites could be classified in two different categories depending on tensile response, specifically either strain-hardening (multiple cracking occurs before reaching the peak value of stress) or strain-softening behaviour (deformations localize in one crack). Following this classification the cementitious composites that show strain hardening behaviour in direct tension are classified as High Performance Fibre Reinforced Cementitious Composites (HPFRCC) if their compressive strength is below 200 N/mm^2, otherwise, if compressive strength is greater than 200 N/mm^2 can be classified as Ultra High Performance Cementitious Composites (UHPFRCC) [*proc.* UHPC, 2004]. The very first stress-strain curve that exhibited multiple cracking was published by [Naaman et al., 1979]. At that time it was not recognized as a HPFRCC. It is demonstrated that by integrating micromechanical models and careful mix-design optimization techniques it is possible to fully exploit pseudo-strain hardening behaviour and practical manufacture, even with fibre content as low as V_f=1%, that has become common in current practice. Undoubtedly, this approach requires a strict procedure based on suitable exploitation of the correlation between fresh state rheological and solid state mechanical properties. As confirmed by recent research [Ferrara et al., 2011; 2012], the link between fresh and hardened state is the dispersion of the fibres which can be controlled through the rheology and the casting process and obviously affects the hardened state performance.

The material classified as strain-softening in tension can exhibit either deflection softening or hardening behaviour in bending (Figure 2.29). Anyway, even if the material shows deflection softening behaviour, monotonically increased loading deformation response can be obtained in redundant structures, where significant stress redistribution are possible (Figure 2.30). From these observations it can be noticed the need of a consistent testing methods to provide equivalent performance classification for these composites, since it becomes boundary value problem as a result the increase of the constraints is associated with increase on toughness at member level.

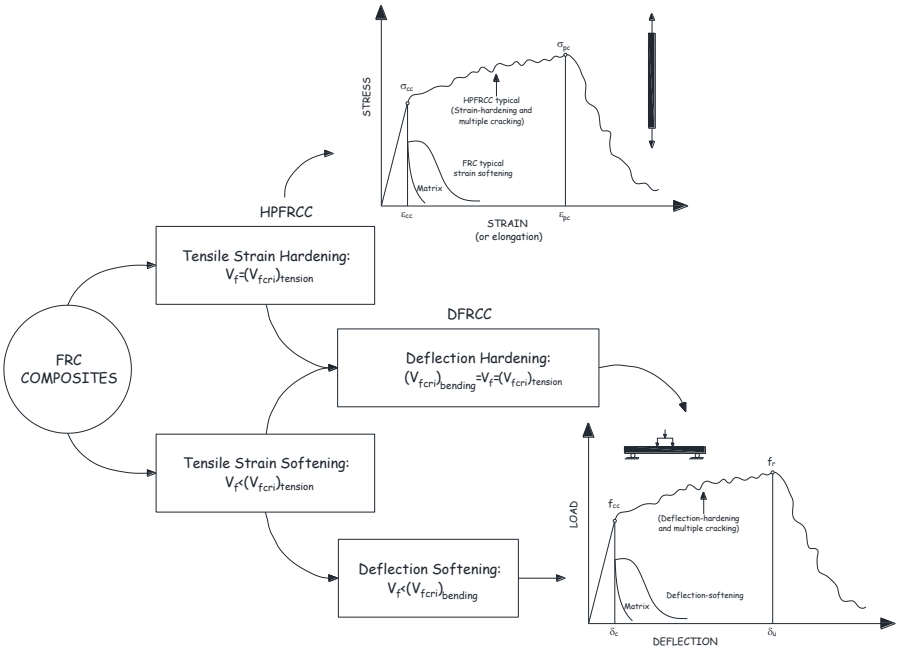

Figure 2.29 – Fibre Reinforced Composites Classification [Naaman et al., 2006]

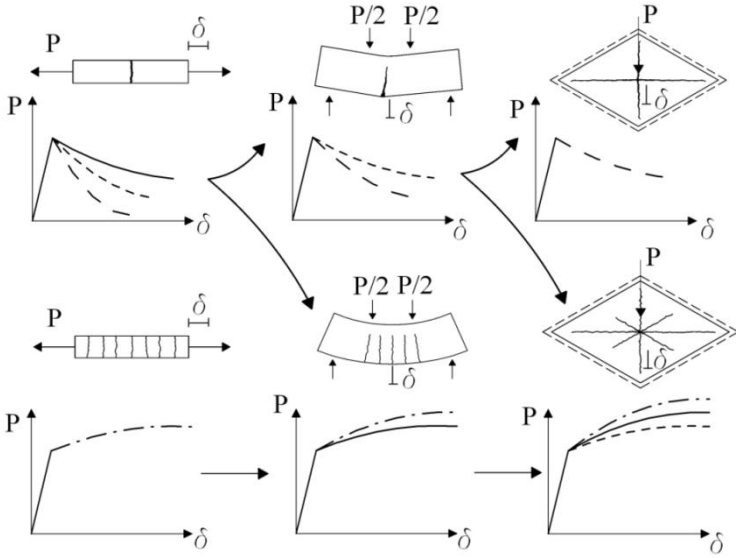

Figure 2.30 – Different response of structures made of FRC having a softening or hardening behaviour under uniaxial tension or bending loads [*fib* Model Code 2010]

Various standard tests are available to identify the tensile behaviour of fibre reinforced cementitious composites. Most of these recommend indirect testing on notched beam in 3 or 4 point bending [CNR-DT 204; Rilem TC 162]. The 3pb test as well is recommended in the prescription of the recently issued [*fib* Model Code 2010] and a "constitutive" model in tension is obtained from inverse analysis of the measured load/crack opening response. This specimen could be representative only when 3D random distribution of fibres is expected. If the composite material is going to be used in thin elements, then the suggested geometry of the specimen is not appropriate, since the fibres tend to be mainly aligned in the plane of the element, resulting in a 2D rather than a 3D distribution. In several studies the characterization of the material is done in uniaxial tension either with doge-bone or notched specimens. However, due to difficulty of specimen manufacturing, definition of boundary conditions and presence of size effect in [*fib* Model Code 2010] is not advised direct uniaxial testing. Since the specimens are conditionally small because of the testing equipment loading capacities, the size would hinder moreover the fibre orientation due to the method of manufacturing.

A novel indirect technique [di Prisco et al., 2010] known as Double Edge Wedge Splitting (DEWS) test has been recently proposed. In this testing method the specimen geometry and the testing conditions have been conceived and designed in order to make it possible to test different correlations between (flow induced) alignment of the fibres and the applied stress. The mentioned testing method has been adopted for characterization of the fibre reinforced cementitious composites and is described more in detail below.

The mechanical properties of the fibre reinforced cementitious composites are influenced by several factors, such as:

- Type and shape of fibres;
- Aspect ratio, defined as the ratio between fibre length (l_f) and fibre diameter (d_f), l_f/d_f ;

- Amount of fibres in volume V_f;
- Strength of the matrix;
- Bond between fibre and concrete matrix;
- Size, shape and casting procedure of the end-product specimen.

For HPFRCC to be applied in engineering applications it is necessary to quantitatively establish a link between structural performance requirement and mechanical properties of the composites. [*fib* Model Code 2010] provides a design procedure with respect to structural performance in bending, other cases such as shear, are more doubtful. As well other trends of applications such as retrofitting are not addressed. Certainly innovative design concepts are necessary to fully exploit strain hardening properties of HPFRCC [Li et al., 2002]. In this framework it is crucial that material behaviour parameters under different stress/load conditions have to be evaluated in order to be used in design approaches to provide structural performance.

2.8.1 Compression

The milestones study by [Fannella et al., 1985] and several other studies which followed, clearly demonstrated that the fibres in compression for High Performance Concrete are beneficial to minimize the sudden failure under static loading that is of an explosive nature. In their study they tested 76x152 mm cylindrical specimens, casted in three equally layers each externally vibrated. They used smooth brass coated steel fibres in three different aspect ratios l_f/d_f, 47 (or l_f=19 mm and d_f=0.4 mm), 83 (or l_f=12.5 mm and d_f=0.15 mm) and 100 (or l_f=25 mm and d_f=0.25 mm). The monotonic compression test were performed using closed loop testing machine, and external LVDT attached to the machine platen was used as a feedback control of the testing machine. It was indicated with reference to the control specimen without fibres that steel fibre reinforcement has marginal influence on stiffness and strength (maximum 15%) whereas it significantly increases the strain at peak stress that is directly related to improved stress transfer mechanism through the micro-cracks.

Fibre addition considerably improves the matrix toughness and ductility in compression as the volume fraction increases, as witnessed by the decreasing slope of descending branch in the post-peak stress strain behaviour. Furthermore, it is evident in (Figure 2.31) that the higher the aspect ratio l_f/d_f, the greater is the energy absorption. As a matter of fact, the improvement which can be obtained through the use of fibres can be even more significant than the one which could be achieved through transverse reinforcement [Compione et al., 1999].

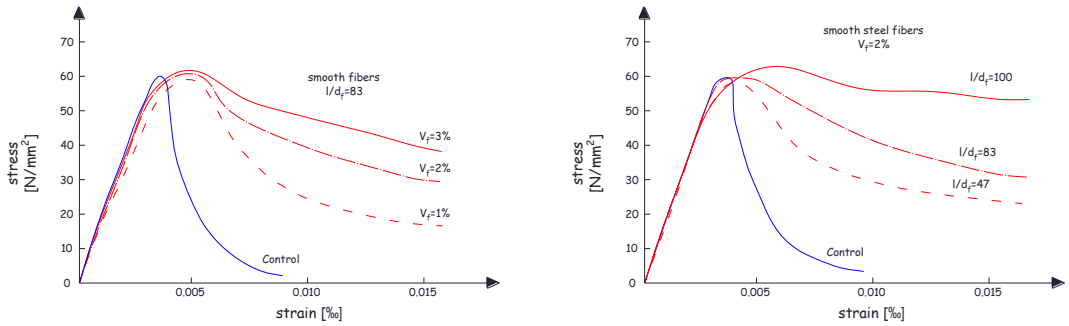

Figure 2.31 – Influence of the volume fraction content on the compression [Fanella et al., 1985]

Several constitutive stress-strain relations have been proposed in the literature to describe the behaviour of ordinary and fibre reinforced concrete under uniaxial compression. It is generally accepted that the same relations as for plain concrete are valid also for fibre reinforced concrete [*fib* Model Code 2010], provided suitable modifications are implemented to take into account the increased residual strength.

2.8.2 Cyclic tension/compression

Limited data are available in the literature about cyclic response of the high performance fibre reinforced cementitious composites (HPFRCC). [Yun et al., 2008] conducted uniaxial cyclic tests under two loading situations to compare with monotonic loading. The first loading scheme determined the complete curve under cyclic loading condition in tension to examine the effect on peak tensile strain (Figure 2.32a). The second loading scheme was to examine how does the compressive stress (up to 1/3 of compressive strength) influence the tensile behaviour under cyclic uniaxial loading (Figure 2.32b). It has been observed that the fibre cementitious composite behave similarly under monotonic and cyclic loading for both loading schemes. Therefore as it is reported by [Kesner et al., 2003], loading that is inevitable on earthquake prone structures (reversed cyclic tension-compression loading) does not limit its unique pseudo-strain hardening capacity, provided that the compressive strength of the material is not exceeded.

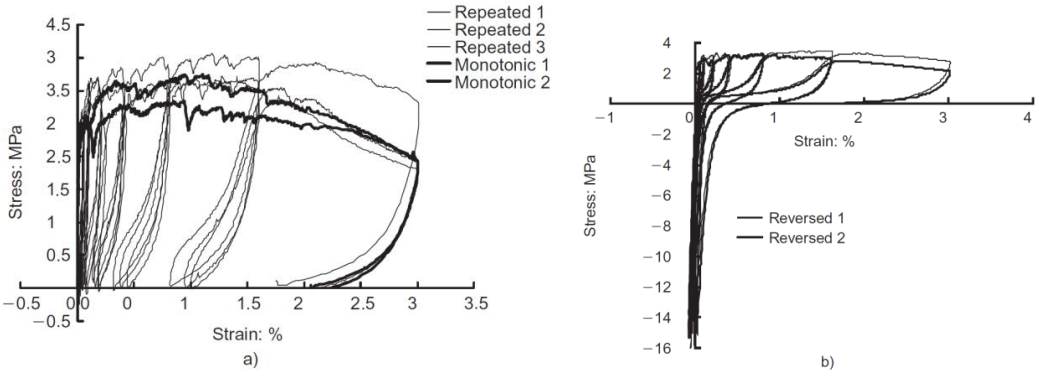

Figure 2.32 – A typical example of comparison between cyclic and monotonic loading for HPFRCC

Summary

In this chapter the importance and necessity of viable techniques for strengthening/retrofitting of coupling beams is highlighted. It has been shown that advanced cement based materials can be an attractive solution for repair or upgrading of various structural elements. Thus, hereafter the use of these new generation materials for rehabilitation of coupling beams is sought.

3

3 Material level investigation: Experimental identification and modelling selected retrofitting material

This chapter highlights the use of advanced cement based composites and their enhanced performance are addressed, hence it is chosen the mix design of High Performance Fibre Reinforced Cementitious Composites (HPFRCC) and Textile Reinforced Cementitious Composites (TRCC) as an upgrading/retrofitting solution of coupling beams. A newly conceived indirect method known as Double Edge Wedge Splitting test for material characterization in tension is employed, moreover the fracture toughness parameters related to fibre density and orientation are correlated with non-destructive and destructive testing. Constitutive laws were proposed in tension for the material at issue which are implemented in "crush-crack" damage model. The robustness of the modelling techniques is highlighted with reference to Double Edge Wedge Splitting test.

3.1 Characterization of fibre reinforced cementitious composites: Non-destructive and destructive testing

In recent years it has been shown that the synergy between the FRC and the Self-Compacting Concrete (SCC) technology, due to the rheological stability of the SCC matrix, may be effective at guaranteeing a randomly uniform dispersion of the fibres within a structural element [Ferrara et al., 2006; 2008]. Furthermore, thanks to both the suitably balanced fresh state properties of the mixture and a carefully designed casting process, it is possible to orient the fibres along the direction of the casting flow [Stahli et al., 2008; Ferrara et al., 2011], thus achieving, along the same direction, superior mechanical behaviour of the material and structural performance. Successful application with advanced fibre reinforced cement based materials relies on reliable design prescriptions and design-oriented test methodologies for the identification of relevant material properties, together with consistent and effective quality control procedures. Hereafter it is tackled a step towards the assessment of non-destructive methods for fibre dispersion monitoring and their inclusion into a sound quality control procedure in a design oriented perspective.

3.1.1 Sample preparation

The FRCC herein employed investigated consists on self levelling high strength mortar with maximum aggregate size of 2 mm. In order to optimize the mix and calibrate the experimental techniques herein illustrated three mixes were cast one without fibres, the other two were reinforced with 50 kg/m^3 and 100 kg/m^3 steel fibres (l_f=13 mm; d_f=0.16 mm, with

aspect ratio equal to 80). The detailed mix designs are reported in (Table 3.1), and the mixing protocol is detailed in (Table 3.3). It clearly appears in mix design that the reduction of fibre content was compensated with equivalent volume of sand. Comparable fresh state performances were observed, by means of V-funnel [UNI EN 12350-9] and slump flow test [UNI EN 12350-2], regardless of fibre addition. To the purpose of the present investigation three slabs 1000 mm long 500 mm wide and 25 mm thick, were cast with materials at issue. The fresh concrete was poured at the centre of one short edge and, due to its self-levelling ability, after having spread to the whole width of the slab, it completely filled the formwork flowing parallel to the long side. In earlier studies reported [Stähli et al., 2008; Ferrara et al., 2008; 2011] that fresh state properties of the matrix may affect fibre distribution and orientation (Figure 3.1), thus by careful controlling of fresh state parameters it is possible to align the fibres in the direction of stresses, which could lead to improved performance of FRCC at structure.

Table 3.1 – Mix design and fresh state performance of the employed cementitious composite

Constituent	FRCC-100	FRCC-50	HPCC
Cement type I 52.5	600	600	600
Slag	500	500	500
Water	200	200	200
Superplasticizer	33 (l/m^3)	33 (l/m^3)	33 (l/m^3)
Sand 0-2 mm	983	1000	1017
Straight steel fibres (l_f = 13 mm;d_f = 0.16 mm)	100	50	0
Fresh state performance			
Slump flow diameter (mm)	750	760	775
T_{50} (s)	6	6	5
V funnel flow time T_V (s)	30	29	25

Table 3.2 – Slag chemical composition

Slag Vitrite LV 425										
Chemical analysis [%]										
SiO_2	Al_2O_3	Fe_2O_3	TiO_2	CaO	MgO	Na_2O	K_2O	PbO	SrO	L.O.I 1100°C
39	11	0.7	0.55	37.5	8.3	0.2	0.3	0.35	0.2	0.75

Mineralogical analysis	Particle size distribution	
Amorphous	Fractions [mm]	Residual [%]
	D50	12 micron

Table 3.3 – Mixing protocol for cementitious composites

Task	
Mix raw cement and slag at 50 rpm	1 min
Add water and SP	1 min
Mix paste at 50 rpm	5 min
Add sand while mixing at 50 rpm	2 min
Mix mortar at 100 rpm	5 min
Add fibres while mixing at 100 rpm	2 min 30 s
Mix FRCC at 100 rpm	5 min

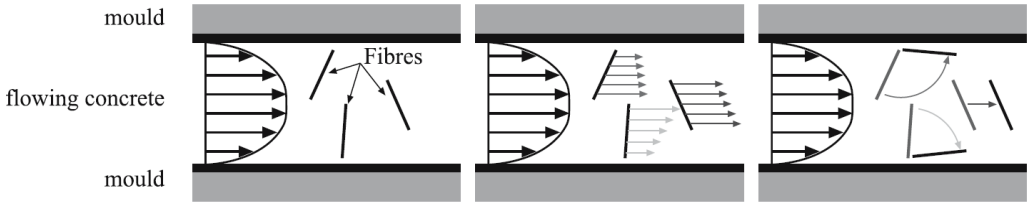

Figure 3.1 – Mechanism of fibre alignment by flowing of concrete [Stähli et al., 2008]

The mean compressive strength of this fibre reinforced cementitious composite (FRCC) and of the matrix without fibres has been in range between 115 N/mm² to 130 N/mm², respectively.

3.1.2 Non-destructive method: physical background

The assessment of fibre dispersion and orientation related issues through a non-destructive method are of the utmost importance in the framework of the aforementioned integrated material and structure design approach. The topic has received lots of attention in the very last lustrum and dramatic progresses have been made since, e.g., the early applications of X-rays [Stroven et al., 1978], also thanks to the use of sophisticated image analysis techniques.

Computer Axial Tomography scanning [Stähli et al., 2008] is able to provide nice 3D visualization of the fibre arrangement within a specimen, but the need of a dedicated equipment (like in the case of X-rays) and software for the quantitative processing of the collected data still stands as a major drawback to a wider use of the method.

Electrical methods have been developed, based on the effects of the conductive fibre reinforcement on either the resistive [Lataste et al., 2008] or the capacitive [Van Damme et al., 2009] properties of the composite, as well as on the whole impedance [Ozyurt et al., 2006]. The sensitivity of each method to either the preferential orientation of the fibres [Lataste et al., 2008] or their local concentration [Van Damme et al., 2009], or both [Ozyurt et al., 2006], has been shown through comparison with destructive monitoring methods [Ozyurt et al., 2006] as well as with the mechanical performance of the same non-destructively monitored material samples [Barnett et al., 2010]. Even if some industrial scale applications have been attempted [Ozyurt et al., 2006], clearly and widely assessed quantitative correlations between non-destructive measurements and actual local fibre concentration and orientation are still lacking. The major drawbacks highlighted so far stand in the influence of the electrical coupling between the electrodes of the test setup and the specimens, as well as in the sensitivity of the matrix resistance to moisture content and

gradients and to the presence of electrolytes in the pores. Measurements can be highly affected by the aforementioned artefacts and the effect of fibre dispersion related parameters jeopardized. In the following a method proposed by [Ferrara et al., 2011] that was employed for the detection and quantification of fibre density and orientation is presented, which was based on the employment of a probe sensitive to the magnetic properties of the steel fibres.

The fundamentals of the method rely on the fact that the presence and relative position of the fibres in a fibre reinforced concrete element modify the magnetic field lines due to the probe winding, when leant on the element/structure surface, thus resulting in a variation of the measured inductance. Based in this concept it is allowed by calibrating the method, the fibre concentration to be determined quantitatively, and the preferential fibre orientation can be predicted. This method benefits by very different magnetic properties of cement based matrix and steel fibres, characterized by magnetic permeability of which has been much lower for the former with respect to the latter. Furthermore, the magnetic field is also influenced by the orientation of the magnetic core (of flux lines) with respect to average direction of fibres.

The measurement of equivalent inductance related to a magnetic field is done using a C-shaped magnetic core with N turn of winding. In (Figure 3.2a) is shown the scheme of magnetic probe with current i_w flowing through N-turn coil; while the permeance Λ_l is assigned to the magnetic path, Λ_c takes into account the drop of magnetic voltage due to the core and Λ_v consider the magnetic flux between two poles. Λ_v is strictly related to the concentration of the steel fibres, their distribution, and the angle between their average direction and that of the ferrite core.

The magnetic circuit can be written into electrical circuit (Figure 3.2c) by converting permeance parameter into the inductance, multiplying the permeance by the square of turn winding N.

The inductances can be defined as:

$$L_l = N^2 \Lambda_l \tag{3.1}$$

$$L_c = N^2 \Lambda_c \tag{3.2}$$

$$L_v = N^2 \Lambda_{v0} + N^2 \Delta\Lambda_v = L_{vo} + \Delta L_v \tag{3.3}$$

The inductance L_v is split into two terms, L_{vo} is the matrix contribution and ΔL_v takes into account the presence of fibres. It should be noted that conductance core losses due to the whole flux are neglected assuming that the employed magnetic core features low losses in our frequency range of interest. Also the conductance losses in the fibre due to alternate magnetic field are assumed to be negligible. Thus, the electrical scheme can be simplified as in (Figure 3.2c). The impedance between two terminal points A-B can have following simplified expression:

$$Z_{AB} \cong R_{ws} + j\omega \left(L_l + \frac{L_c L_v}{L_c + L_v} \right) \tag{3.4}$$

Where R_{ws} is the coil resistance representing the real part of the impedance which is not affected by fibre presence, while the imaginary part might be affected by the magnetic effects due to presence of fibres.

Since the inductance L_c is much higher than L_v, the impedance can be approximated in following form:

$$Z_{AB} \cong R_{ws} + j\omega(L_l + L_v + \Delta L_v) \tag{3.5}$$

It can be written:

$$\Delta L_v = \mathrm{Im}\left(\frac{Z_{AB} - Z_{AB0}}{\omega}\right) \tag{3.6}$$

It clearly appears that the winding inductance is influenced by concentration of fibres, the higher the inductance the higher is the concentration.

Z_{AB0} is the impedance measured when the probe is placed on specimen without fibres. At the same time, the average direction of the fibre can be detected by rotating the magnetic probe around its axis of symmetry and by finding the angular position where the quantity becomes $\mathrm{Im}(Z_{AB}/\omega)$ maximum.

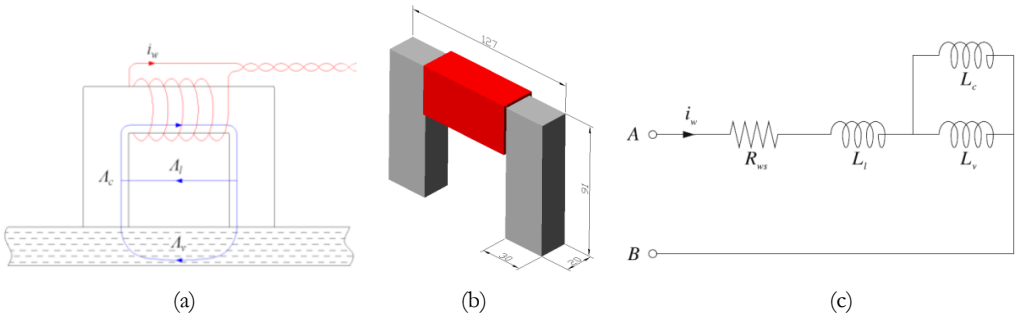

Figure 3.2 – (a) Scheme of the measurement setup; (b) the magnetic probe and (c) electrical model

For detection of steel fibres in the slab a magnetic probe is used, consisting of a C-shaped N87 ferrite core. The excitation is provided by a 100 mA current flowing through a 78-turn coil. By using virtual instrument (VI) techniques it has been possible to measure the voltage applied to the magnetic probe and the consequent current signals. The acquired results were processed using fast Fourier transformation (FFT) analysis in order to obtain the measured impedance.

3.1.3 Non-destructive measurement for fibre reinforced cementitious composites application

After the slabs were hardened, for non-destructive (ND) purposes, a grid was drawn on slab surface dividing virtually into 18 equal squares (165x165 mm). For the three casted slabs, i.e. plain mortar, with 50 kg/m³ and 100 kg/m³ fibre content respectively, measurements of magnetic inductance each of the 18 squares measurements were garnered along four different directions i.e. parallel and orthogonal to the flow lines and at ±45° with respect to it (Figure 3.3b). These measurements would give information about fibre orientation in the

matrix. Along each direction measures were repeated five times, for statistical significance, and reference was made hereafter to their average. The measurements were acquired in range between 1 and 10.2 kHz. In (Figure 3.4a) are shown the measured inductance versus frequency trends, for one cell of each tested slab (No. 8 from the scheme). Measured trends resulted similar everywhere else. The sensitivity of the measured inductance to both nominal fibre content and to the local concentration and most likely alignment clearly appears. Furthermore, it can be observed a certain frequency dependence of the measurements, which is by the way insensitive to either the fibre content or orientation, as highlighted by the parallel curve trends. This depends on the frequency dependent behaviour of the ferromagnetic material the employed probe is made of. Significantly, in fact, the same trend has also been detected for the inductance of the plain matrix, which also coincided with the one measured in free air.

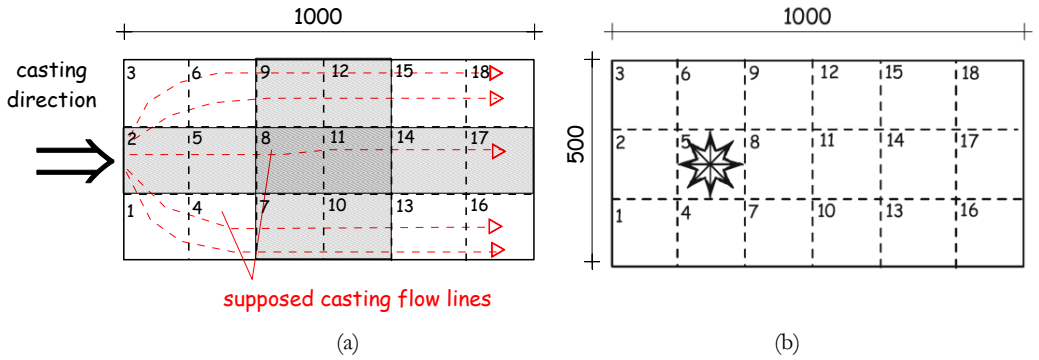

Figure 3.3 – (a) the hypothesized casting flow kinematics and (b) acquisition of magnetic measurements

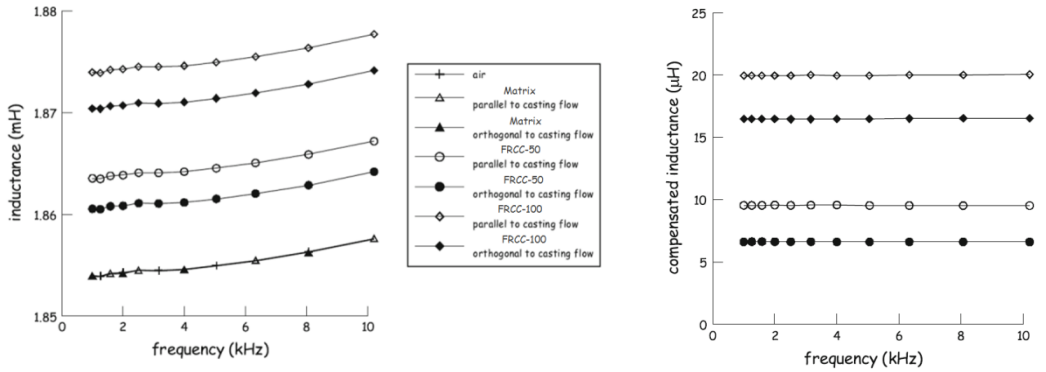

Figure 3.4 – (a) Measured probe inductance for different fibre concentrations, both parallel and orthogonal to fibre orientation and (b) compensated inductances (referred to cell No. 8)

By considering the latter value as the reference one, the so-called "compensated inductances" can be calculated as the differences between the inductance measured for each of the investigated cells and directions and the reference free air value itself. Because of the aforementioned statements, the compensated inductances turned out independent of the frequency (Figure 3.4b).

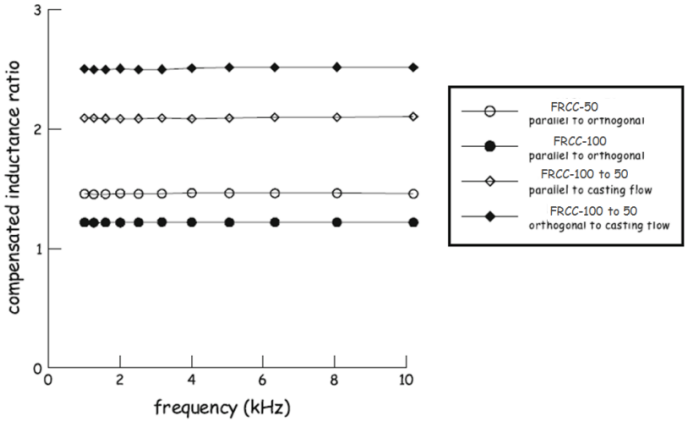

Figure 3.5 – Compensated inductance versus frequency for different fibre dosages and alignment (referred to cell No. 8)

The ratios between compensated inductances along two directions, respectively parallel and perpendicular to the flow direction, confirm the guessed orientation of the fibres. It can be also observed (Figure 3.5) that the higher the nominal content of the fibres, the smaller the aforementioned ratio. This may be most likely attributed to the fact that because of their higher number, fibres are supposed to form a more isotropic network. The ratio between compensated inductances along the same direction but for two different fibre contents results significantly coherent with the nominal fibre content itself. The aforementioned statement, demonstrated with reference to a single monitored cell and confirmed all over the slab specimens, has hence dictated the criteria for further processing the whole set of garnered data (as summarized in detail in Figure 3.6) in order to obtain a more meaningful quantitative information about both the local concentration and orientation of the fibres.

	1		2		3	
Direction		ΔL (μH)		ΔL (μH)		ΔL (μH)
	0°	9.67	0°	9.82	0°	9.87
	90°	9.02	90°	8.01	90°	8.98
	+45°	9.68	+45°	8.96	+45°	9.83
	-45°	9.17	-45°	8.64	-45°	10.00
	4		5		6	
Direction		ΔL (μH)		ΔL (μH)		ΔL (μH)
	0°	11.58	0°	11.86	0°	11.17
	90°	9.70	90°	9.04	90°	9.33
	+45°	10.43	+45°	10.44	+45°	11.61
	-45°	11.47	-45°	10.28	-45°	10.63
	7		8		9	
Direction		ΔL (μH)		ΔL (μH)		ΔL (μH)
	0°	10.36	0°	11.02	0°	11.08
	90°	8.32	90°	8.42	90°	8.56
	+45°	9.45	+45°	9.93	+45°	10.07
	-45°	9.89	-45°	9.46	-45°	9.35
	10		11		12	
Direction		ΔL (μH)		ΔL (μH)		ΔL (μH)
	0°	9.69	0°	10.36	0°	11.18
	90°	7.87	90°	7.71	90°	8.39
	+45°	8.83	+45°	8.83	+45°	10.41
	-45°	9.06	-45°	8.88	-45°	9.36
	13		14		15	
Direction		ΔL (μH)		ΔL (μH)		ΔL (μH)
	0°	9.37	0°	9.27	0°	10.28
	90°	7.56	90°	7.04	90°	7.64
	+45°	8.45	+45°	8.04	+45°	9.39
	-45°	8.97	-45°	8.10	-45°	8.85
	16		17		18	
Direction		ΔL (μH)		ΔL (μH)		ΔL (μH)
	0°	7.18	0°	6.84	0°	7.12
	90°	6.17	90°	6.18	90°	6.42
	+45°	6.64	+45°	6.69	+45°	6.89
	-45°	6.55	-45°	6.46	-45°	6.45

(a)

	1		2		3	
Direction		ΔL (μH)		ΔL (μH)		ΔL (μH)
	0°	21.41	0°	21.68	0°	22.24
	90°	16.46	90°	15.17	90°	17.48
	+45°	21.78	+45°	19.32	+45°	17.81
	-45°	18.15	-45°	17.17	-45°	22.04
	4		5		6	
Direction		ΔL (μH)		ΔL (μH)		ΔL (μH)
	0°	22.55	0°	21.17	0°	22.16
	90°	17.73	90°	18.12	90°	17.64
	+45°	19.59	+45°	19.75	+45°	21.36
	-45°	20.81	-45°	18.96	-45°	19.41
	7		8		9	
Direction		ΔL (μH)		ΔL (μH)		ΔL (μH)
	0°	21.23	0°	20.50	0°	21.50
	90°	16.85	90°	16.77	90°	16.48
	+45°	19.05	+45°	19.27	+45°	19.79
	-45°	19.08	-45°	18.07	-45°	18.86
	10		11		12	
Direction		ΔL (μH)		ΔL (μH)		ΔL (μH)
	0°	19.74	0°	19.77	0°	21.19
	90°	15.97	90°	16.34	90°	15.86
	+45°	17.86	+45°	18.16	+45°	19.07
	-45°	18.21	-45°	17.94	-45°	18.60
	13		14		15	
Direction		ΔL (μH)		ΔL (μH)		ΔL (μH)
	0°	18.58	0°	18.46	0°	19.44
	90°	15.06	90°	15.16	90°	15.28
	+45°	16.91	+45°	16.94	+45°	18.47
	-45°	17.43	-45°	17.06	-45°	17.13
	16		17		18	
Direction		ΔL (μH)		ΔL (μH)		ΔL (μH)
	0°	14.24	0°	13.12	0°	17.26
	90°	12.75	90°	14.06	90°	14.74
	+45°	14.09	+45°	15.33	+45°	16.52
	-45°	13.63	-45°	14.28	-45°	15.48

(b)

Figure 3.6 – Compensated inductances from measured inductance along four directions: (a) FRCC-50 and (b) FRCC-100

As for the latter, (Figure 3.7) shows the direction along which the maximum value of the compensated inductance has been measured, for each cell, which most likely coincided with the preferential alignment of the fibres. Results appear to be coherent with the hypothesized casting flow kinematics as well as with the wall effects due to the formwork boundaries.

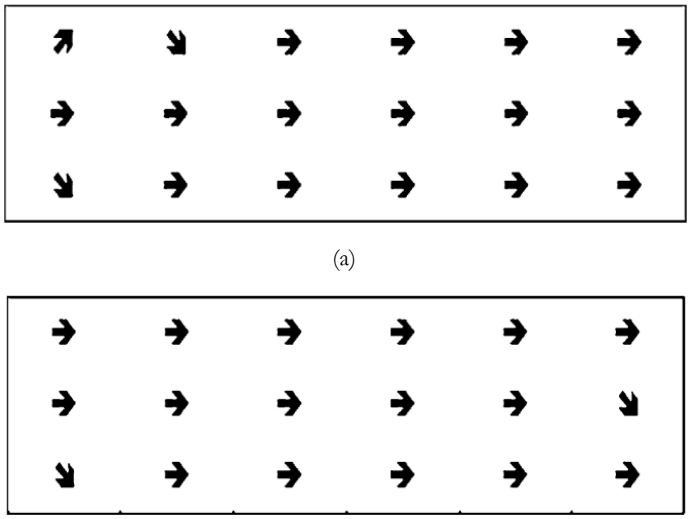

(a)

(b)

Figure 3.7 – Direction of maximum inductance measured: (a) FRCC-50 and (b) FRCC-100

For the assessment of fibre orientation "fractional" compensated inductance, were coherently calculated based on procedure adopted [Ozyurt et al., 2006], along the directions parallel and orthogonal to the flow direction:

$$f_{//} = \frac{\Delta L_{//}}{0.5(\Delta L_{//} + \Delta L_{\perp})} \tag{3.7}$$

$$f_{\perp} = \frac{\Delta L_{\perp}}{0.5(\Delta L_{//} + \Delta L_{\perp})} \tag{3.8}$$

Where subscripts // and ⊥ stand for parallel or orthogonal to direction of supposed flow lines, and coefficient 0.5 is the expected value in the case of perfectly in-plane isotropic dispersion. The results are reported in (Figure 3.8).

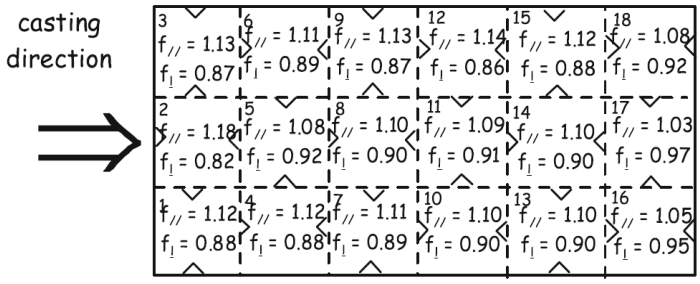

(a)

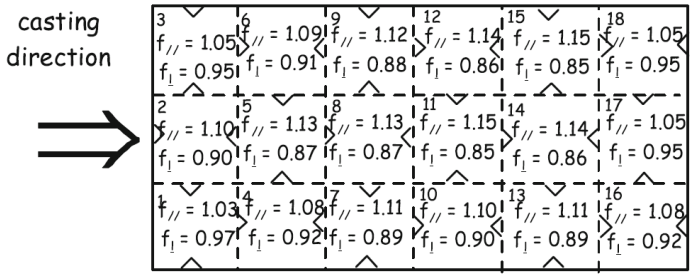

(b)

Figure 3.8 – Fractional compensated inductances: (a) FRCC-50 and (b) FRCC-100

As for the quantitative assessment of the local concentration of fibres, the following approach has been followed. First of all it has been assumed that, in the average, the slab as a whole contains a specific amount of fibres equal to the nominal fibre content in the mix.

Such a guessed nominal reference fibre content has been plotted versus a "nominal average compensated inductance" value, defined as the average, over the whole slab, of the averages of the values measured along the four directions for each cell. The calibration of the "nominal average compensated inductance" versus nominal fibre content correlation is shown in (Figure 3.9). A linear dependence on the fibre content has been hypothesized because of the low fibre volume fraction and the consequently negligible interactions between fibres. By means of such a calibrated law, the average values of compensated inductance for each cell could be processed to assess whether and to what extent the local concentration of fibres differed from the assumed nominal value.

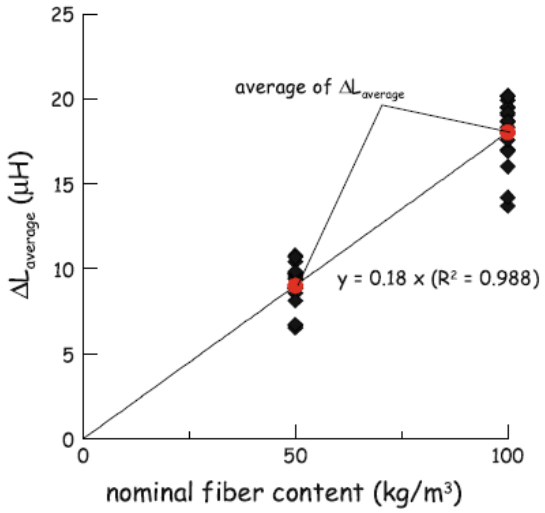

Figure 3.9 – Average compensated inductance versus nominal fibre content

Results are shown in (Figure 3.10). The detected dispersion of the fibres inside the slabs appears to be featured by an acceptable degree of homogeneity and once again coherently understandable on the basis of the casting flow kinematics. It can be observed that the initial higher peak in the fibre content, which is most likely due to the onset of the laminar casting flow after the turbulence which occurs where the fresh cementitious composite was poured, was followed by a slight progressive impoverishment of the fibres (anyway lower than 20%) along the flow, as a result of a dynamic segregation, which to some extent seems to be unavoidable.

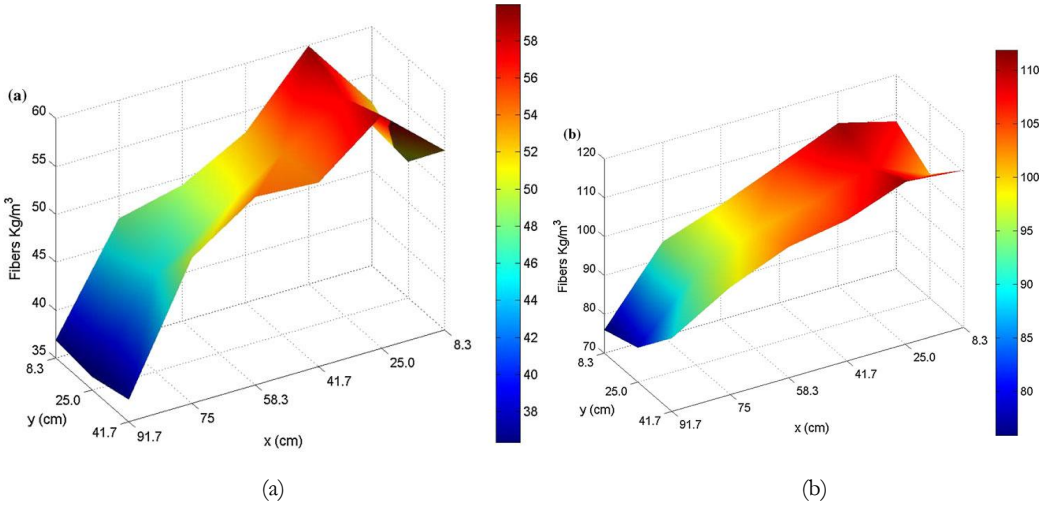

(a) (b)

Figure 3.10 – ND measurements on local concentrations of fibres: (a) FRCC-50 and (b) FRCC-100

3.1.4 Correlation of non-destructive and destructive measurements to tensile fracture toughness

After magnetic survey, each FRCC slab was cut into eighteen tiles and tensile fracture toughness tests were performed on those specimens with a notch-preordained fracture plane either orthogonal or parallel (respectively odd and even numbered cells) to the casting flow direction and hence to the preferential orientation of the fibres employing the DEWS test geometry described below.

3.1.4.1 Double Edge Wedge Splitting test – DEWSt

An indirect technique known as Double Edge Wedge Splitting test developed by [di Prisco et al., 2010; Ferrara et al., 2010] has been employed hereafter to characterize the tensile strength and post crack behaviour of FRC composites. The geometry of sawn specimens from the slab is shown in (Figure 3.11a) The compressive load P is applied through two steel cylinders supported on steel plates at 45 on the V shaped grooves to generate pure tensile state over the ligament by deviating compressive loading through arching action (Figure 3.12b). The principle is the same as in brazilian splitting test: apply longitudinal compression to induce transverse tension. In the DEWS specimen, as discussed above, the wedge shaped grooves deviate the trajectories of compressive stresses far from the ligament, along which is pure tensile stress is applied (due to transverse tensile stresses generated through wedging action by the applied load). Transverse tensile stresses and longitudinal compressive stresses are always coupled and this is a drawback in high performance materials because of t he confinement of fibres which can alter the measured performance. Thus, the analytical expression based on flow of forces for estimation the force in tension provided by [Timoshenko, 1951] is valid just on pre-cracking stage, provided by equation (3.9).

$$F_{sp} = \frac{2}{\pi} P \tag{3.9}$$

The contact between steel plates and the cylinders was lubricated by graphite to minimize the friction contribution. The friction coefficient has been experimentally quantified. By definition of the equilibrium between applied compressive load P and tensile load applied at ligament F_{sp} as in (Figure 3.12b), it comes out that equation (3.10) is valid all along the loading path. An S shaped load cell was used to measure the transverse force during axial

loading and unloading process the splitting force was quantified equal to equation (3.11), which friction coefficient corresponds to a estimated equal to $\mu = 0.06$ (Figure 3.11c). Assuming the uniformity of the stress and strain distribution over the cross-section all along the loading path the nominal tensile stress can be calculated as in equation (3.12); t – specimen thickness and h_{lig}– ligament depth. To establish a Stress vs. COD relationship, the crack opening displacement have been measured by LVDT (at this specific case the measuring length is 50 mm) on both faces of the specimen at the upper and lower tip of the notch and in the centre. of both faces. As whole 6 LVDTs were employed.

$$F_{sp} = P\frac{\cos\vartheta - \mu\sin\vartheta}{\sin\vartheta + \mu\cos\vartheta} \tag{3.10}$$

$$F_{sp} = 0.89P \tag{3.11}$$

$$\sigma_n = \frac{F_{sp}}{th_{lig}} \tag{3.12}$$

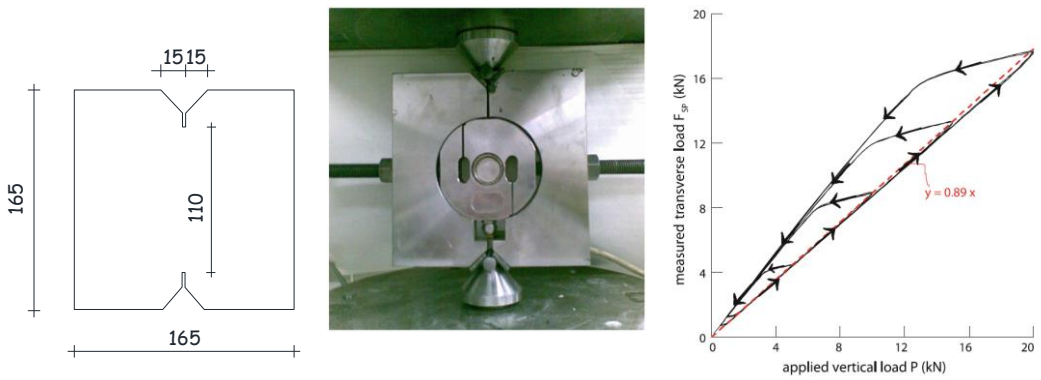

(a) (b) (c)

Figure 3.11 – (a) Geometry of the specimen; (b) setup for determination of friction coefficient and (c) loading-unloading curve

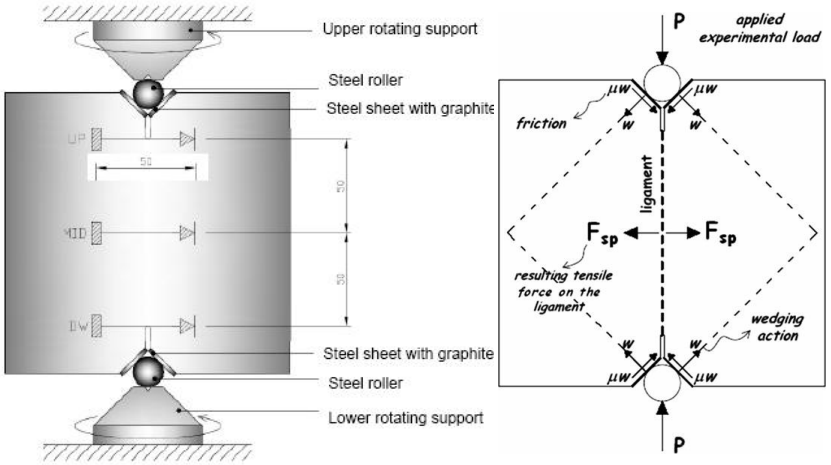

(a) (b)

Figure 3.12 – (a) Position of LVDTs and (b) free body force scheme

Figure 3.13 – View of a specimen on the loading setup

Each cut tile specimens were employed to identify the tensile stress-crack opening behaviour of the composite according to a novel testing methodology called the Double Edge Wedge Splitting test explained above. The groove and notch cutting was done in such a way that the preordained fracture plane resulted either parallel or perpendicular to the preferential flow-induced fibre alignment. The test were performed using an electromechanical machine Instron 8562 with maximum capacity of 100 kN, the load is applied in terms of displacement with velocity ranging between 0.2÷0.5 μm/s, in general is followed the concept that before the first cracking is used lower velocity as further increase of crack width is associated with increased velocity. Usually to perform a single test it requires around 2h. It is important to highlight for this type of test it is not required a closed loop machine as the material possesses stable residual strength.

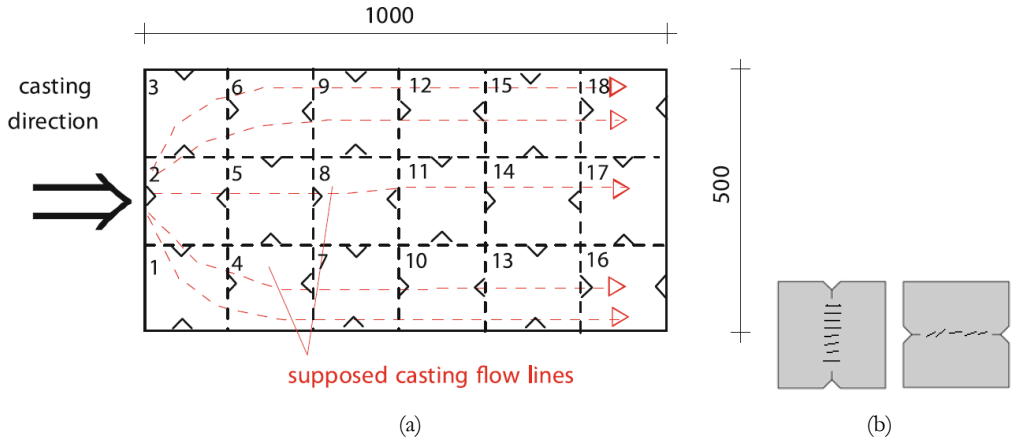

Figure 3.14 – (a) Casting procedure and extraction of DEWS specimens and (b) supposed flow driven orientation of fibres

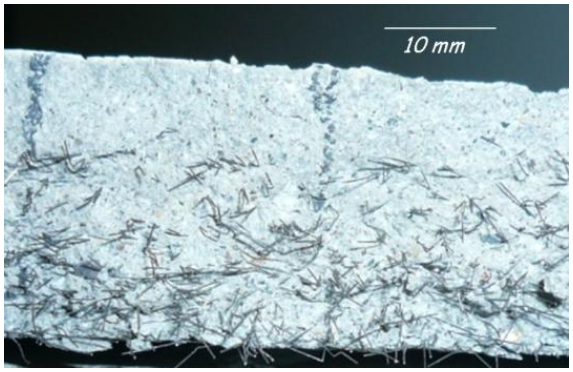

Figure 3.15 – Fibre segregation

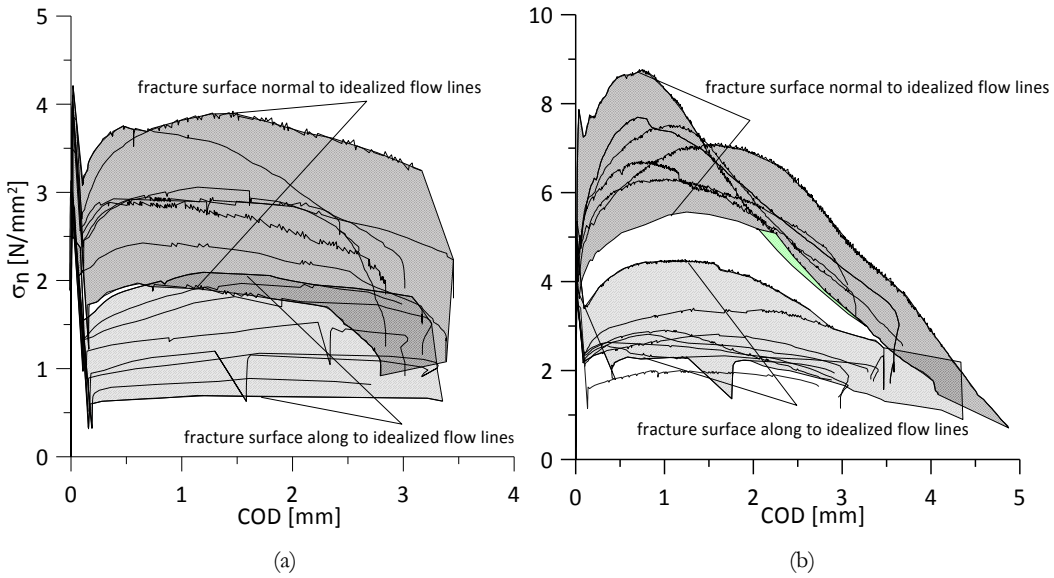

Figure 3.16 – Nominal Stress-COD curves: DEWS tests from: (a) FRCC-50 and (b) FRCC-100 slabs

The experimental results, shown in (Figure 3.16a) the case HPFRCC with 50 kg/m^3 fibre content, in terms of tensile stress vs. Crack Opening Displacement (COD), highlight that the material has post-cracking softening performance in all tested specimens. Whereas, for the case of HPFRCC with 100 kg/m^3, shown in (Figure 3.16b), the same material can exhibit either hardening or softening post-cracking behaviour in tension, which depends mainly on local density and alignment of fibres.

The mechanical experimental evidences show a large scattering of the results due to flow induced alignment and also local dispersion of the fibres to the applied tensile stress. Though, it is obvious that supposed flow lines play an important role on the favourable fibre alignment with respect to direction of the applied tensile load. Moreover, it was observed the downward settlement of fibres occurred by their higher specific gravity (Figure 3.15).

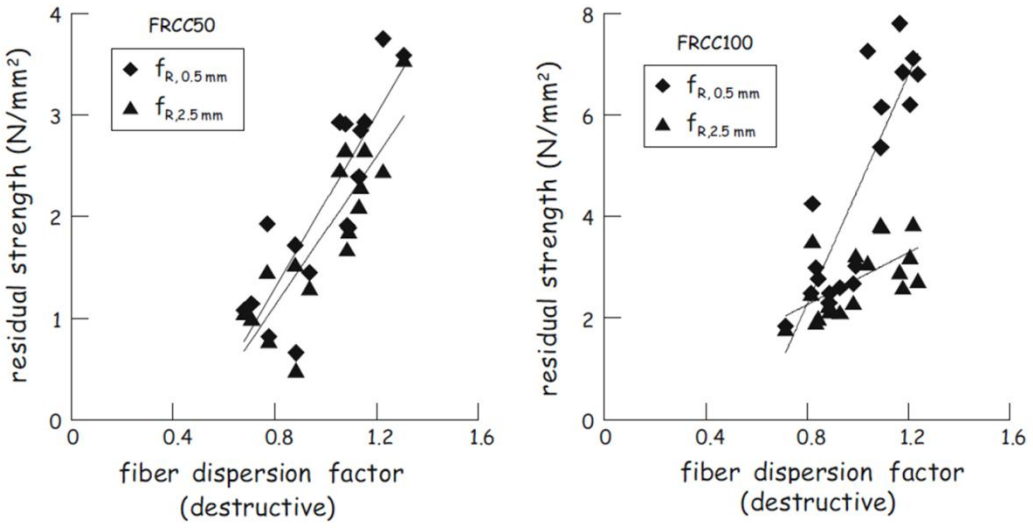

Figure 3.17 – Material fracture toughness parameters versus fibre dispersion factor destructively measures

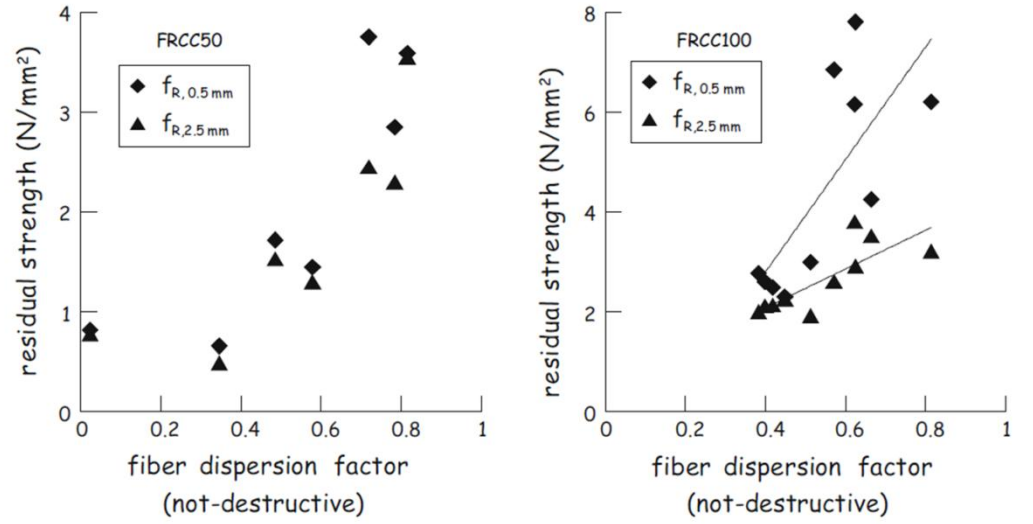

Figure 3.18 – Material fracture toughness parameters versus fibre dispersion factor non destructively measures

A local "fibre dispersion factor" can be hence calculated as the product between the fibre concentration factor, either destructively or non-destructively evaluated, and, respectively, either the fibre orientation factor α or the fractional compensated inductance in the direction normal to the ligament $f_{\perp,lig}$.

The residual stresses at a COD value equal to either 0.5 mm (f_{R1}) or 2.5 mm (f_{R3}) has been taken as representative of material behaviour, e.g. at SLS and ULS. For specimens exhibiting a pre- peak multiple cracking, the aforementioned COD limits were measured with reference to the COD value at peak stress. Correlation between tensile fracture toughness parameters and the fibre dispersion factor defined as above are plotted in (Figure 3.17 and Figure 3.18) for the different investigated cases and with reference to both destructive measurements and non-destructive estimates. In a code-wise perspective, an estimate could be provided from

such calibrated relationships of the orientation factor to be applied to design material parameters to take into account the effects of either favourable or unfavourable fibre orientation.

After the aforementioned tests had been completed, specimens were broken along the ligament and, also through the aid of micro-imaging, fibres protruding from either side of the fracture surface were counted.

Fibre orientation factor was calculated as $\alpha = n_f(A_f/V_f)$, with n_{fibres} specific number of fibres on the cross section, A_f cross-section area of the single fibre and V_f nominal fibre volume fraction. It can be noticed that α is reliably correlated to the fractional compensated inductance in the same direction (Figure 3.19).

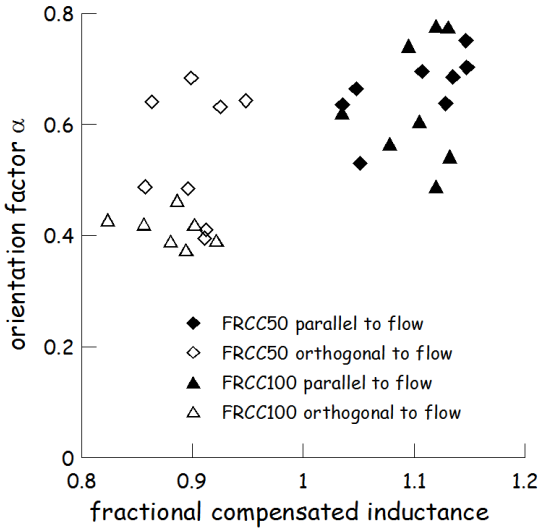

Figure 3.19 – Fibre orientation factor α (from destructive test) vs. fractional compensated inductance from non-destructive measurements

Finally destructive evaluation of fibre concentration was performed by crushing specimens into a cast iron pot, separating fibres with a magnet and weighing them; weight was then referred to the measured dimensions of each specimen. Such an operation, because of its time consumption and labour intensiveness, was performed for a limited number of specimens (actually 10 out of 18 for each slab) and namely the ones which appear shadowed in (Figure 3.3a).

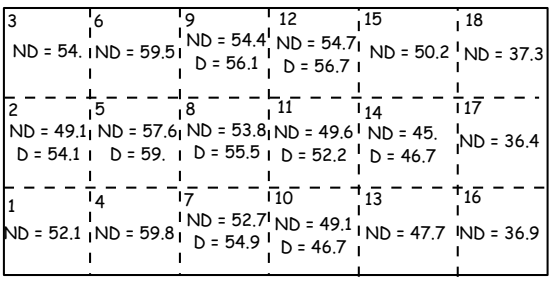

(a)

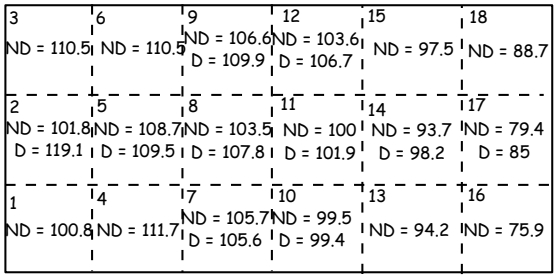

(b)

Figure 3.20 – Fibre concentration: ND vs. destructive for: (a) FRCC-50 and (b) FRCC-100

Local average concentration of fibres, as from specimen crushing and fibre weighing, has been finally correlated to the one estimated from non-destructive measurements. Results shown in (Figure 3.20) highlight a reasonably homogeneous fibre dispersion inside the elements and coherent with the hypothesized casting flow kinematics. The reliability of the current non-destructive evaluation is confirmed by aforementioned correlation between destructive and non-destructive testing, by measuring the same quantities, except in the tile 2 of the case FRCC-100 which coincides with point where the cementitious composite was poured.

3.2 Continuum damage modelling

In order to validate the identification procedure of the stress-crack opening behaviour of FRCC, a finite element analysis has been performed with reference to experimental cases based on damage mechanics. To the purpose of the analysis the "crush crack" damage model has been employed. A "crush-crack" damage model has been firstly developed by [di Prisco et al., 1996] considering damage as isotropic, internal and scalar variable that allows decoupling between cracking and crushing phenomenon of concrete. It has been proven to be a reliable and well calibrated [Ferrara et al., 2001] tool to predict complex conventional concrete structural behaviour under complex monotonic loadings paths with reference to several sets of experiments. The model describes the concrete failure as a combination of three basic failure modes (uniaxial tension, uniaxial and biaxial compression). Thus, it required the identification of material response under these conditions by constitutive laws to be assigned in the model, by reduced number of points or as many parameters of any kind of the analytical curve.

Benefiting from its formulation, the crush-crack damage model has been explored also to be applied to predict the material behaviour of fibre reinforced cementitious composites.

3.2.1 Scalar damage model – [Mazars, 1984]

From historical point of view the first significant tentative to model accurately the stress-strain response of concrete in the framework of damage mechanics has been done in early 1980s [Krajcinovic, 1984; Mazars, 1984]. In the Mazars model the material is assumed elastic and to remain isotropic during loading and its elastic behaviour is coupled with a damage evolution law to provide decay of elastic stiffness in the softening branch of the material. According to Mazars the damage essentially depends on principal tensile deformation.

The model formulation adopts the widely used concept for representation of damage based through effective stress, proposed by [Kachanov, 1986] and employed by [Lemaitre, 1996] mainly for ductile materials. Let σ be the nominal stress defined as a force per unit initial area S. And $\tilde{\sigma}$ is effective stress that relates the area which effectively supports the load, which is the actual stress at microstructure illustrated in (Figure 3.21).

$$\tilde{\sigma} = \frac{F}{S - S_D} \tag{3.13}$$

becomes,

$$\tilde{\sigma} = \frac{\sigma}{1 - D} \tag{3.14}$$

where,

$$D = \frac{S_D}{S} \tag{3.15}$$

S_D – surface of voids and micro-cracks;

S – total area of the cross section is stress bearing surface;

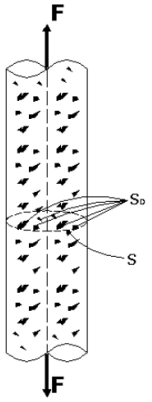

Figure 3.21 – Uniaxial damaged element

The damage is presented as an internal variable D and is defined as the net area of a unit surface for a given plane corrected by the presence of micro-cracks. Assuming that the damage state at any material point is isotropic, it can be represented as a single scalar parameter varying between 0 and 1, where 0 stands for a completely intact material and 1 corresponds to the rupture of the element (zero stress).

The constitutive law can be written $\tilde{\sigma} = \Lambda_0 (1 - D) : \varepsilon^e$ (3.16);

Λ_0 - is the initial stiffness matrix of fourth order.

The loading surface is formulated by Mazars through maximum principal strain and becomes:

$$f = \tilde{\varepsilon} - K(D) \tag{3.17}$$

With $\tilde{\varepsilon}$ equivalent strain that is a function of positive part of the strain tensor $\langle \varepsilon_i \rangle_+$, the $\langle\ \rangle$ indicate the McAuley or angle brackets, provides a closed solution of positive or negative part, according to the sign in index.

$$\langle \varepsilon_i \rangle_+ = \varepsilon_i \quad \text{if} \quad \varepsilon_i \geq 0 \tag{3.18}$$

$$\langle \varepsilon_i \rangle_+ = 0 \quad \text{if} \quad \varepsilon_i < 0 \tag{3.19}$$

$$\tilde{\varepsilon} = \sqrt{\sum_1^3 \left(\langle \varepsilon_i \rangle_+ \right)^2} \tag{3.20}$$

$K(D)$ is softening parameter and assumes the largest value $K(D) = \max\{\varepsilon_{D0}, \tilde{\varepsilon}\}$, ε_{D0} is strain at onset of which damage starts to grow. The evolution function should satisfy the following rule:

$$f < 0 \quad \Rightarrow \ \dot{D} = 0 \tag{3.21}$$

$$f = 0 \ \text{and} \ \dot{f} < 0 \quad \Rightarrow \ \dot{D} = 0 \tag{3.22}$$

$$f = 0 \ \text{and} \ \dot{f} > 0 \quad \Rightarrow \ \dot{D} > 0 \tag{3.23}$$

$$f\dot{D} > 0 \tag{3.24}$$

Damage D is split in two parts as the weighted sum of D_c and D_t, to take into account the different damage evolution in compression and tension. Damage takes the following form: $D = \alpha_c D_c + \alpha_t D_t$, if e.g. the case of uniaxial tension is when $\alpha_t = 1,\ \alpha_c = 0 \Rightarrow D = D_t$.

The weight functions are defined as:

$$\alpha_t = \sum_{i=1}^{3} H_i \frac{\varepsilon_{ti}(\varepsilon_{ti} + \varepsilon_{ci})}{\tilde{\varepsilon}^2} \tag{3.25}$$

$$\alpha_c = \sum_{i=1}^{3} H_i \frac{\varepsilon_{ci}(\varepsilon_{ti} + \varepsilon_{ci})}{\tilde{\varepsilon}^2} \tag{3.26}$$

And damage evolution laws are defined as

$$D_t = 1 - \frac{\varepsilon_{t0}(1 - A_t)}{\tilde{\varepsilon}} - \frac{A_t}{\exp[B_t(\tilde{\varepsilon} - \varepsilon_{t0})]} \tag{3.27}$$

$$D_c = 1 - \frac{\varepsilon_{D0}(1 - A_c)}{\tilde{\varepsilon}} - \frac{A_c}{\exp[B_c(\tilde{\varepsilon} - \varepsilon_{D0})]} \tag{3.28}$$

$\varepsilon_{t0} = \frac{f_t}{E}$ is the threshold for damage initiation; A_t, A_c, B_t and B_c are empirical parameter to be determined based uniaxial tension and compression tests.

3.2.2 "Crush-crack" damage model

The "crush crack" damage model was developed to better capture the behaviour of concrete under multi-axial loadings. It considers as a starting point the damage model developed by Mazars, maintaining the damage as scalar isotropic. It introduces an additional internal variable δ to control the reversible transverse strains in elastic regime by correlating the Poisson coefficient with the accumulated damage in compression, furthermore it introduces the irreversible strains.

The inelastic strain tensor is expressed as superposition of reversible strain tensor to relate with cracking and irreversible strains tensor to relate with crushing.

$$\varepsilon_{ij} = \varepsilon_{ij}^{el} + \varepsilon_{ij}^{ir} = \varepsilon_{ij}^{el} + \varepsilon_{ij+}^{ir} + \varepsilon_{ij-}^{ir} = \varepsilon_{ij-}^{*} + \varepsilon_{ij-}^{ir} \tag{3.29}$$

The stress relationship is characterized by internal variable D, and δ;

$$\sigma_{ij} = \frac{E_0(1 - D)}{1 + \nu_0(1 + \delta)} \varepsilon_{ij}^{el} + \frac{E_0(1 - D)\nu_0(1 + \delta)}{[1 + \nu_0(1 + \delta)][1 - 2\nu_0(1 + \delta)]} \varepsilon_{ij}^{el} \delta_{ij} \tag{3.30}$$

δ_{ij} – Kronecker symbol;

According to this description of damage, it may be assumed that the concrete remains isotropic in its mechanical behaviour, but it also shows induced anisotropy by introducing the inelastic strains.

$$\left\langle \varepsilon_i^* \right\rangle_+ = \varepsilon_i^* \quad \text{if} \quad \varepsilon_i^* \geq 0 \tag{3.31}$$

$$\left\langle \varepsilon_i^* \right\rangle_+ = 0 \quad \text{if} \quad \varepsilon_i^* < 0 \tag{3.32}$$

$$\tilde{\varepsilon} = \sqrt{\sum_{1}^{3}\left(\left\langle \varepsilon_i^* \right\rangle_+\right)^2} \tag{3.33}$$

ε_i^* – principal strains;

The elastic domain before reaching the damage threshold surface is defined by:

$$F(\bar{\varepsilon}_+) = \bar{\varepsilon}_+ - \varepsilon_{t0} \le 0 \tag{3.34}$$

Damage is activated when F=0, afterwards the yield surface is described by $F = F_1 \cup F_2$ with:

$$F_1 = \alpha_c D_c(\bar{\varepsilon}_+) + \alpha_t D_t(\bar{\varepsilon}_+) - D \le 0 \tag{3.35}$$

$$F_2 = \alpha_c \delta_c(\bar{\varepsilon}_+) - \delta \le 0 \tag{3.36}$$

And the evolution function should satisfy the following rule:

$$F_1 < 0 \text{ with } \dot{D} = 0 \tag{3.37}$$

$$\dot{F}_1 \dot{D} = 0 \text{ with } \dot{D} \ge 0 \text{ and } \dot{F}_1 < 0 \tag{3.38}$$

$$F_2 < 0 \text{ with } \dot{\delta} = 0 \tag{3.39}$$

$$\dot{F}_2 \dot{\delta} = 0 \text{ with } \dot{\delta} \ge 0 \text{ and } \dot{F}_2 < 0 \tag{3.40}$$

α_t and α_c are the weight functions defined as:

$$\alpha_t = \sum_{i=1}^{3} \frac{\varepsilon_{ti}^{el}\left(\varepsilon_{ti}^{el} + \varepsilon_{ci}^{el}\right)}{\tilde{\varepsilon}_+^{el}} \tag{3.41}$$

$$\alpha_c = \sum_{i=1}^{3} \frac{\varepsilon_{ci}^{el}\left(\varepsilon_{ci}^{el} + \varepsilon_{ci}^{el}\right)}{\tilde{\varepsilon}_+^{el}} \tag{3.42}$$

Finally, to improve the algorithm to have a stable numerical solution, [Ferrara, 1998] modified 'crush-crack' by introducing the total energies dissipated in tension g_t and compression g_c.

$$\alpha_t = \frac{\sum_{i=1}^{3}\int_0^t \frac{\langle \sigma_i \rangle_+ \langle \varepsilon_i \rangle_+}{g_t} dt}{\int_0^t \left(\sum_{i=1}^{3}\int_0^t \frac{\langle \sigma_i \rangle_+ \langle \varepsilon_i \rangle_+}{g_t} + \sum_{i=1}^{3}\int_0^t \frac{\langle \sigma_i \rangle_- \langle \varepsilon_i \rangle_-}{g_c} dt \right)} \tag{3.43}$$

Ensuring the complementary condition $\alpha_t + \alpha_c = 1$.

The non-local invariance is introduced to control the associated damage law depending on the 3 failure modes.

$$\bar{\varepsilon}_{+}(x) = \frac{1}{V_r(x)} \int_V \tilde{\varepsilon}_{+}(s)\varphi(s-x)dV \tag{3.44}$$

x – coordinate vector for and internal point in continuum.

φ – averaging weight function.

s – vector describing the neighbouring point x.

3.3 Constitutive laws

The "crush-crack" damage model requires as input to assign the constitutive relationships. Thus, in the following are presented in detail the adopted constitutive laws used for numerical modelling, which are defined for uniaxial compression and tension.

3.3.1 Uniaxial Compression Constitutive law

The stress strain relationship for the concrete in compression hereafter has been adopted from the prescriptions of the [*fib* Model Code 2010], as shown in (Figure 3.22).

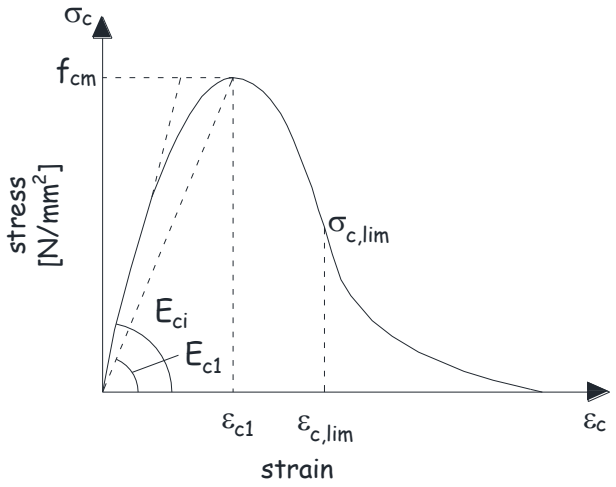

Figure 3.22 – Constitutive law for concrete behaviour in compression

Described by the following parabolic curve:

$$\frac{\sigma_c}{f_{cm}} = -\left(\frac{k\eta - \eta^2}{1+(k-2)\eta}\right) \quad \text{if} \quad |\varepsilon_c| < |\varepsilon_{c,lim}| \tag{3.45}$$

Where:

$$\eta = \frac{\varepsilon_c}{\varepsilon_{c1}} \tag{3.46}$$

$$k = \frac{E_{ci}}{E_{c1}} \tag{3.47}$$

k – is the plasticity number.

ε_c – is the strain at maximum compressive stress.

E_{c1} – is the secant modulus from the origin to the peak compressive stress.

3.3.2 Uniaxial Tension

The tensile strength of concrete is not explicitly used in design calculations. Even that it is well known fact that the shear failure of the various concrete structural elements lightly reinforced is indirectly governed by the tensile cracking of the concrete making this property essential to properly identified evidently by testing. The wide experimental investigations by 14 different labs reported [Hillerborg, 1985] has established that the tensile strength and fracture toughness could be related as a constitutive property of the material in mode I. It is highlighted the test procedure should give representative values of fracture toughness, as results may be contradictory from type of testing geometry and applied load, size of the specimen with respect to maximum aggregate size and boundary conditions. Theoretically the most straightforward way to determine the above mention property is the direct tension test. In practice this procedure becomes cumbersome to be performed as it requires stiff machine, and as a consequence the size of the specimen has to be limited. Moreover there is the need of guaranteeing high bond between plates and the specimen.

Regarding the presence of fibre in cementitious composites, experimental results have shown that the orientation of fibres, triggered by the casting flow, may generate an orthotropic material behaviour. Based on these considerations, a different procedure has been herein adopted to describe the mechanical response of cementitious composite in tension, whether strain softening (for unfavourable fibre orientation) or hardening (for favourable orientation). Based on [*fib* Model Code 2010] analogy the pre-crack is defined by stress strain description and post-crack with stress-crack opening displacement.

3.3.3 Strain softening constitutive law – Consideration on conventional concrete

The stress-strain curve for the plain matrix recommended in [*fib* Model Code 2010] prescription is adopted for modelling of plain concrete. The tensile strength and fracture energy are evaluated from measured compressive strength experimentally. The constitutive relationship consist of four branches; firstly it has been specified the linear elastic branch up to 90% of tensile strength; afterwards to consider the micro crack formation, a further ascending branch up to tensile strength and a strain equal to 0.015% is considered; at this point hence localization occurs. After crack localization there is linear softening descending until the residual strength reaches the 15% of tensile strength and the slope is estimated based on fracture energy release by definition of first crack opening displacement w_1; the softening continues with reduced slope linearly until there is no residual tensile strength respectively ultimate crack opening displacement.

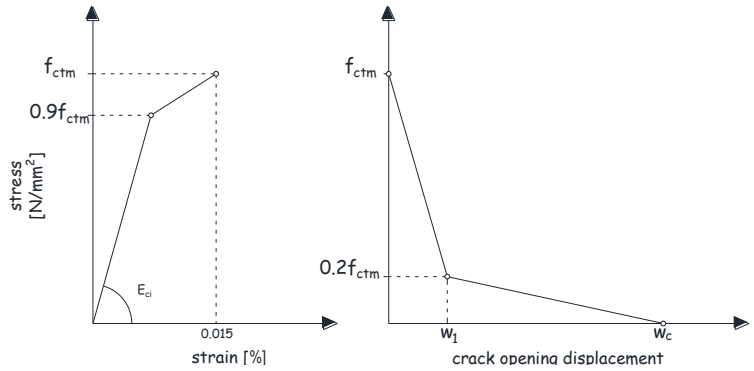

Figure 3.23 – Constitutive law for concrete to describe strain softening of conventional concrete

The analytical formulation and the parameters defining the constitutive relationship are shown in (Figure 3.23).

$$\begin{cases} \sigma_{ct} = E_{ci}\varepsilon_{ct} & \text{if} \quad \sigma_{ct} \le 0.9f_{ctm} \quad (3.48) \\ \sigma_{ct} = f_{ctm} - \dfrac{0.1f_{ctm}\left(0.00015 - \varepsilon_{ct}\right)}{0.00015 - \dfrac{0.9f_{ctm}}{E_{ci}}} & \text{if} \quad 0.9f_{ctm} < \sigma_{ct} \le f_{ctm} \quad (3.49) \\ \sigma_{ct} = f_{ctm}\left(1 - 0.8\dfrac{w}{w_1}\right) & \text{if} \quad w \le w_1 \quad (3.50) \\ \sigma_{ct} = f_{ctm}\left(0.25 - 0.05\dfrac{w}{w_1}\right) & \text{if} \quad w_1 < w \le w_c \quad (3.51) \end{cases}$$

E_{cm}– elastic modulus (N/mm^2).

f_{ctm}– tensile strength (N/mm^2).

σ_{ct}– tensile stress (N/mm^2).

ε_{ct} – tensile strain.

$$w_1 = 2\frac{G_f}{f_{ctm}} - 0.15w_c \quad (3.52)$$

$$w_c = \alpha_f \frac{G_f}{f_{ctm}} \quad (3.53)$$

w – the crack opening (mm).

w_1 – the crack opening (mm) at $\sigma_{ct}=0.15f_{ctm}$.

w_c – the crack opening (mm) at $\sigma_{ct}=0$.

G_f – fracture energy (Nmm/mm^2).

α_f – coefficient depending on maximum aggregate size defined as in (Table 3.4).

Table 3.4 – Aggregate size coefficient

d_{max} (mm)	8	16	32
α_f	8	7	5

For lower aggregate sizes the α_f is extrapolated accordingly from (Table 3.4).

3.3.4 Strain softening constitutive law – Consideration on FRCC

The tensile behaviour for strain softening description of Fibre Reinforced Cementitious Composites (FRCC) in the un-cracked state is considered to be identical as for the plain matrix since fibres play no role. After the peak strength is attained, there is a sudden release of energy which is hindered by fibre activation, limiting the softening stress along up to a breaking point level f_{bp}.

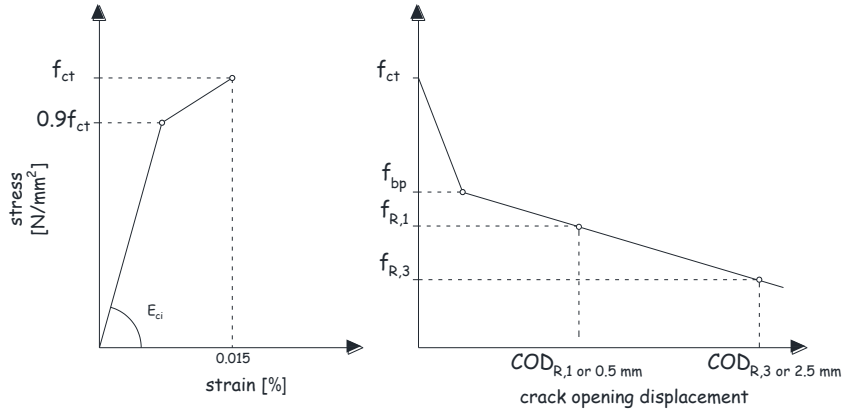

Figure 3.24 – Constitutive law for concrete to describe strain softening of fibre reinforced cementitious composites

The softening branch is defined through the residual strengths ($f_{R,1}$ and $f_{R,3}$) at different levels of crack openings displacements, in correspondence with values equal to 0.5 and 2.5 mm coinciding with (SLS) and (ULS) respectively. The adopted constitutive law is shown in (Figure 3.24) and notifications are explained below.

$$\begin{cases} \sigma_{ct} = E_{ci}\varepsilon_{ct} & \text{if} \quad \sigma_{ct} \le 0.9f_{ct} \quad (3.54) \\ \sigma_{ct} = f_{ct} - \dfrac{0.1f_{ct}\left(\varepsilon_{ct,1} - \varepsilon_{ct}\right)}{\varepsilon_{ct,1} - \dfrac{0.9f_{ct}}{E_{ci}}} & \text{if} \quad 0.9f_{ctm} < \sigma_{ct} \le f_{ct} \quad (3.55) \\ \sigma_{ct} = f_{bp} - \left(f_t - f_{bp}\right)\left(\dfrac{COD_{bp} - COD_t}{\varepsilon_{ct,1}l_{inst} - COD_{bp}}\right) & \text{if} \quad COD_t \le COD_{bp} \quad (3.56) \\ \sigma_{ct} = f_{R,3} - \left(f_{bp} - f_{R,3}\right)\left(\dfrac{COD_{R,3} - COD_t}{COD_{bp} - COD_{R,3}}\right) & \text{if } COD_{bp} < COD_t \le COD_{R,3} \quad (3.57) \end{cases}$$

$$f_{bp} = \frac{AD - BC}{A - C} \quad (3.58)$$

$$COD_{bp} = \frac{D - B}{A - C} \quad (3.59)$$

$$A = \frac{f_{R,3} - f_{R,1}}{COD_{R,3} - COD_{R,1}} \quad (3.60)$$

$$B = f_{R,1} - COD_{R,1}\frac{f_{R,3} - f_{R,1}}{COD_{R,3} - COD_{R,1}} \quad (3.61)$$

$$C = \frac{0.85f_{ct}}{\varepsilon_{ct,1}l_{inst} - COD_w} \quad (3.62)$$

$$D = f_{ct}\left(\frac{0.15\varepsilon_{ct,1}l_{inst} - COD_w}{\varepsilon_{ct,1}l_{inst} - COD_w}\right) \tag{3.63}$$

$\varepsilon_{ct,1} = 0.00015$ – strain at peak stress.

l_{inst} – instrument measuring length.

$$COD_W = \left(\frac{2G_f}{f_t} - \frac{0.15\alpha_f G_f}{f_t}\right) \tag{3.64}$$

f_{ct} – nominal peak stress.

f_{ct} – nominal stress at break point.

$f_{R,1}$ – nominal stress at crack opening displacement COD_1.

$f_{R,3}$ – nominal stress at crack opening displacement COD_3.

3.3.4.1 Strain hardening constitutive law – Consideration on HPFRCC

In the case of strain hardening behaviour, differently from the previous cases, in the branch between ($0.9f_{ct}$ and f_{ct}) it is assumed to be the multiple cracking developments, which after reaching the maximum tensile strength occurs crack localization. The peak strain is obtained from experimental evidences by converting the crack opening displacement measured at peak stress, (COD_{peak}) dividing by the length of the instrument. As well the softening regime is defined by the residual stresses ($f_{R,1}$ and $f_{R,3}$) in correspondence of COD values equal to (COD_{peak}+0.5 mm) and (COD_{peak}+2.5 mm) or (SLS) and (ULS) respectively, illustrated in (Figure 3.25).

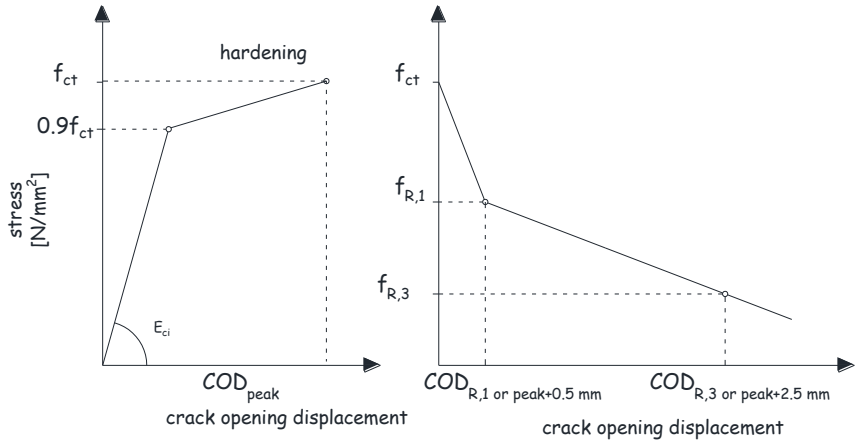

Figure 3.25 – Constitutive law for concrete to describe strain hardening of fibre reinforced cementitious composites

f_{ct} – nominal peak stress.

$f_{R,1}$ – nominal stress at crack opening displacement COD_1.

$f_{R,3}$ – nominal stress at crack opening displacement COD_3.

Piecewise linear function for strain hardening constitutive law.

$$\begin{cases} \sigma_{ct} = E_{ci}\varepsilon_{ct} & \text{if} \quad \sigma_{ct} \le 0.9f_{ct} \quad (3.65) \\ \sigma_{ct} = f_{ct} - \dfrac{0.1f_{ct}\left(\varepsilon_{peak} - \varepsilon_{ct}\right)}{\varepsilon_{peak} - \dfrac{0.9f_{ct}}{E_{ci}}} & \text{if} \quad 0.9f_{ctm} < \sigma_{ct} \le f_{ct} \quad (3.66) \\ \sigma_{ct} = f_{ct} + \left(f_{R,1} - f_{ct}\right)\left(\dfrac{COD_t - COD_{peak}}{COD_{R,1} - COD_{peak}}\right) & \text{if} \quad COD_t \le COD_{R,1} \quad (3.67) \\ \sigma_{ct} = f_{R,1} + \left(f_{R,3} - f_{R,1}\right)\left(\dfrac{COD_t - COD_{R,1}}{COD_{R,3} - COD_{R,1}}\right) & \text{if} \quad COD_{R,1} < COD_t \le COD_{R,3} \quad (3.68) \end{cases}$$

$$\varepsilon_{peak} = \frac{COD_{peak}}{l_{inst}} \quad (3.69)$$

ε_{peak}– strain at nominal peak stress.

$$COD_{R,1} = COD_{peak} + 0{,}5 \text{ mm} \quad (3.70)$$

$$COD_{R,3} = COD_{peak} + 2{,}5 \text{ mm} \quad (3.71)$$

3.3.4.2 Size of fracture process zone

Size of fracture process zone is described as material property that governs the minimum possible width of a zone of strain softening damage. Different authors have suggested different approaches with different meanings to determine it; [Irwin et al., 1958] estimates it as function of elastic modulus, fracture energy and tensile strength where fracture energy is dependent on aggregate size, whereas [Bazant et al., 1989] relates it simply as function of maximum aggregate size.

The softening and localization problems that could be regarded as material instability which are caused by micro-cracks affecting as a result the macrostructure behaviour, it is important to establish the model to be independent from the mesh. Thus, it should be carefully examined the definition on constitutive relations in descending branch. Different energy based regularization techniques are available to avoid spurious mesh sensitivity; as a matter of fact, the "crush-crack" damage model is developed for this purpose on non-local theory. However, in the approach herein followed, the crack opening displacement is converted into strain by dividing with numerical characteristic length equal to $h_{el}=\sqrt{2A_{el}}$.

3.3.5 Numerical modelling

In the framework described above the numerical analyses of the DEWS test have been performed. The mesh employed for the analyses is shown in (Figure 3.26).

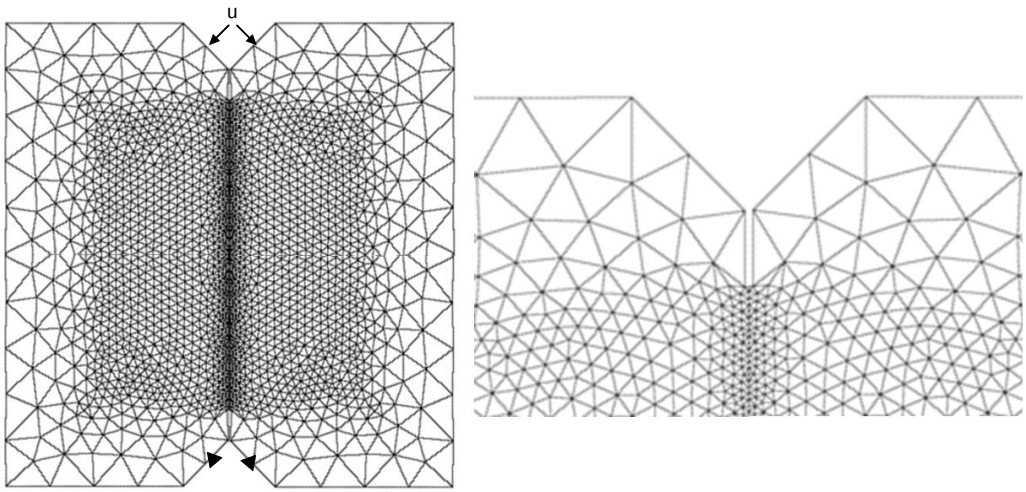

Figure 3.26 – Mesh employed for numerical modelling

Experimental results have shown that the orientation of fibres, triggered by the casting flow, may generate an orthotropic material behaviour. For numerical investigations several curves are selected to be modelled for both cases with 50 kg/m³ and 100 kg/m³. They are priori distinguished between either strain softening/hardening behaviour, and their behaviour in tension has been described by piecewise linear functions as defined above. The values of different parameters describing the employed constitutive laws are summarized in (Table 3.5).

Table 3.5 – Input parameters of constitutive relationships for numerical modelling

Tensile behaviour	Name of specimen				
	4B/Softening	5B/Hardening	9A/Softening	15B/Hardening	6A/Softening
E [N/mm²]	42600	42600	42600	42600	42600
$f_{ct,crack}$ [N/mm²]	3.55	7.87	4.2	5.05	2.79
$f_{ct,peak}$ [N/mm²]	3.55	8.77	4.2	5.61	2.79
COD_{peak} [mm]	-	0.75	-	1.22	-
ε_{peak}	1.50E-04	1.50E-02	1.50E-04	2.44E-02	1.50E-04
$f_{R,1}$ [N/mm²]	2.77	7.11	3.71	5.42	1.68
COD_1 [mm]	0.51	1.25	0.56	1.79	0.52
$f_{R,3}$ [N/mm²]	2.33	3	2.45	4.57	1.91
COD_3 [mm]	2.51	3.25	2.51	2.86	2.57

First of all it was observed that the adopted energy based regularization technique is effective in providing a solution independent on the discretization, as shown in (Figure 3.27). Moreover, not only the effectiveness of the numerical modelling approach is confirmed but also the proposed procedure for the identification of tensile constitutive relationship which can be obtained in a straightforward way from DEWS tests, and this for both strain hardening and softening behaviour with no need for back analyses (Figure 3.28 and Figure 3.29).

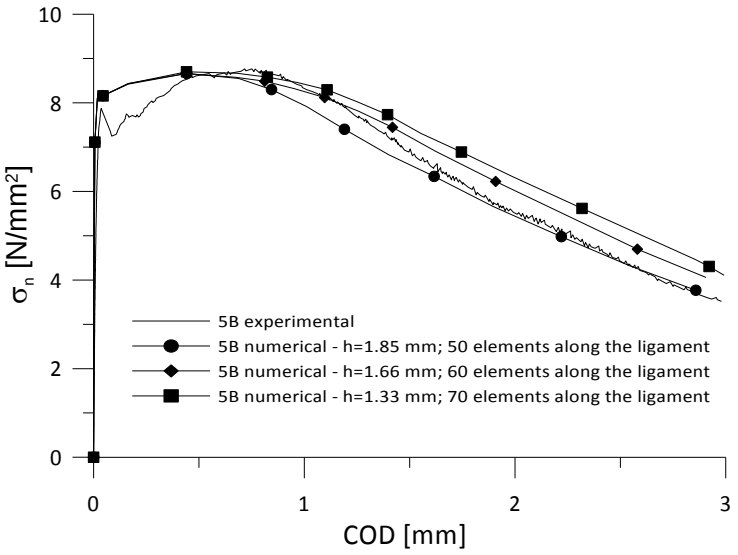

Figure 3.27 – Effect of mesh refinement on numerical results

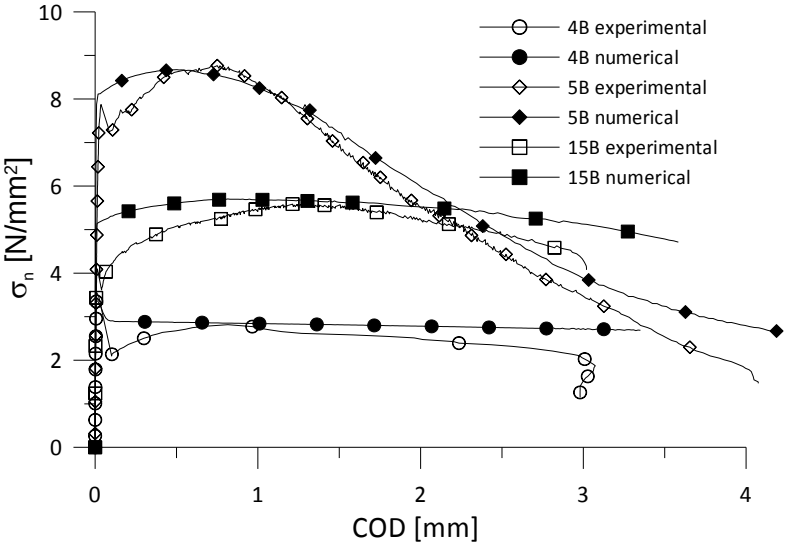

Figure 3.28 – Numerical and experimental comparison for strain softening and hardening specimens for FRCC-100

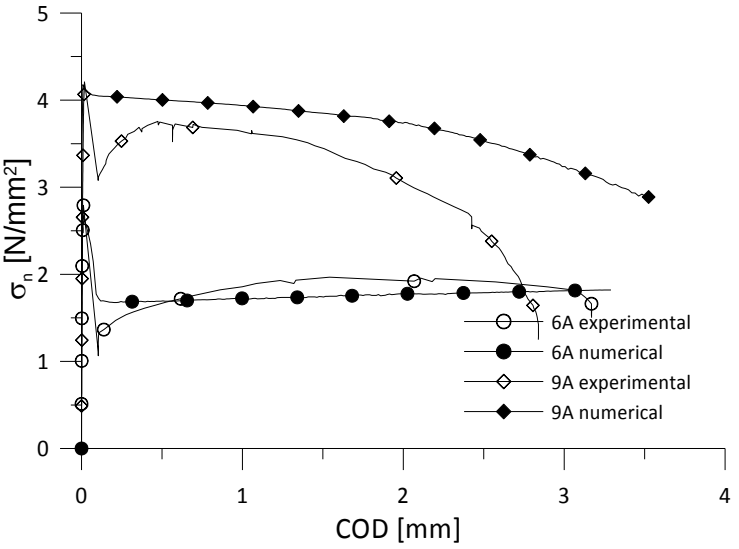

Figure 3.29 – Numerical and experimental comparison for strain softening specimens for FRCC-50

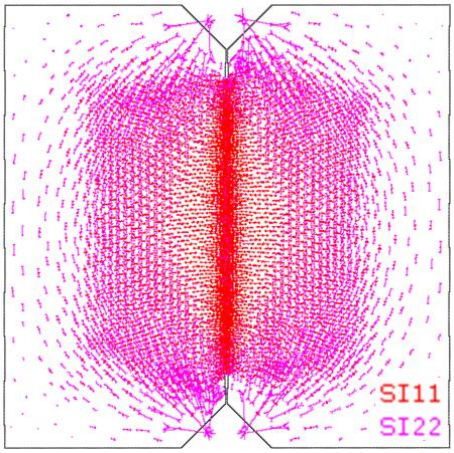

COD_{crack} = 0.03 mm

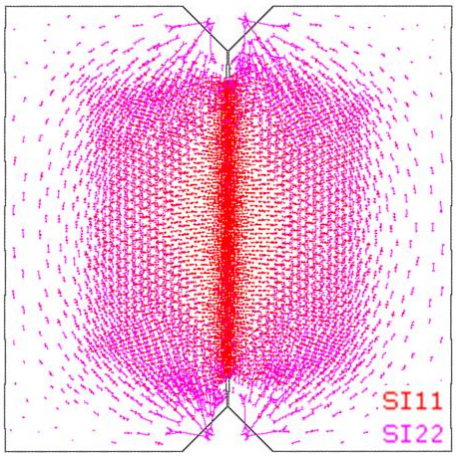

COD = 0.05 mm

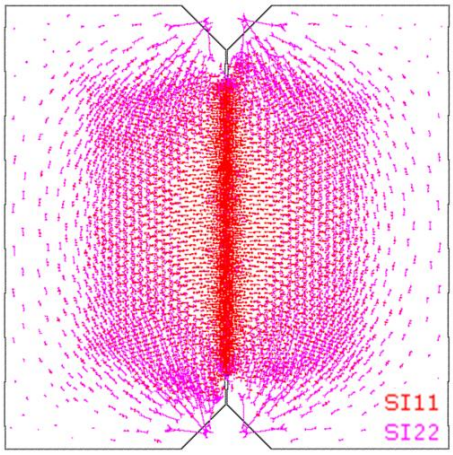

COD = 0.5 mm

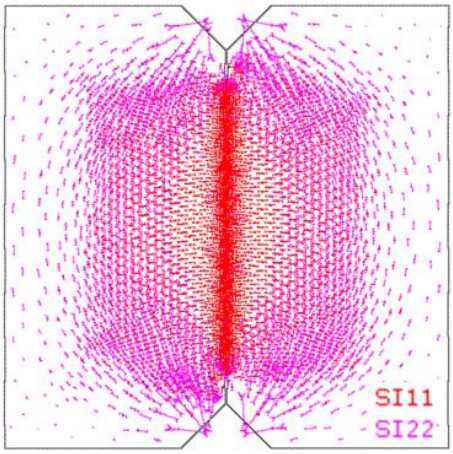

COD = 1.5 mm

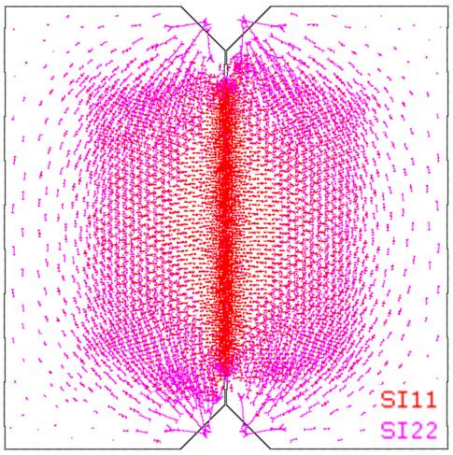

COD = 2.5 mm

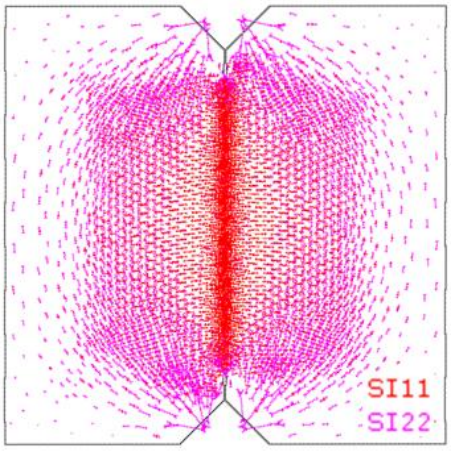

COD = 3.1 mm

Figure 3.30 – Principal stresses evolution at different COD for the specimen 4B (strain softening case; SI11 – tensile; SI22 – compressive)

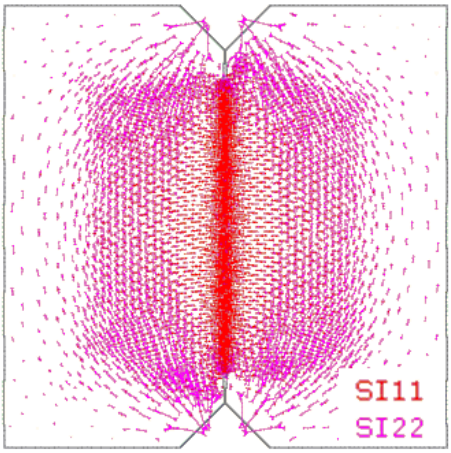

COD_{crack} = 0.05 mm

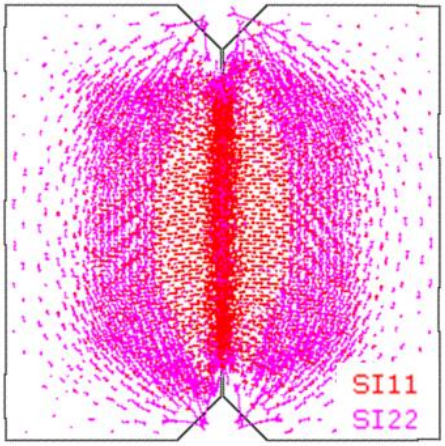

COD = 0.5 mm

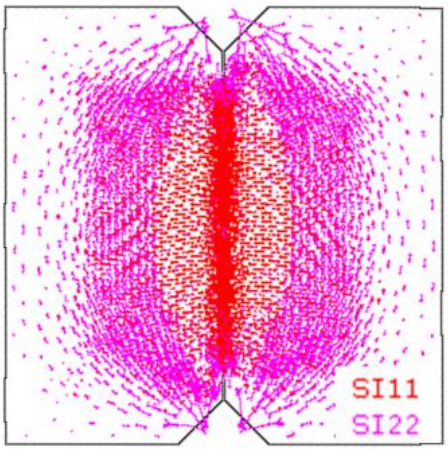

COD_{peak} = 0.75 mm

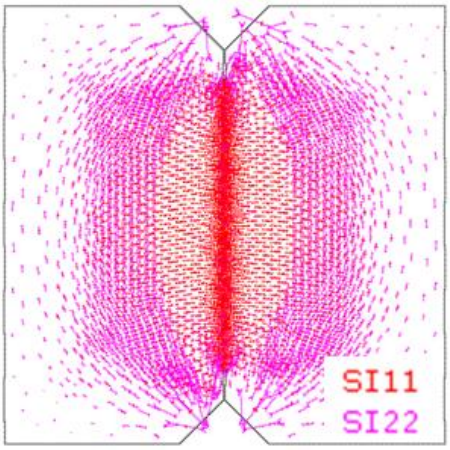

COD = COD_{peak}+ 0.5 mm

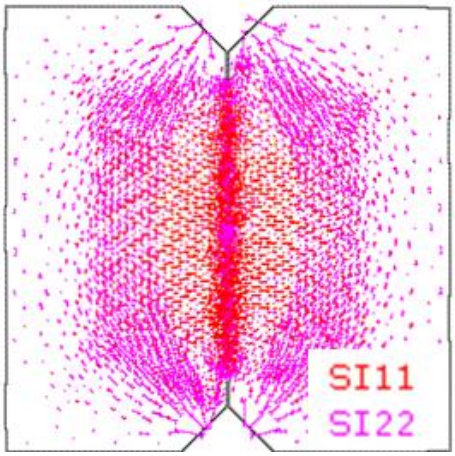

COD = COD_{peak}+ 2.5 mm

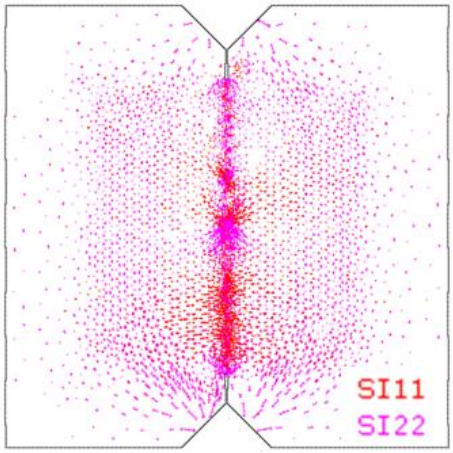

COD = 4.0 mm

Figure 3.31 – Principal stresses evolution at different COD for the specimen 15B (strain hardening case; SI11 – tensile; SI22 – compressive)

From the computed pattern of the principal tensile and compressive stresses (Figure 3.30 and Figure 3.31) it is demonstrated the ability of the test specimen to uncouple tensile and compressive stresses, deviating along arch trajectories the compressive stresses, inducing pure mode I fracture along the ligament, thanks to the wedge shaped groove of the specimen.

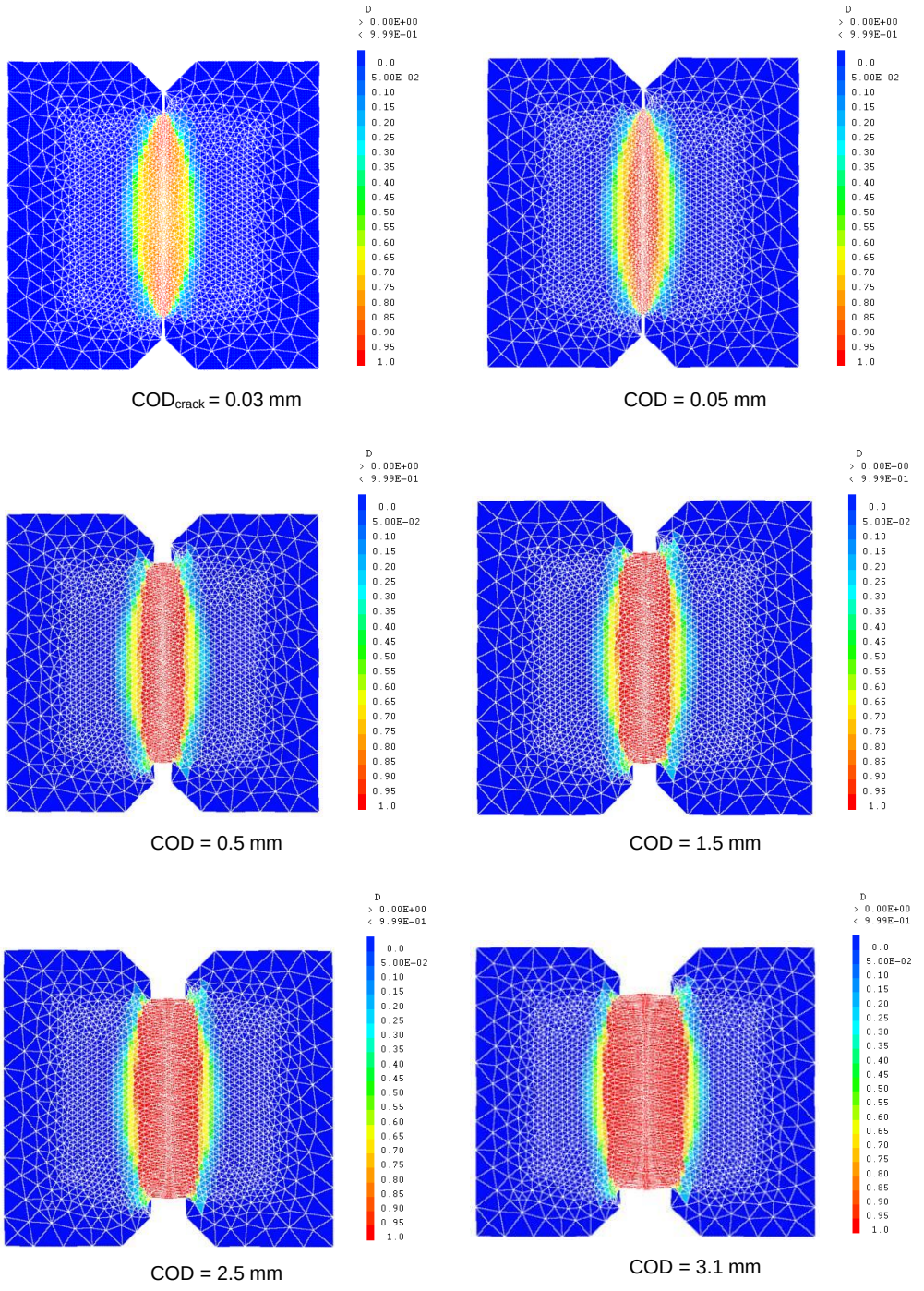

Figure 3.32 – Damage evolution on deformed mesh with amplification factor 9 for the specimen 4B (strain softening case)

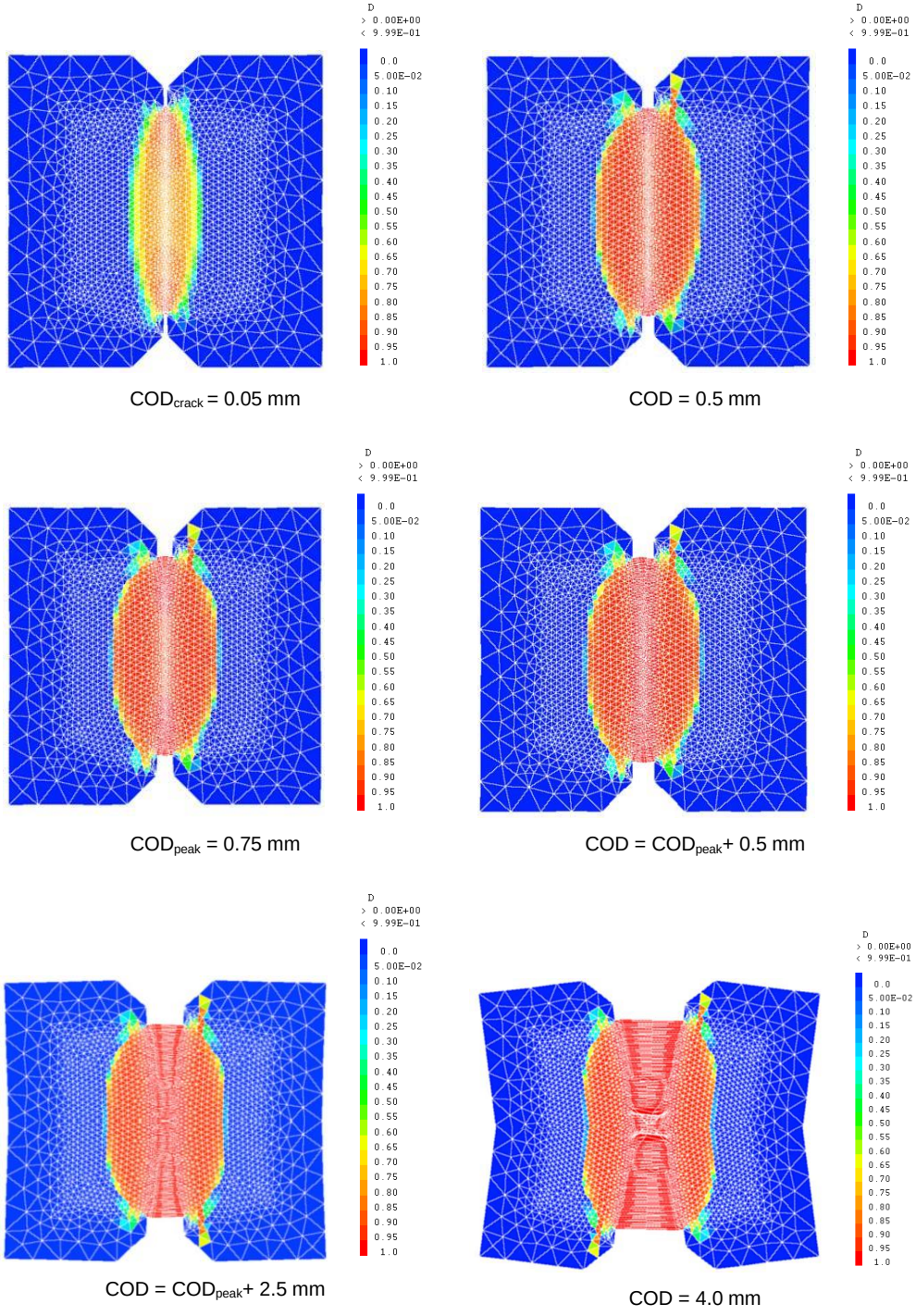

Figure 3.33 – Damage evolution on deformed mesh with amplification factor 9 for the specimen 15B (strain hardening case)

In (Figure 3.32 and Figure 3.33) the damage evolution has been shown with increased applied displacement for both cases of strain softening and hardening behaviour. In the first case localization occurs very early and the width of the damaged zone holds constant all along the loading path. In the latter case the damage spreading in the pre-peak regime is well described as it corresponds with multiple cracking in the hardening stage. Once the crack localizes the damage zone no longer spreads.

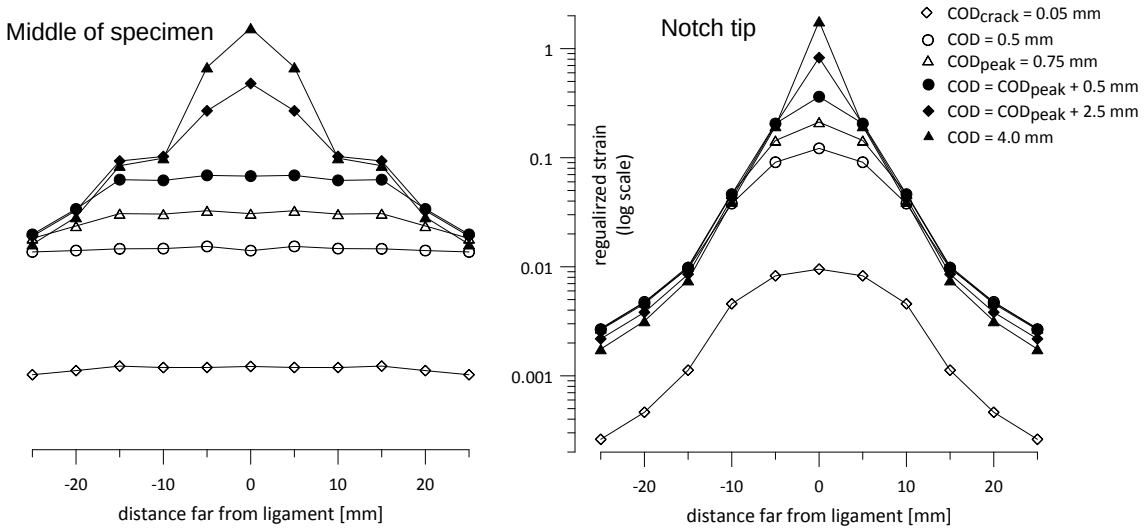

Figure 3.34 – Strain evolution under increased loading at different positions for strain hardening case

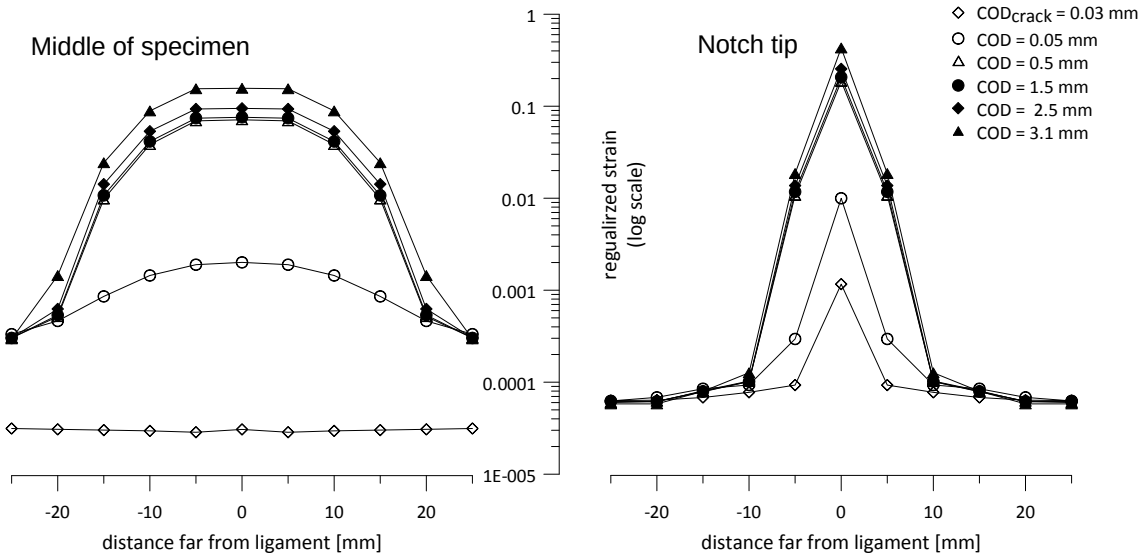

Figure 3.35 – Strain evolution under loading at different positions for strain softening case

A further description and contribution to the aforementioned statements can be found by observing the plots tensile strain norm $\tilde{\varepsilon}$, which governs the damage evolution, in correspondence of same the crack opening displacements values. The values of $\tilde{\varepsilon}$ are extracted in the positions where the LVDTs are placed in the experiments, respectively near to the tips notch and in the centre of the specimen. It could be observed that at the notch tips there is higher peak due to the stresses and strain concentration, whereas in the middle there is more smooth distribution. The strain hardening material features a reasonably uniform straining across the ligament up to the peak, followed by crack localization; this, on the other hand, immediately occurs after first cracking in the case of a strain softening material (Figure 3.34 and Figure 3.35).

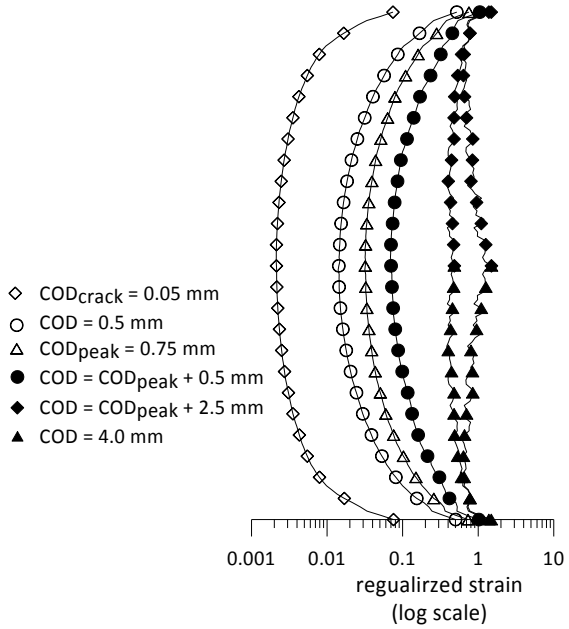

Figure 3.36 – Strain evolution along ligament for specimen for strain hardening case

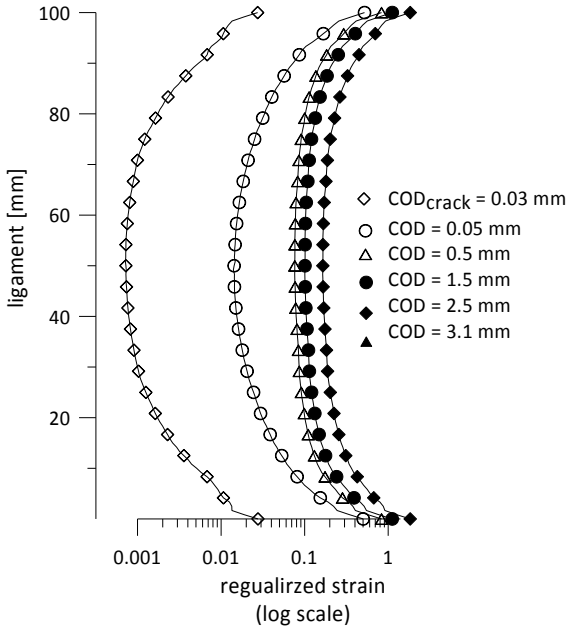

Figure 3.37 – Strain evolution along ligament for specimen for strain softening case

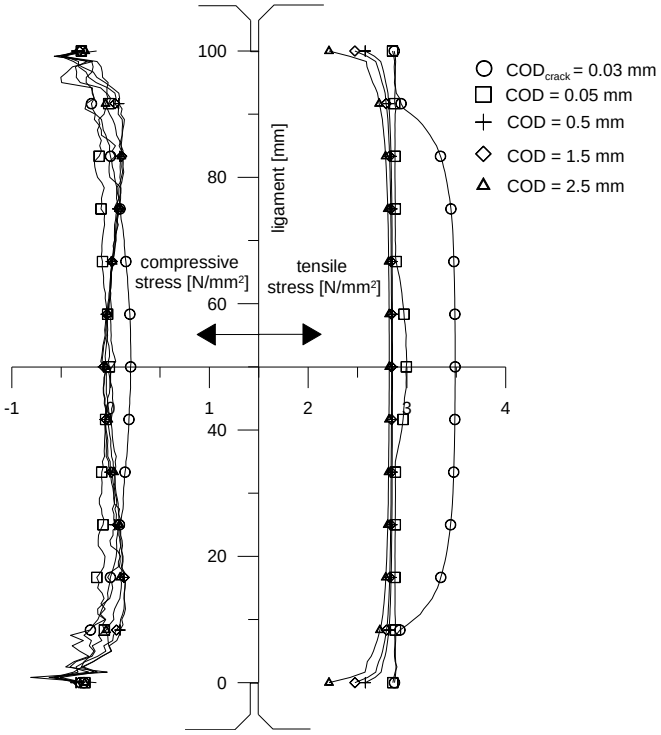

Figure 3.38 – Principal stress evolution with increased displacement for strain softening

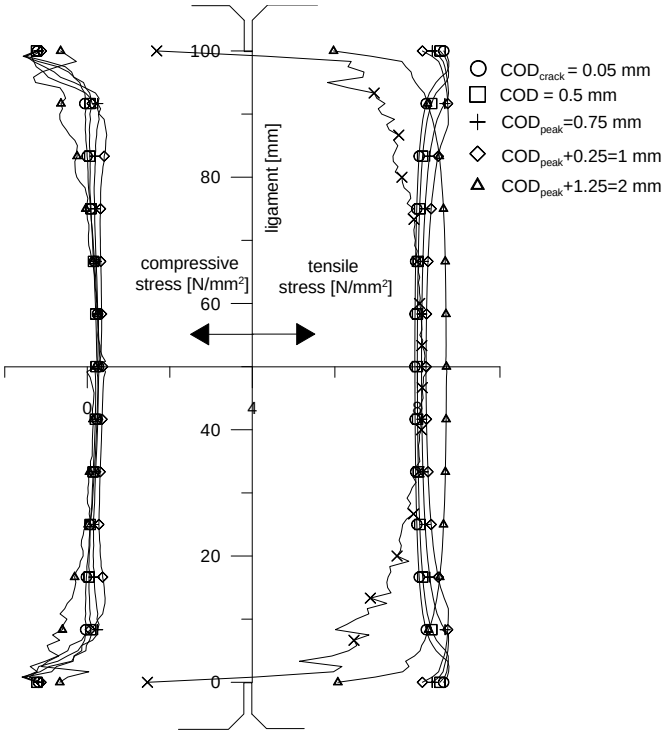

Figure 3.39 – Principal stress evolution with increased for strain hardening case

The principal stress evolution along the ligament has been also computed in correspondence with different crack opening displacements and that confirms that the principal compressive stresses are almost negligible and the fracture has been induced mainly by tensile stresses almost uniformly distributed along the ligament itself.

3.4 Textile Reinforced Cementitious Composites (TRCC)

Several research studies have shown that textile reinforced cementitious composites (TRCC) and high performance fibre reinforced cementitious composites (HPFRCC) are promising candidates to be used both in precast industries and as a strengthening material, due to enhancement not only on strength performance but also on durability requirements. Thus, with TRCC is not anymore required to obey the minimum cover thickness requirements and fibres can be aligned in the desired direction in 2D and even in 3D according to the recent research [Peled et al., 2012]. This composite material has been investigated for some years now at Politecnico di Milano, and so far the main work has been focused on the characterization of the material observing different factors that might influence their behaviour.

The matrix used requires the maximum aggregate size to be less than 1 mm. The composite performance is greatly affected by the choice of volume fraction and type of fabric that could be for e.g. Alkali resistant glass (AR), carbon or aramid fibres.

Hereafter are presented the experimental results by [Colombo et al., 2013] mainly based on uniaxial tension, since the choice of the strengthening TRCC has been based on this campaign. Various mixture compositions have been developed to meet consistency performance. All the mixes consisted by cement (CEM II 52.5), aggregate (with maximum size of 0.6 mm), water, slag and superplasticizers. Regarding the textile reinforcement AR glass fabric has been employed always with different warp and weft configurations and different volume fraction.

The TRCC composites are characterized by a complex tensile behaviour. [Heger et al., 2004] provides simplified concepts to describe the typical behaviour of TRCC in four different branches as in (Figure 3.40). (I) is the first linear branch representing the linear elastic behaviour of the composite, (IIa) after the first crack appearance when reaching tensile strength of mortar, the load is transferred from matrix to the fabrics and by increased loading at other weaker section crack appears and mechanism of load transfer is repetitive, where multiple cracking occurs, (IIb) region where crack localization occurs, instead the (III) branch does not exist due to brittle failure nature of glass fibres. The comparison between TRCC and only textile reveals the tension stiffening effect.

The stress strain curve shape depends on many factors such as bond between fibres and matrix, geometry strength and orientation of fibres, textile amount, curing procedure etc..

[Colombo et al., 2013] recently emphasized the influence of some of these parameters

a) Reinforcement amount and position;
b) Fabric geometry;
c) Composite curing procedure.

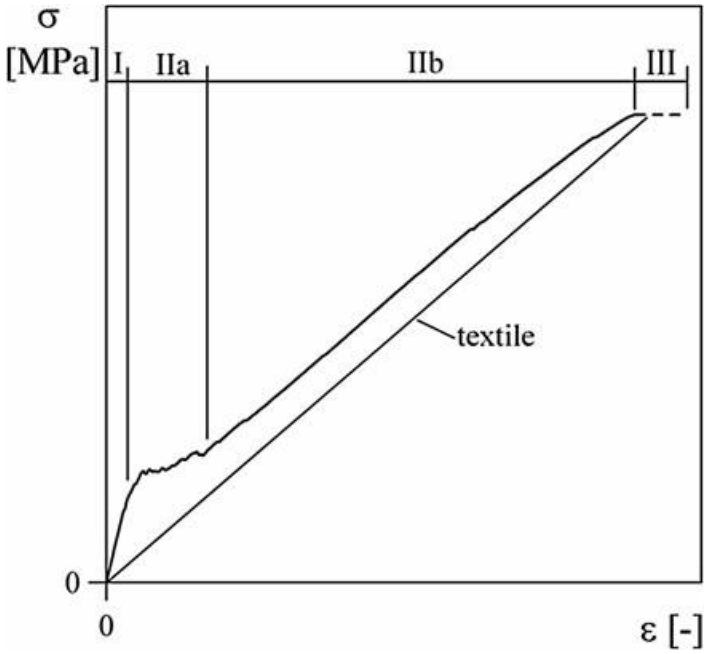

Figure 3.40 – Direct tension behaviour of TRCC [Hegger et al., 2004]

The TRCC behaviour is strongly influenced by the level of reinforcement; the experimental evidences (Figure 3.41) clearly show this aspect both from stress strain curve and on number of formation of multiple cracking.

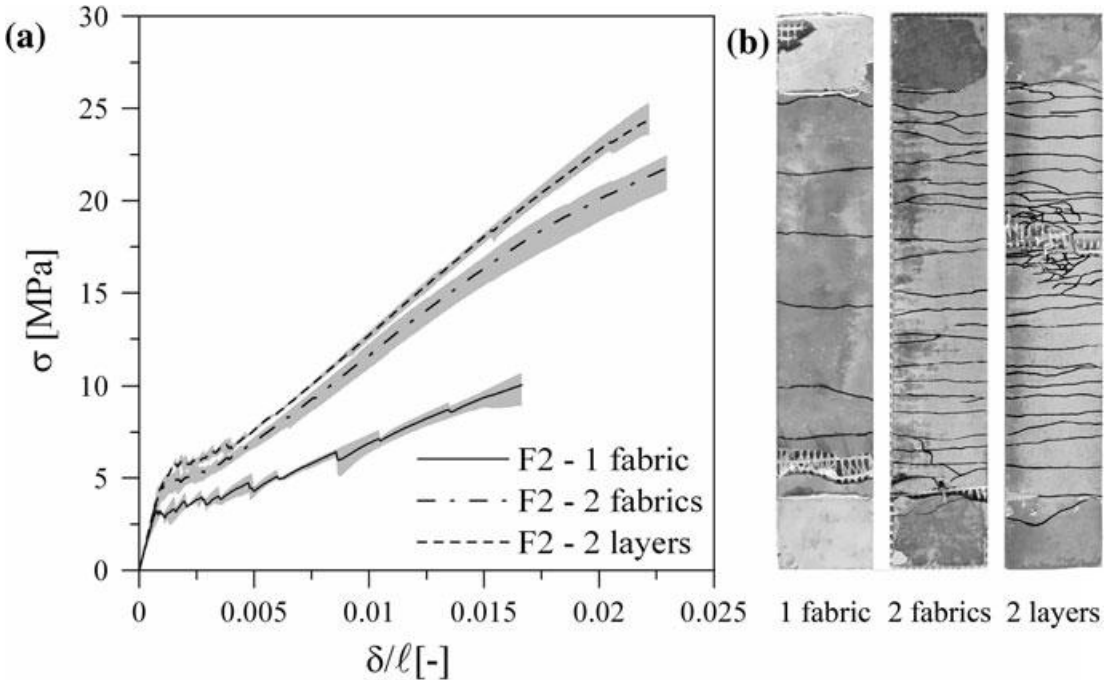

Figure 3.41 – Uniaxial tension behaviour of TRCC with different level of reinforcements

The fabric geometry is an important factor to be considered regarding the bond between the matrix and fabrics, manifested by cross sectional non homogeneity governed by various properties between inner and outer filaments. Fabrics with same warp cross-section but different weft spacing have been investigated, and it was shown that for the lowest weft

spacing better ductility was obtained in contrast, for increased weft spacing the tension stiffening improves (Figure 3.42).

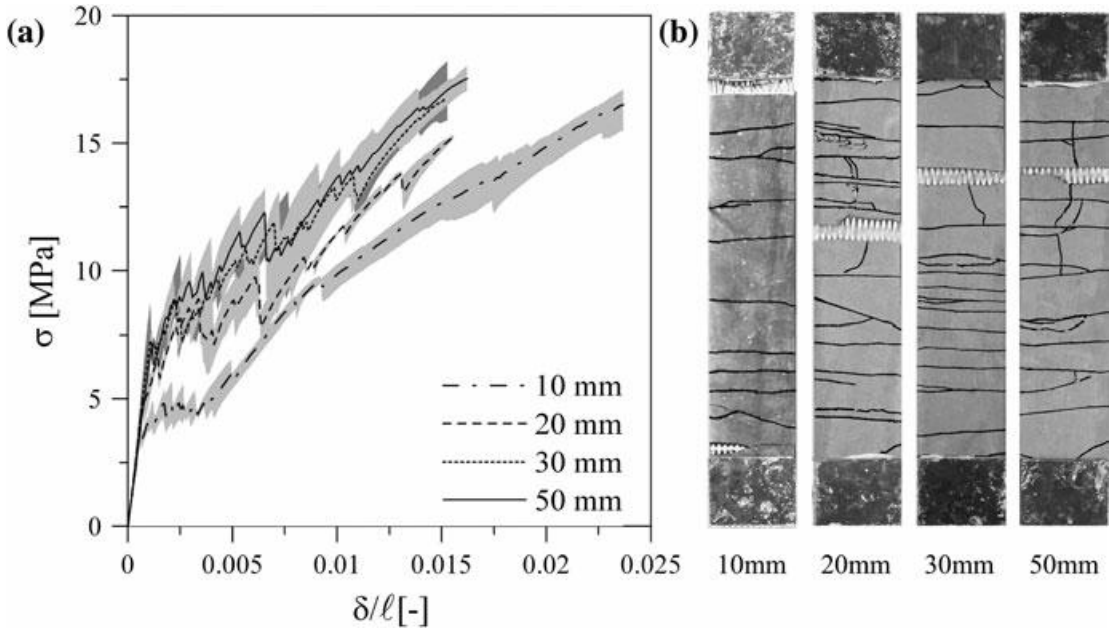

Figure 3.42 – Uniaxial tension behaviour of TRCC with different weft spacing

The importance of curing condition clearly appears in (Figure 3.43), considering as variable the relative humidity. This is directly related to matrix shrinkage; the lower relative humidity the higher is the shrinkage which is likely to provide the higher bond and better performance. However, since shrinkage strains are very high due high cement content, care should be taken when these materials are applied as an overlay to existing structures, as it may lead to delamination.

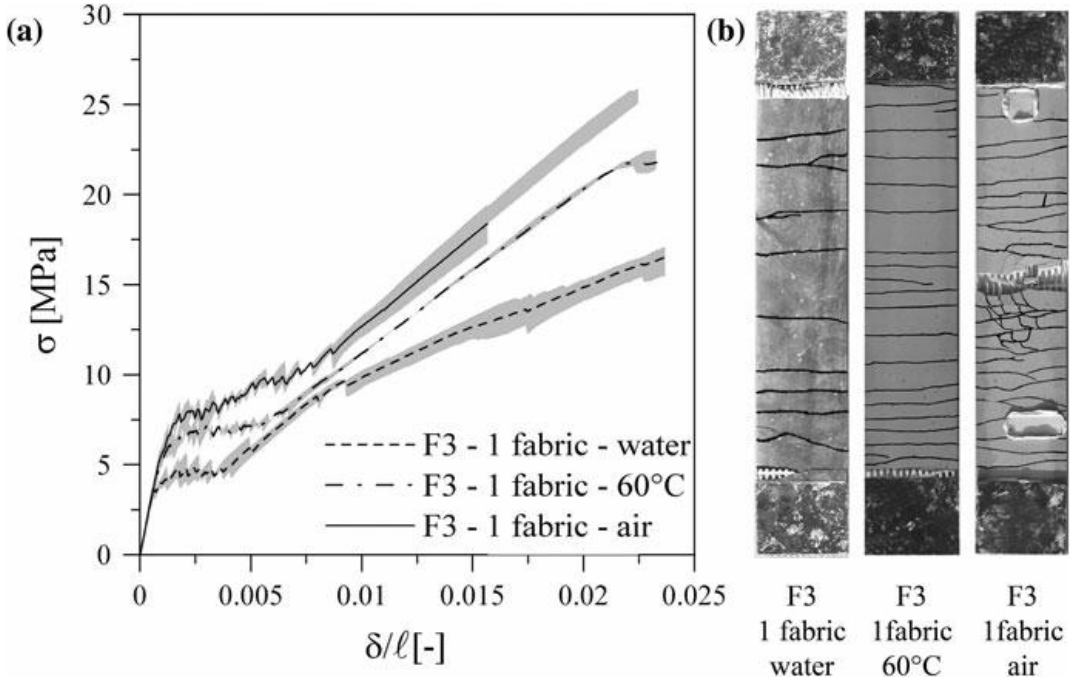

Figure 3.43 – Uniaxial tension behaviour of TRCC with different curing conditions

4

4 Investigation at member level: Numerical modelling of the behaviour of coupling beams

The same numerical model used for modelling DEWS specimens, has been then applied to model the behaviour of FRCC coupling beams under monotonic loading, making reference to the experimental campaign performed by [Canbolat et al., 2005] on 4 individual coupling beams, cast with either conventional reinforced concrete or HPFRCCs and with different reinforcement arrangements.

As a further step, because of computational efficiency, the possibility was explored to use a multi-fibre Timoshenko beam element, incorporating reliable description of unilateral effects of concrete cyclic behaviour as well as suitable assumptions resulting from the previous modelling phase. This approach has been then adopted to predict the cyclic behaviour of coupling beams made of or retrofitted with HPFRCCs.

4.1 "Crush-crack" damage modelling

The "crush-crack" model has been shown to be effective in capturing the behaviour of HPFRCC in tension and has been instrumental in the DEWS test for the straightforward identification validity of the tensile constitutive behaviour of this category of advanced cementitious composites. The calibrated numerical tool has been herein used for further modelling of experimental tests to reproduce the behaviour of HPFRCC coupling beams making reference to the experimental campaign performed at University of Michigan by [Canbolat et al., 2005]. The constitutive behaviour of HPFRCC has been described as from experimental results provided by the authors, coherently with assumptions described in the previous chapter. The geometry and of the specimen has been already described in the chapter of literature review and is herein briefly summarized.

The same geometry of the test sample reported with a coupling beam of span to depth ratio equal to 1 has been modelled, together with two additional stiff blocks which were functional of assigning specimen loading and boundary conditions (

Figure 4.1). In the coupling beam "crush-crack" damage model has been employed, while the blocks have been considered as elastic since were out of scope of study. Moreover they were reported to remain undamaged. This was also instrumental to reduce significantly the computational time. Triangular elements are used to discretize the mesh with same size in all the partitions, and in the damage constitutive model the strain is converted to a regularized

strain as a function of the element size. Regarding the reinforcement, embedded truss elements were used, the nodal points of which are connected to the closest node of the mesh, perfect bond was hence considered. To simulate the boundary conditions of experimental tests, the upper block was axially restrained and was allowed to laterally slide, while the lower block was fixed at the bottom (Figure 4.1). The load was applied in terms of displacements all over the length of the upper block to avoid local stress concentration, and the resultant shear force was obtained as the sum of each nodal force of triangular elements along the boundary of the imposed displacements.

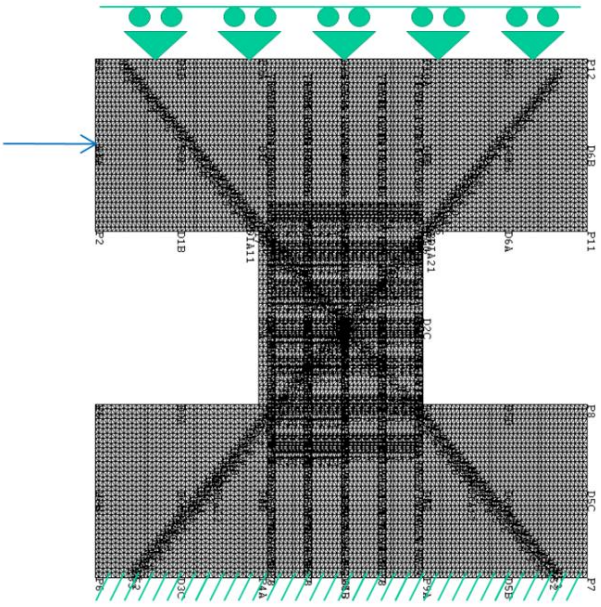

Figure 4.1 – FE discretization and boundary conditions

The tested coupling beams have length and height both equal to 600 mm, and width equal to 200 mm and 150 mm for r/c and HPFRCC respectively (they were designed at a ¾ scale to the full scale case study). The compressive strength of regular concrete was assumed equal to 41 N/mm², as from experimental investigations; other parameters needed for the analysis, such as tensile strength and fracture energy, were computed from [*fib* Model Code 2010] formulae. As for FRCC its compressive strength was taken equal to 57 and 63 N/mm², and its post cracking tensile strength equal to 3.1 and 5.5 N/mm², both as reported either for PE or twisted steel fibres. The representative material characteristics of three different matrixes are reported in (Table 4.1). The yielding strength of the steel was equal to 450 N/mm², with a 726 N/mm² tensile rupture strength, once again accordingly to what reported by the authors. The steel reinforcement has been defined through elastic perfectly plastic response without defining the rupture strain. This assumption is sufficiently true considering the plateau observed on experimental results. Moreover, this was confirmed from the analysis that in the steel the rupture strain threshold has been not exceeded.

Table 4.1 – Material parameters used for numerical modelling of coupling beams

Material	f_{ck} [N/mm²]	f_{res} [N/mm²]	E_{cm} [N/mm²]	f_t [N/mm²]	$f_{R,1}$ [N/mm²]	$f_{R,3}$ [N/mm²]
Conventional concrete	41	0	34000	3.086	–	–
PE fibres	57	0	35000	3.1	2.7	1.0
Twisted fibres	63	0	36000	5.5	4.8	2.0

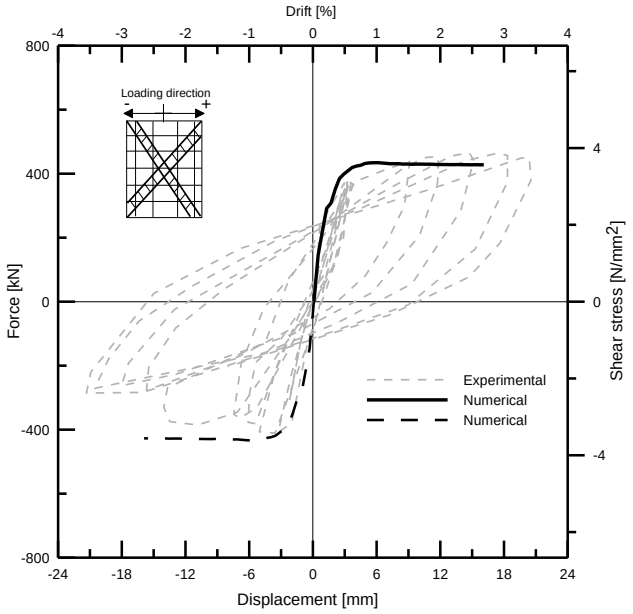

Figure 4.2 – Behaviour of coupling beam (CB1) with conventional concrete

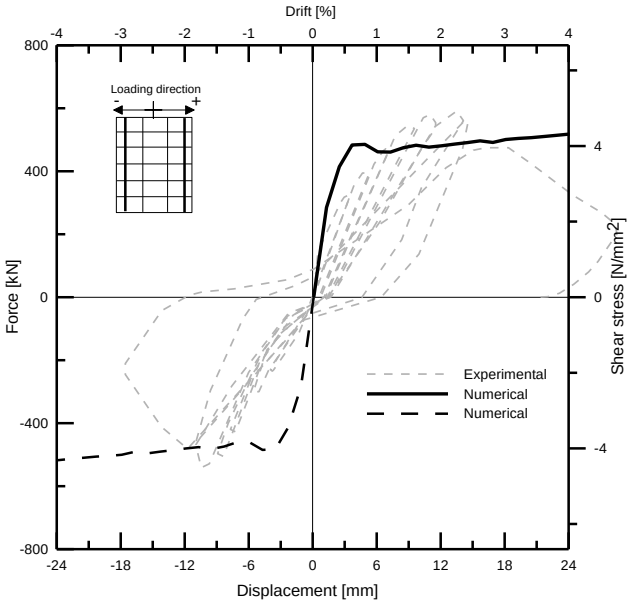

Figure 4.3 – Behaviour of coupling beam (CB2) with PE fibres

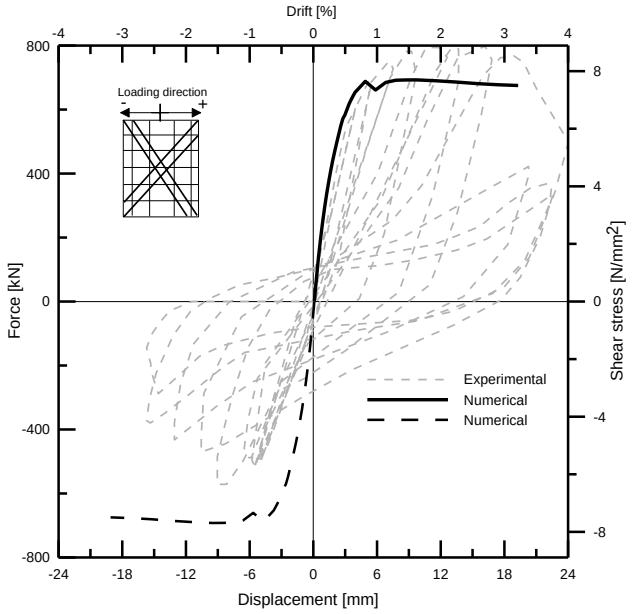

Figure 4.4 – Behaviour of coupling beam (CB3) with PE fibres

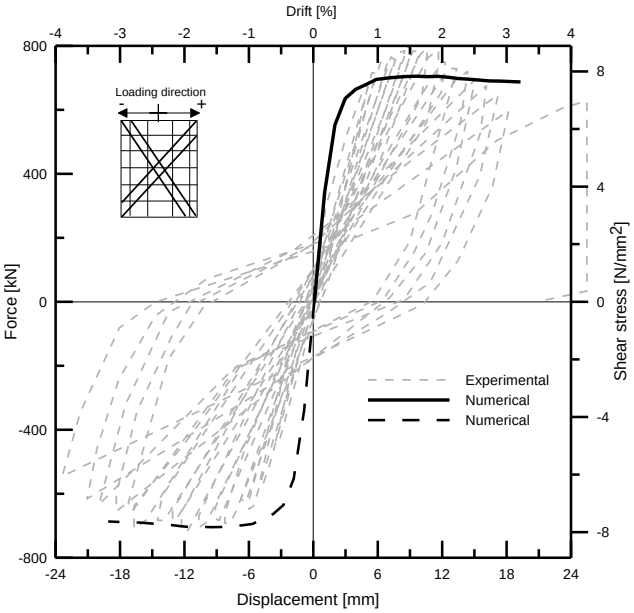

Figure 4.5 – Behaviour of coupling beam (CB4) with twisted steel fibres

In numerical analysis a monotonic load path was modelled. As matter of fact, as shown in (Figure 4.2 to Figure 4.5) the predicted monotonic response matches reasonably well with the envelope of the experimental cyclic load-drift response for all four cases. For diagonally and longitudinally reinforced specimens and with PE fibres HPFRCC, the initial stiffness was well captured in the positive loading direction whereas it has been a little overestimated in the negative one (most likely because of some damage accumulated in the previous loading step which affected the response once load was reverted). For the other two specimens a slight overestimation in both directions does occur which may be attributed to boundary conditions.

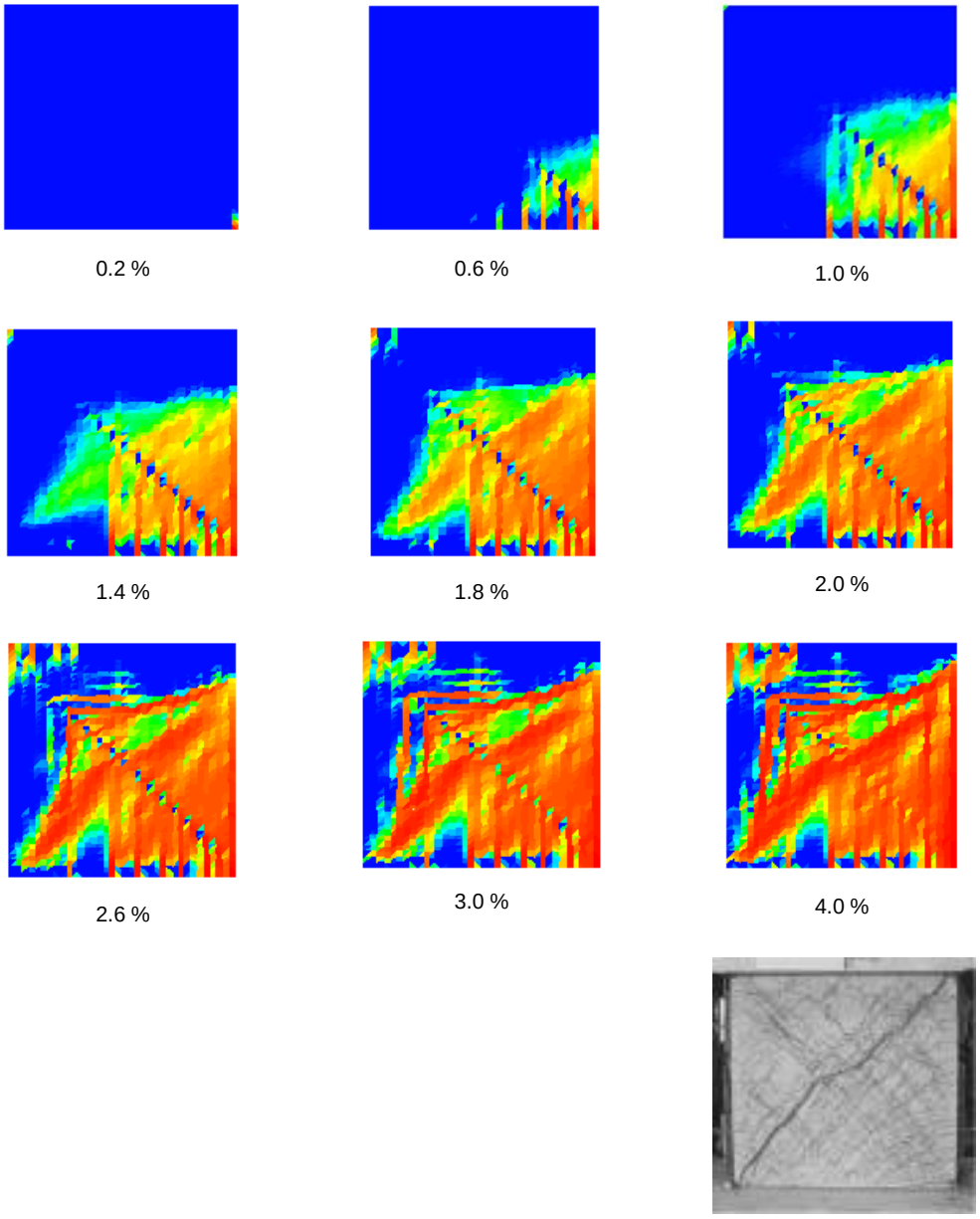

Figure 4.6 – Damage pattern for the case (CB3)

The simulated damage evolution under increasing displacements is illustrated in (Figure 4.6), for different drifts. The computed damage pattern for the (CB3) at the maximum drift interestingly reproduces quite well the experimental crack pattern (Figure 4.6) reported for the same level of drift, furthermore highlighting the high level of damage which the material can tolerate before the localization of a major unstable crack steps.

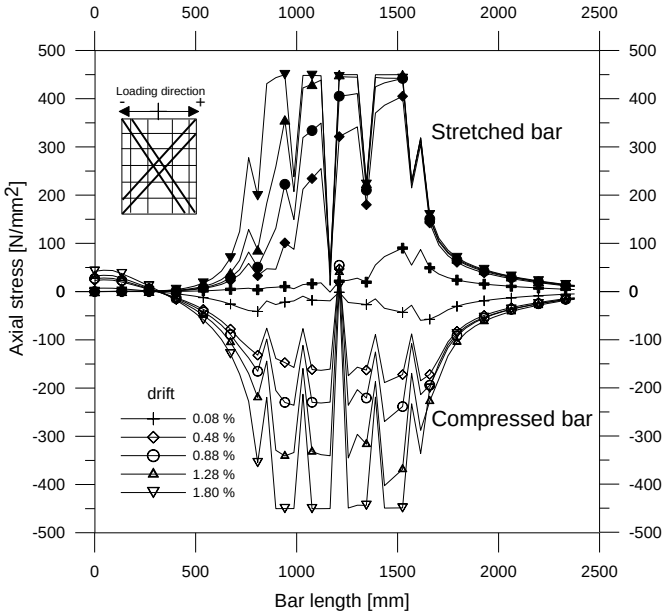

Figure 4.7 – Stress evolution under increased displacement for the diagonal bars in tension and compression

Continuum Damage Modelling also allows a deeper insight to be cast into local phenomena occurring in the tested specimens along the loading path. (Figure 4.7) shows the increasing stresses along the loading for both diagonal bars, either in compression or tension. Even if there were no experimental evidences to confirm these numerical results, it has been clearly shown the maximum stresses develop at the centre of the specimen and the spikes represent the position where the bars interact with stirrups, the yielding of the bars it has been observed to start at 1.80% drift. Going further from the centre to both end sides of coupling beams the stress decreases until it diminishes inside of the block which corresponds to what was reported, that the walls remain intact during all loading phase.

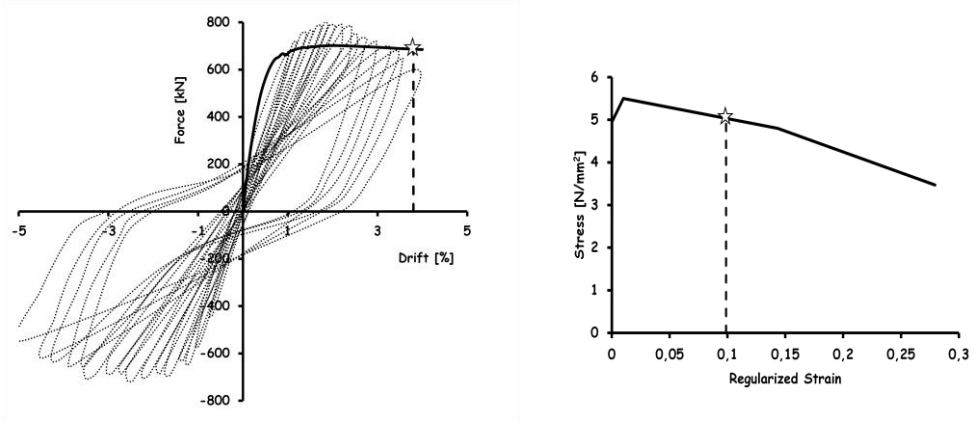

(a) (b)

Figure 4.8 – Corresponding stress/strain on HPFRCC for large deformations

Numerical analyses further showed that, at 4% drift (Figure 4.8a), which can be consistently assumed as the ultimate deformation demand for this kind structures, the principal tensile strain nowhere exceeds a threshold corresponding to a crack opening equal to 0.5 mm beyond the peak strain. In other words the first residual strength in this case was never reached (Figure 4.8b). This supports the assumption of an elastic-perfectly plastic description of HPFRCC tensile strain-hardening behaviour in further "member level" modelling, with a

"plateau" stress assumed equal to the residual stress corresponding to the aforementioned strain threshold, as hereafter detailed.

4.2 Timoshenko-beam fibre modelling

The "crush-crack" model has been very expensive in terms of computational time and unable to capture the cyclic response of concrete. Thus, to overcome these issues it has been shifted to fibre beam model. A fibre beam model based on Timoshenko beam theory implemented in Cast3M [Guedes et al., 1994; 2010] has been used for the further level of numerical analyses. The fibre model hypothesizes that the section remains plane after deformation but not necessarily perpendicular to the deformed axis. So, different interactions between axial, shear and bending actions can be considered. The approach operates at two levels: the beam level allows to discretize the boundary value problem in beam elements, and the section level allows to specify the geometry and material characteristics by longitudinal fibres defining the mesh at the level of the transverse section parallel to the axis of the beam as illustrated in (Figure 4.9). Ability of this approach to assign a single constitutive law for each fibre in the section makes this approach suitable to consider different materials in the same section.

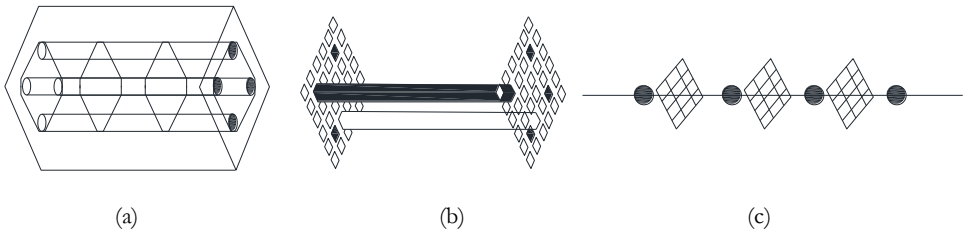

Figure 4.9 – (a) r/c member; (b) multi-fibre elements and (c) section level

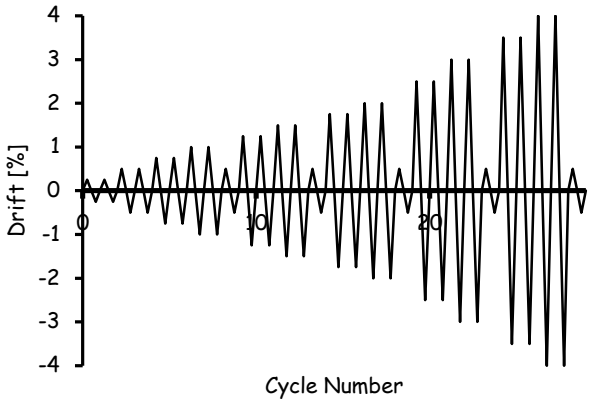

Figure 4.10 – Applied displacement history

Regarding the constitutive law for material definition, concrete compressive behaviour has been described by means of a parabola up to the peak stress, followed by a linear softening (Figure 4.11a). The concrete tensile behaviour was included through linear model with post-peak linear softening. Suitable description of the cyclic behaviour is provided, in order to take into account the stiffness degradation and crack closure effects (Figure 4.11b). A simplified bilinear elastic-perfect plastic stress-strain relationship has been adopted to

describe the tensile response of HPFRCC (Figure 4.12a), according to the assumptions explained above. Steel behaviour was assumed to be elastic-hardening and perfectly bonded to concrete and/or HPFRCC (Figure 4.12b).

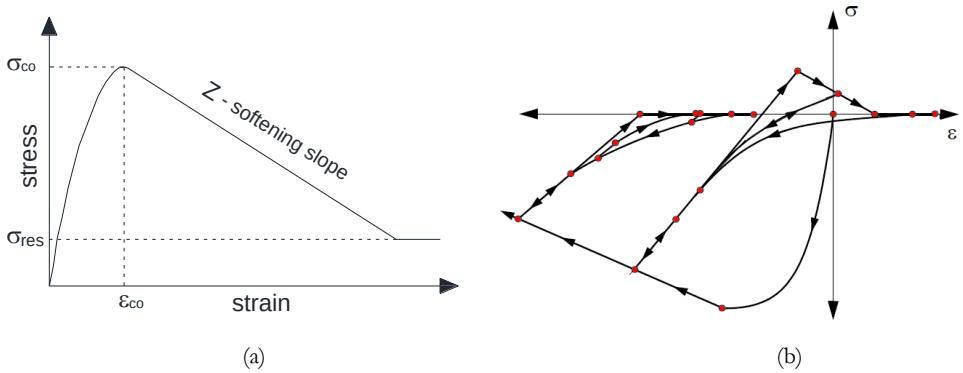

Figure 4.11 – Constitutive law for: (a) concrete in compression and (b) cyclic behaviour of concrete

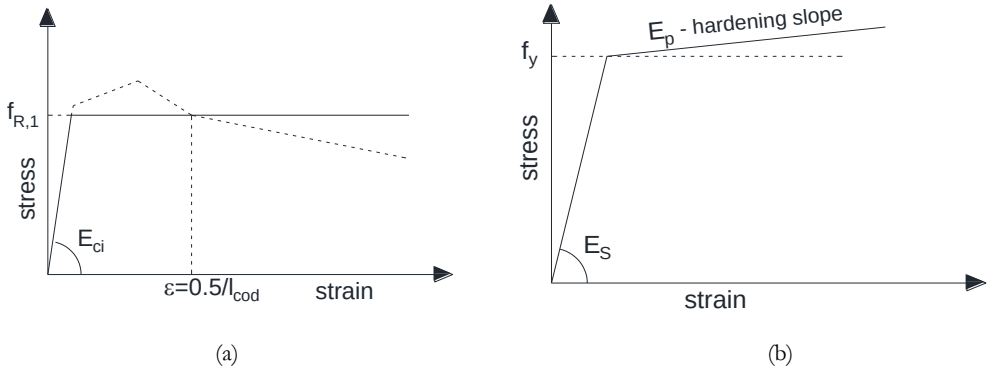

Figure 4.12 – Elastic-perfect plastic description in tension of: (a) HPFRCC and (b) steel reinforcement

Because of lack of data about the cyclic behaviour of HPFRCC, this material has been modelled equal to that of a conventional concrete having the same compressive and tensile strength. Experimental evidence about the cyclic behaviour of HPFRCC is very limited: anyway it has been shown that the monotonic stress-crack opening response is the envelope of the cyclic and there is no influence on the ultimate strain level [Yun et al., 2008; Jun et al., 2008].

The numerical approach has been validated based once again on the experimental tests performed by [Canbolat et al., 2005], with reference to coupling beams made of either conventional r/c or HPFRCC when subjected to reversal shear loading, under increasing amplitude cycles.

The influence of transverse reinforcement that provides confinement to the inner core of the element can be considered by assigning a non-zero residual strength in compression, set equal to 20% of the compressive strength was chosen in this study. A relatively good agreement between numerical prediction and experiments is observed for the case of conventional concrete (Figure 4.13), where also the influence of a residual compressive strength, in the aforementioned sense, can be appreciated (Figure 4.14).

With reference to HPFRCC coupling beams, the elastic-perfect plastic description of the material tensile behaviour, has proven to be a reliable assumption which provides satisfactory agreement between experimental and numerical predictions (Figure 4.13 to Figure 4.17).

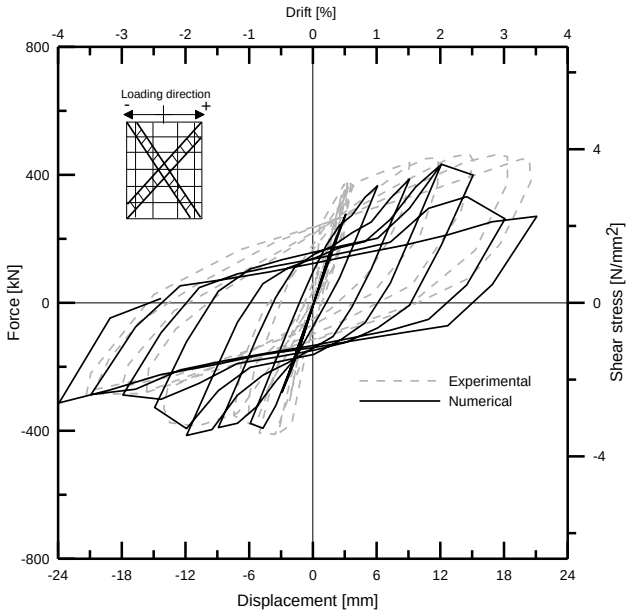

Figure 4.13 – Numerical and experimental comparison without residual strength in compression, coupling beam (CB1)

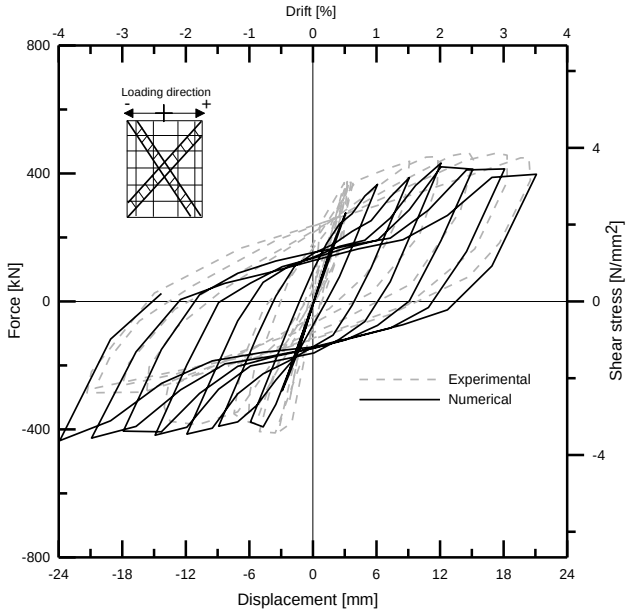

Figure 4.14 – Numerical and experimental comparison with residual strength in compression, coupling beam (CB1)

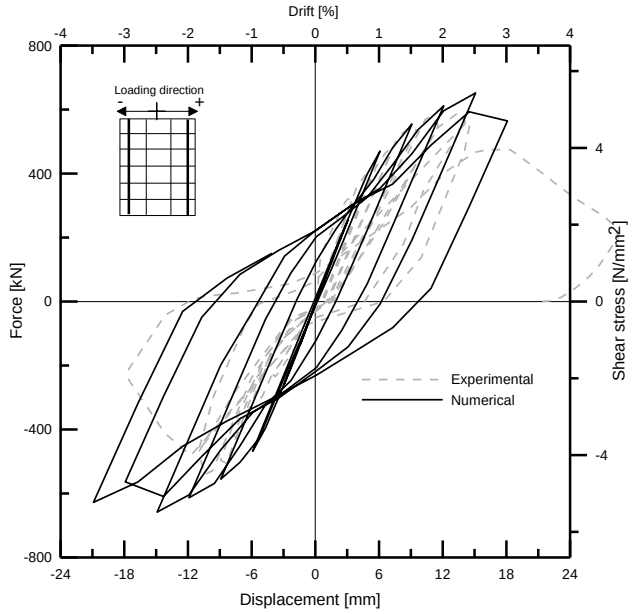

Figure 4.15 – Numerical and experimental comparison for coupling beam (CB2), HPFRCC with PE fibres

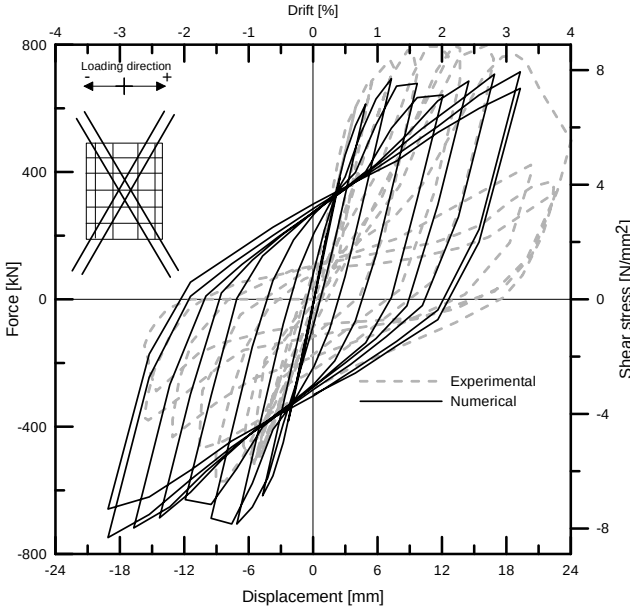

Figure 4.16 – Numerical and experimental comparison for coupling beam (CB3), HPFRCC with PE fibres

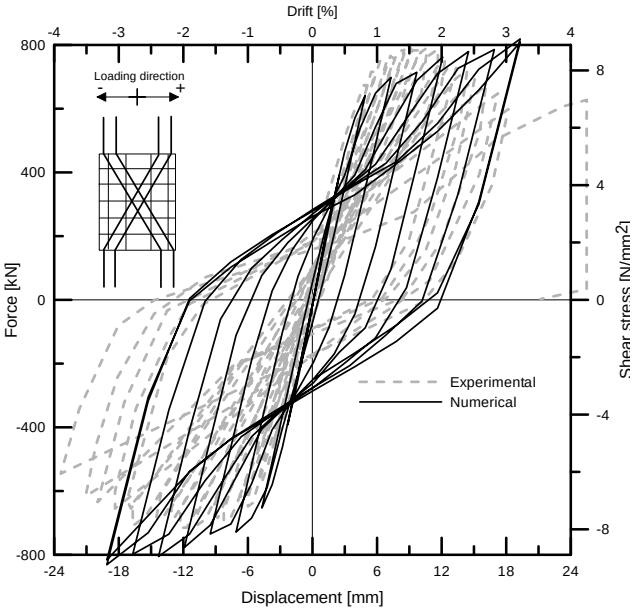

Figure 4.17 – Numerical and experimental comparison for coupling beam (CB4), HPFRCC with twisted steel fibres

5

5 Investigation at structural member level: Design and planning of the experimental campaign

5.1 Specimen design: reinforcement cages

In order to design the experimental test specimens reference has been made to the case of a shear wall containing a typical door opening 900 mm wide (equal to the length of the coupling beam) and 2.1 m high; this resulted (assuming the inter-storey height equal to 2.7 m) in a depth of coupling beam equal to 600 mm and hence in a span/depth ratio of 1.5. In order to comply with capacity of available experimental equipments the geometry of test specimens was scaled at a ratio 1:2 with respect to the full scale. It was chosen to design the samples basically composed of three different parts; two rigid blocks and a connecting beam between the two blocks which represents the structural element to be investigated. The blocks represent the two shafts of the shear wall connected by the coupling beam and were designed to remain undamaged.

All specimens have been designed with the same material characteristics. The two rigid blocks have always the same type and configuration of reinforcement. Whereas the part regarded as the "coupling beam" properly was built with different reinforcing arrangements, hence the specimens are distinguished between three types:

- 2 specimens without any reinforcement in the beam;
- 2 specimens with only longitudinal bars in the beam;
- 10 specimens with both longitudinal and transverse reinforcement of the beam.

The blocks have been heavily reinforced in order to avoid any damage. In the coupling beam reference was made to the portions, as the case of study was the coupling beam that was "poorly designed" element, just satisfying the minimum reinforcement requirement supposed by design codes for non-seismic design situations. Four bars ϕ8 mm have been inserted as a longitudinal reinforcement to comply with minimum required reinforcement ratio equal to 0.33%, and transverse reinforcement ϕ6 mm stirrups spaced at 100 mm were provided.

The upper and lower blocks were meant to be stiff enough to transfer the load to the beam and guarantee the intended boundary conditions. Since the specimens will be tested at lab

with respect to the direction they have in real structural assembly, the block will be referred as upper and lower block.

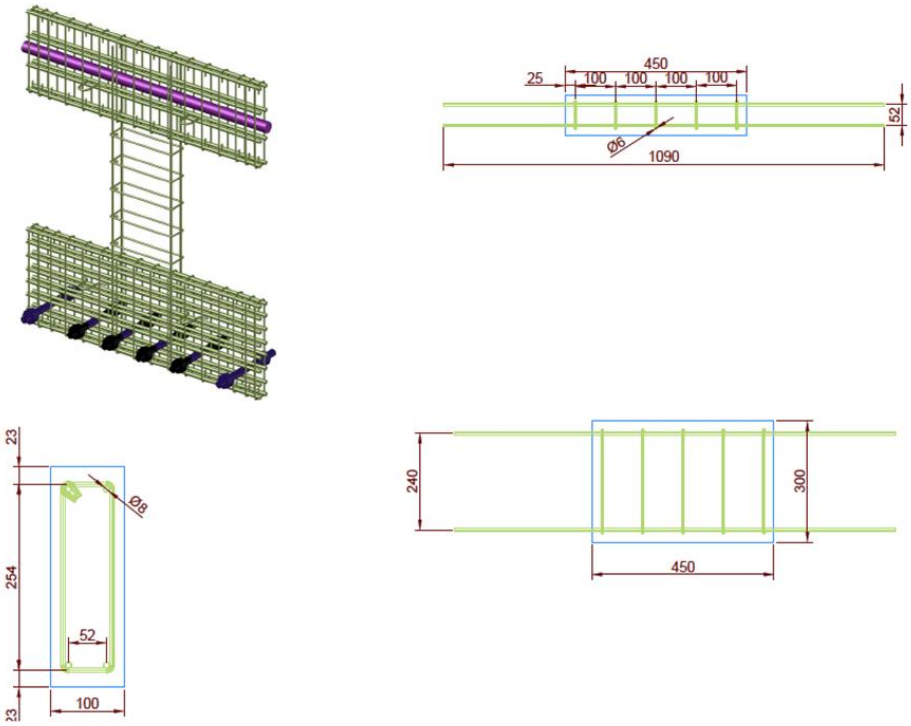

Figure 5.1 – Reinforcement cage detailing – Coupling beam

The details of the lower block reinforcement are shown in (Figure 5.2). In the lower block at 105 mm from the bottom 6 threaded bushings have been placed in order to accommodate the passing threaded bars, through which the specimen can be fixed to the frame.

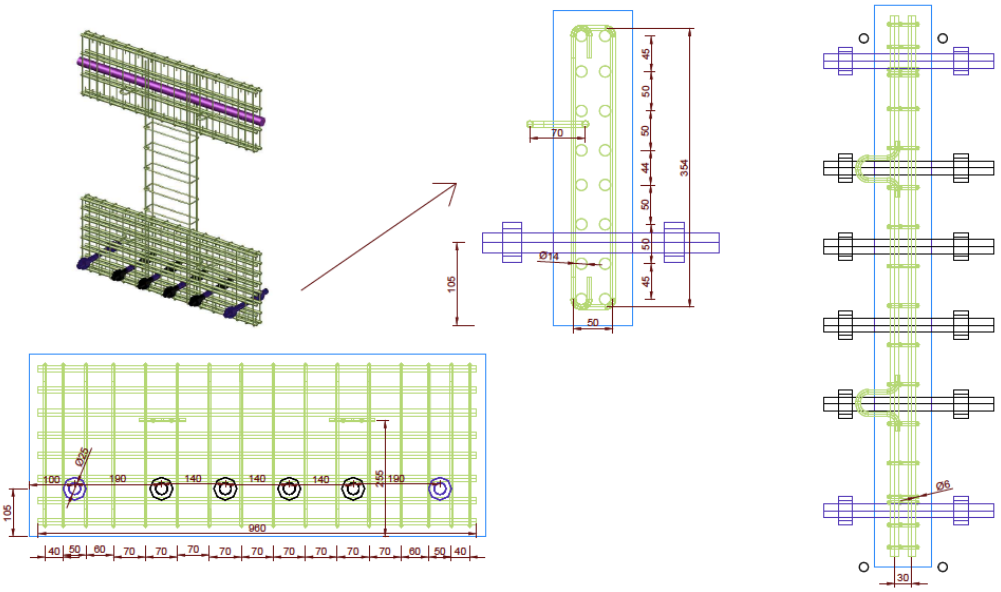

Figure 5.2 – Reinforcement cage detailing – Lower block

The upper block, has been characterized by the presence of a PVC pipe of 40 mm diameter passing through the whole length and at the mid depth of the block. Inside this tube, for

performing the test, will be inserted a steel Dywidag bar, passing through the sample, which allows to transfer the load to the specimen during the test. The details of reinforcement of the upper block are shown in (Figure 5.3).

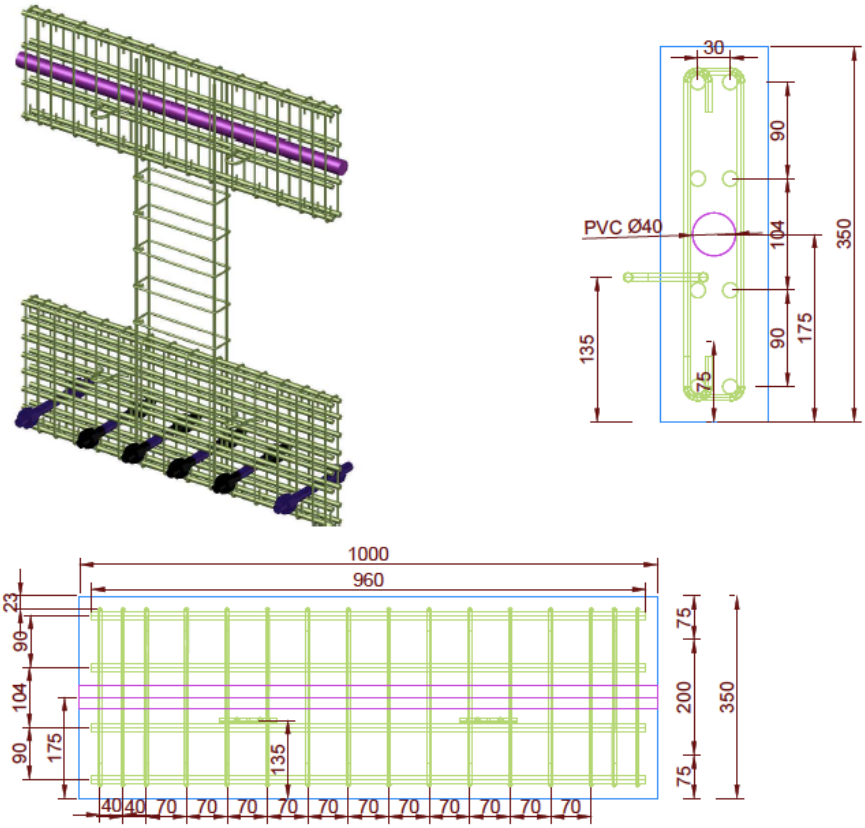

Figure 5.3 – Reinforcement cage detailing – Upper block

5.2 Strengthened coupling beams

With the same approach previously calibrated, numerical analyses have been performed in order to understand the effectiveness of using HPFRCC as a retrofitting solution for poorly designed coupling beams and design a dedicated experimental campaign. The beam dimensions were scaled by a 1:2 ratio to full scale size (Figure 5.4), to comply with the maximum capacity of 400 kN of the loading jacks to be employed in the experimental stage of this research. This resulted in a length equal to 450 mm and a rectangular cross-section 300 mm high and 100 mm wide. Grade B450 longitudinal reinforcement was considered (3ϕ10 bars at the top and at the bottom). Class C20/25 concrete was chosen for the beam; the other parameters for the constitutive laws were obtained according to [*fib* Model Code 2010]. The strengthening HPFRCC material, consistently with tests described in Chapter 3, has a compressive strength of 115 N/mm²; the residual tensile strength at 0.5 mm crack opening is equal, as from experiments, to 7.11 N/mm² and 1.8 N/mm², respectively for favourable and unfavourable fibre orientation.

Perfect bond between the old concrete and the HPFRCC overlay has been assumed. This assumption, mainly due to the lack of suitable experimental reference data, is debatable, because of the influence that both the surface treatment of the existing structural element and its pre-existing damage conditions may have on the interface behaviour.

In (Figure 5.5) the response of retrofitted beams is shown in terms of monotonic load-drift curves, for the different investigated retrofitting options. The jacketing has been modelled along two or three sides of the cross section, that might be the real situation during execution; two different strengthening thicknesses have been evaluated, also considering the effects of the residual strength of HPFRCC, as it may be affected by the flow induced orientation of fibres. The effectiveness of the strengthening is shown, also through the comparison with the performance of an r/c jacketing, which, assuming a ϕ6 spaced at 100 mm welded wire mesh skin reinforcement should be at least 40 mm thick on each side.

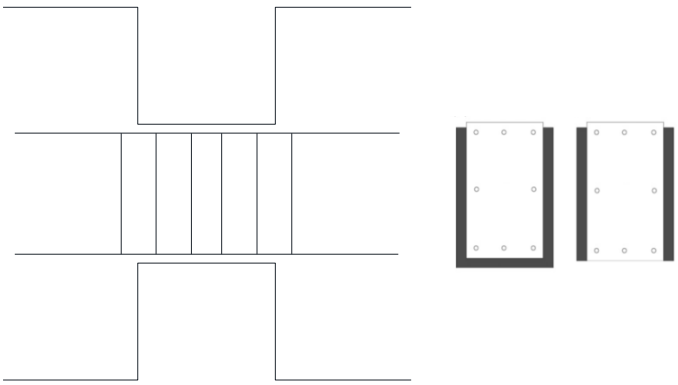

Figure 5.4 – Coupling beam upgraded in three or two sides

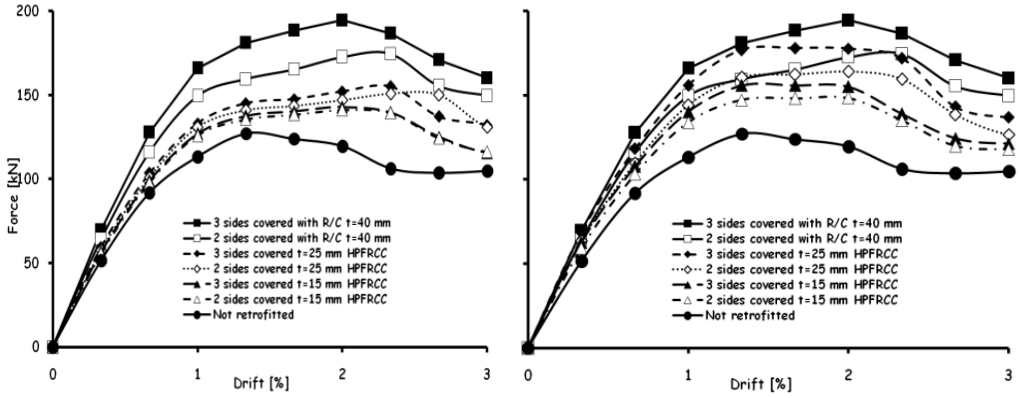

Figure 5.5 – Coupling beam performance with different upgrading typologies

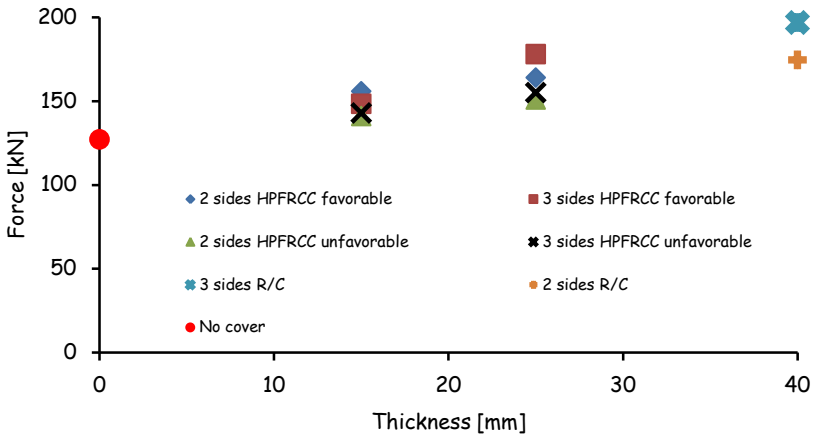

(a)

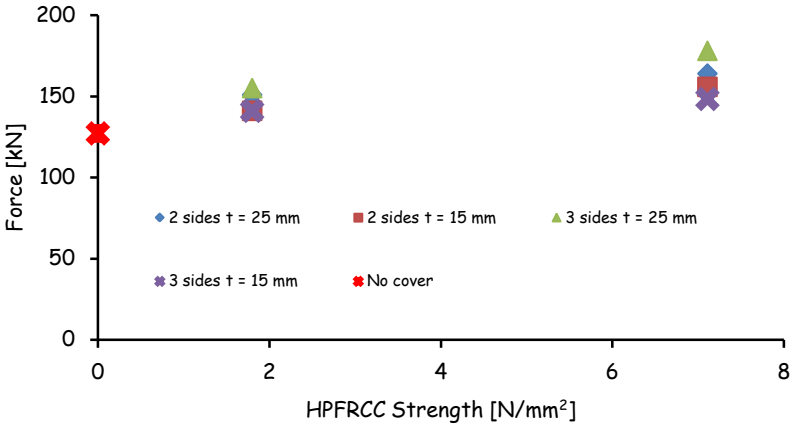

(b)

Figure 5.6 – (a) Load capacity of strengthened beam vs. thickness and (b) residual tensile strength of HPFRCC for different load capacities

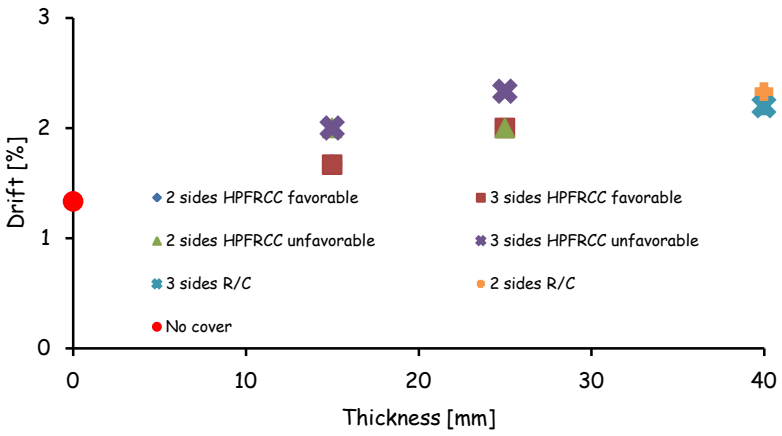

(a)

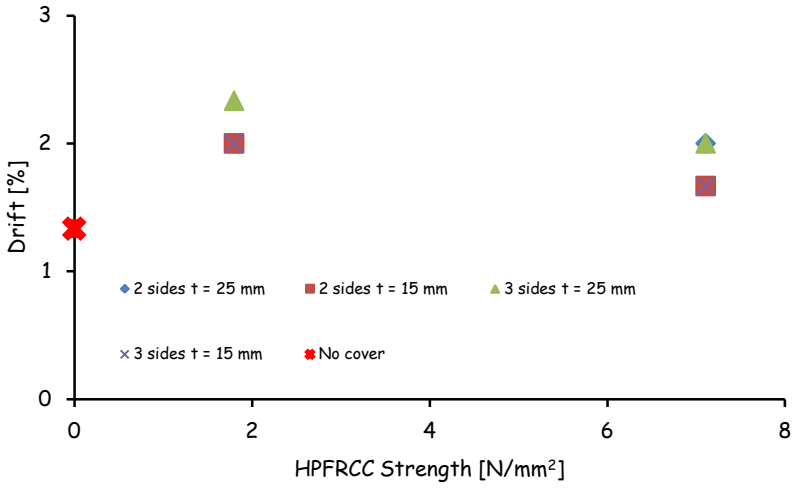

(b)

Figure 5.7 – (a) Peak load drift of strengthened beam vs. thickness and (b) residual strength of HPFRCC for different drifts

The effects of both the thickness of the retrofitting layer and of the residual tensile strength of the retrofitting material on the load bearing capacity and ductility of the retrofitted beam were separately analyzed in (Figure 5.6 and Figure 5.7). Influence is as expected, even if residual tensile strength of HPFRCC appears to have quite a moderate affect on the load bearing capacity, most likely due to the limited thickness of the overlay, and a negligible one on the ductility, as obvious and also implied by the elastic-perfectly plastic assumed behaviour. This outcome may be not as worse as it can appear. As a matter of fact discrepancies as huge as these herein considered for residual tensile strength of HPFRCC may occur due to either defective casting or strong flow induced orientation of fibres. The latter implies a strong anisotropy in the material behaviour, the material providing one rather than the other residual strength whether stressed parallel or orthogonal to the fibre alignment.

5.3 Pre-design considerations

Based on the previously performed experimental campaigns analyzed in the literature review chapter designed for testing of the coupling beams under shear loading, and on available laboratory equipments the test setup is required to satisfy the following needs:

- A frame has to be built able to guarantee that the upper block of the specimen does not rotate but it permitted to slide in the loading direction, in order to maintain no rotations between two blocks, the boundary conditions shown in (Figure 5.8).
- The frame should be stiff enough to transfer the axial force passively generated by the strut from the coupling beam into the base floor, without any significant deformations.
- The frame should be easy to be dismounted and remain undamaged since a large number of tests should be done to maximize the utilisation.
- In most of the cases of experimental tests on coupling beams [Canbolat et al., 2005; Lequesene, 2011], the blocks representing the shafts of the wall are wider than the coupling beam. Whereas in our case the specimen should be designed of the same thickness to permit anchorage length of the strengthening/retrofitting layer.

- The loading system should be able to apply reversed cyclic loading with maximum load of 300 kN. This was likely to be the expected maximum load baring capacity for the tested coupling beams based on numerical analyses performed above.

To satisfy the following conditions as well to minimize the construction costs of the specimens and the testing rig, the detailed procedure followed is discussed hereafter.

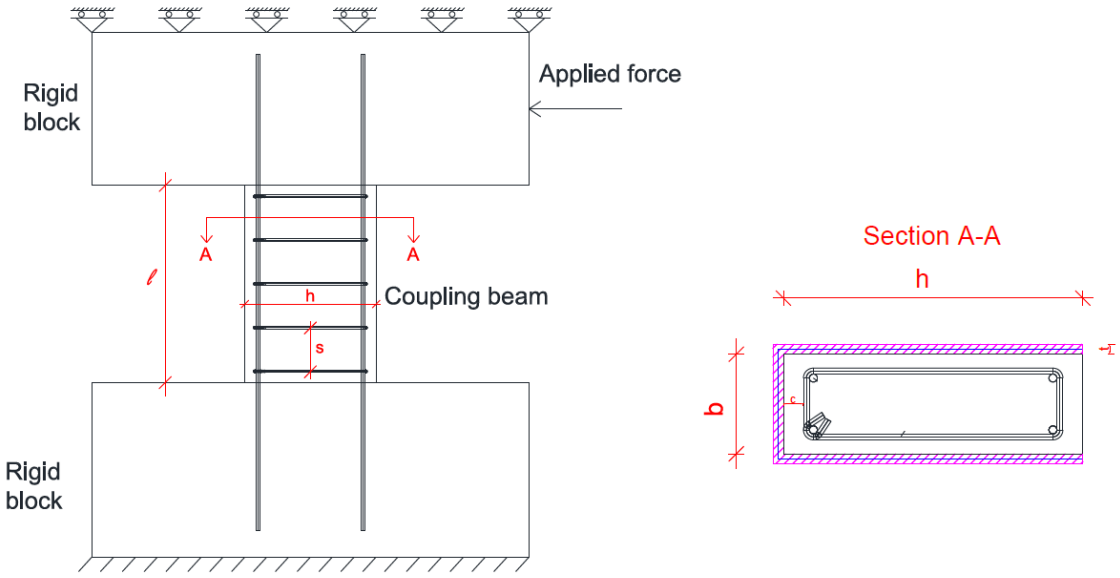

Figure 5.8 – Boundary condition scheme

5.4 Elastic design of the setup

Linear elastic analysis have been performed to design the frame setup using finite element software CAST3M, in order to optimize and guarantee the frame remains in the elastic range with a large enough safety margin. Moreover, a special attention was devoted to the design of the connection to transfer the load from the specimen into the base floor through suitable angular steel profiles. Half of the specimen has been modelled benefiting from its symmetry (assigning suitable boundary conditions for sake of symmetry) and the load applied in the middle of the upper block is equal to 150 kN (respectively 300 kN for the entire specimen), shown in (Figure 5.9).

For sake of the safety this applied load is overestimated with a safety factor of 1.5 of what was observed from previous numerical analyses, the testing rig should be designed to remain elastic at applied loading on specimen equal to 300 kN. It is assumed the load would be transferred from the lower block through 6 bolts connected to angular profile, connected on its horizontal leg by 6 other bolts to the base girder on which the frame is mounted. In (Figure 5.10) is shown the stress state based on Von Mises criterion, in the angular profile corresponding to the maximum load.

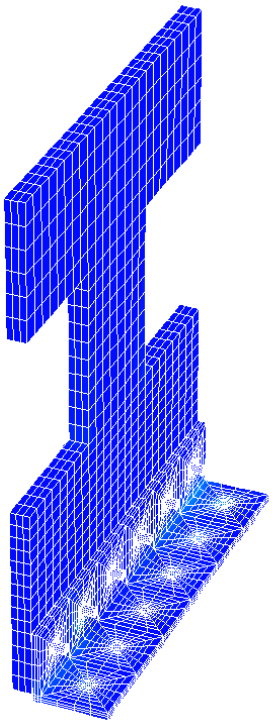

Figure 5.9 – Symmetric mesh

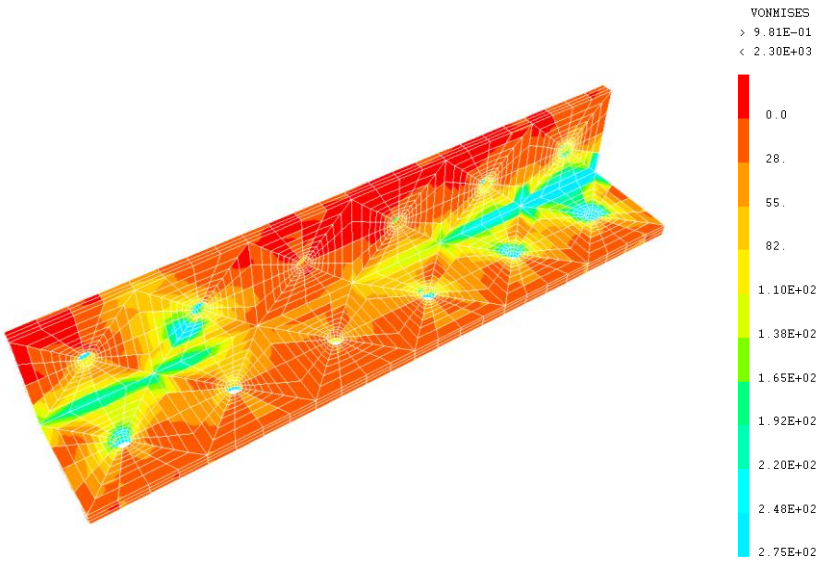

Figure 5.10 – Von Mises stresses at load 300 kN in the angular element

Based on the computed Von Mises stresses, has been decided to employ grade S250 steel with yielding strength of 250 N/mm² and ultimate strength of 400 N/mm². The stresses never exceed the yield strength, except in very localized parts. These local problems were overcome by adding suitable well distributed stiffeners. The Von Mises stresses in the bolts were also calculated, demonstrating that bolts M24 of grade 8.8 would be able to sufficiently transfer the load and still to remain in elastic condition.

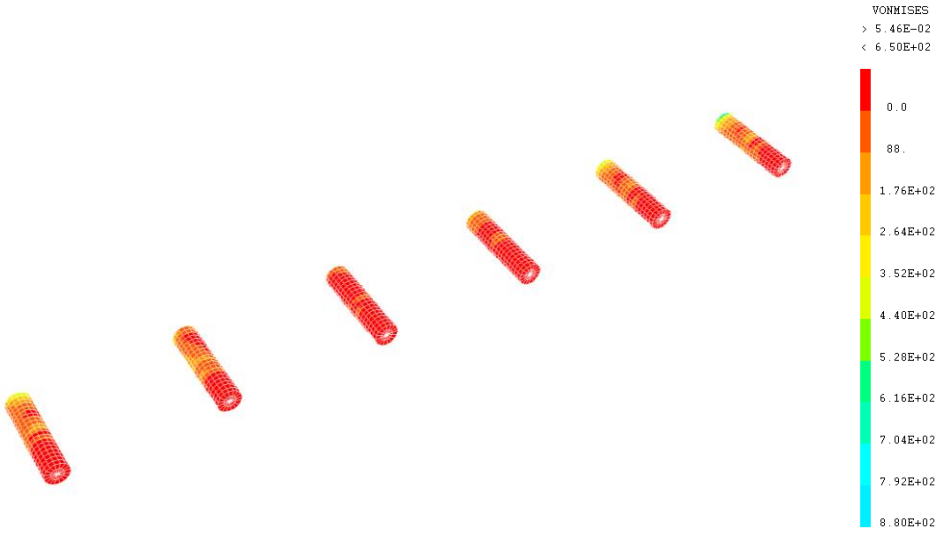

Figure 5.11 – Von Mises stresses in the bolts

5.5 Final frame design

Based on the results of the analysis simulated in the previous section, and some conditionally geometrical and practical constrains the testing steel frame employed hereafter has been constructed by a local steel manufacturing company.

The frame consists of the following parts:

4 UPN 400 profiles, made of grade S250 steel, serving as columns of the frame with additional 20 mm steel plates welded on top and bottom. Each column (Figure 5.13a) has a hole to provide a connection between the specimen and column through threaded bar.

2 angular L shaped profiles reinforced with 20 mm thick steel stiffeners, which are the main element to transfer the load from the specimen to the contrast system with 4 bolts M24 grade 8.8 in slotted (Figure 5.13b).

1 HEB 400 profile with 5 steel stiffeners and 2 lifting bolts; the beam is used to maintain the frame closed providing also axial restraining, and it should be easy to be removed as it requires placing and replacing the specimens (Figure 5.13c). The connection with the 4 UPN 400 columns is done through threaded holes by 16 bolts M27, grade 10.9.

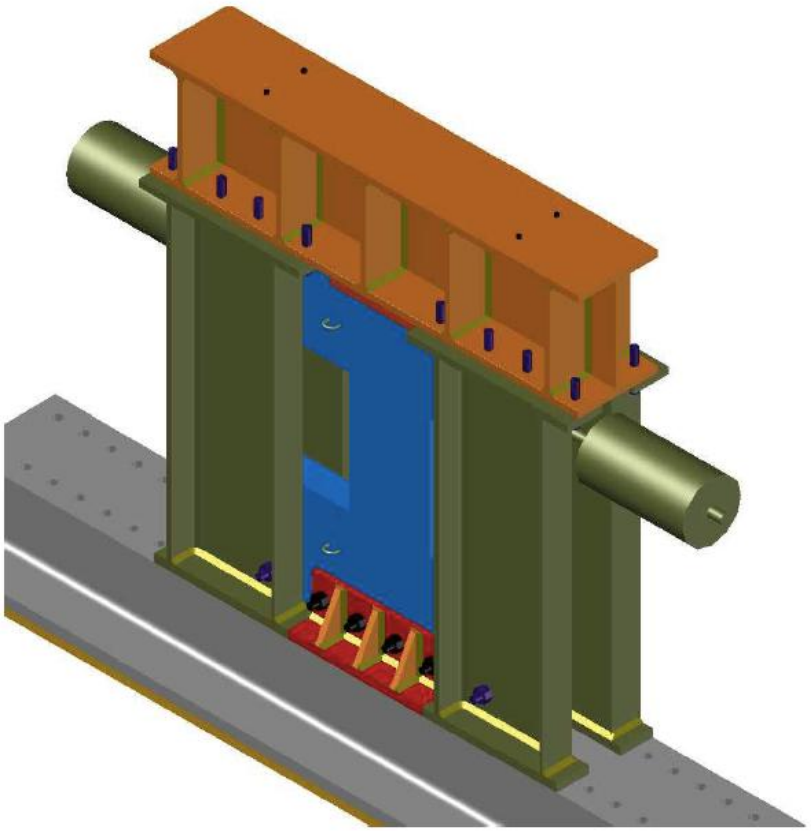

Figure 5.12 – 3D view of the frame

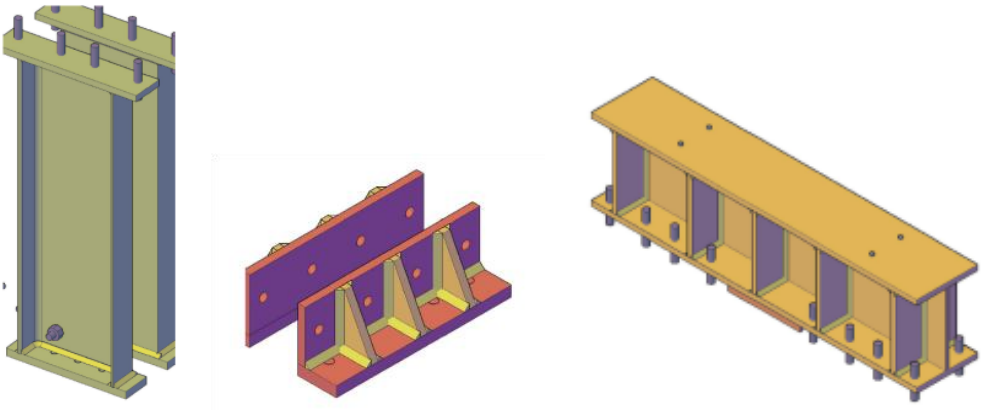

(a) (b) (c)

Figure 5.13 – (a) UPN 400 Columns; (b) angular profiles and (c) HEB 400 beam

In the Appendix the technical details of each component are shown further.

5.6 Test setup description

Figure 5.14 – Test rig fixed at base floor

Two jacks with maximum load capacity of 400 kN and stroke length of 200 mm, have been used to apply the load to the specimen. A hydraulic pump is used with a control panel directly connected to the jacks to generate the pressure in piston of the jack. The pump has two sets of inlet and outlet of the oil; for our purpose was sufficient only one valve. Through two extensions and four tubes it has been possible to create a closed loop of oil flow between the two jacks. This system allowed to effectively implement and apply to the specimen a cyclic loading path with two jacks counter acting each other, as illustrated in (Figure 5.15). The jack is divided in two compartments and has a double acting servo-valve allowing the inlet and outlet pressures to be proportional, making the system to quickly respond to the pressure changes. With this loading system it has been possible to perform displacement controlled tests, by controlling the rate of loading with the generated feedback signal by a desired LVDT. The two valves in the hydraulic pump allow controlling the oil flow, so when one piston moves forward the other proportionally moves backward and vice-versa, generating as a result always a compressive load into the cell.

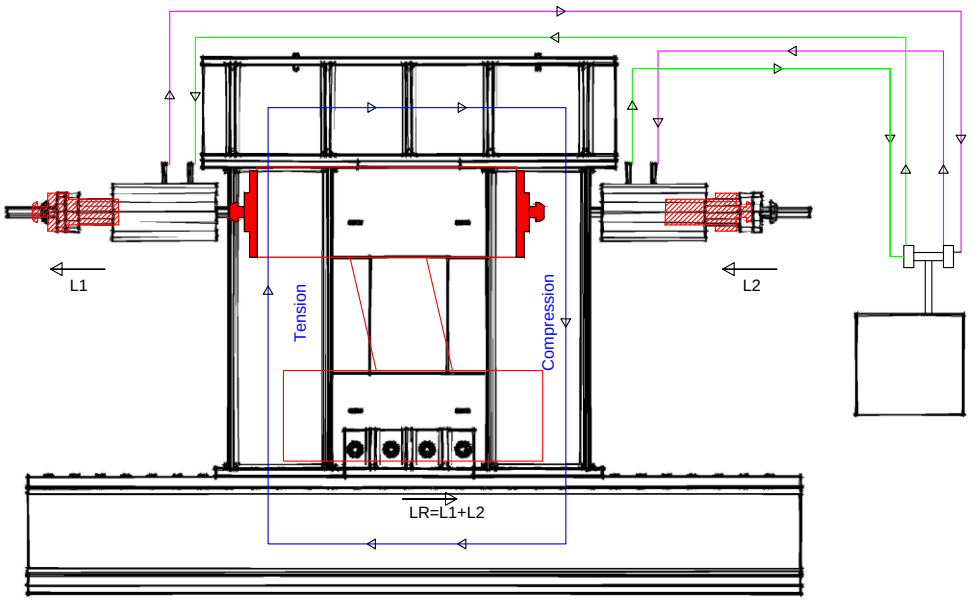

Figure 5.15 – Schematic representation of setup under unidirectional loading. Flow of forces inside the frame; flow of oil in closed circuit

The controlling parameter was the drift, calculated as the ratio between imposed displacement in the centre of upper block and the length of the beam.

$$\text{Drift } (\%) = \frac{\delta}{l} \cdot 100 \tag{5.1}$$

Where δ is imposed displacement and l the coupling beam length equal to (450 mm).

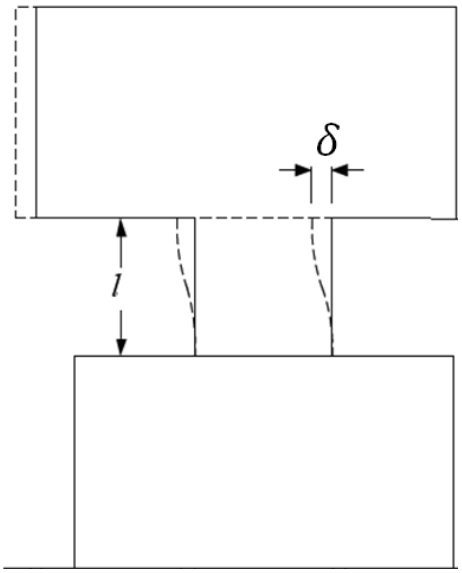

Figure 5.16 – Schematic representation of drift

In all the tests the load has been applied under displacement control, either monotonically or according to a predefined quasi-static reversed cyclic loading. The following cyclic displacement pattern has been assigned (Figure 5.17). Three cycles per each predefined drift level were performed, with drift increment equal to 0.25% up to 2% and with 0.5% increment up to failure. A displacement velocity equal to 0.01 mm/s has been assigned and maintained constant up to failure during monotonic loading tests. Instead for the cyclic tests a frequency of 0.01 Hz has been assigned.

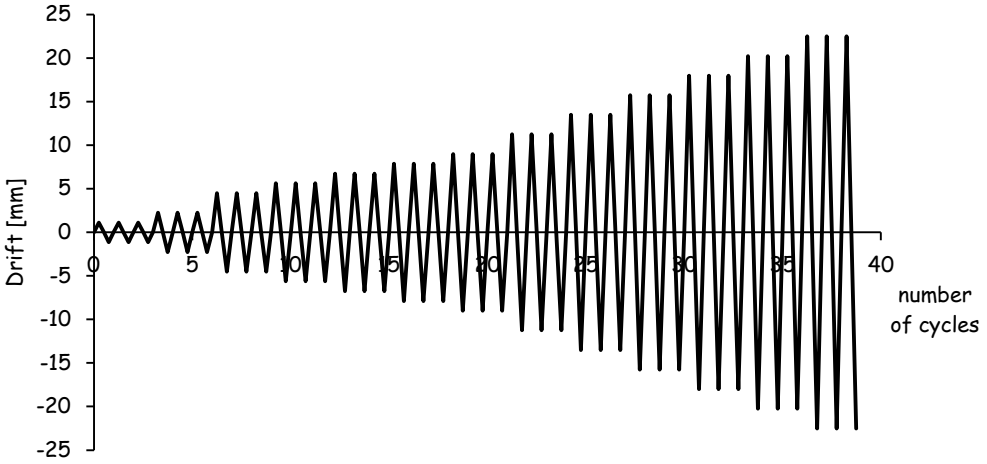

Figure 5.17 – Cyclic displacement history

5.7 Testing programme

Code names were assigned for each specimen and are summarized in the following (Table 5.1), distinguishing between the type of testing either monotonic or cyclic. It should be highlighted that geometry of the specimen and the material is the same, the span depth ratio is a/h=1.5 and the specimens consist form of the beam connected with two rigid blocks. Part of the specimens are constructed and tested with a purpose to understand the contribution of various components on the failure mechanism of the beams, such as the beam without any reinforcement denoted as (PC), or including the longitudinal reinforcement but not the stirrups (OL), or with both longitudinal and transverse reinforcement denoted as (CR) that were considered as reference specimens. The other specimens had both longitudinal and transverse reinforcement and were furthermore repaired/upgraded with either high performance fibre reinforce cementitious composite (HPFRCC) or textile reinforced cementitious composite layer.

Notations used:

- CB: coupling beam;
- PC: plain concrete;
- OL: only longitudinal reinforcement;
- CR: completely reinforced (longitudinal and stirrups);
- HP: repaired/upgraded with HPFRCC;
- TX: upgraded with textile;
- 0: specimen no pre damage;
- 1: specimen pre-damaged at 1% drift;
- 2: specimen pre-damaged at 2% drift;
- A: monotonic test;
- A': monotonic test;
- B: cyclic test.

Table 5.1 – Identification notation for each tested specimen

Conventional coupling beams	Strengthened coupling beams	Retrofitted coupling beams
Coupling beam without any reinforcement 2 monotonic tests (CB-PC/A) (CB-PC/A')	Coupling beam strengthened with HPFRCC 1 monotonic test (CB-HP-0/A)	Coupling beam pre-damaged with (1% drift) monotonically and retrofitted with HPFRCC 1 monotonic test (CB-HP-1/A)
Coupling beams with only longitudinal bars 2 monotonic tests (CB-OL/A) (CB-OL/A')	Coupling beam strengthened with HPFRCC 1 cyclic test (CB-HP-0/B)	Coupling beam pre-damaged with (1% drift) cyclically and retrofitted with HPFRCC 1 cyclic test (CB-HP-1/B)
Coupling beam with both longitudinal and transverse reinforcement 1 monotonic test (CB-CR/A)	Coupling beam strengthened with TRCC 1 monotonic test (CB-TX/A)	Coupling beam pre-damaged with (2% drift) monotonically and retrofitted with HPFRCC 1 monotonic test (CB-HP-2/A)
Coupling beam with both longitudinal and transverse reinforcement 1 cyclic test (CB-CR/B)	Coupling beam strengthened with TRCC 1 cyclic test (CB-TX/B)	Coupling beam pre-damaged with (2% drift) cyclically and retrofitted with HPFRCC 1 cyclic test (CB-HP-2/B)

Due to the expected brittle nature of the failure, the specimens without any reinforcement and only longitudinal reinforcement were tested only under monotonic loading. Instead all other specimens were tested either monotonically or under reversed cyclic loading. The pre-damage was induced both under monotonic and cyclic displacements. It should be emphasized that the specimens pre-damaged under monotonic loading after being repaired were tested monotonically up to failure, likewise for the cyclic tests. In total 14 specimens were tested.

5.8 Production of specimens

Three wooden formworks for manufacturing of the specimens were provided to the concrete producer and all the specimens were casted during 7 working days. The prepared reinforcement cages as for the different intended reinforcement layouts were placed into the formwork with plastic holders to provide the required concrete cover. Filleted steel tubes M24 with thickness of 10 mm were embedded on the lower block for connection of the specimen with base floor, and a hollowed plastic tube with 30 mm diameter was used on the

upper block to accommodate the Dywidag threaded bar for applying the load. Concrete was mixed and poured into formworks for three specimens at the same time, afterwards vibrated and flattened. The de-moulding was done after 24 hours and specimens were cured by maintaining there under plastic cover. A few days after, all the specimens were transported to the laboratory of department where tests were done. The procedure is illustrated in (Figure 5.18 and Figure 5.19).

(a) (b)

Figure 5.18 – (a) Reinforcement cage of the block and (b) reinforcement cage in the formwork

Figure 5.19 – Pouring and vibration of concrete

5.9 Surface treatment

Before applying the repair/upgrading cementitious layer it was necessary to provide a certain degree of roughness at the surface of specimens, with the purpose of having a equal surface quality and uniform interaction between the two different layers. To this purpose, a rotary diamond disk has been used as shown in (Figure 5.20).

(a) (b)

Figure 5.20 – (a) Roughening technique and (b) before and after treatment: top-upper surface; bottom-lower surface

5.10 Materials

5.10.1 Concrete C 20/25

For the preparation of the specimens a commonly used strength concrete was employed, assuming that the structures requiring retrofitting or upgrading have ordinary strength. For this reason a class C20/25 concrete was chosen. The concrete producer provided a mix design to achieve these characteristics listed, as in (Table 5.2), with maximum aggregate size 15 mm and the class of slump consistency S4 according to [En 12350-2]. The cubic specimens to be tested in compression were prepared on daily basis with the size 100x100x100 mm for each concrete batch according to [EN 12390-1]. From tests carried out was obtained an average value of compressive strength for concrete cubes provided by the concrete factory of 36.61 N/mm², the detailed results are shown in Appendix. According to [Eurocode2], the characteristic strength on cubes can be assumed equal to average value -10 N/mm² and hence the obtained results show that the concrete we employed can be classified as C20/25.

Table 5.2 – Conventional concrete mixture

Material	**kg/m³**
CEM I 52,5 R	260
Limestone filler	140
Sand 0/3	620
Natural Sand 0/12	640
Crushed gravel 4/8	410
Crushed gravel 8/15	150
Super flux acrylic	3.2
Water	135

5.10.2 Steel reinforcement

B450 steel reinforcement, in three different diameters, was used: ϕ6 mm for the stirrups, ϕ8 for the longitudinal reinforcement, and ϕ14 for the longitudinal reinforcement of the rigid blocks. For each size 2 uniaxial tensile tests to confirm the class of steel reinforcement were performed, shown in Appendix.

5.11 Casting procedure of the retrofitting/strengthening layer

5.11.1 HPFRCC

The procedure for the characterization of HPFRCC has been described in Chapter 3. The same material with 100 kg/m^3 of fibres was used for this case with mix design and protocol as reported in Chapter 3.

For a single specimen repair about 15 l of the fibre reinforced material were required. It was prepared in a Controls mixer with the maximum capacity of 40 l. The sand was maintained in oven to provide low relative humidity since the uncontrolled water content could affect the fresh state performance and hence mechanical behaviour in the hardened state.

For mixture casting and its visual inspection, a transparent plexiglass mould was prepared installed around the specimen to apply the repair layer as shown in (Figure 5.21). The specimens are rotated in such a way simulate the real situation of the typical coupling beams.

It was chosen to assemble the formwork with slabs of plexiglass to visually ascertain if the material HPFRCC fills all the formwork, in order to have a constant thickness of 2 cm over the entire area of retrofitting, namely the two lateral faces of the lintels and a third face on the intrados of the coupling beam. As the flow direction of the mixture influences the orientation of the fibres, and thus affecting the material mechanical behaviour, the mixture was poured from the top using a trowel to direct it into formwork.

Figure 5.21 – Casting process of HPFRCC

The plexiglass could be removed after 24 h, so the successive casting could be performed, and the specimens were maintained under plastic cover until the day of testing.

5.11.2 Textile reinforced cementitious composite

In two specimens after preparation of the roughness the upgrading with textile reinforced mortar was applied. As the mortar volume required for the specimen was much lower than of HPFRCC a mixing machine with lower capacity was used. The current mixture was with reference to a large campaign of tests done for different mixtures and different textile configurations [Zani, 2013], described in Chapter 3. Fine grained sand with maximum size of 0.6 mm was used to provide sufficient penetration in the textile.

Table 5.3 – TRCC mixture

Material	**kg/m³**
Cement CEM 52,5	600
Slag	957
Water	209
Sand(0/0.6)	500
Superplasticizer	44

Table 5.4 – Mixing protocol for TRCC matrix

Task	
Mix dry cement and slag	30 s
Add water and SP (75%)	30 s
Mix paste at 50 rpm	1 min
Mix paste at 100 rpm	2 min
Add sand while mixing at 100 rpm	3 min
Mix mortar at 100 rpm and add remaining SP(25%)	3 min

Lamination technique was employed to manufacture the strengthening layer, without any induced pressure shown in (Figure 5.22). Firstly, a layer of mortar was poured and levelled on the specimen than the textile was stretched and finally the layer of mortar above the fabric was applied as shown in (Figure 5.22), and the thickness of the entire TRCC application reached about 6 mm. A day after it was possible to rotate the specimen and apply the other layer by following the same method. The warp direction of the textile was oriented orthogonally to the axis of the beam, to represent a sort of a widespread stirrup.

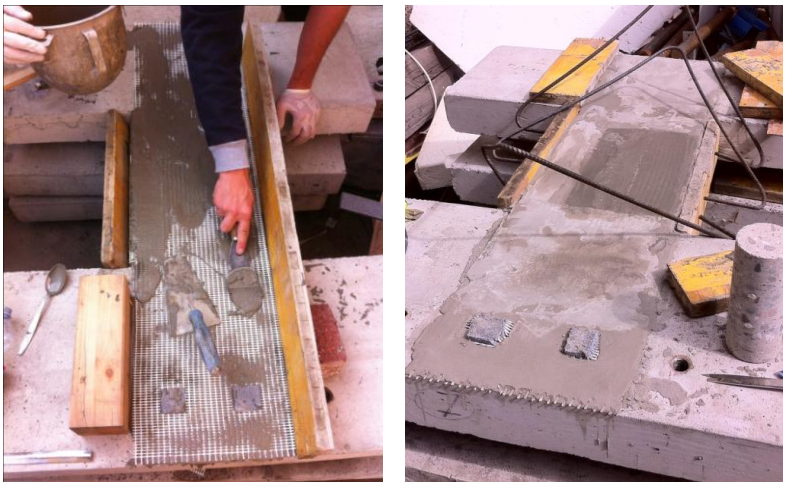

Figure 5.22 – Casting process for application of TRCC layer

6

6 Investigation at structural member level: Experimental results

In this chapter the results are described obtained from the experimental campaign presented in the previous chapter. The coupling beams that have been tested can be divided into two broad categories: the first category includes all the coupling beams non strengthened/retrofitted, in the second category the beams which have been strengthened or repaired are included. As for the strengthening/retrofitting technique, there are two subcategories depending on the material used; high performance fibre reinforced cementitious composites (HPFRCC) or textile reinforced cementitious composites (TRCC).

6.1 Coupling beams non-strengthened/retrofitted

The first set of results deals with non retrofitted/strengthened coupling beams specimens which will stand as reference specimens. In this set are included the coupling beams without any reinforcement, with only longitudinal reinforcement and with longitudinal and transverse reinforcement. These tests would provide a better understanding of shear behaviour of coupling beams with span to depth ratio of 1.5, involving reinforcement contribution on the failure mechanism, load bearing capacity, ductility and energy dissipation.

6.1.1 Coupling beam without any steel reinforcement

Two specimens were casted without any steel reinforcement taking special care during lifting to avoid any unpredictable crack, which would lead to collapse of the beam. The specimens were tested under monotonic loading.

The two specimens gave equivalent results in terms of load bearing capacity, respectively equal to 97 kN and 103 kN, with drift values around 12 mm and 15 mm. The initial stiffness, as evaluated through a linear regression, for both cases, resulted equal to about 10 kN/mm. The lack of reinforcement resulted in diagonal brittle failure of the beam and sudden energy release, which split the beam into two parts. In both cases the crack which causes the failure was initiated at the centre of the specimen and propagated diagonally, in catastrophic way due to the brittle nature of failure.

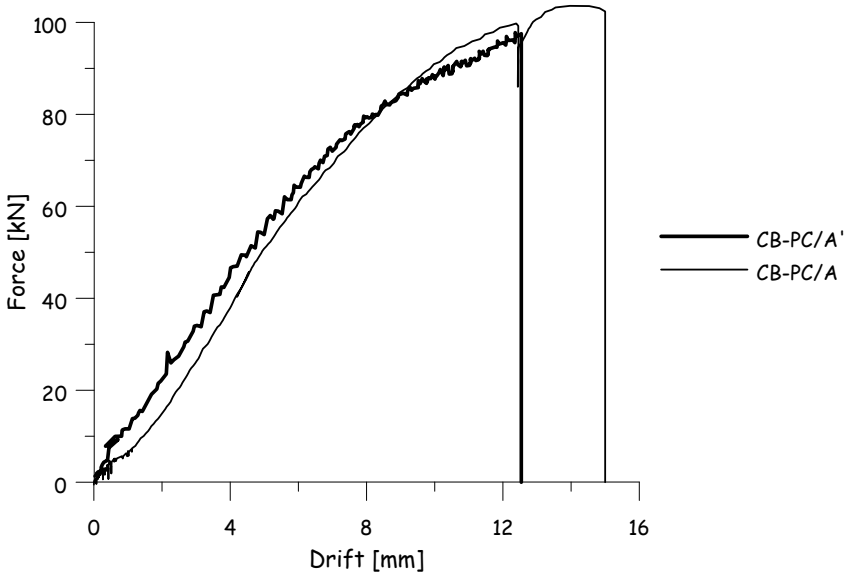

Figure 6.1 – Load displacement curve

Figure 6.2 – Diagonal cracking of the beam without any reinforcement

It has been attempted to predict the ultimate strength attained during the test with a simple calculation, taking into account the tensile strength of the concrete. The resistant mechanism is shown schematically (Figure 6.3). The tensile strength of the concrete has been taken in accordance with equation proposed in [Eurocode2].

$$f_{ct} = 0.3 f_{ck}^{2/3} \tag{6.1}$$

$$f_{cm} = 0.83 f_{cm,cube} \tag{6.2}$$

$$f_{ck} = f_{cm} - 8 \tag{6.3}$$

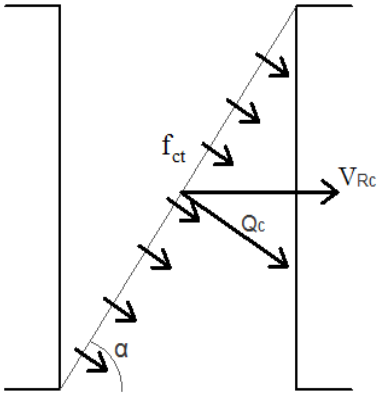

Figure 6.3 – Diagonal failure mechanism of the beam

The average cube strength at testing day for the companion specimen was $f_{cm,cube}$=36.2 N/mm², which leads to f_{ck}=22.1 N/mm² and f_{ct}=2.36 N/mm². Assuming the angle α=33°, it is estimated the shear strength of coupling beam, from the resistant mechanism shown in (Figure 6.3) it comes out $V_{Rc} = 106.3\,\text{kN}$, or the ratio $\frac{V_{exp}}{V_{calc}} = \frac{97}{106} = 0.91$ respectively $\frac{V_{exp}}{V_{calc}} = \frac{103}{106} = 0.97$.

6.1.2 Coupling beams with only longitudinal reinforcement

Also in the beams reinforced with only longitudinal bars a brittle failure was experimentally observed. In the graph below (Figure 6.4) results of the two tests under monotonic loading are shown. It has to be mentioned that one of the tests was not completed as it was necessary to stop it a at force of about 70 kN, due to the problems observed on the specimen alignment during loading. As a matter of fact during casting process the bushings in the lower block moved slightly, causing a problem on fixing the specimen correctly. Thus, with increased lateral displacement on the upper block, contact between the sample and the frame was observed, which caused the test to be stopped.

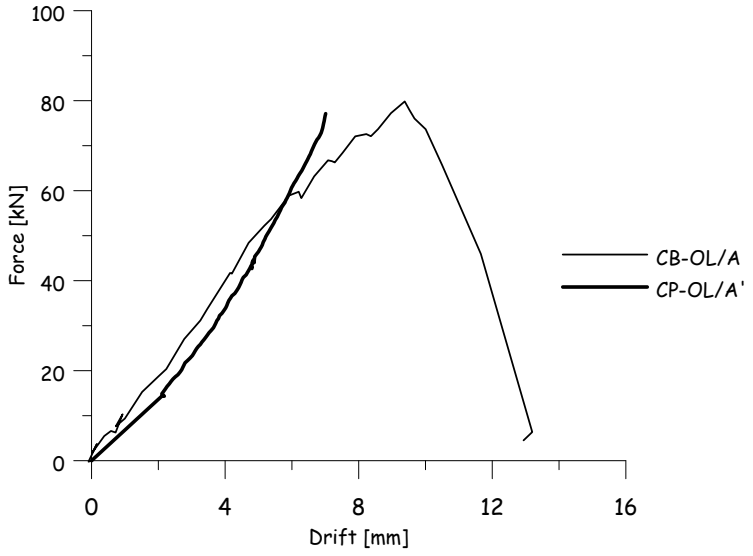

Figure 6.4 – Load displacement curve specimen with longitudinal reinforcement

The specimen (CB-OL/A) showed a load bearing capacity equal to 80 kN, in correspondence of a displacement drift slightly lower than 10 mm. The initial slope of the curve is calculated to be 10 kN/mm, equal to that of the two samples without reinforcement. The first cracking appeared in the tension zone and propagated longitudinally along the reinforcement and then along an inclined path towards the compression zone, as typical of shear loaded members. It can be argued that the onset of the activation of the strut and the tie mechanism required the longitudinal reinforcement to elongate thus activating bond and hence the observed crack propagation. Anyway the necessary elongation was not possible because of the axial confinement provided by the HEB profile; this resulted in axial compression force which modified the compression stress field trajectory resulting in more sub vertical strut and in the failure mechanism shown in (Figure 6.5). It is an interesting mode of failure, not anticipated in advance; giving suggestion that the presence of longitudinal reinforcement acted as defect causing prior failure of the beam, however the diagonal cracking appear to be a rotating. Unconditionally the coupling beams on the wall systems are subjected to the passive confinement, which is provided by the rigid walls.

Regarding the second test of pushover on coupling beams with longitudinal reinforcement, despite that was not fully performed, the load displacement curve recorded are comparable.

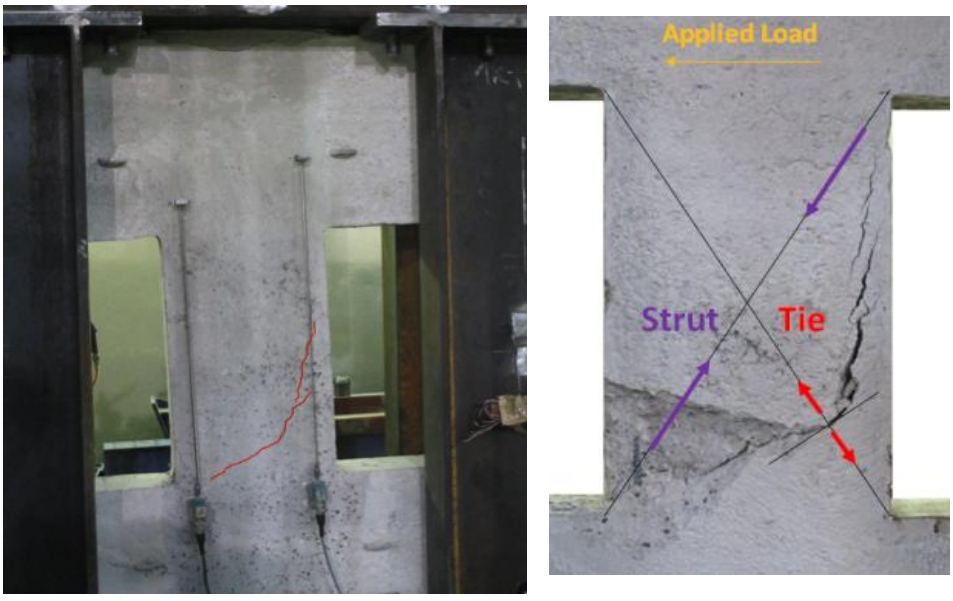

(a) (b)

Figure 6.5 – Coupling beam with longitudinal reinforcement: (a) crack initiation and (b) crack propagation and failure of the specimen

The maximum bearing capacity of coupling beams with longitudinal reinforcement has been calculated following the approach proposed by [Toniolo et al., 2010] based on strut and tie model. The scheme has been illustrated in (Figure 6.6).

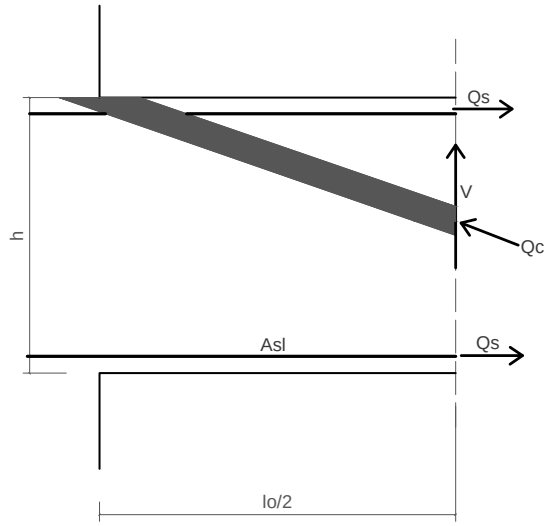

Figure 6.6 – Strut and tie mechanism for coupling beam with longitudinal reinforcement

Accordingly the strut and tie bearing capacity could be estimated from the following equations:

$$Q_{Rd,c} = 0.4 \frac{bhf_{cm}}{\left(1+\lambda^2\right)} \tag{6.4}$$

$$Q_{Rd,s} = \frac{A_{sl}f_{yk}}{\left(\frac{\lambda}{2}+\frac{e}{z}\right)} \tag{6.5}$$

b and h are the width and height of the beam section, in our case b=100 mm and h=300 mm, with lever arm assumed as $z = 0.84h = 252\,mm$. For the estimation of λ it is taken the length of the beam $l_0 = 450\,mm$, and assuming effective length is $l = l_0 + 0.16h = 498\,mm$, $\lambda = l/z = 1.97$. In this case eccentricity is e=0 assumed considering that the test is symmetric.

Regarding the material characteristics the average values of the tests are assumed, from the tensile test on reinforcement and compressive tests on concrete cubes of the same batch of concrete used to cast the tested specimen. The longitudinal reinforcements were considered in the portion that works in tension respectively 2ϕ8.

The shear strength estimated from resisting mechanism of concrete and reinforcement is calculated as follows:

$$Q_{Rd,c} = 63.6\,kN$$

$$Q_{Rd,s} = 57\,kN$$

Based on the obtained values the failure of the coupling beams would have caused by weaker mechanism i.e. the yielding of longitudinal reinforcement. Anyway in this approach the axial confinement provided by the frame is neglected (Figure 6.7). This confining action, acting in

compression along the axis of the coupling beam beneficially affects the ultimate strength, restraining as remarked above the axial elongation of the longitudinal reinforcement, hence it turns out that the yielding of longitudinal reinforcement does not occur, as it was observed the strut failure. The contribution of axial elongation restrain of the specimen was estimated as the ratio between the observed experimental load bearing capacity and the calculated resistance. It comes out $k_{axial} = 1.25$.

$$k_{axial} = \frac{V_{exp}}{Q_{Rd,c}} \tag{6.6}$$

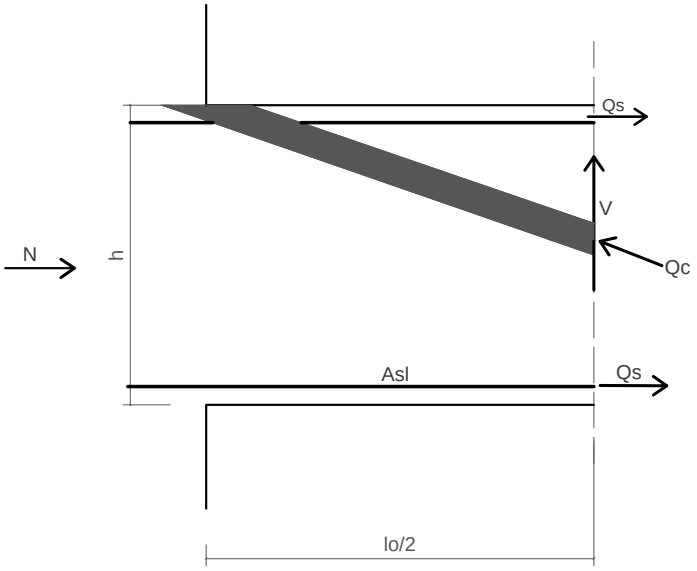

Figure 6.7 – Axial action effect on strut and tie mechanism

6.1.3 Coupling beam with longitudinal and transverse reinforcement

The beams with complete reinforcement will serve as reference specimens for further investigation of upgrading/retrofitting. They were reinforced with 4 longitudinal bars ϕ8 (2 on the top and 2 on the bottom), and transverse reinforcement ϕ6 spaced at 100 mm. From the results both monotonic and reversed cyclic displacement tests on two coupling beam specimens, it is determined the effectiveness of the reinforcement, both in terms of load bearing and displacement capacity shown in (Figure 6.8).

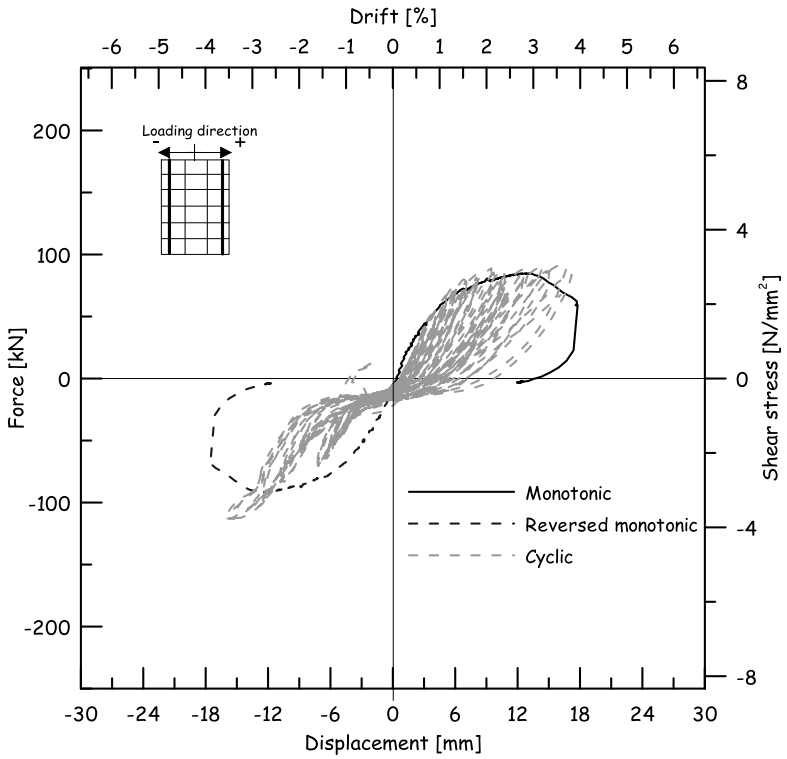

Figure 6.8 – Load displacement curve for monotonic and reversed cyclic loading on beams with complete reinforcement (CB-CR/A) and (CB-CR/B)

The specimen (CB-CR/A) tested under monotonic loading, exhibited an initial elastic behaviour, with initial stiffness measured equal to 16.3 kN/mm, up to a load equal to 64 kN which correspond to a drift displacement of 4.5 mm (or 1%). The slope of the curve progressively decreases with increased loading until was reached maximum load capacity of 95 kN, corresponding to a drift displacement 13 mm (or 2.92%). Unlike the previous tests, with only longitudinal reinforcement and no reinforcement in the coupling beams, this test showed a more stable behaviour providing greater ductility, observed from softening branch (Figure 6.8).

In the following pictures (Figure 6.9 and Figure 6.10) is shown the specimen from crack formation to failure under monotonic loading. At around 1% drift, after passing the elastic phase, inclined crack first appears at the bottom region of the coupling beam. Shortly after the dominant diagonal crack appears, accompanied with additional finer inclined cracks (Figure 6.10b).

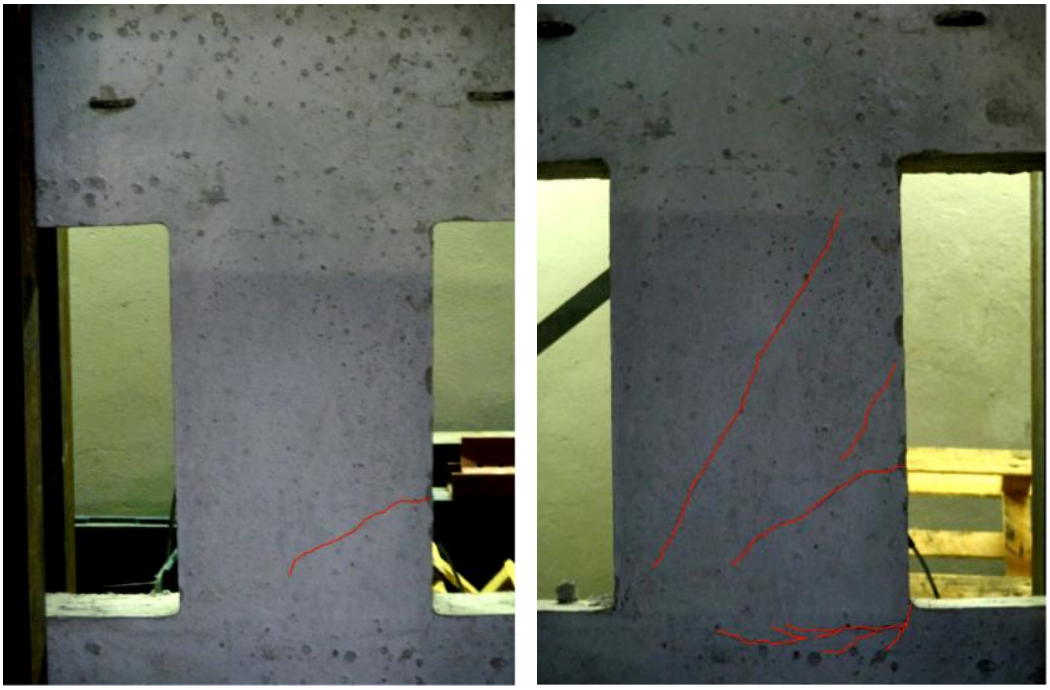

(a) (b)

Figure 6.9 – Coupling beams with complete reinforcement under monotonic loading: (a) crack initiation and (b) multiple cracks formation

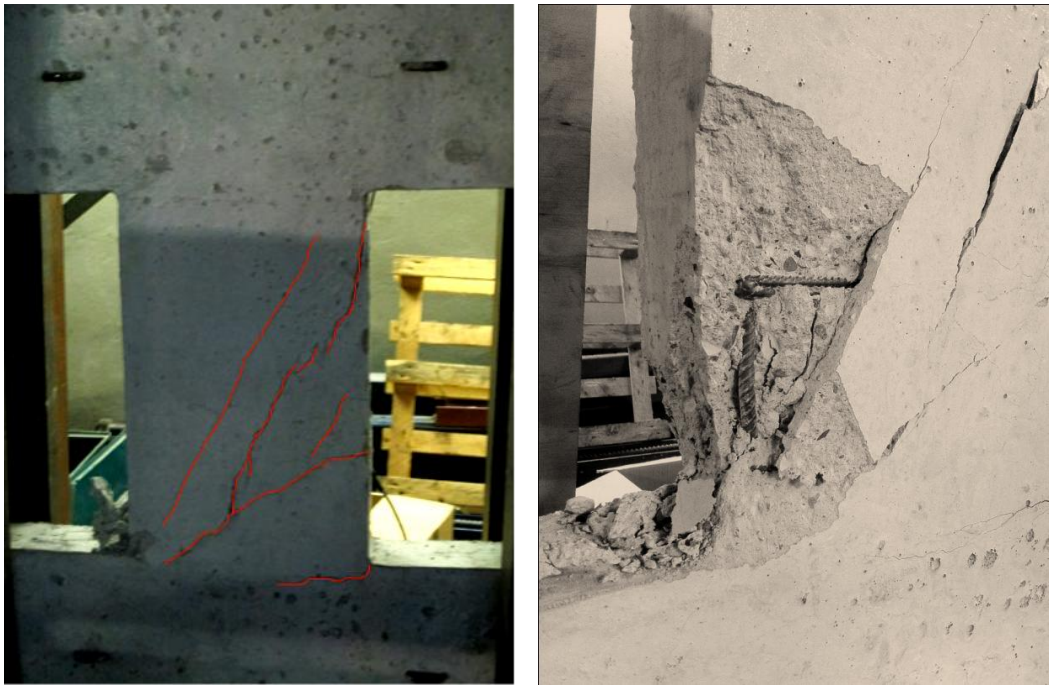

(a) (b)

Figure 6.10 – Coupling beams with complete reinforcement under monotonic loading: (a) crack evolution and (b) failure of the specimen

From the test (CB-CR/B) which represents the specimen with complete reinforcement subjected to reverse cyclic loading, globally speaking it was observed a good correspondence with the test under monotonic loading (CB-CR/A). The monotonic test shows a similar load

displacement curve as the envelope of cyclic test. The maximum load bearing capacity in the monotonic test was equal to 90 kN, and in the cyclic test was equal to 98 kN. With exceeding amplitudes of cycles a progressive loss of stiffness has been observed, especially after 2% drift. Even with increased amplitude of cycles or increased imposed displacement, a stable behaviour it was observed.

In (Figure 6.8) it can be also observed that cyclic test behaviour is not completely symmetric.

The maximum load reached on the reversed direction has been equal to 110 kN which was greater than the corresponding positive but the cycles were significantly less stable. This non symmetrical behaviour can be justified by two reasons:

- Possible imperfection during fixing of the specimen.
- Progressive deterioration and damage of the specimen, since the cyclic test always started in the positive direction (coinciding with the direction of the pushover).

Like in monotonic test also in cyclic test the failure of coupling beam occurs due to crushing of concrete. The evolution of crack initiation, propagation and failure is shown in (Figure 6.11 and Figure 6.12). At 1% drift (the first inclined crack) appeared, accompanied shortly after by other cracks. With increased loading crushing of concrete was observed accompanied by local instability of longitudinal reinforcement which is typical of cyclic failure of r/c elements. This phenomenon takes place between the spacing of two stirrups; it could be hence argued that as denser stirrup reinforcement would reduce the buckling length of the bars and likely result in an improved global performance of the coupling beam.

(a) (b)

Figure 6.11 – Coupling beams with both longitudinal and transverse reinforcement under cyclic loading (a) at 1% drift and (b) at 1.5% drift

Figure 6.12 – Coupling beams with both longitudinal and transverse reinforcement under increased cyclic displacements

Figure 6.13 – Coupling beams with complete reinforcement at final step of displacement

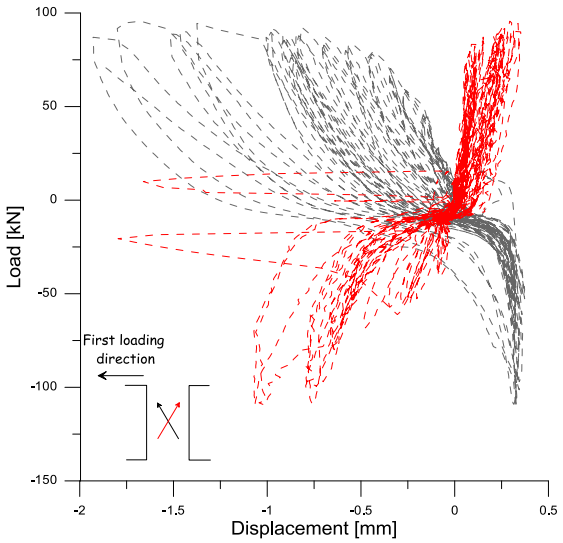

Figure 6.14 –LVDT diagonal displacement measurements between for the specimen with both longitudinal and transverse reinforcement

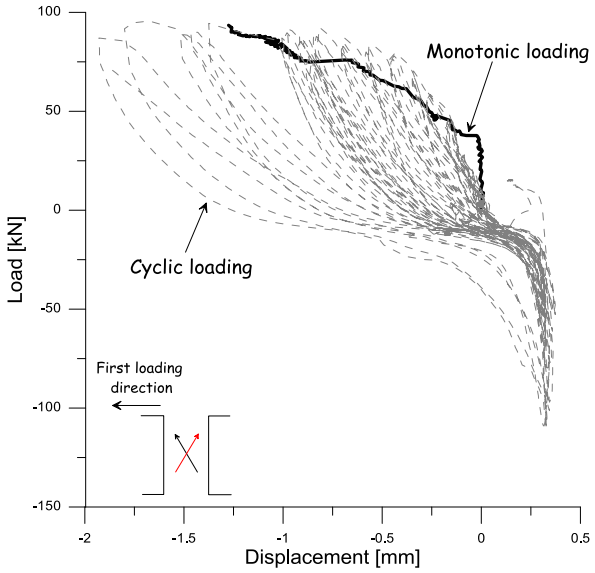

Figure 6.15 – Comparison between LVDT diagonal displacement measurements between monotonic and cyclic test for the coupling beam with both longitudinal and transverse reinforcement

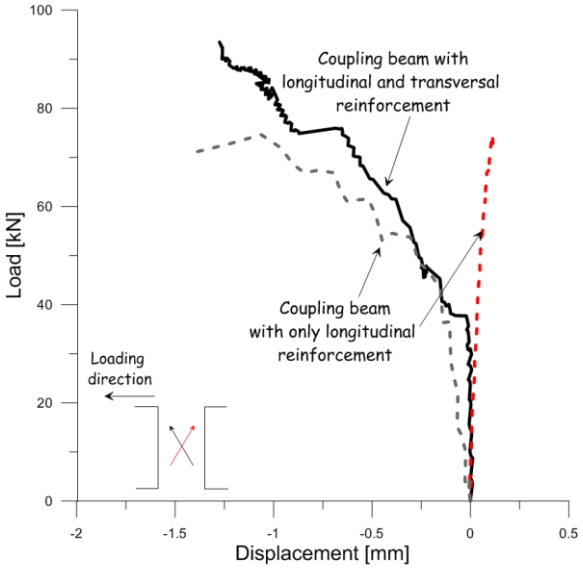

Figure 6.16 – Comparison between LVDT diagonal displacement measurements between two monotonic tests

Regarding the prediction of maximum shear strength reached during the test, the approach provided by [Toniolo et al., 2010], taking into account the compressed concrete and longitudinal bars gives the same results as in the case of beam with only longitudinal reinforcement. Concrete crushing was estimated to be equal to Q_{Rc}=63.6 kN or of reinforcement yielding at 57 kN. Also in this case the axial and stirrup confinement was omitted. In order to take into account the confinement contribution provided by stirrups was used the equation proposed by [Park et al., 1982], and it comes out that the contribution provided is $k_{stirrup} = 1.1$.

$$k_{stirrup} = 1 + \rho_{sw}\frac{f_{yw}}{f_{cm}} \tag{6.7}$$

$$Q_{Rd,c} = 0.4k_{axial}\frac{bhf_{cm}k_{stirrup}}{\left(1+\lambda^2\right)} \tag{6.8}$$

It comes out that:

$$Q_{Rd,c} = 0.55\frac{bhf_{cm}}{\left(1+\lambda^2\right)} \tag{6.9}$$

The coefficient 0.55 interestingly corresponds with what was proposed by [Toniolo et al., 2010] for design of coupling beams.

And the bearing capacity estimated considering the contribution of axial and stirrup confinements, is equal to 87.61 kN, and the shear strength ratio is estimated to be $\frac{V_{exp}}{V_{calc}} = \frac{90}{87.6} = 1.02$, for the monotonic case and equal to $\frac{V_{exp}}{V_{calc}} = \frac{98}{87.6} = 1.11$, for the cyclic case respectively.

To take into account the presence of the stirrups [*fib* Model Code 2010; Bentz, 2010] approaches will be adopted for estimation of maximum load capacity.

It has been proposed a method on verification of the beams subjected to shear forces. It used the method based on increased levels of approximation which leads to increased level of accuracy and in meantime of complexity, which at certain level requires an iterative procedure. The shear capacity is estimated as the sum of offered by combined concrete and steel contribution, is written as:

$$V_{Rd}=V_{Rd,s}+V_{Rd,c} \tag{6.10}$$

The load capacity should not exceed the maximum capacity from crushing of concrete, calculated as:

$$V_{Rd} \le V_{Rd,max} = 0.6\left(30/f_{cm}\right)^{1/3} f_{cm} bz \frac{\cot\theta}{1+\cot^2\theta} \tag{6.11}$$

b indicates the width of the beam and z is the effective lever arm. If this condition is verified, it comes out the shear capacity form steel and concrete contribution is:

$$V_{Rd,s} = \frac{A_{sw}}{s} z f_{yw} \cot\theta \tag{6.12}$$

$$V_{Rd,c} = k_v \sqrt{f_{cm}}\, bz \tag{6.13}$$

A_{sw} and f_{yw} respectively indicate the area, and the yield strength of the web reinforcement, k_v is parameter to take into account the aggregate interlock which provides improvement of shear capacity on reinforced concrete beam. The bearing capacity estimated at this level of the approximation was the sum of two contributions:

$$V_{Rd,s} = 117.9 \text{ kN}$$

$$V_{Rd,c} = 22.7 \text{ kN}$$

$$V_{Rd}=V_{Rd,c}+V_{Rd,s}=140.6 \text{ kN}$$

[*fib* Model Code 2010] provides an approach considering the III level of approximation. In this case it is suggested to assume an arbitrary value of the strain ε_x and then as a function of it has been calculated the cracking angle θ and k_v can be calculated according to the following relations:

$$\theta = 29 + 7000\varepsilon_x \tag{6.14}$$

$$k_v = \begin{cases} \dfrac{0.4}{1+1500\varepsilon_x}\dfrac{1300}{1000+0.7k_g z} & \text{if } \rho_w = 0 \quad (6.15) \\ \dfrac{0.4}{1+1500\varepsilon_x} & \text{if } \rho_w \geq 0.08\dfrac{\sqrt{f_{cm}}}{f_y} \quad (6.16) \end{cases}$$

Where k_g is parameter defining the roughness of crack, calculated based on maximum aggregate size using for the concrete composition.

After calculating it comes out:

$$V_{Rd,s} = \frac{A_{sw}}{s} z f_{yw} \cot\theta \quad (6.17)$$

$$V_{Rd,c} = k_v \sqrt{f_{cm}} b z \quad (6.18)$$

$$V_{Rd} = V_{Rd,c} + V_{Rd,s} \quad (6.19)$$

The strain ε_x is then iteratively calculated starting from $\varepsilon_x = 0.001$;

$$\varepsilon_x = \frac{0.5V_{Rd}}{2E_s A_{sl}} \quad (6.20)$$

The procedure is repeated iteratively until the last ε_x is equal to the previous value. The bearing capacity at III level approach results as the sum between two contributions:

$$V_{Rd,s} = 81.1 \text{ kN}$$

$$V_{Rd,c} = 14.3 \text{ kN}$$

$$V_{Rd} = V_{Rd,c} + V_{Rd,s} = 95.4 \text{ kN}$$

According to this method the shear capacity of the coupling beam is estimated equal to 95.4 kN, and with ratio $\frac{V_{exp}}{V_{calc}} = 0.94$, for monotonic loading and 1.03 for cyclic loading respectively. This approach evidentially provides as well accurate prediction of experimental results.

6.2 Retrofitted/strengthened coupling beams

In the following section the experimental results are presented of tests on coupling beams strengthened or repaired using cement based composites, respectively steel fibre and textile reinforced cementitious composites.

6.2.1 Retrofitted/strengthened coupling beams with HPFRCC

The first technique employed for repair or strengthening of coupling beams consists of jacketing the concrete section with a HPFRCC layer 2 cm thick on three sides as sketched in

scheme (Figure 6.17) and as detailed in previous chapter. The results are presented considering the global behaviour of coupling beams under shear loading, through load-drift displacement curve under both monotonic and cyclic loading. The minimum time from casting of HPFRCC to the testing of coupling beam was 10 days.

Figure 6.17 – Three sided jacketing

6.2.1.1 Coupling beams strengthened with HPFRCC

In (Figure 6.18) the results are presented obtained for the specimens (CB-HP-0/A) and (CB-HP-0/B); the coupling beam of the specimen, reinforced with both longitudinal and transverse reinforcement, were strengthened with layer of HPFRCC in three sides, subjected to monotonic (A) and reversed cyclic loading (B).

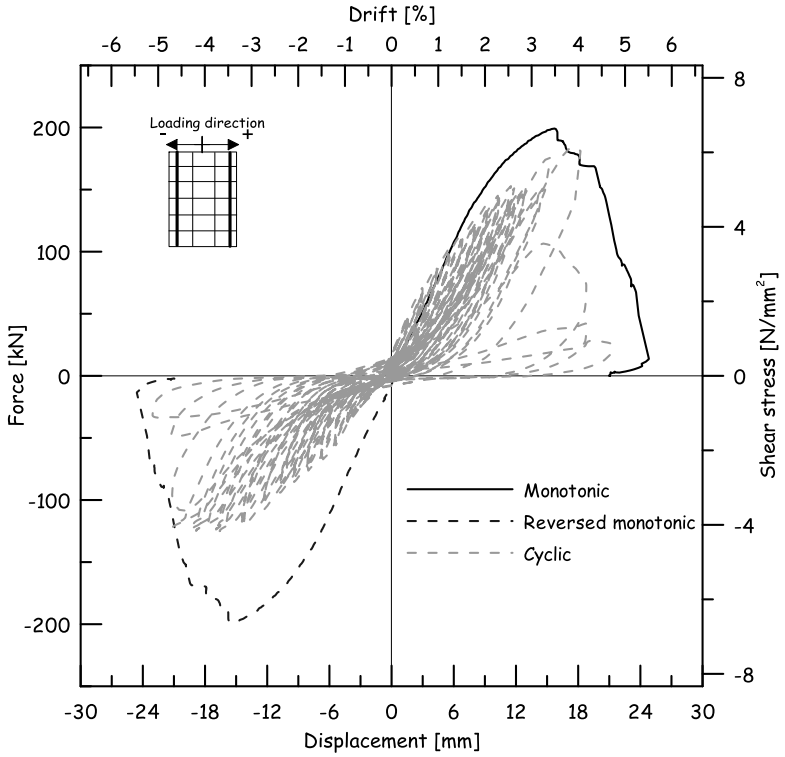

Figure 6.18 – Load displacement curve for monotonic and reversed cyclic loading on beams strengthened with HPFRCC (CB-HP-0/A) and (CB-HP-0/B)

The specimen (CB-HP-0/A) was tested under monotonic loading. A maximum load capacity of 199 kN was recorded at corresponding drift displacement of 15 mm (or 3.33%). Another interesting observation is that in the softening branch of the specimen maintains certain stability, providing a beneficial ductility. The initial elastic stiffens was measured equal to 16.7 kN/mm. In (Figure 6.19 and Figure 6.20) the crack evolution under increasing displacement is shown.

It has been observed visually a single inclined crack leading to final collapse, associated with a certain delamination of the HPFRCC layer. The delamination has not occurred to the same extent on both sides of the specimen but more significantly on one side, giving insight that the layer of HPFRCC could not be fully functional. Whereas, in the other side the strengthening layer is more effective, provided from better bonding achieved between concrete and HPFRCC. In retrofitting layer mainly in terms of post peak ductility (delamiantion was observed to start almost in correspondence of the peak load).

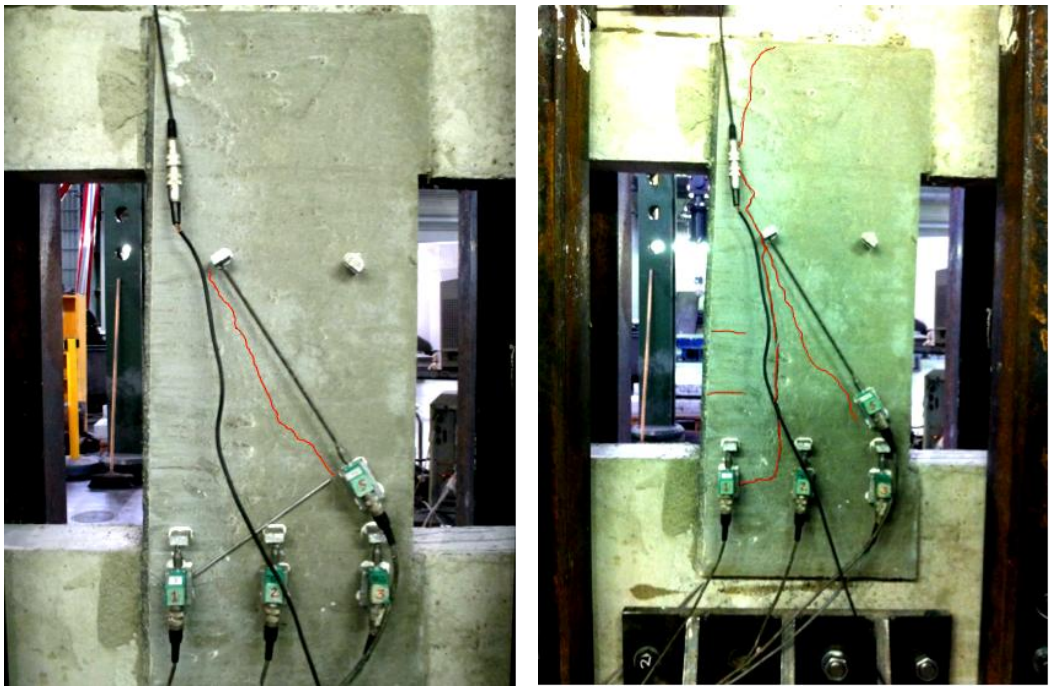

Figure 6.19 – Coupling beams strengthened with HPFRCC under monotonic loading at increased drift level

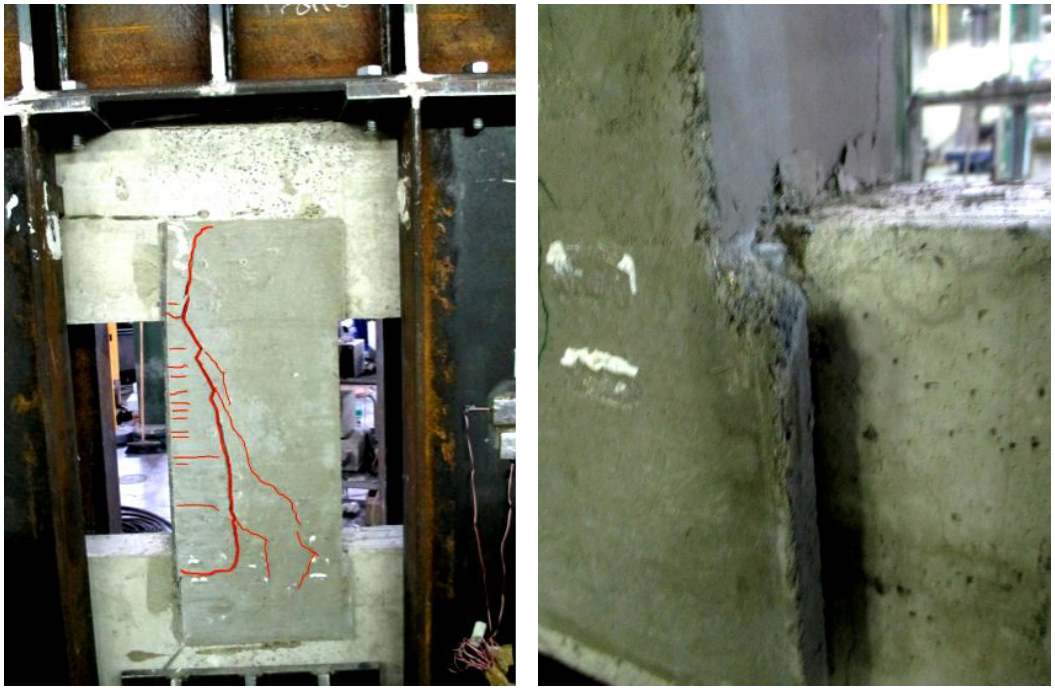

(a) (b)

Figure 6.20 – Coupling beams strengthened with HPFRCC under monotonic loading: (a) deformations and cracking at final step and (b) delamination of HPFRRC

With reference to cyclic test, a good correspondence of the envelope of the cycles has been observed with the pushover, the maximum load capacity achieved is equal to 186 kN at a drift equal to 3.55%. The cyclic behaviour along the positive side has been stable up to values of drift 3% then the stability is significantly reduced, however not lost completely. Observing the cyclic behaviour as a whole, positive and negative, the symmetry was not very well maintained; in the negative loading direction has been observed a lower load capacity about 120 kN. This lack of symmetry can be obviously and reasonably accepted keeping in mind that the specimen was not symmetrically strengthened with HPFRCC. Moreover the failure occurred trough crushing of the compressive strut on the side which was not straightforward with HPFRCC. It is worth remarking that the choice of providing this kind of retrofitting is reasonably representative of what could and will be really accomplished on the job site where the extrados of the coupling beam (where failure of the strut occurred, is not accessible).

As can be seen in (Figure 6.22), there was delamination also in cyclic testing, even more evident with respect to monotonic test. As a matter of fact the associated delamination could hence jeopardize the efficiency of the HPFRCC layer.

(a) (b)

Figure 6.21 – Coupling beam strengthened with HPFRCC under cyclic loading: (a) visible crack on the surface of HPFRCC and (b) initiation of crushing under negative loading

(a) (b)

Figure 6.22 – Coupling beam strengthened with HPFRCC under cyclic loading: (a) delamination and (b) buckling of bars under negative loading

Moreover, in cyclic tests, because of repeated loadings degradation of interface bond and hence characterization could have started earlier than in monotonic tests, thus justifying also the difference between the envelope of the cyclic response and monotonic curve.

As evidence of delamination in (Figure 6.23) is shown as in our case, the HPFRCC layer on one of the two faces, at the end of the test, could be easily removed as a single piece. The main reasons that caused problems of delamination between the reinforcing layer and concrete substrate could have likely been due to (1) the difference in stiffness between ordinary concrete and high performance concrete and (2) the high autogeneous shrinkage, which is a particular drawback of this category of advanced cement based materials because of low water-to-binder ratio.

Figure 6.23 – Coupling beam strengthened with HPFRCC under cyclic loading – manual remove of the HPFRCC layer at the end of test

It has been considered that in coupling beam made with concrete and complete reinforcement is added the contribution of HPFRCC, and is assumed the perfect bond the cracking angle is kept fixed with one obtained in level III approach, and coefficient of aggregate interlock has been taken equal. The $f_{R,1}$ has been taken the maximum value obtained from HPFRCC tested in tension equal to residual strength at 0.5 mm after peak which is equal to 7.11 N/mm^2.

$$V_{Rd}=V_{Rd,c+HPFRCC}+V_{Rd,s+HPFRCC} \tag{6.21}$$

$$V_{Rd,c+HPFRCC}=\left(\frac{A_{sw}}{s}f_{yw}+f_{R,1}2t\right)z\cot\vartheta \tag{6.22}$$

$$V_{Rd,s+HPFRCC}=\sqrt{f_{cm}}(b+2t)k_v z \tag{6.23}$$

$$V_{Rd,s+HPFRCC}=177\ \text{kN}$$

Even that strength ratio $\frac{V_{exp}}{V_{calc}} = 1.15$ it seems quite accurate, this calculation is very rough as from experiments it was obvious that one face was not completely effective due to debonding, and the other parameter k_v for HPFRCC equal to conventional concrete it does not hold true as in reality it should higher as fibres increase the interlock. However, at this peculiar case it seems these two parameters were balancing these anomalies of each other.

6.2.2 Retrofitted pre-damaged coupling beams

In addition to providing upgrading of coupling beams it is also investigated the possibility of using this as a repair solution. For this reason, four specimens were damaged at two controlled levels and were repaired with HPFRCC layer of 2 cm on three sides and then retested up to failure.

6.2.2.1 Coupling beams with 1% pre-damage level

Two of the specimens were intentionally pre-damaged up to 1% drift level, assuming that this level corresponds to the Serviceability Limit State (SLS). One of the two specimens was pre damaged under monotonic loading and the other under reversed cyclic loading (Figure 6.24); the specimens were subsequently repaired with HPFRCC and finally subjected to the same type of loading until failure. Below (Figure 6.25) are reported the results in terms of load-drift displacement curve for both cases.

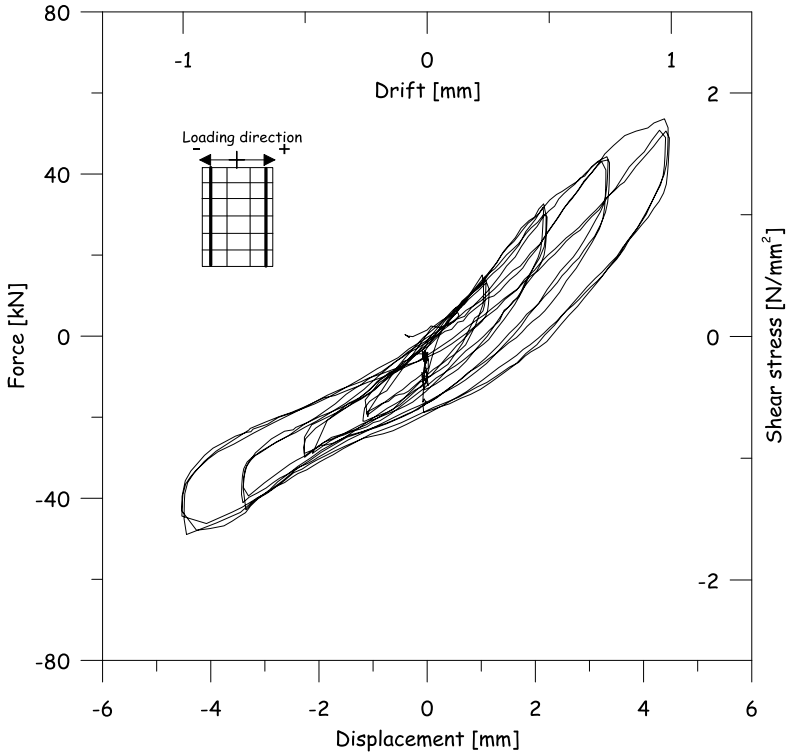

Figure 6.24 – Load path of assigned pre-damage at 1% (SLS)

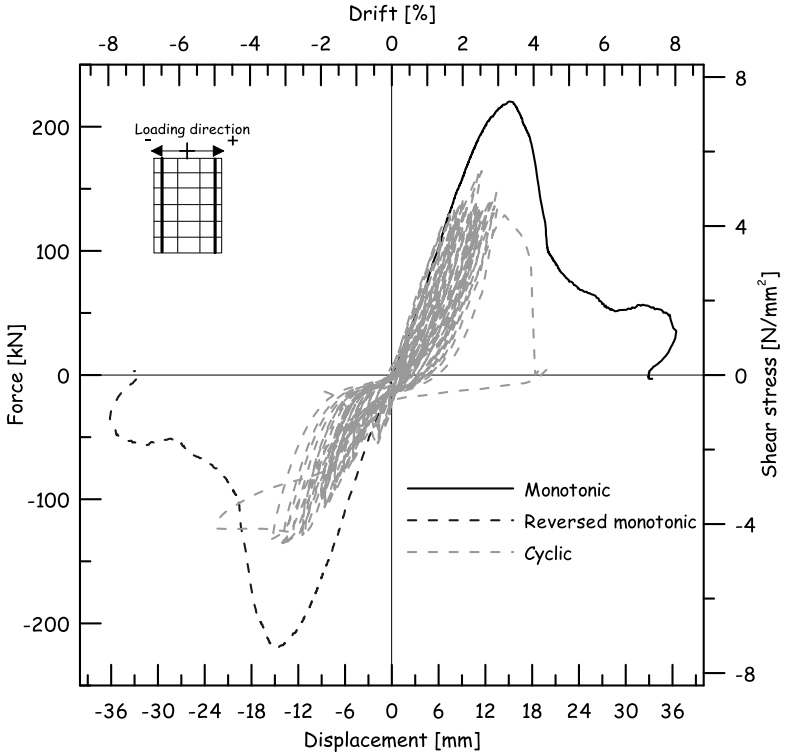

Figure 6.25 – Load displacement curve for monotonic and reversed cyclic loading retrofitted with HPFRCC at 1% pre-damage level (CB-HP-1/A) and (CB-HP-1/B)

The maximum load capacity of the repaired specimen under monotonic loading was equal to 216 kN at drift of 13 mm (or 2.9%). After peak the curve showed a stable softening branch, which stabilizes on a plateau at a force level equal to 50 kN, continuing up to a drift equal to 5.5%, at which point the specimen was unloaded. The behaviour exhibited by this coupling beam was one of the best, providing high ductility. Despite being pre-damaged it appears that it did not just recover but also slightly improved its behaviour with reference e.g. to the intact upgraded specimen. It has been most likely that some pre-damage also helped in spreading the strain in the HPFRCC thus helping to take better profit from it. Even in this case, like in the other cases, the use of HPFRCC was associated with a certain degree of delamination (Figure 6.26b). Anyway the bond between HPFRCC and concrete substrate is well established at least along one of the sides. It may be noted in (Figure 6.27b), at the end of the test, there were several cracks distributed in HPFRCC, which may be attributed to the effectiveness of bond between two materials.

(a) (b)

Figure 6.26 – Coupling beam retrofitted with HPFRCC at 1% pre-damage level monotonic: (a) initiation of crushing and (b) delamination in one of the sides

(a) (b)

Figure 6.27 – Coupling beam retrofitted with HPFRCC at 1% pre-damage level monotonic: (a) crushing failure and (b) visible distributed cracks

With reference to the specimen tested under reversed cyclic loading specimen (CB-HP-1/B) it was worth remarking that, there was a prior damage of the specimen, presumably caused by handling and transportation. The presence of these cracks could have affected the final behaviour of the specimen (CB-HP-1/B), which could justify its poor performance with respect to the companion specimen under monotonic loading (CB-HP-1/A).

As a matter of fact, along one loading direction, the load bearing capacity reached was 163 kN, while in the opposite direction was 152 kN. Regarding the deformation capacity, a better behaviour was observed in the negative loading direction, 18 mm against 13 mm. The overall behaviour has been un-symmetric as in the other cases jacketed with HPFRCC layer, and the same reasons mentioned above could be related to justify also this case. Cycles in both directions were very close, until reaching the maximum value of force; this is because of incomplete transfer of force to HPFRCC which does not provide much energy dissipation. In this test in both loading directions the specimen was unable to show the softening behaviour. Certainly the delamination has played an important role on this issue, as could be argued also by looking at the specimen at the end of the test shown in (Figure 6.28). Once removed one face of the HPFRCC layer from the coupling beam, a pronounced diagonal crack has been observed, which is typical type of shear brittle failure.

Figure 6.28 – Coupling beam repaired with HPFRCC at 1% pre-damage level – Failure of the beam

6.2.2.2 Coupling beams with 2% pre-damage level

Out of the four specimens planned to be repaired, two of them were pre-damaged at 9 mm drift level (or 2%), assuming that this drift level represents the Ultimate Limit State (ULS) for these structural elements, as shown in (Figure 6.29) the pre-damage assigned for reversed cyclic loading. Unfortunately it was not possible to complete the test on one the sample (CB-HP-2/A); as it happened to the specimen (CB-OL/A'), inaccuracies in the construction phase of the specimen prevented the completion of the test, because of the accidental contact which occurred between the sample and the frame, most likely due to improper placement of bushings.

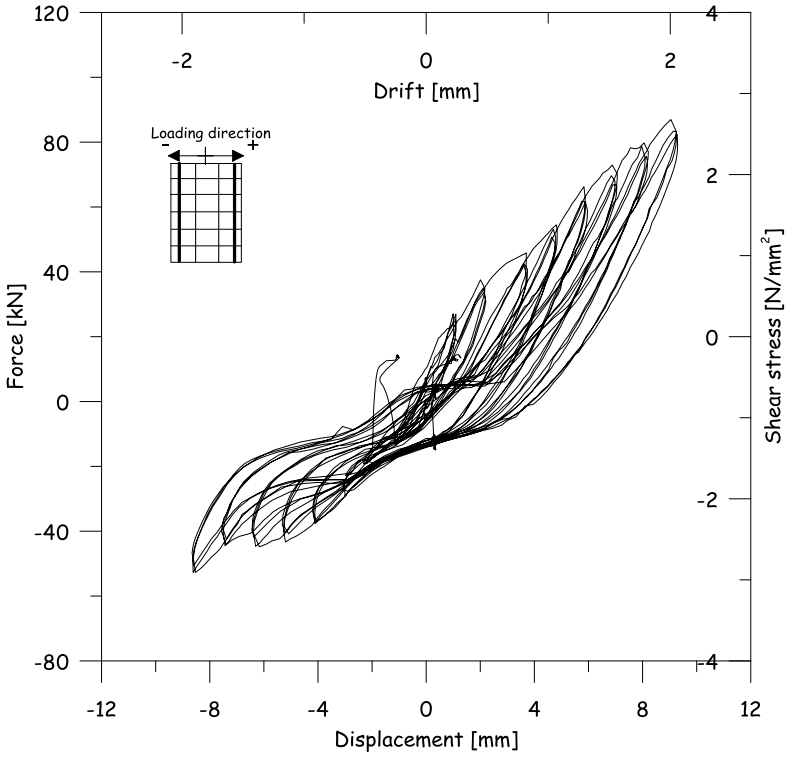

Figure 6.29 – Load path of assigned pre-damage at 2% (ULS)

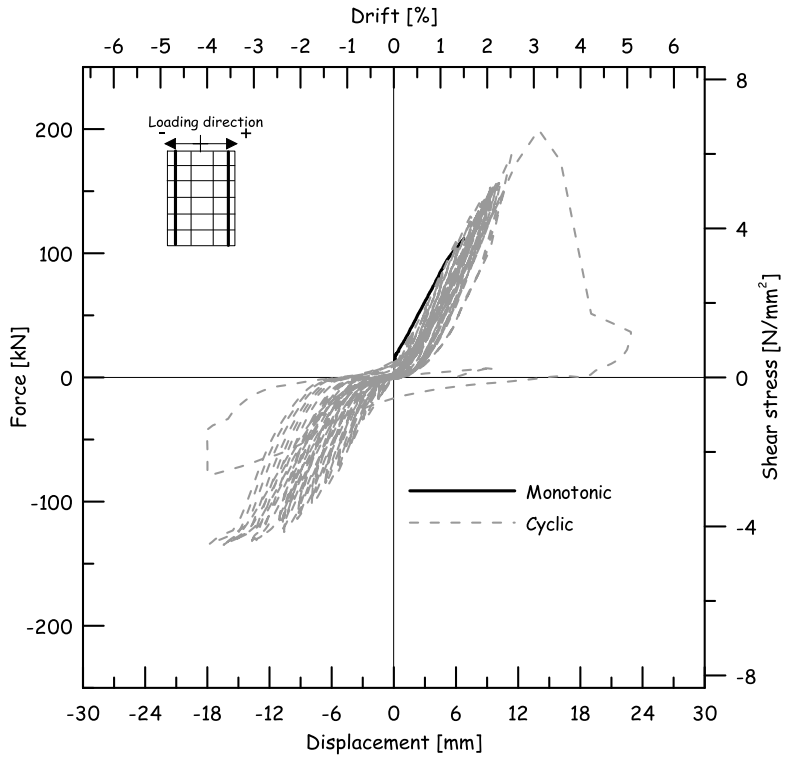

Figure 6.30 – Load displacement curve for monotonic and reversed cyclic loading retrofitted with HPFRCC at 2% pre-damage level (CB-HP-2/A and CB-HP-2/B)

Despite this the force-drift curves has been plotted in (Figure 6.30) as far as the test could be performed. The disturbance appeared at load equal to about 120 kN, when the specimen was

still under elastic regime. Nevertheless it can be observed the same initial stiffness as from the cyclic test.

With reference to the cyclic test, like in other tests, a non symmetric behaviour was observed, which is due to the non presence of HPFRCC layer on one side. As a matter of fact the specimen has reached the maximum load capacity of 200 kN along one direction, and 135 kN along the opposite direction, at displacements equal to 16 mm against 13 mm. Very narrow cycles were anyway recorded, because of the reason explained above.

As it can be seen in (Figure 6.31), during the test, the first crack appeared on the coupling beam retrofitting layer in a diagonal direction. With increased magnitude of the displacements crack opening increased and, at the failure were observed the presence of several cracks with different orientations. The failure was reached by concrete crushing of the strut in the short side where there was not the presence of HPFRCC layer as occurred also for the non retrofitted coupling beams.

(a) (b)

Figure 6.31 – Coupling beam repaired with HPFRCC (at 2% pre-damage level) at failure: (a) front and (b) rear

Figure 6.32 – Coupling beam retrofitted with HPFRCC at 2% pre-damage level – Failure of the beam

6.2.2.3 Coupling beams strengthened with textile reinforced cementitious composite

The second technique investigated for strengthening of coupling beams has been the application of a TRCC on two faces of the coupling beam and on one of two transverse sides. The bond of fabric with the coupling beam is achieved through mortar with fine particle size.

The specimens were intact without any pre-damage applied to check the effectiveness of this technique; after a proper surface treatment the textile composite was applied to two specimens, and one of them was subjected to the monotonic loading (CB-TX/A), whereas the other one was tested under reversed cyclic loading.

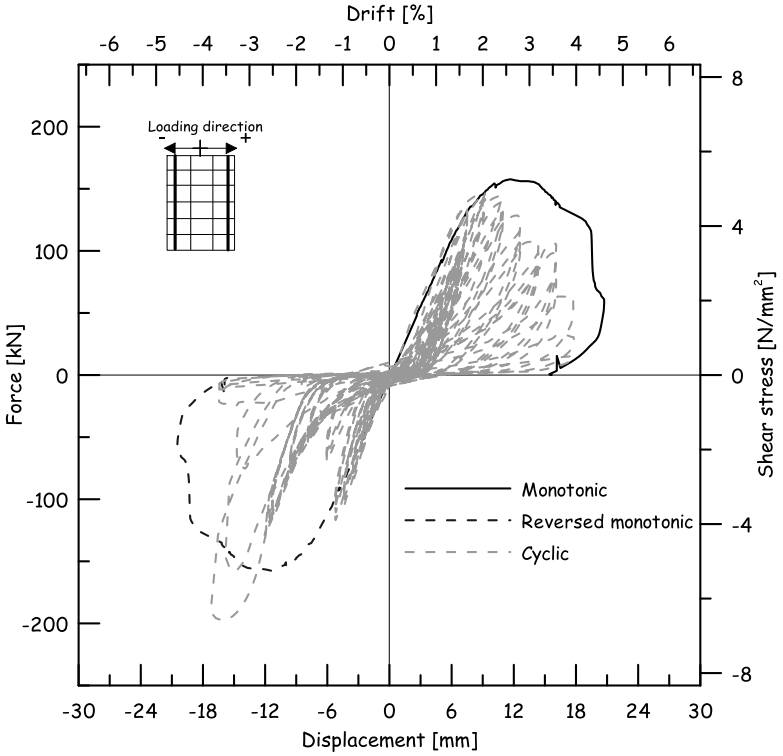

Figure 6.33 – Coupling beam strengthened with textile reinforce cementitious composite

The specimen (CB-TX/A) during pushover test showed a maximum load capacity of 156 kN, corresponding to a drift displacement of 17 mm (or 3.7%). The initial stiffness measured was equal to 14 kN/mm, which is in the range between the values of the upgraded (with HPFRCC) and non upgraded specimen. This fact is related to sectional enlargement due to addition of a layer, at this specific case the TRCC layer was less thick than HPFRCC layer. Up to 110 kN the sample remained in elastic regime, thereafter the slope of the curve decreased until the peak resistance was reached. With increased displacement the coupling beam exhibits good stability and ductility, as it can also be appreciated from the gradual softening branch which continues up to the measured drift equal to 27 mm (or 6%) (Figure 6.33). The TRCC applied on the ordinary concrete of which was made the specimen showed good bond. The initiation of cracking (Figure 6.34) has appeared in the lower part of the coupling beam in inclined direction, starting from region where the strut acts.

After reaching the maximum load capacity one of the two layers of TRCC was detached; the beam continued to sustain the load until the concrete crushing of the strut occurred. At the several inclined cracks in the TRCC layer were observed which could be related to justify the good stability of the post peak response (Figure 6.35).

Figure 6.34 – Coupling beam strengthened with TRCC monotonic – Crack initiation and propagation under increased displacement

Figure 6.35 – Coupling beam strengthened with TRCC monotonic – Multiple cracks initiation and propagation under increased displacement

The specimen (CB-TX/B), i.e. coupling beam strengthened with TRCC and subjected to reversed cyclic displacement, the envelope of the cycles along the loading direction (Figure 6.33), up to the peak has the same shape as the curve of pushover test. Between the idealized cyclic envelope and the monotonic curve there was a certain distance, however lower than the one observed from the tests strengthened or repaired with HPFRCC. This phenomenon can be attributed to interface degradation during cyclic loading between the TRCC layer and concrete substrate which was evidently less severe than for HPFRCC. It has been interesting to observe that the maximum resisting force achieved was equal to 145 kN, along one loading direction a stable behaviour was maintained up to drift displacement value equal to 23 mm (or 5.1%).

As for the other tests of the coupling beams also in these strengthened with TRCC there was a strong asymmetry. This could be justified with the same reasons mentioned above. In this specific case, the symmetry is disturbed also by problems in loading system. In fact it was necessary to stop and resume the test 3 times and always in the moment in which the loading direction was negative. Part of the problem could be hence attributed to these undesirable interruptions. Nevertheless, also along opposite loading direction, the specimen shows a certain strength and stability of the cycles with maximum strength equal to 197 kN at drift 16 mm (or 3.5%). In (Figure 6.36) the crack evolution is shown along cyclic load path. In this test, practically all the damage is localized in the TRCC layer between the coupling beam and the lower block, a crack formed in this zone allowed to observe the deformation of the textile under reversed displacement (Figure 6.37).

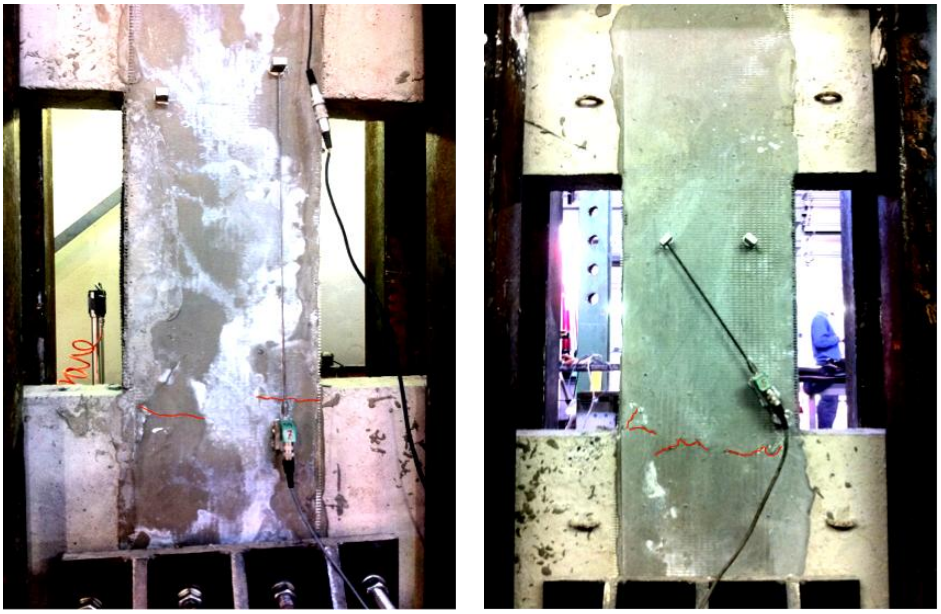

Figure 6.36 – Coupling beam strengthened with TRCC under cyclic displacement – Crack evolution under increased reversed displacements

Figure 6.37 – Failure of the coupling beam strengthened with TRCC under cyclic displacements

6.3 Comparisons

In this section some interesting comparisons are summarized between the results of different tests and described previously. The first comparison shown is between the curves obtained from the monotonic tests on the conventional coupling beams with no strengthening or repairing. In (Figure 6.38) are presented the test results of the coupling beams with both longitudinal and transverse steel reinforcement, without any steel reinforcement and with only longitudinal bars.

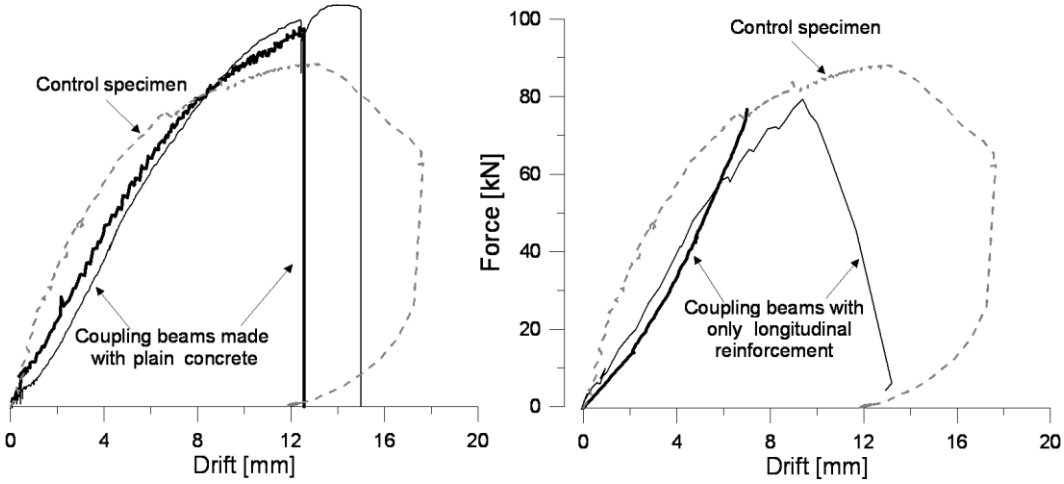

Figure 6.38 – Comparison of load drift displacement curves for conventional coupling beams

Firstly, the most interesting observation was that from three types of the coupling beams one is characterized with complete reinforcement, (4 longitudinal bars of 8 mm diameter, and stirrups of 6 mm diameter spaced at 100 mm) shows a ductile behaviour, whereas in the other cases failure is as expectable brittle. The maximum force reached in the cases with only concrete is slightly higher than those obtained from specimens reinforced with both longitudinal and transverse bars (90 kN) and only with longitudinal bars (80 kN). Among the reasons that may explain the variability of the maximum load reached could be attributed to the concrete strength and confinement provided by stirrups and the axial restraint provided by the frame and stirrups as explained in detail above.

The other comparison is between the pushover tests on the specimen reinforced with both longitudinal and transverse steel reinforcement, considered as a control specimen, compared with the pushover tests on specimens repaired or upgraded with different techniques (Figure 6.39).

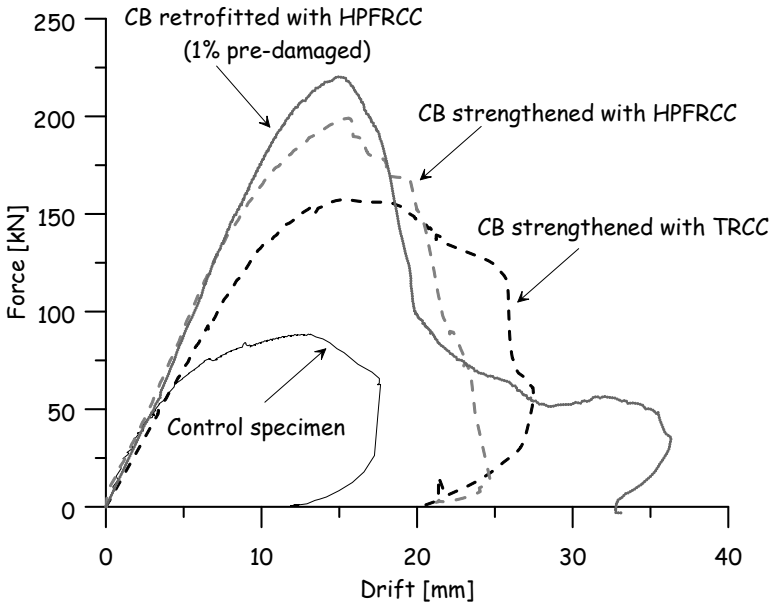

Figure 6.39 – Comparison of the experimental results under monotonic loading considering different strengthening/retrofitting techniques

The differences between the curve relative to the control coupling beam and the others are remarkable, especially in terms of load-bearing capacity. From the coupling beam strengthened with HPFRCC a load capacity of 199 kN is obtained, whereas for the case of repaired coupling beam with HPFRCC (under 1% monotonic pre-damage) the maximum load recorded was 220 kN. The load capacity with respect to the control beam is respectively 2.27 and 2.5 times higher. Also considering the strengthening of coupling beams with TRCC composite a significant increase in load capacity is observed reaching 156 kN, 1.77 times higher with respect to the control coupling beam.

Another important aspect is the increased performance in terms of ductility. It should be highlighted that none of the coupling beams showed brittle failure, but all after the peak load maintained certain stability, in the case of the coupling beam repaired with HPFRCC, where it was even possible to observe a plateau of residual bearing capacity at about 50 kN.

After presenting the comparison between the experimental pushover curves of the reference and strengthened or retrofitted coupling beams, in the following the results will be shown obtained for the same case under reversed cyclic displacement (Figure 5.34).

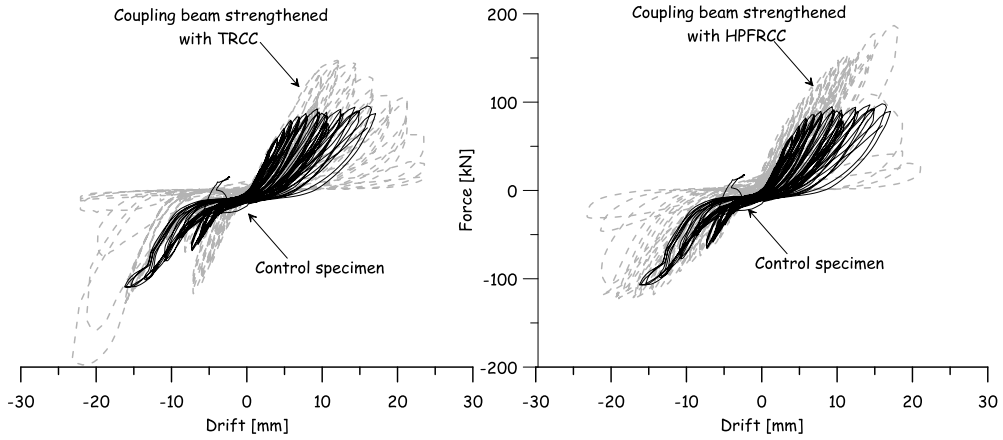

Figure 6.40 – Comparison results of cyclic tests with of reference coupling beam with respect to the strengthened beams with HPFRCC or TRCC

From the results shown in (Figure 6.40) it is possible to appreciate the difference in distribution of cycles, particularly focusing the positive loading direction. Interestingly the cycles performed by reference coupling beam are concentrated below 100 kN and 15 mm drift displacement. On the other hand considering the evidences relative to the coupling beam strengthened with TRCC the cycles are extended in the x-axis direction, and there is a significant increase in displacement capacity, associated with strong cycle stability. On the other hand, the results of the coupling beam strengthened with HPFRCC show a significant increase in terms of stiffness and load bearing capacity with respect to the other cases, especially to the control coupling beam. Moreover the descending branch behaviour is improved with respect to the control beam; however it slightly less stable than the one performed by TRCC strengthening and along in the x-axis there is not much gain.

Another comparison is shown in the graphs (Figure 6.41) of reversed cyclic tests, between the specimens strengthened or repaired with HPFRCC. It is more qualitative comparison to show the presence of certain correspondence between the cycles. In particular, by observing the initial slope characterizing the first few cycles, it can immediately observed how the HPFRCC layer addition manages to recover for the pre-damaged coupling beams the elastic characteristics prior to pre-damage. Strengthening or retrofitting in terms of load-displacement curves are not very different, so HPFRCC layer is also able to recover pre-damage effects.

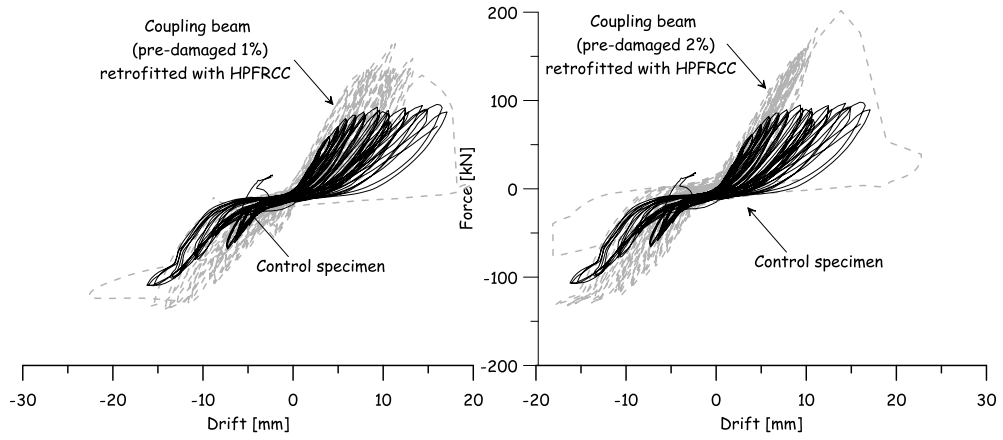

Figure 6.41 – Comparison between cyclic tests of coupling beams retrofitted with HPFRCC

6.4 Energy dissipation

In order to better understand the performance of various coupling beams tested, in terms of ductility and energy dissipation capacity, a specific analysis is carried out by calculating the energy dissipated, both under monotonic and reversed cyclic displacements. From this analysis are excluded the cases featuring a brittle failure, specifically the coupling beams with only longitudinal steel reinforcement and without any steel reinforcement at all.

6.4.1 Energy dissipation of coupling beams tested under monotonic loading

In the monotonic tests the energy dissipation measured represents the area recorded by load displacement curve. The area is calculated with a simple integration scheme using trapezoidal rule. (Table 6.1) shows the values obtained:

Table 6.1 – Total energy dissipation for the tested specimens under monotonic loading

Testing case	Dissipated energy [kN·mm]
Coupling beam with complete reinforcement	1138
Coupling beam strengthened with TRCC	2979
Coupling beam strengthened with HPFRCC	3100
Coupling beam retrofitted with HPFRCC	3795

From the results obtained it can be observed a significant difference in energy dissipation capacity between conventional coupling beam, characterized with minimum reinforcement, and the ones strengthened or repaired either with HPFRCC or TRCC. (Figure 6.42) shows the graphical representation of the values obtained:

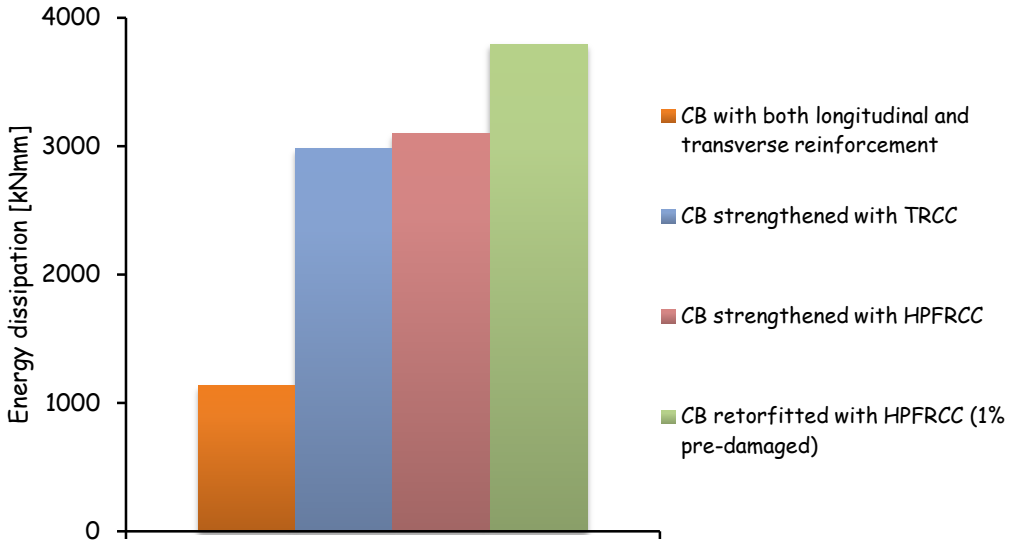

Figure 6.42 – Energy dissipation of coupling beams under monotonic loading

In addition to this assessment of energy dissipation at the end of the test, the evolution of energy dissipation during the test was considered, for fixed levels of drift. The energy dissipation was calculated based upon the assumption of elastic unloading.

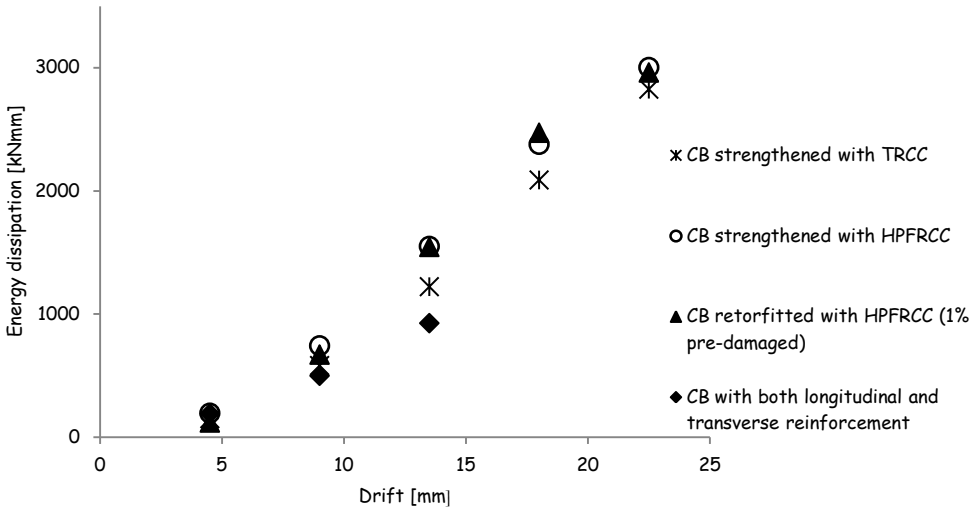

Figure 6.43 – Energy dissipation at fixed levels of drift, coupling beams under monotonic loading

From the graph of (Figure 6.43) it can be appreciated the energy dissipation evolution with increased displacements, at 1% drift level, all the specimens are still in the elastic regime and energy dissipation is approximately the same for all. At 2% drift level the differences begin to emerge. For the drift equal to 3% the control specimen has come to failure and the energy dissipation is significantly less than that of other specimens, which are still continuing to maintain the load. From 3% to 4% there is some difference between the results of coupling beams strengthened with HPFRCC and TRCC, however, at 5% this difference becomes less evident, and this stability continues until the end of the test.

6.4.2 Energy dissipation of coupling beams tested under cyclic displacements

The calculation of the energy dissipation has been performed for coupling beams under imposed reversed cyclic displacements. Specifically, the energy dissipation was calculated for each individual cycle of drift imposed in the specimen, using the trapezoid rule. The results for all performed tests are summarized in (Figure 6.44).

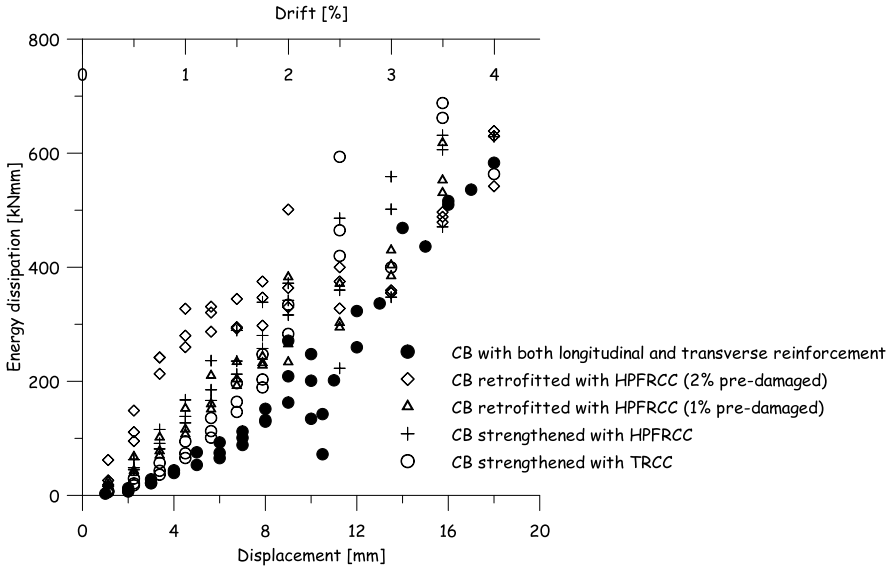

Figure 6.44 – Energy dissipation for each cycle for all the tests

The high number of points in the graph at first may appear confusing, but the interesting thing to observe is the energy dissipation evolution with increased drift displacements. The values of energy dissipation of the control specimen represent a kind of lower limit for the other tests. This is physically reasonable; in fact, the energy dissipation can be considered as parameter directly related to ductility. Based on this consideration, it can be stated that the test cases of repaired and strengthened coupling beams have improved performance in terms of ductility. And, in general, cycles at same drift level, showed similar magnitude as the first cycle. This indicates that low number of repeated cycles (3 for each drift level) does not degrade the mechanism of energy dissipation.

In the following graphs for each repaired or strengthened beams are provided the energy dissipation comparison with respect to the control beam. (Figure 6.45 to Figure 6.48).

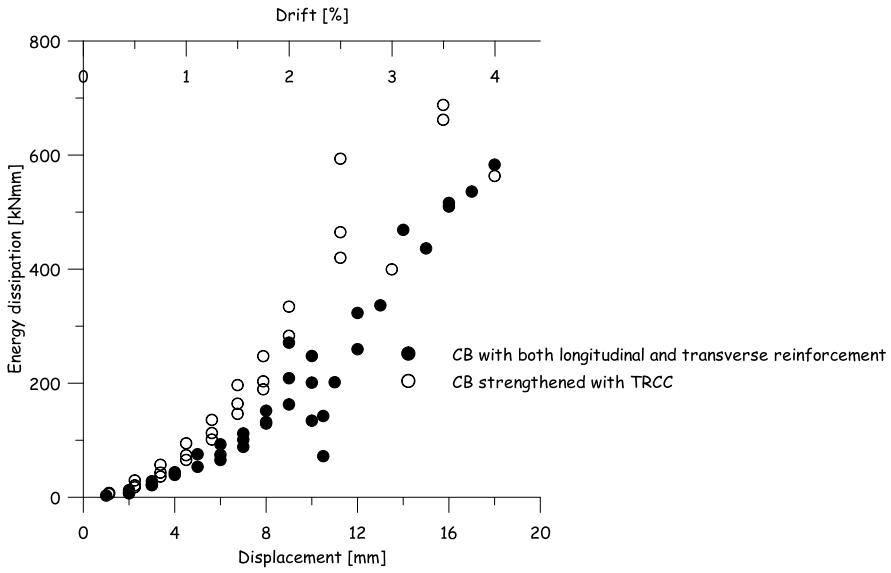

Figure 6.45 – Comparison of energy dissipation for each cycle - control specimen and coupling beam strengthened with TRCC

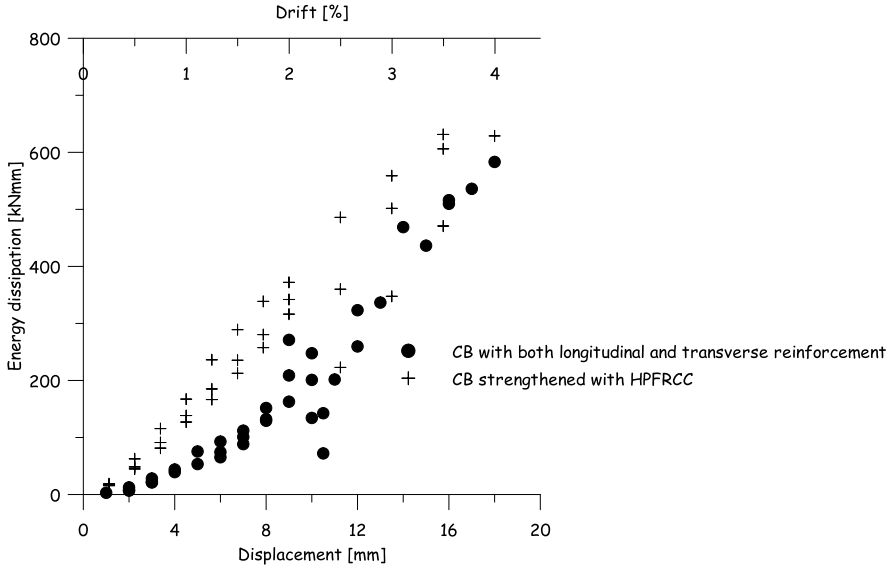

Figure 6.46 – Comparison of energy dissipation for each cycle – control specimen and coupling beam strengthened with HPFRCC

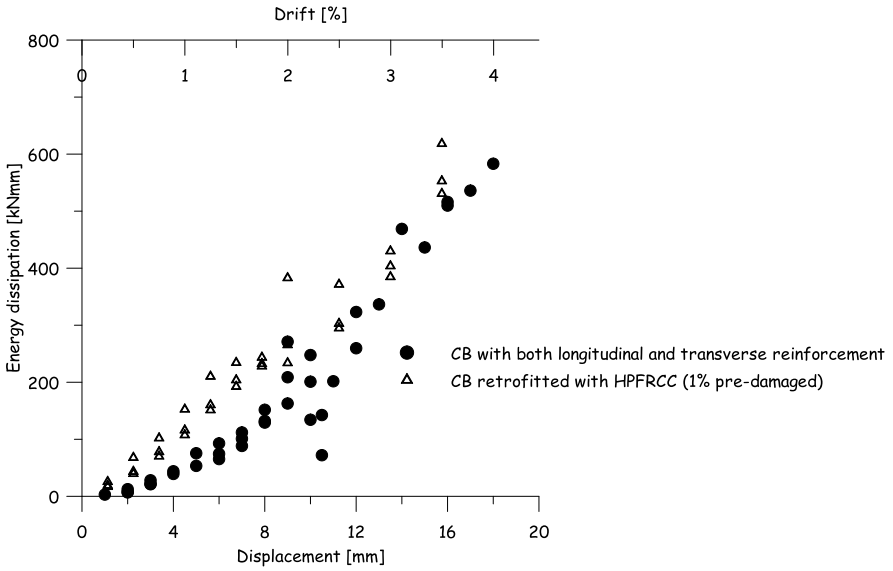

Figure 6.47 – Comparison of energy dissipation for each cycle – control specimen and coupling beam retrofitted with HPFRCC (with 1% pre-damage)

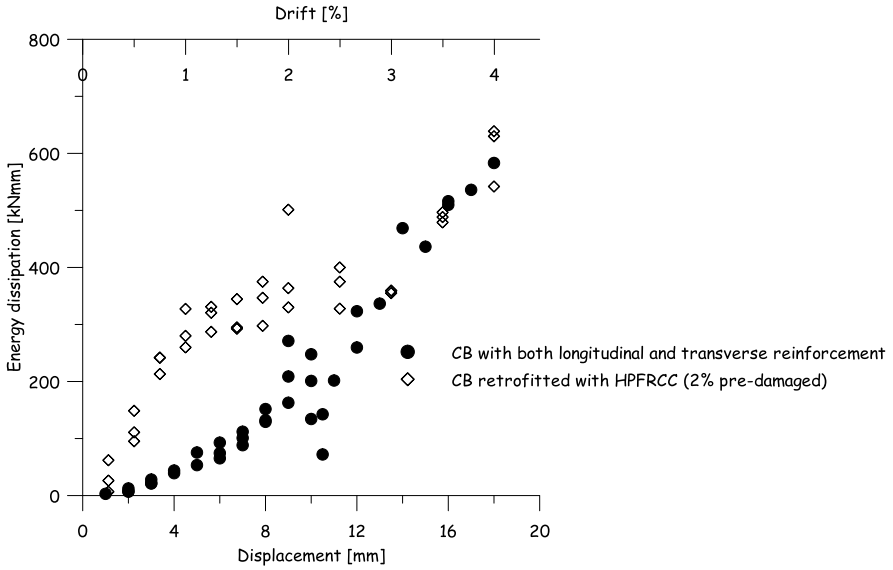

Figure 6.48 – Comparison of energy dissipation for each cycle – control specimen and coupling beam retrofitted with HPFRCC (with 2% pre-damage)

Out of these last four graphs the most interesting is undoubtedly that of (Figure 6.48), related to results of the repaired coupling beams with HPFRCC after a 2% pre-damage level. It can be seen an anomaly with respect to the usual increased trend observed for the other cases, at early stage of loading the repaired specimen exhibited increased energy dissipation with respect to the control specimen, however at later loading stages this parameter becomes comparable. The explanation of this variance could be related to the fact that the pre-damaged sample, after it is repaired and it continues to be subjected to increased reversed cyclic displacements, it appears that after 2% drift the ductility has been not improved. Despite the fact that the up to 2% all the strengthened or repaired specimens showed a significant increase on energy dissipation, it is interesting to note that with increased pre-damage level after 2% drift on both repaired coupling beams, there have been a tendency on energy dissipation to decrease, especially in the case of specimen pre-damaged at 2% drift level where the energy dissipation has been similar with control specimen. To have better

understanding in the following are plotted (Figure 6.49 to Figure 6.53) the ratio of energy dissipation of coupling beams either upgraded or retrofitted with respect to the reference specimen which is the coupling beam with both longitudinal and transverse reinforcement. For strengthened coupling beams either with HPFRCC or TRCC the trend of energy dissipation demand continues and was more stable with respect to retrofitted specimens with HPFRCC.

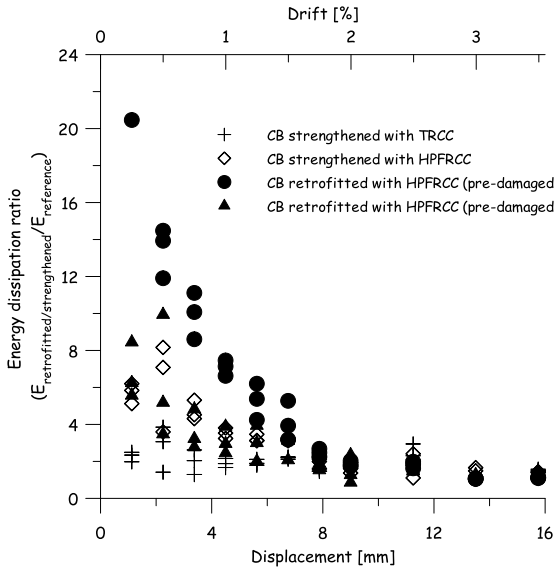

Figure 6.49 – Energy dissipation ratio for coupling beams under cyclic loading both strengthened and retrofitted

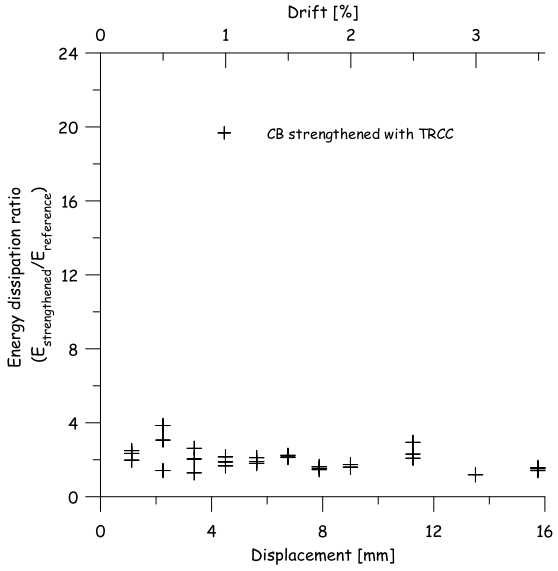

Figure 6.50 – Energy dissipation ratio for coupling beam under cyclic loading strengthened with TRCC

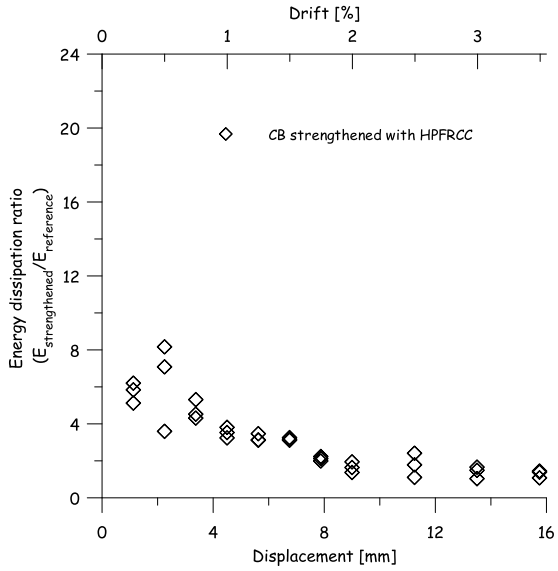

Figure 6.51 – Energy dissipation ratio for coupling beam under cyclic loading strengthened with HPFRCC

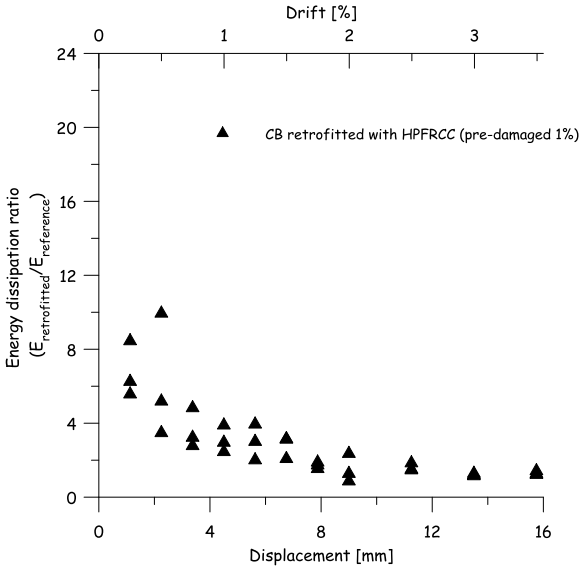

Figure 6.52 – Energy dissipation ratio for coupling beam (pre-damaged 1%) under cyclic loading retrofitted with HPFRCC

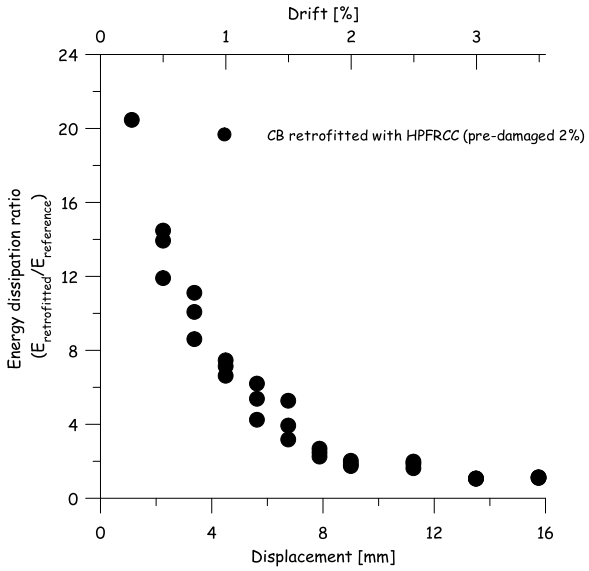

Figure 6.53 – Energy dissipation ratio for coupling beam (pre-damaged 2%) under cyclic loading retrofitted with HPFRCC

6.4.3 Axial Elongation

In reality in all the coupled wall systems, the coupling beams tend to expand longitudinally, which is prevented by the walls due to their high in-plane stiffness and also by surrounding slabs [Teshigawara et al., 1998]. In most of the available tests the axial restraint action is not considered at all, however, in some of the studies there is tendency to investigate the importance of this interference on the global behaviour.

The axial force is generated by the fact that as long as lateral force is applied, cracks form and besides sliding of the upper block the specimen would tend to axially expand so it will clearly depend on the stage of loading/testing.

There is not straightforward correlation between the axial strains and the axial force, as the mechanism leading to the strain development is not well understood [Lequesne, 2011]. The axial forces are expected to increase chiefly the shear capacity, while they limit the ductility. In the following (Figure 6.54 and Figure 6.56) are shown the results of the axial elongation measured for the coupling beams with HPFRCC jacketing, under monotonic and reversed cyclic displacements. It is clearly highlighted the effect of axial elongation with increased displacements of the upper block for both cases. From (Figure 6.58) it can be seen that between the monotonic and cyclic cases there is coincidence of axial strain up to failure of coupling beam under cyclic loading. Than the axial strain continues to progressively increase which could be related to the increased damage of the specimen at this stages of drifts. A likely explanation for the lower displacement capacity provided for the cyclic case is mostly associated to interface degradation between the concrete substrate and jacketing layer caused from the cyclic loading. Another statement can be made, from the measurement of the two instruments their response is very similar with each other giving explanation that the upper block remained always parallel with the lower block under increased displacements.

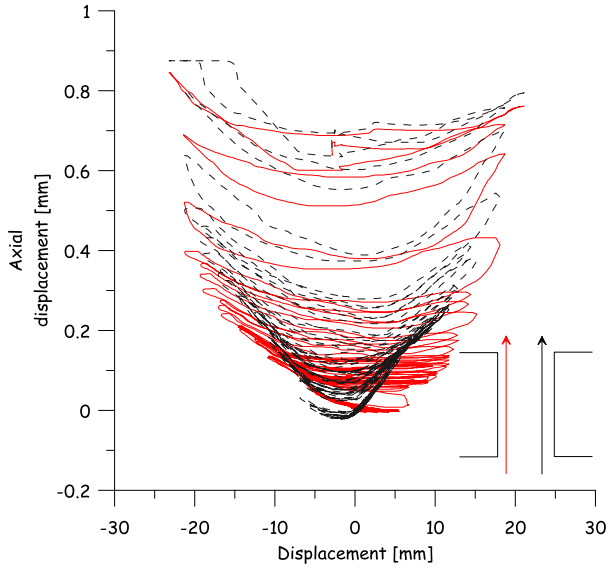

Figure 6.54 – Axial displacement measured from two instruments for the specimen (CB-HP-0/B)

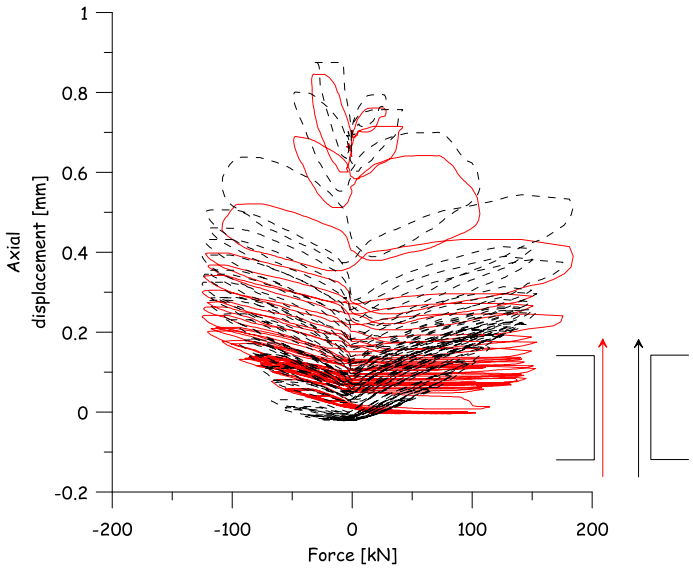

Figure 6.55 – Axial displacement measured from two instruments for the specimen (CB-HP-0/B)

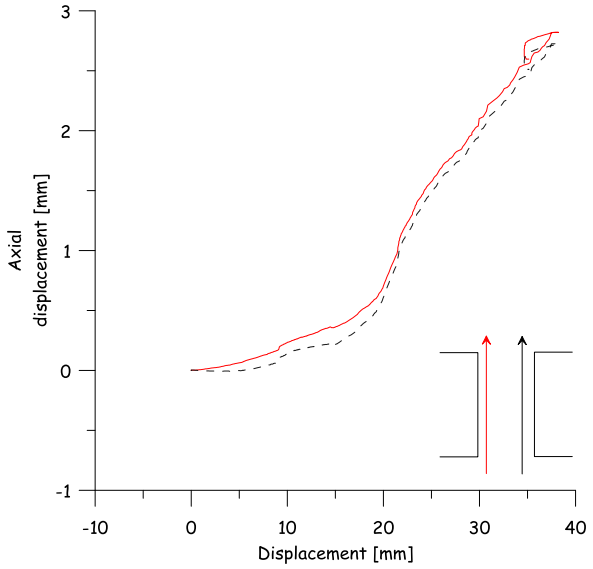

Figure 6.56 – Axial displacement measured from two instruments for the specimen (CB-HP-1/A)

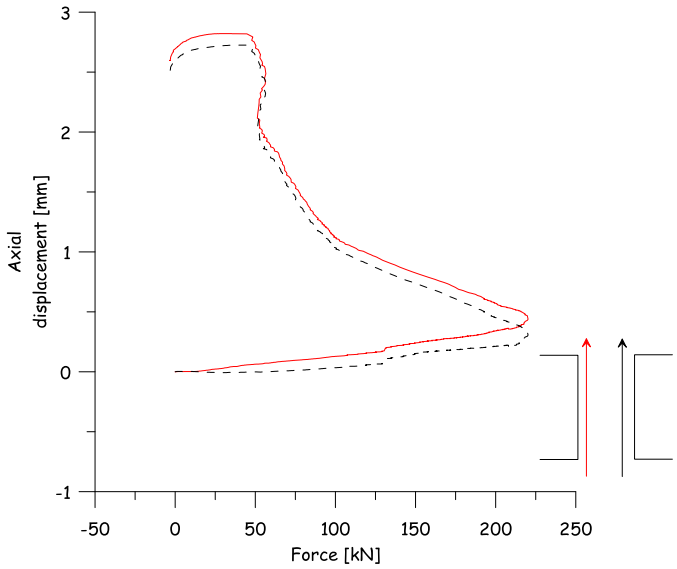

Figure 6.57 – Axial displacement measured from two instruments for the specimen (CB-HP-1/A)

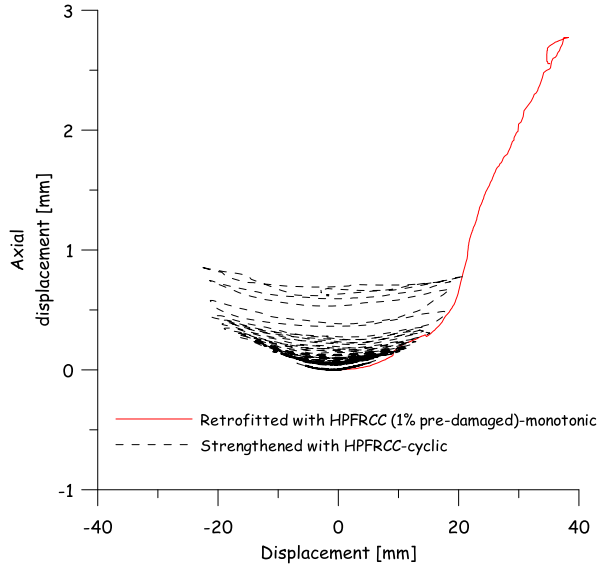

Figure 6.58 – Comparison between average axial displacement under monotonic and cyclic displacements

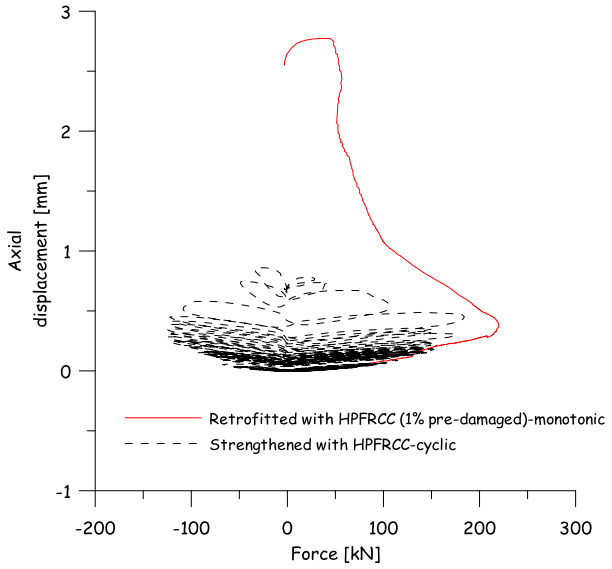

Figure 6.59 – Comparison between average axial displacement under monotonic and cyclic displacements

6.5 Modelling

Using the previously calibrated numerical method based on multi-fibre Timoshenko beam element, are modelled the coupling beams from this experimental campaign. Two cases were chosen: the coupling beam with both longitudinal and transverse reinforcement and the coupling beam upgraded with HPFRCC layer. The constitutive relations were adopted same as in previous modelling, and the parameters were defined from the experimental evidence of the materials tested e.g. compressive strength on concrete cubes, tensile behaviour of the bars, HPFRCC tensile behaviour from DEWS test and so on. The perfect bond condition between HPFRCC layer and concrete substrate has been assumed. The results are reported

in (Figure 6.60 and Figure 6.61) and good agreement appears between numerical results and experimental investigations For the experimental investigation of the specimen upgraded with HPFRCC at 15 mm drift it was observed delamination whereas in numerical model the load continues to increase, as a result it was not able to capture the response correctly because of the perfect bond consideration between the HPFRCC and substrate layer.

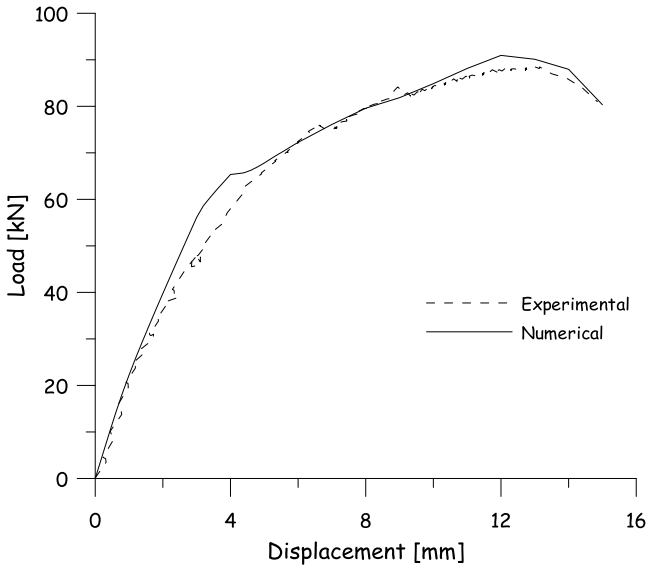

Figure 6.60 – Load displacement response of coupling beam with both longitudinal and transverse reinforcement

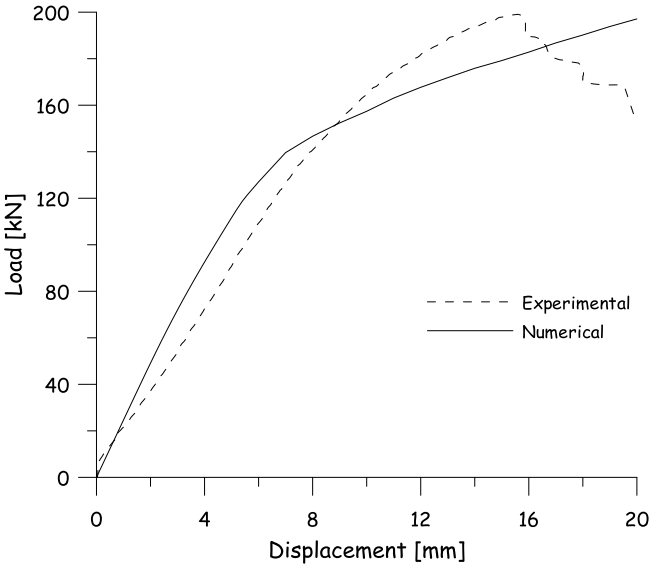

Figure 6.61 – Load displacement response of coupling beam strengthened with HPFRCC

7

7 Structural level

In the following chapter it has been assumed that coupling beams can be retrofitted using both conventional r/c jacketing and HPFRCC, it is investigated the efficiency of the retrofitting on the behaviour of shear walls. In the literature could not be found experimental tests on this kind subassemblies, it has been conceived an ideal benchmark since it has been shown that Timoshenko beam fibre model may be reliable for capturing the overall global behaviour of coupling beams. This kind of approach is used and sifted to the use of a commercial code for structural design MIDAS GEN.

Shear walls with different configurations and design options for non reinforced coupling beams will be considered and the global structural performance will be evaluated mainly with reference to the coupling action.

The wall structure has been modelled using the beam elements implemented in multi fibre concept, and the same constitutive laws described in chapter four for the beam element were employed for material characterization.

7.1 Geometry

For the subsequent analysis it has been chosen a reinforced concrete shear wall with a total length of 3.3 m and storey height of 3 m. The wall consists of two lateral portions with section 1200 mm x 200 mm, separated each other by an opening 900 mm. The coupling beams employed to link two lateral walls were 900 mm long and 600 mm high, respectively; the aspect ratio was equal to 1.5. The geometry of the coupling beams coincides exactly with the one to which reference was made of the 1:2 scale specimens experimental tests.

In the analysis were considered two different shear wall configurations, one case has been with three floors or of 9 m total height, the second wall treated was 5 stories or of 15 m total height (Figure 7.1). For all the analysis the load has been applied on top of the wall in terms of increased displacements.

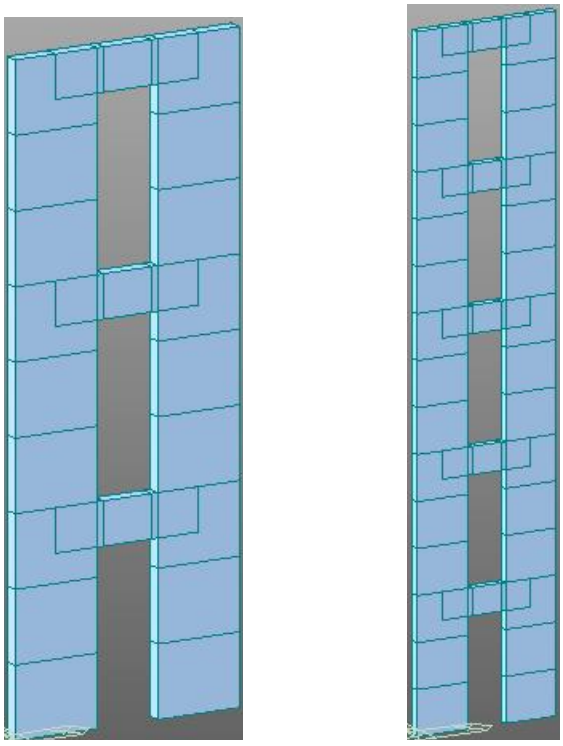

(a) (b)

Figure 7.1 – Geometry of the shear walls (a) 3 storeys and (b) 5 storeys

The aim of this analysis was to evaluate the effectiveness of strengthening of either shear walls or/and of coupling beams, with reference to the wall without openings.

Basically two possible strengthening were sought, the strengthening of the base of shear wall and of the coupling beams.

For both cases, the 3 storeys and 5 storeys walls, firstly the wall without openings was analyzed, then the model of coupled wall without strengthening of the wall base section was studied, and of this last situation 5 different cases were examined.

The same analyses were repeated assuming that both walls were strengthened, considering two strengthening techniques. The first strengthening mode was conceived with reinforced concrete jacketing with thickness 40 mm and the other with HPFRCC layer of 25 mm.

Below are summarized the cases analyzed:

3 storeys and 5 storeys

- Shear wall without opening (3300 mm long and 200 mm thick)
- Two single shafts (1200 mm long and 200 mm thick)
- Non strengthened coupled shear wall
    - Coupling beams without reinforcement
    - Coupling beams with minimum reinforcement
    - Coupling beams with reinforcement correctly designed
    - Coupling beams strengthened with r/c jacketing
    - Coupling beams strengthened with HPFRCC

- Coupled shear wall strengthened with HPFRCC
    - Coupling beams without reinforcement
    - Coupling beams with minimum reinforcement
    - Coupling beams with reinforcement correctly designed
    - Coupling beams strengthened with HPFRCC

- Coupled shear wall strengthened with r/c jacketing
    - Coupling beams without reinforcement
    - Coupling beams with minimum reinforcement
    - Coupling beams with reinforcement correctly designed
    - Coupling beams strengthened with r/c jacketing
    - Coupling beams strengthened with HPFRCC

For the coupling beams correctly designed it has been followed the design procedure for design of coupling beams by [Toniolo et al., 2010]. The resistant mechanism is shown in (Figure 7.2) which is provided by strut and tie approach. In order to calculate the amount of reinforcement of each coupling beams, firstly it was necessary to calculate the bending resistance at the base floor; afterwards it is calculated the lateral force at each floor by following relationship:

$$M_{Rd} = \sum F_i \, h_i \tag{7.1}$$

Where F is the lateral force; and h is the inter-storey height.

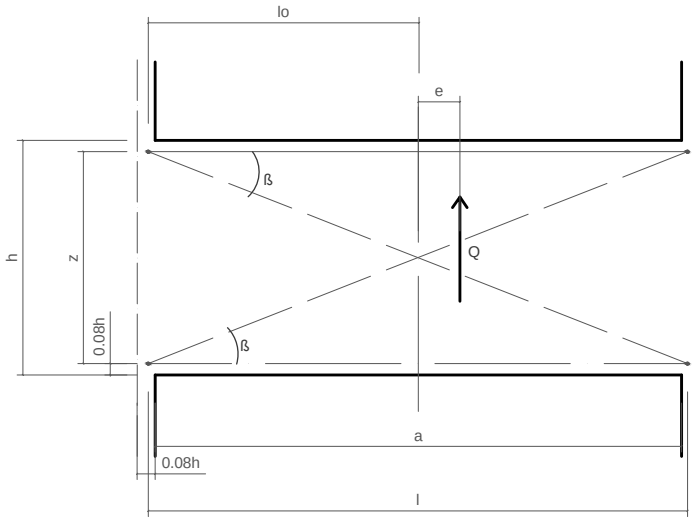

Figure 7.2 – Strut and tie mechanism for design of coupling beams [Toniolo et al., 2010]

After it is determined the force F it was possible to calculate the acting shear force on each coupling beam.

$$Q_{Sd} = \gamma_f \cdot F_i \cdot h_i / z_i \tag{7.2}$$

z is the sectional lever arm of the coupling beam and γ_f is taken equal to 1.5.

At this point it is possible to determine the strut resistance by equation.

$$Q_{rd} = 0.55 \cdot h \cdot b \cdot f_{c1} / (1+\lambda^2) \tag{7.3}$$

Where $\lambda = l/z$, with $l = l_0 + 0.16 \cdot h$.

And then it is calculated the required longitudinal reinforcement

$$A_{l0,req} = Q_{Sd} \cdot (\lambda/2 + e/z) / f_{sd} \tag{7.4}$$

In the following (Table 7.1 and Table 7.2) are reported the shear forces and the required reinforcement, for both three and five storeys wall.

Table 7.1 – Resisting shear force and required longitudinal reinforcement for three storeys wall

Storey	F_i [kN]	Q_{sd} [kN]	Q_{Rd} [kN]	$A_{lo,req}$ [cm²]
1	1927	1923	2691	4.86
2	1606	1602	2691	4.05
3	963	961	2691	2.43

Table 7.2 – Resisting shear force and required longitudinal reinforcement for five storeys wall

Storey	F_i [kN]	Q_{sd} [kN]	Q_{Rd} [kN]	$A_{lo,req}$ [cm²]
1	1226	1223	2691	3.09
2	1144	1142	2691	2.88
3	981	978	2691	2.47
4	735	734	2691	1.85
5	408	408	2691	1.03

7.2 Reinforcement of the wall

In this situation were considered the case studies of three different wall configurations: 1) without openings, 2) un-coupled and 3) coupled. The walls were assumed to be lightly reinforced based on minimum reinforcement geometrical ratio.

Thus the section of the wall has been reinforced with 20 bars of 12 mm diameter (Figure 7.3), corresponding to geometric ratio of reinforcement equal to 0.35% complying with minimum reinforcement requirements for non seismic situations. The reinforcements were arranged only in the end of the wall, whereas the central portion of 900 mm remains only with concrete. The reinforcement layout of the two-side parts of the wall has been the same for all the other modelling cases. The central part of 900 mm could be either neglected for

the case of non coupled shear wall system, or could be the place where coupling beams were placed between the storeys to develop the coupled wall system.

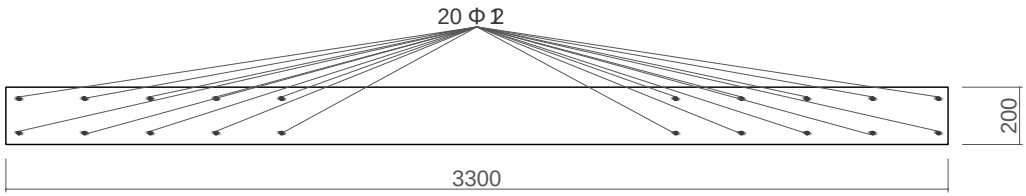

Figure 7.3 – Geometry and reinforcement arrangement of shear wall

7.3 Strengthening configuration of the wall

The first strengthening technique chosen to improve the performance of the shear walls was the most traditional one, using reinforced concrete jacketing with 4 cm thickness in outer sides of the wall (Figure 7.4a). The jacket is applied throughout first two stories respectively at height equal to 6 m. In addition the concrete cover is reinforced with 12 bars of 12 mm diameter, with total reinforcement geometrical ratio equal to 0.7% to comply with seismic requirements.

The alternative strengthening solution provided in the walls was with a 25 mm HPFRCC layer (Figure 7.4b), applied on the lateral sides, equivalently as previous configuration applied in the first 2 storeys.

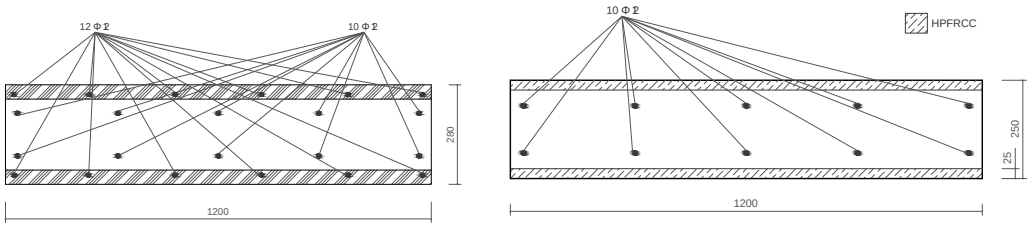

(a) (b)

Figure 7.4 – Strengthened wall with: (a) r/c jacketing and (b) HPFRCC layer

7.4 Coupling beam reinforcement

A series of analysed cases were the coupled wall system where the coupling beam has no reinforcement. The other series consists by coupling beams provided with minimum longitudinal reinforcement geometrical ratio, respectively with 4 bars of 8 mm diameter. In the current modelling approach it has not been possible to introduce directly the transverse reinforcement, however through the compression constitutive law by taking into account the residual strength it has been possible to take into account the confinement provided by stirrups.

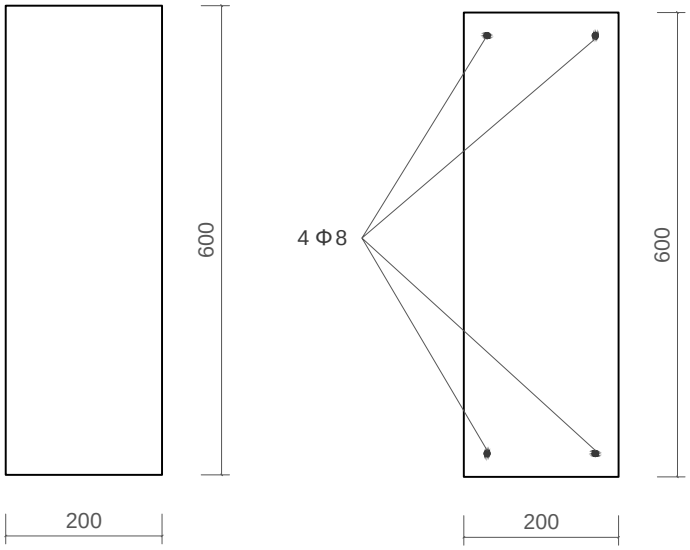

Figure 7.5 – Coupling beams employed for numerical analysis

The series of analysis with coupling beams correctly designed were the beams designed for the (ULS) based on the [Toniolo et al., 2010] proposed equations. And it came out that the reinforcement of coupling beams for 3 storeys should comply with (Table 7.3) and for the case of 5 storeys with (Table 7.4).

Table 7.3 – Three storeys

Storey	Reinforcement	Area (cm²)	ρ (%)
1	4ϕ8 + 4ϕ16	10.05	0.84
2	4ϕ8 + 4ϕ14	8.34	0.69
3	4ϕ8 + 4ϕ10	5.14	0.43

Table 7.4 – Five storeys

Storey	Reinforcement	Area (cm²)	ρ (%)
1	4ϕ8 + 2ϕ8	3.02	0.25
2	4ϕ8 + 2ϕ12	4.53	0.38
3	4ϕ8 + 4ϕ10	5.14	0.43
4	4ϕ8 + 4ϕ12	6.53	0.54
5	4ϕ8 + 4ϕ12	6.53	0.54

7.5 Strengthening of the coupling beams

One of the strengthening solutions employed was with reinforced concrete jacketing. The jacketing has been provided along three sides of the beam, considering that in the existing structures the upper part is generally not accessible because it intersects with the slab. The thickness of the cover has been adopted equal to 40 mm and 8 bars of diameter 8 mm were included, according to the reinforcement layout shown in (Figure 7.6a). The second

strengthening solution proposed was by using HPFRCC layer equal to 25 mm thick and similarly as the previous solution, it has been applied along three sides (Figure 7.6b).

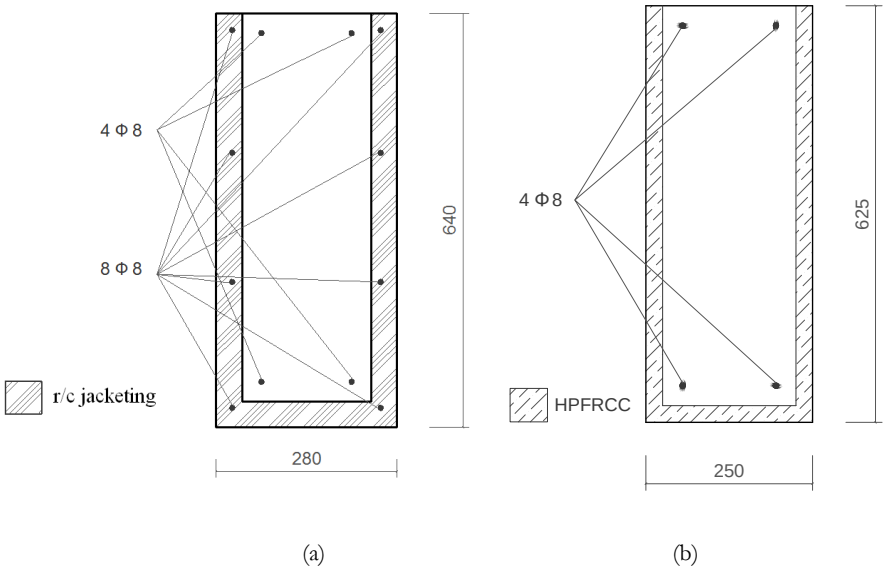

Figure 7.6 – Upgrading of coupling beams in three sides: (a) with r/c jacketing and (b) HPFRCC

7.5.1 Material definition

The constitutive laws for the material are defined based on their uniaxial behaviour in tension and in compression. The reinforcement has been described through the elastic-hardening law with yield strength of f_y=450 N/mm^2, elastic modulus E=200000 N/mm^2 and the ratio between elastic and plastic slope has been taken equal to 0.005.

Regarding the unconfined concrete the strength in compression has been assumed equal to 20 N/mm^2, while the confined concrete has been assumed to have a same strength as unconfined one, but the residual strength has been taken as 20% of the value 20 N/mm^2.

The compressive and residual strength for HPFRCC has been taken equal to 100 N/mm^2, whereas the tension behaviour has been defined as elastic perfectly plastic description with tensile strength equal to 7.11 N/mm^2.

7.6 3 storeys shear wall

In this section a series of analysis are performed, highlighting the influence of different strengthening techniques applied on the 3 storeys shear wall.

7.6.1 Non strengthened coupled shear wall (3 storeys)

A series of the results are reported of which the section of the wall contains minimum area of reinforcement.

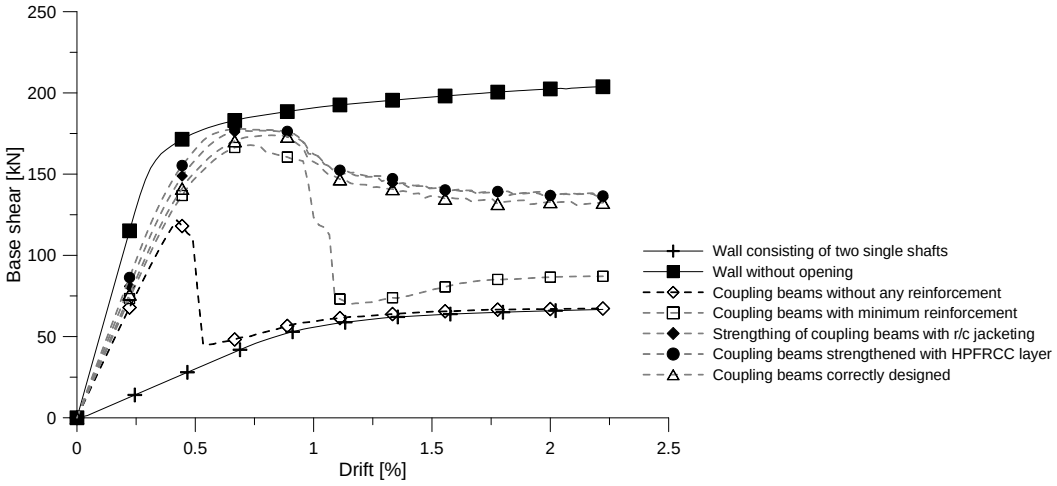

Figure 7.7 – Base shear for the wall without any strengthening (3 storeys)

In (Figure 7.7) it is clearly shown that with coupling beams non reinforced or with just minimum reinforcement after cracking the load bearing capacity decreases abruptly to the level of uncoupled wall; retrofitting of poorly designed beams is able to provide equivalent performance as if designed for the yielding of the base of the wall.

It is interesting to observe how the curves relating the wall consisting of two single shafts and the wall without opening represent two bounds, while all other coupled wall case are distributed in this zone. In particular, the residual capacity of the coupled wall with beams without reinforcement coincides perfectly with the curve of the wall consisting of two single shafts.

Analogically, one can observe that although it provided a significant improvements using different configuration of the coupling beam, it has been impossible to achieve a same performance as the wall without openings especially in terms of initial stiffness.

7.6.2 Coupled shear wall strengthened with HPFRCC (3 storeys)

The first technique proposed for strengthening of the wall has been conceived using two layers of HPFRCC in the base section of the wall through 6 m. With the same configuration has been investigated what happens with different coupling beams configurations.

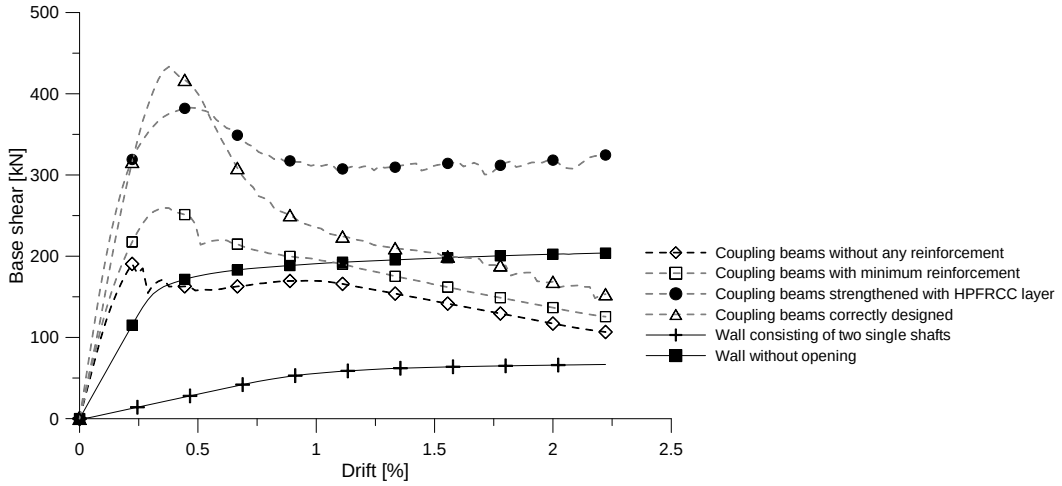

Figure 7.8 – Base shear for the wall strengthened with HPFRCC layer (3 storeys)

The load drift curves of the wall, shown in the (Figure 7.8) highlight a clear difference between the maximum load bearing capacity reached by the wall coupled with beams properly designed and the wall coupled with beams with minimum or without reinforcement. In the first case is reached the peak at force equal to 418 kN, while in the other cases respectively equal to 180 kN and 254 kN. The wall with properly designed beams even that provides a significant improvement in terms of the load capacity, it has been shown a substantial decrease in post peak resistance. While the solution of applying the HPFRCC in poorly designed coupling beams provided improved load capacity equal to 395 kN with low decrease in the residual load capacity equal to 300 kN, which is associated with a stable plateau. An important aspect appears that if the coupling beams are not reinforced even if the wall is strengthened it performs poorly.

7.6.3 Coupled shear wall strengthened with r/c jacketing (3 storeys)

The second alternative proposed for the strengthening of the wall is based on conventional reinforced concrete jacketing at the base section of the wall, in two sides along 6 m height.

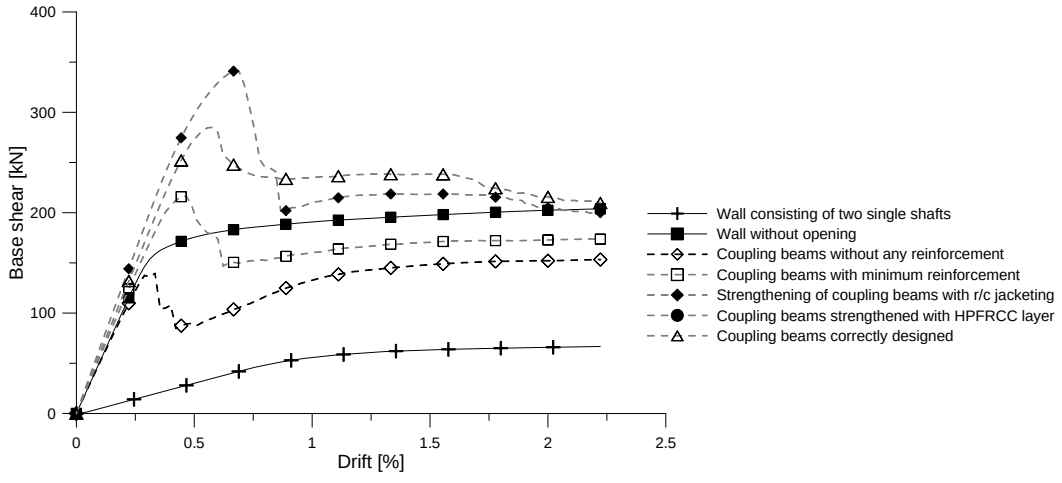

Figure 7.9 – Base shear for the wall strengthened with r/c jacketing (3 storeys)

From numerical (Figure 7.9) investigations it has been observed that with the proposed strengthening technique applying both in wall and beams could be reached a load capacity of 341 kN. While with a adequate design of the beams it has been achieved the peak at 281 kN,

whereas for the case with beams minimum or without reinforcement has been reached the maximum load capacity of 212 kN and 135 kN. All the curves show a certain degree of ductility with residual resistance capacity between 199 kN (beams properly designed) and 153 kN (un reinforced coupling beams). The maximum load capacity is reached at drift equal to 0.66%, and regarding the initial stiffness of the wall it appears almost coincident for all the analyzed cases.

7.7 5 storeys shear wall

The same geometry of the shear wall is analyzed as above, but instead of three storeys it has been changed to a five storeys with a total height of 15 m. Moreover, the same analyses were repeated as for the previous case study in order to highlight the significance of the results obtained.

7.7.1 Non strengthened coupled shear wall (5 storeys)

A series of analysis were performed with different configurations of the coupling beams. The wall without opening and the uncoupled wall represent the two extreme load capacities that the wall could withstand. Nevertheless, it has been clearly shown that initial stiffness is well maintained in the entire coupling configurations with reference to the wall without opening. Expect from the case of the wall with coupling beams without reinforcement, all the coupled wall cases reach the maximum value of load bearing capacity equal to 110 kN at corresponding 1.37% drift, after the peak a gradual decrease has been observed at 80 kN which afterwards remain quasi constant. In the case study of the wall coupled with beams without any reinforcement, the maximum load bearing capacity has been reached at 107 kN at drift 1%, and that was followed with abrupt loss of bearing capacity which has been stabilized correspondingly with load capacity curve of the non coupled shear wall.

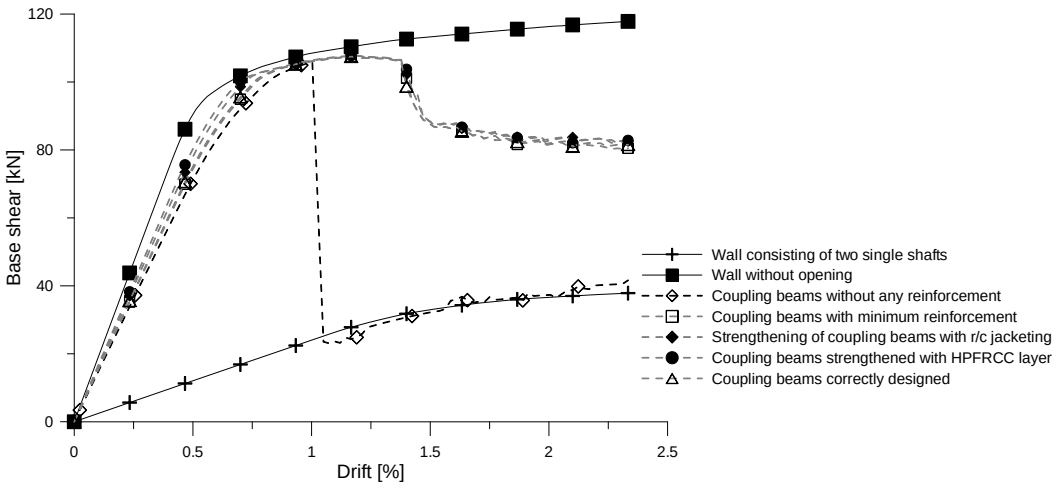

Figure 7.10 – Base shear for the wall without any strengthening (5 storeys)

7.7.2 Coupled shear wall strengthened with HPFRCC (5 storeys)

Also in this case it has been proposed the shear wall to be strengthened at base over two storeys respectively 6 m, by applying the layer in two lateral sides with thickness equal to 25 mm. The strengthening of coupling beams with HPFRCC has demonstrated to give the best performance, while not differing much from the wall coupled with beams properly designed. The difference between two curves is distinguished mainly but not that significantly only in terms of the in initial stiffness (the greater stiffness provided by wall with coupling beams

strengthened with HPFRCC which could be related mainly to the sectional enlargement). While in terms of load bearing capacity they are similar respectively equal to 178 kN and 174 kN, as well the behaviour in descending branch it has been almost identical around 130 kN. Considering the case of the wall with minimum reinforcement in coupling beams the maximum load bearing capacity has been slightly below to what was observed in the previous cases equal to 163 kN. After the peak reached the bearing capacity decrease sharply and it remains stable at load 83 kN. The worst case as it was expected is the wall coupled with beams without any reinforcement, with maximum load bearing capacity reached at 107 kN. The residual load bearing capacity is stabilized at 60 kN with slight growing with increased drifts, and this could be related to the fact that the assigned constitutive law for reinforcement was with hardening after the yield strength.

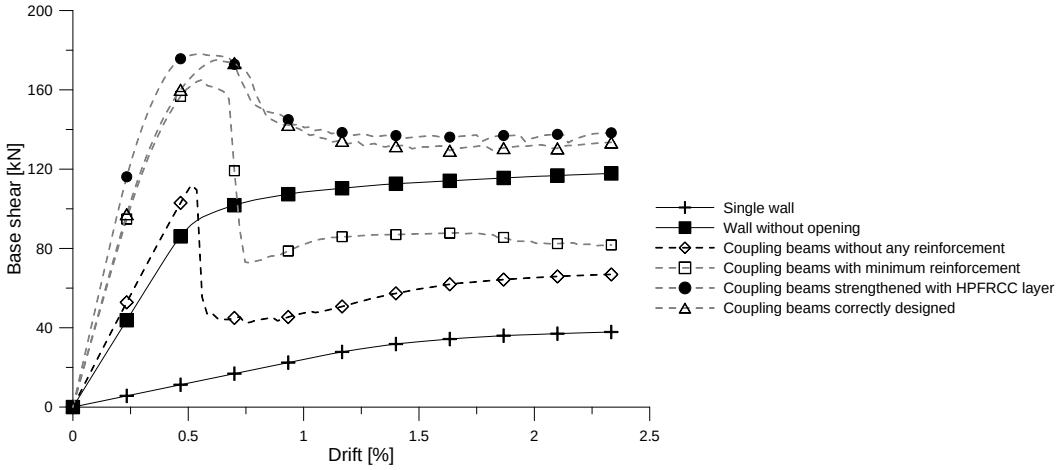

Figure 7.11 – Base shear for the wall strengthened with HPFRCC layer (5 storeys)

7.7.3 Coupled shear wall strengthened with r/c jacketing (5 storeys)

The second strengthening methodology adopted has been with reinforced concrete jacketing.

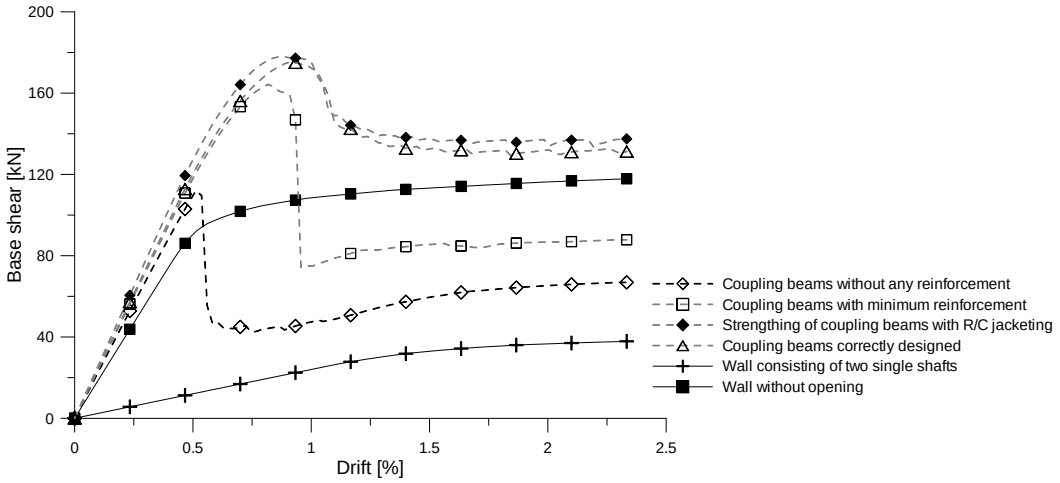

Figure 7.12 – Base shear for the wall strengthened with r/c jacketing (5 storeys)

From the numerical analysis it could be observed, that the wall and beams strengthened with jacketing show similar behaviour with the strengthened wall coupled with accordingly designed. The load bearing capacity for both solutions is around 180 kN reached at drift equal to 0.93%, and the residual bearing capacity provided has been equal to 135 kN. Regarding the solution with minimum reinforcement in the coupling beams, it has been achieved maximum load bearing capacity of 164 kN, which was followed with abrupt decrease and stabilized at 85 kN. Obviously even less efficient solution reveals in the case of the coupled wall with beams without any reinforcement, reaching the load capacity of 112 kN and residual capacity of 60 kN.

7.7.4 Strengthening efficiency on coupled shear walls

Based on the concept introduced by [Nollet et al., 2002] on efficiency concept for upgrading the lateral stiffness of reinforced concrete wall systems, a series of analysis was performed determining the efficacy of the strengthening technique.

It has been highlighted that the upgrading of the coupled wall system would reduce the overall drift of the wall itself. By definition, the uncoupled wall system has efficiency equal to 0 while the perfectly coupled wall system has efficiency factor equal to 1. Base on this concept it has been proposed to upgrade the coupling beams in the wall system to make possible a better transfer of forces from one wall to the other. In particular, it has been analyzed the optimum number of beams and their position to obtain an improved structural performance.

The basic concept of the [Nollet et al., 2002] imply that it is not necessary to upgrade all the coupling beams in the shear wall system to obtain the best performance, but they propose that it is sufficient to upgrade just some of the beams and at adequate level of the shear wall. Based on this idea we tried to replicate a series of analysis for the previous case study of 5 storeys shear wall, by upgrading different coupling beams at different storeys.

7.7.5 Efficiency parameter

As in previous analysis, the nonlinear pushover analyses were performed by imposing displacement at the top of the shear wall. As a output to define η the efficacy factor, were appreciated the forces obtained thorough the series of analysis.

$$\eta = \frac{F_{max} - F}{F_{max} - F_{min}} \tag{7.5}$$

Where:

F_{max}– is the maximum shear force recorded in the analysis at the base of the shear wall, and in particular is the force recorded in the case of the wall without openings;

F_{min}– is the minimum shear force recorded in the analysis at the base of the shear wall, and in particular is the force recorded in the case of the single wall;

F – is the maximum shear force recorded in the analysis in a specific case study, namely the mazimum load bearing capacity of the wall in any given configuration.

Based on the proposed efficiency factor it has been tried to identify which and how many coupling beams need to be upgraded to increase the wall performance with reference to the wall without openings.

7.7.6 Results of 5 storeys coupled shear wall

In order to have a better understanding which and many are the coupling beams to be upgraded, a series of analysis were carried out corresponding to different wall configurations of wall in which one or more coupling beams are upgraded. Same geometry of the wall has been chosen as in previous analysis with 10 bars in a single wall, where instead of diameter 12 mm it was taken 16 mm, to comply with reinforcement ratio for seismic requirements.

For each study configuration were obtained the capacity curve of the wall and is calculated the efficiency factorη. All the case studied are summarized in (Figure 7.13). In this way it could be appreciated the difference in performance with various configurations.

The following analyses were performed:

- Shear wall without openings
- A single wall
- Coupled shear wall with all beams upgraded
- Coupled shear wall without any beam upgraded
- Coupled shear wall upgrading the first beam
- Coupled shear wall upgrading the second beam
- Coupled shear wall upgrading the third beam
- Coupled shear wall upgrading the fourth beam
- Coupled shear wall upgrading the fifth beam

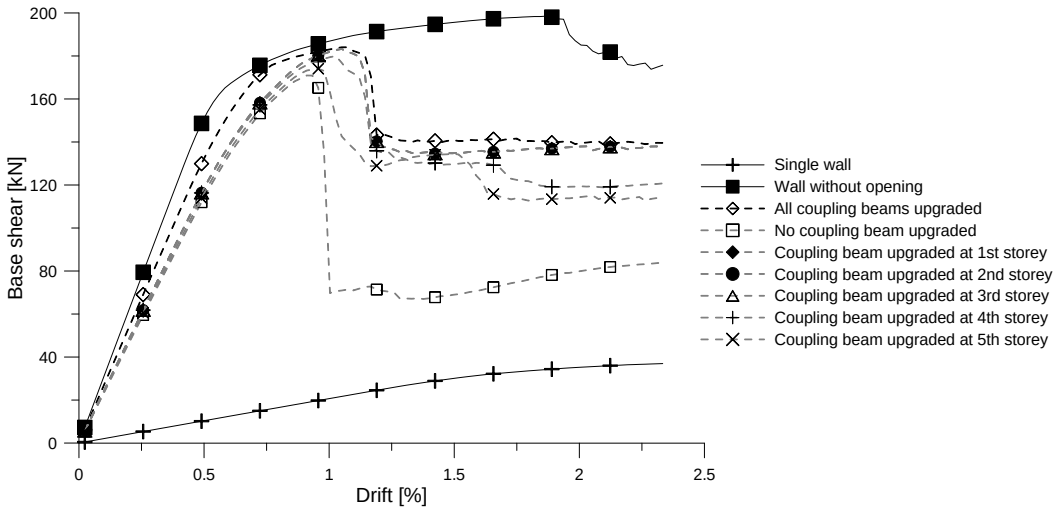

Figure 7.13 – Shear force at base for 5 storeys wall

Obviously the cases of the single wall and the wall without opening are respectively the upper and lower bound out of which region no other curve can be. From the (Figure 7.13) it could be observed how the load capacity has been improved by upgrading all the beams and

the curves corresponding to the upgrade of beams at second and third storey do coincide with it. The difference in terms of maximum load and residual capacity were minimal.

For each case study it has been calculated the efficiency factor, all the values of this parameter are shown in (Table 7.5) below.

Table 7.5 – Efficiency factor of 5 storeys wall

	η
All beams strengthened	0.911
1° beam strengthened	0.885
2° beam strengthened	0.906
3° beam strengthened	0.906
4° beam strengthened	0.885
5° beam strengthened	0.849

In the analyzed case where all the beams are upgraded it has been reached the efficiency factor equal to 0.911. All the results are reported in (Figure 7.14).

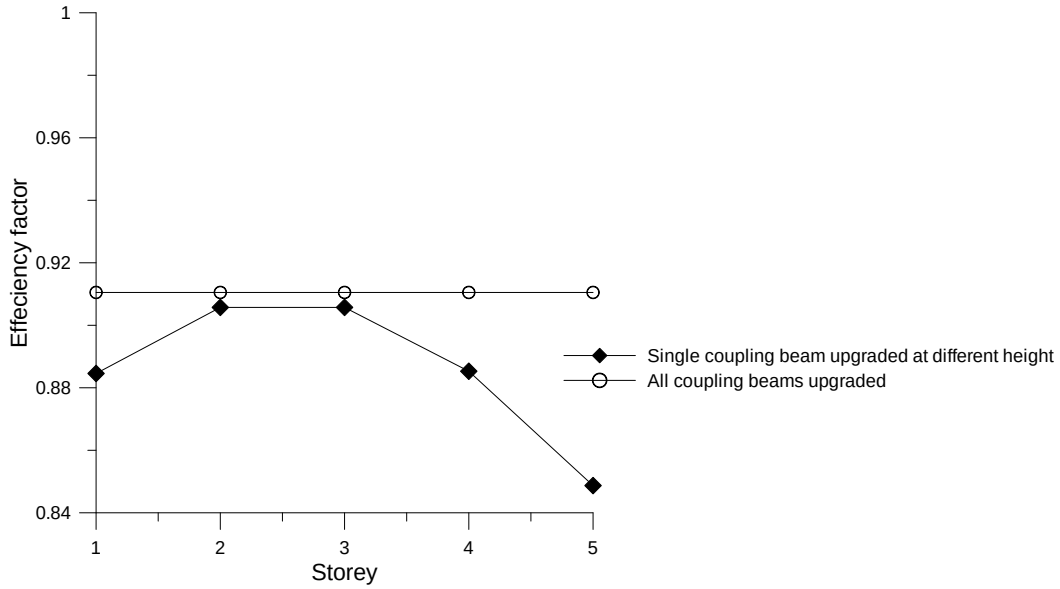

Figure 7.14 – Effect of upgrading a single coupling beam at different storey

From the performed analysis it has been highlighted the possibility of upgrading only one beam in second and third storey and basically having the same performance as all the beams upgraded.

8

8 Conclusions and future research needs

The focus of the thesis is the retrofitting/upgrading of existing coupling beams by advanced cement based materials. Two different materials namely HPFRCC and TRCC were investigated.

Main findings of the experimental campaign on members are summarized hereafter:

- From the first set of tests (which included coupling beams: without any reinforcement, with only longitudinal reinforcement and with both longitudinal and transverse reinforcement) it has been revealed the well known fact that stirrups have a crucial role on providing a more stable behaviour. From the results on coupling beams with longitudinal and transverse reinforcement, the load displacement curve under monotonic displacements has been identical with envelope of the tests under reversed cyclic displacements. Thus, the monotonic test could be considered representative enough of the overall coupling beam performance under complex loading paths.

  The newly proposed equations on [*fib* Model Code 2010] for shear design, herein adopted the III level approach, has been demonstrated to be accurate on prediction of the load bearing capacity for the coupling beams. Moreover, the numerical method based on beam element, has demonstrated to estimate the load displacement curve.
- The other set of experimental tests consisted of coupling beams strengthened or retrofitted with HPFRCC layer. It has been shown that use of this strengthening/retrofitting solution leads to enhanced performance both under monotonic and reversed cyclic displacements. However, always the cyclic tests showed less stable response after the maximum load was reached, and that could be attributed to the increased interface deterioration between substrate and the HPFRCC layer under reversed displacements. It has been interestingly observed on monotonic tests that the specimens with increased pre-damage level performed even better in terms of load capacity. This could be explained that the cracks present on damaged specimens, makes the HPFRCC to be more effective as the crack allows employing a wider zone of HPFRCC.
- The final set of experimental test provided on coupling beams upgraded with TRCC, once again shows improved performance. Moreover, the reversed cyclic test showed more stable response after maximum load capacity, which was similar to the

monotonic load displacement curve. These upgrading methods are intriguing also due to their easiness of use, as they do not require a skilled labour. However, the retrofitting technique with TRCC with respect to HPFRCC requires higher care on the placing of textile mesh.

As a matter of fact the choice of HPFRCC retrofitting options also involved extensive study at the material level, which formed an integral part of this thesis.

- The new test methodology "Double Edge Wedge Splitting" test, has shown to be an effective and a straightforward technique to quantify tensile "constitutive relationship" in code design wise perspective.
- Robust correlation of material parameters (toughness-residual strength) to fibre dispersion parameters assessed both through destructive and non-destructive method.
- Based on the experimental investigations the fibre reinforced cementitious composites were divided in two categories based on their tensile performance either strain-softening or strain-hardening. For each category the suitable constitutive laws were proposed based on [*fib* Model Code 2010] analogy. The "crush-crack" damage model has shown it could be successfully employed also for this new generation materials, by reproducing the experimental results of DEWS tests.

Member level modelling

- Once damage model suitable for HPFRCC, was used also for modelling coupling beam cases with reference to the experimental results on coupling beams found in literature [Canbolat et al., 2005]. The specimens were adequate to check the accuracy of the model as they were constructed either with conventional concrete or fibre reinforced cementitious composites. By suitable adjustment of parameters it has been demonstrated the ability of "crush-crack" damage model to well predict the behaviour of coupling beams and reproduce the crack pattern. Besides it has been observed that at very high deformations of such elements composed by HPFRCC, the local strains nowhere exceed the value which corresponds to the value of (SLS) at material level. Thus, based on this assumption the constitutive law for further analysis has been simplified to elastic perfect plastic law.

  The crush-crack damage model has been found not to be suitable for two reasons: 1) it is not able to reproduce the concrete behaviour under reversed loading and 2) high computation cost.

  Nevertheless, the assumption achieved by using "crush-crack" damage model allowed us to proceed with another simpler modelling technique, using beam element. By this modelling technique the computation time was much lower and the experimental results could be well reproduced with reference to [Canbolat et al., 2005], not only the envelope of load displacement curve but also was able to capture the reversals, which proved to be quite satisfactory.

  With this modelling technique the upgrading of the coupling beams with either r/c jacketing or HPFRCC has been successfully assessed, which were instrumental to the experimental campaign.

Structural Level

- This calibration has been also instrumental to assess the effectiveness of retrofitting of coupling beams on the overall structural performance of a wall system. The effectiveness of the retrofitting with HPFRCC is comparable with conventional jacketing solutions.
- It has been emphasized the importance of not only the retrofitting technique but also it has been highlighted the significance of overall intended structural behaviour of shear wall. Thus, before taking any retrofit measures the design engineer should carefully evaluate overall behaviour of shear wall and that would lead on much optimized solution by not necessarily retrofitting all coupling beams.

Future research needs

- The cement based composites due to their high content of cement are very prone to autogeneous shrinkage. It would be very interesting hence to investigate the surface treatment e.g. with primers, in order to avoid water absorption from the substrate, or the use of expansive agents in order to reduce shrinkage mainly with reference to delamination.
- This work highlighted that cement based composites are a very promising application on retrofitting technique, so further hybrid solutions should be explored, e.g. HPFRCC with combination of AR glass textile, HPFRCC with stainless steel mesh etc..
- Possibility of studying the cases of r/c cores and retrieve through retrofitting of coupling beams the torsional stiffness.

Appendix

Detailed drawings of the testing frame (Figure A.1 to Figure A.4).

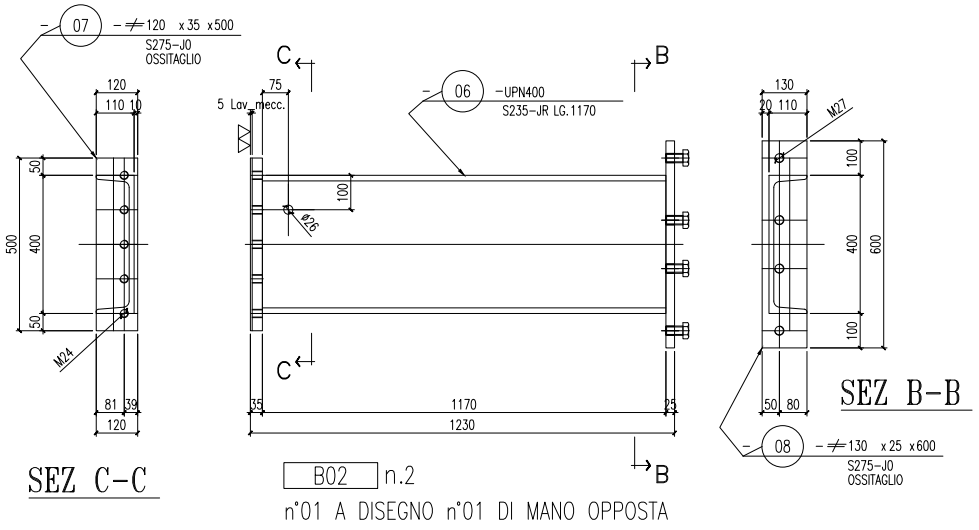

Figure A.1 – UPN 400 column, 2 pieces

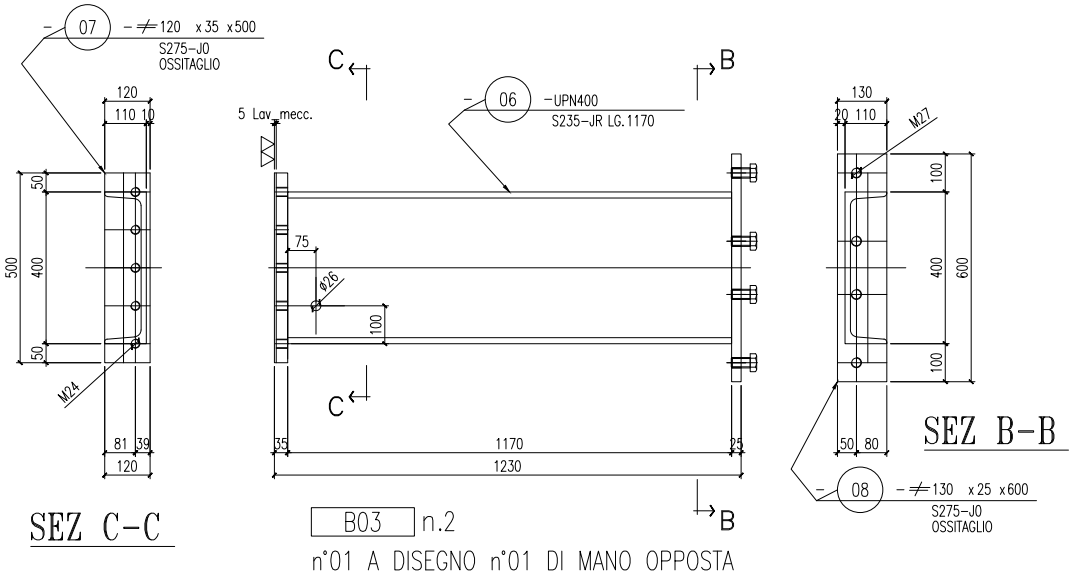

Figure A.2 – UPN 400 column, 2 pieces

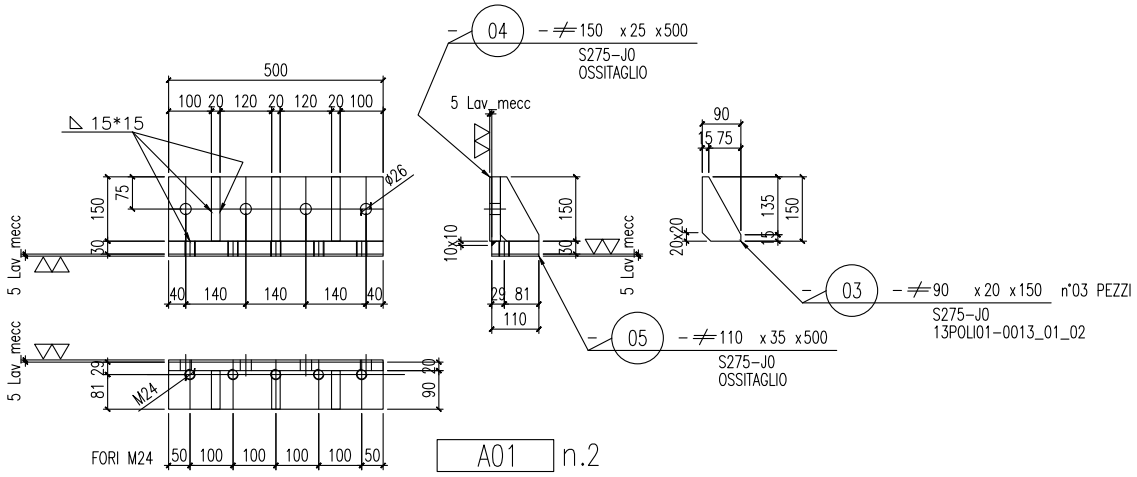

Figure A.3 – Angular profile, 2 pieces

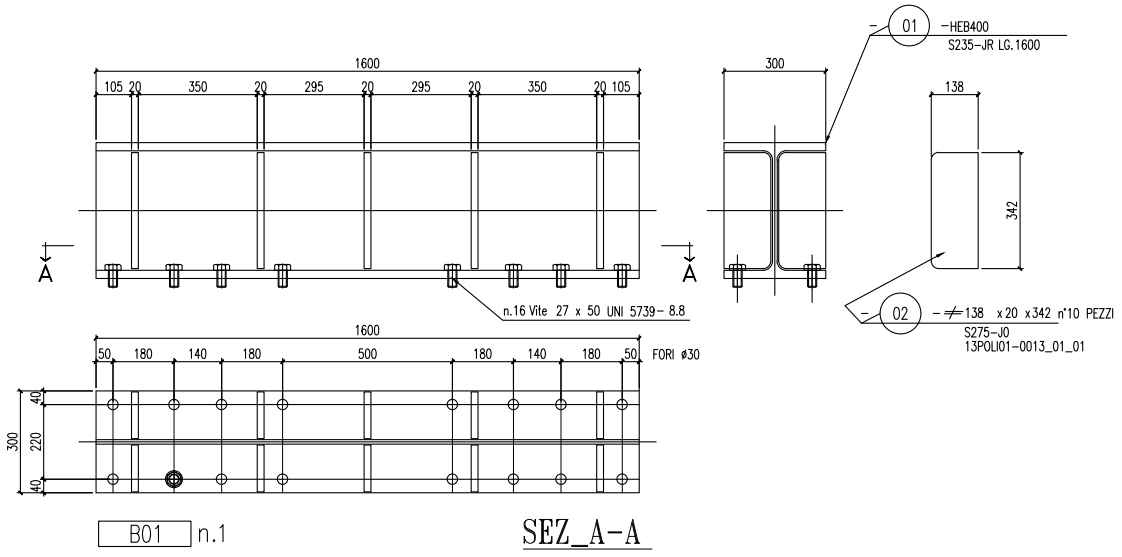

Figure A.4 – HEB 400 profile, 1 piece

Equipments and instrumentation

(a) (b) (c)

Figure A.5 – (a) closed loop of jack; (b) and (c) different views of pump

The load has been transferred to the specimen through the Dywidag bar which was connected to the jacks and passes through the specimen; the force collected by the bar from the jacks was then applied to the specimen via steel plates 30 mm thick. This system allows always applying a compressive load to the specimen further reducing the preparation cost. The use of two jacks allowed applying the load in both directions simulating the cyclic loading.

Figure A.6 – Load transfer from bar to the specimen

After placing of the specimen by crane into the frame in its exact position, the specimen was fixed to the angular profiles by threaded bolts passing through the specimen throughout threaded tubes pre-inserted inside of it. All the bolts are tightened with washers to provide suitable connection between the angular profile and the specimen.

(a) (b)

Figure A.7 – (a) fixing of specimen and (b) steel plate to guarantee planarity and provide sliding boundary condition

On the top of the specimen a 8 mm thick steel plate was applied, through the grouting of fibre reinforced rapid strength mortar (Mapegrout MAPEI). Two Teflon sheets were put on the top of the steel plate (between the plate and HPB 400 beam) in order to minimize the friction forces that could be produced during loading of the specimen.

Placing of HEB 400 beam was done one day after casting the mortar to allow it to achieve a sufficient strength. Finally the threaded bar was inserted in the specimen and the contrast steel plates to transfer the load to the UPN 400 columns were fixed (Figure A.8b).

(a) (b)

Figure A.8 – (a) Jack utilized and (b) Fixing of the jack

After mounting the jacks it was necessary to proceed with the placing of the load cells on both jacks; from each side of the frame the cell was resting on the piston with a suitable spherical node. Two 400 kN load cells were with voltage output 2 mV/V, and working only in compression, but thanks to counteraction previously described it was possible to move the pistons in both directions.

Figure A.9 – Compression load cell with capacity 400 kN

For the execution of the test a specific instrumentation for monitoring and control of the pump has was employed. The monitoring, control and data acquisition was performed by means of a LabVIEW software developed by National Instruments.

Figure A.10 – Data acquisition

The controlling parameter was the drift, calculated as the ratio between imposed displacement in the centre of upper block and the length of the beam.

The first control instrument was placed on the first jack to measure the jack movements and sometimes as a load control for large displacements, and has an excursion of 150 mm. A second control instrument was placed on top of the specimen, with the aim of measuring the displacement of the upper block of the specimen relative to the frame, with a free available length equal to 25 mm.

(a) (b) (c)

Figure A.11 – LVDT employed with different maximum capacities: (a) 150 mm; (b) 25 mm and (c) 10 mm

Gefran PY2 rectilinear displacement transducers with stroke capacity of 10 mm were used to measure local displacements on the specimen as in (Figure A.11).

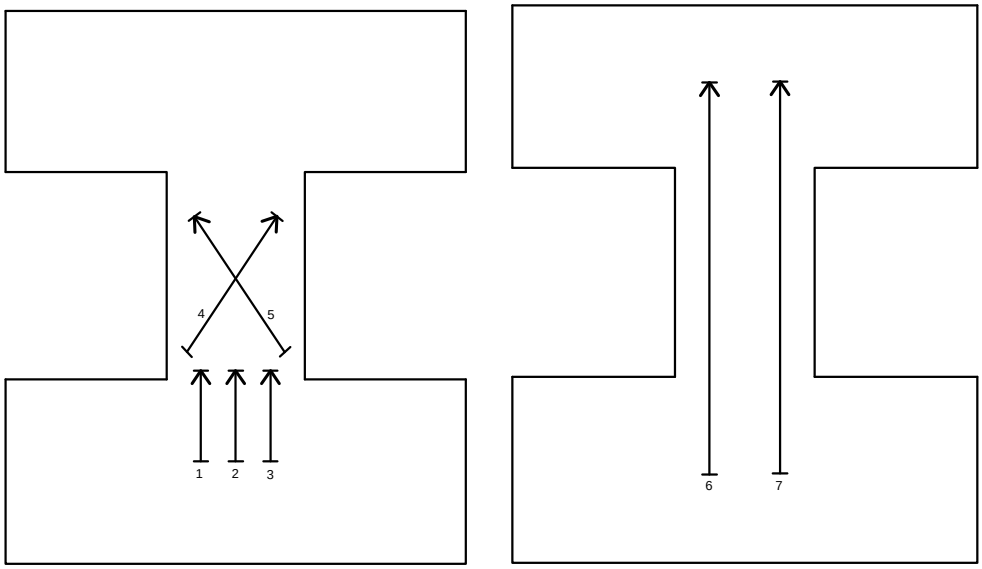

(a) (b)

Figure A.12 – Gefran PY2 LVDT position for local measurements (a) front and (b) rear face

All the measuring instruments, were connected to a control and data acquisition controller PXI in order to manage all the electrical signals from the instruments; these signals are directly converted into physical displacement or load by LabVIEW software and the entire test can be managed and controlled by a computer.

Figure A.13 – Acquisition controller

Ordinary concrete C20/25 compressive tests

The cubic specimens to be tested in compression were prepared on daily basis with the size 100x100x100 mm for each concrete batch according to [EN 12390-1]. The specimens were maintained in same conditions as the coupling beam specimens and were tested on the same testing day as the companion coupling beams. The tests were performed using a Controls Automax5 testing machine. Test results are shown in the (Table A.1).

Table A.1 – Concrete strength in compression

Day of casting	Average value [N/mm²]	Minimum value [N/mm²]	Maximum value [N/mm²]	Standard deviation [N/mm²]
1	48.40	39.78	51.02	3.37
2	38.87	36.80	40.34	1.33
3	35.55	33.44	33.67	0.16
4	37.68	34.38	40.15	2.78
5	31.17	30.03	32.54	0.88
6	30.33	27.07	32.55	2.21
7	36.28	32.51	40.09	2.52
Total	36.61	30.33	40.40	6.10

From tests carried out was obtained an average value of compressive strength for concrete cubes provided by the concrete factory of 36.61 N/mm². It was also noted that the specimens from mixture of the first day provided the highest strength up to 50 N/mm² and that concrete mixture corresponds to the plain concrete coupling beams.

Steel reinforcement tensile tests

For each size 2 uniaxial tensile tests have been performed to identify the stress vs strain behaviour, shown in (Figure A.15 to Figure A.17). The representative values according to the [UNI EN ISO 15630-1] are reported in (Table A.2).

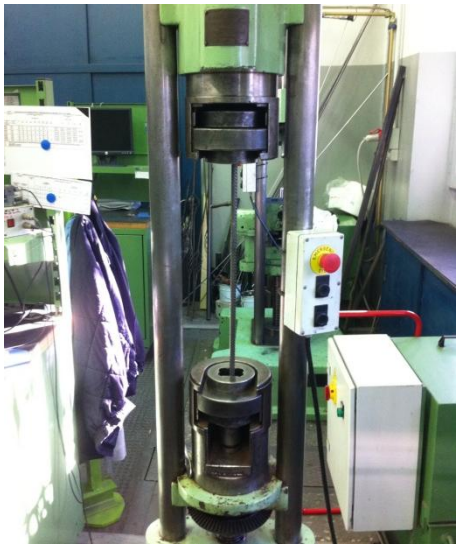

Figure A.14 – Tensile testing machine

Table A.2 – Uniaxial tension of steel reinforcement

	Nom. Diam.	Yield strength		Ultimate strength		Elong. Ag		Elong. Agt
N°	mm	kN	N/mm²	kN	N/mm²	mm	%	%
1	6.0	15.6	552	16.7	591	108.0	8.0	8.3
2	6.0	15.6	552	16.7	591	105.5	5.5	5.8
3	8.0	28.6	569	32.5	647	105.5	5.5	5.8
4	8.0	28.6	569	32.8	653	110.0	10.0	10.3
5	14.0	83.9	545	99.0	643	110.0	10.0	10.3
6	14.0	81	526	97.1	631	112.0	12.0	12.3

- Elong. Ag: non proportional elongation according to [UNI EN 15630-1];
- Elong. Agt: proportional total elongation under maximum loading according to [UNI EN 15630-1].

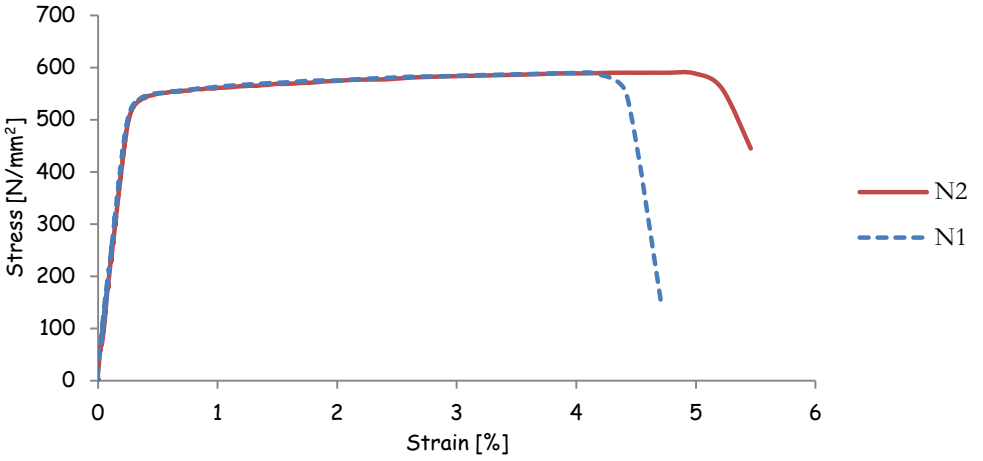

Figure A.15 – Uniaxial test results of 2 bars ϕ6: stress vs. strain

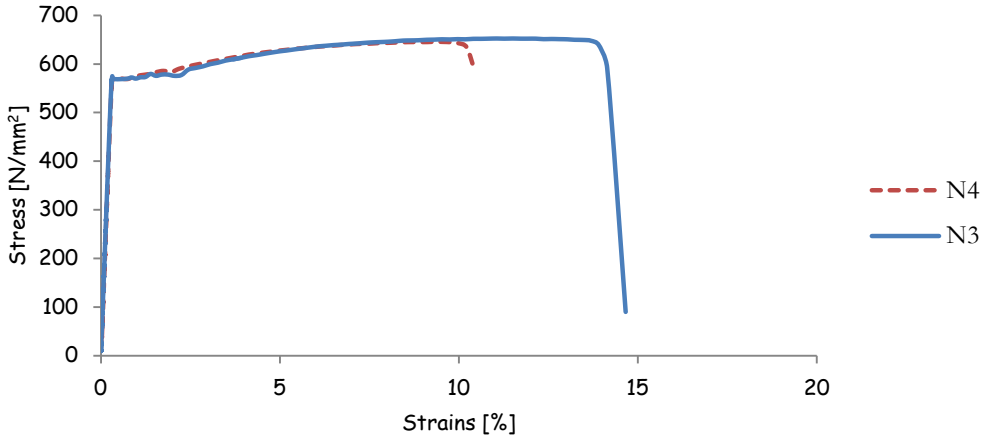

Figure A.16 – Uniaxial test results of 2 bars ϕ8: stress vs. strain

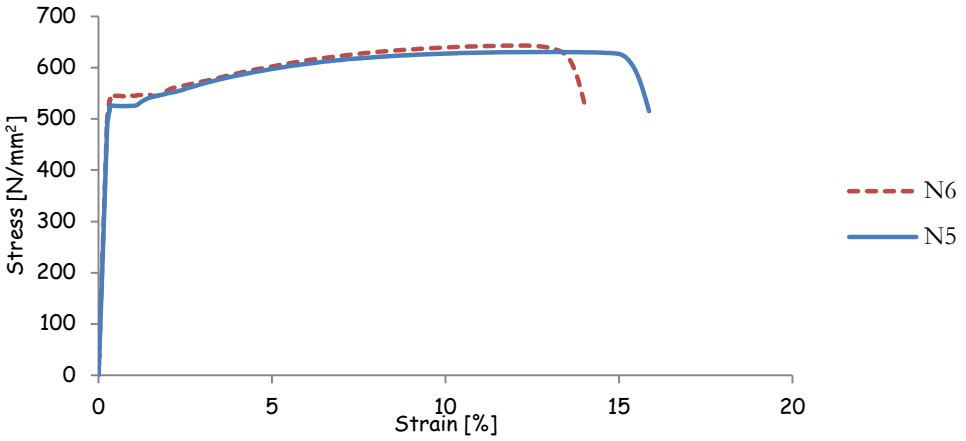

Figure A.17 – Uniaxial test results of 2 bars ϕ14: stress vs. strain

References

ACI 318-05 (2005). Building Code Requirements for Structural Concrete and Commentary. American Concrete Institute.

ACI Committee 318 (2008). Building code and commentary, Report ACI 318-08/318R-08. American Concrete Institute, Farmington Hills, MI, 430 pp.

ACI Committee 544 (1988a). Design Considerations for Steel Fiber Reinforced Concrete. ACI Structural Journal, 85(5), pp 563-580.

Al-Jamous, A.; Ortlepp, R.; Ortlepp, S.; Curbach, M.; (2006). Experimental investigations about construction members strengthened with textile reinforcement. 1st International RILEM Conference on Textile Reinforced Concrete, pp 161-170.

Athanasopoulou, A.; (2010). Shear Strength and Drift Capacity of Reinforced Concrete and High-Performance Fiber reinforced Concrete Low-Rise Walls Subjected to Displacement Reversals, PhD. Dissertation, University of Michigan, Ann Arbor, MI, 302 pp.

Baczkowski, B.J.; (2007). Steel Fibre Reinforced Concrete Coupling Beams. PhD. Dissertation, The Hong Kong University of Science and Technology, 306 pp.

Barnett, S., Lataste, J.F., Parry, T., Millard, S. G., Soutsos, M.N.; (2010). Assessment of fibre orientation in ultra high performance fiber reinforced concrete and its effect on flexural strength", Materials and Structures, 43(7), pp 1009-1023.

Bažant, Z., Pijaudier-Cabot, G. (1989). Measurement of characteristic length of nonlocal continuum. J. Eng. Mech., 11, pp 755–767.

Bentz, E.C.; (2010). MC2010: Shear strength of beams and implications of the new approaches. fib Bulletin 57, pp 15-30.

Breña, S., Ihtiyar, O.; (2010). Performance of Conventionally Reinforced Coupling Beams Subjected to Cyclic Loading Journal of Structural Engineering, 137(6), pp 665–676.

Brena, S., Ruiz M.F., Kostic, N., Muttoni, A.; (2009). Modelling techniques to capture the backbone envelope behaviour of coupling beams subjected to seismic loading. Studies and researches – V. 29, Graduate School in Concrete Structures – Fratelli Pesenti Politecnico di Milano, Italy.

Bufalino, S.; (2011). Dispersione delle fibre e proprietà meccaniche in compositi cementizi fibrorinforzati ad alte prestazioni. BSc thesis, Politecnico di Milano, Italy, 85 pp.

Canbolat B.A., Parra-Montesinos G.J., Wight J.K.; (2005). Experimental study on seismic behavior of high performance fiber-reinforced cement composite coupling beams. ACI Structural Journal, 102, No. 1, pp 159–166.

Chan, H.C., Kuang, J.S.; (1989). Stiffened coupled shear wall. J. Eng. Mech, pp 689-703.

CNR-DT 204, (2006). Guidelines for design, construction and production control of fiber reinforced concrete structures. National Research Council of Italy.

Colombo, I.G., Magri, A., Zani, G., Colombo, M., di Prisco, M.; (2013). Textile Reinforced Concrete: Experimental investigation on design parameters. Materials and Structures, 46(11), pp. 1933-1951.

Compione, G., Mindess, S.; (1999). Compressive Toughness Characterization of Normal and High-Strength Fiber Concrete Reinforced with Steel Spirals. Structural Applications of Fiber Reinforced Concrete, SP-182, American Concrete Institute, Farmington Hills, MI, pp 141-161.

di Prisco M., Ferrara L., Lamperti M.; (2013). Double edge wedge splitting (DEWS): an indirect tension test to identify post-cracking behaviour on fibre reinforced cementious composites", Materials and Structures, 46(11), pp 1893-1918.

di Prisco, M., Lamperti, M.G.L., Lapolla, S.; (2010). On Double Edge Wedge Splitting test: preliminary results. In: Oh BH et al (eds) Proceedings FraMCoS 7, Jiejiu, South Korea. pp 1533–1540.

di Prisco, M., Mazars, J.; (1996.) Crush-crack: a non-local damage model for concrete. Journal of Mechanics of Cohesive and Frictional Materials, 1, pp 321-347.

Emmons, P. H., Vaysburd, A. M., and McDonald, J. E.; (1994). Concrete repair in the future turn of the century - any problems?. Concrete International, pp 42-49.

EN 1992-1-2 (2004) Eurocode 2: Design of concrete structures.

EN 1998 (2004) Eurocode 8: Design of structures for earthquake resistance.

Fanella, D. A., Naaman, A.E.; (1985). Stress-strain properties of fiber reinforced mortar in compression. ACI Journal, 82(4), 475-483.

Ferrara, L., di Prisco, M., Lamperti, M.G.L.; , (2010). Identification of the stress–crack opening behavior of HPFRCC: the role of flow-induced fiber orientation. In: Oh BH et al (eds) Proceedings FraMCoS 7, Jiejiu, South Korea. pp 1541–1550.

Ferrara, L., di Prisco, M.; (2001) Mode I Fracture behavior in concrete: Nonlocal damage modelling, ASCE Journal of Engineering Mechanics, pp 678-692.

Ferrara, L., di Prisco, M.; (2011). The role of fiber orientation on strain gardening/softening FRCCs: continuum damage modelling. RIO-SHCC2 RILEM international conference, Rio de Janeiro, Brasil.

Ferrara, L., Faifer, M., Muhaxheri, M., Toscani, S., Ottoboni, R.; (2011) "Sull'impiego di materiali cementizi fibrorinforzati ad alte prestazioni: dall'orientamento delle fibre all'ortotropia del comportamento meccanico" Atti Giornate Aicap 2011, Padova. pp 513-520.

Ferrara, L., Faifer, M., Muhaxheri, M., Toscani, S.; (2012). A magnetic method for non destructive monitoring of fiber dispersion and orientation in steel fiber reinforced cementitious composites: part 2: correlation to tensile fracture toughness. Materials and Structures, 45(4), pp 591-598.

Ferrara, L., Faifer, M., Muhaxheri, M., Toscani, S.; (2012). Connecting Non-destructive Fiber Dispersion Measurements with Tensile HPFRCC Behavior High Performance Fiber Reinforced Cement Composites 6 RILEM State of the Art Reports 2, pp 43-50.

Ferrara, L., Faifer, M., Toscani, S.; (2012). A magnetic method for non destructive monitoring of fiber dispersion and orientation in steel fiber reinforced cementitious composites—part 1: method calibration. Materials and Structures, 45(4), pp 575-589.

Ferrara, L., Ozyurt, N., di Prisco, M.; (2011). High mechanical performance of fiber reinforced cementitious composites: the role of "casting-flow" induced fiber orientation. Materials and Structures, 44(1), pp 149–168.

Ferrara, L., Park, Y.D. and Shah, S.P.; (2008). Correlation among fresh state behaviour, fiber dispersion and toughness properties of SFRCs. ASCE Journal of Materials in Civil Engineering, 20(7), pp 493-501.

Fib Bulletin no. 24, (2003). Seismic assessment and retrofit of reinforced concrete buildings. State-of-art report. Losanne: FIB.

Fib Model Code 2010, 1st complete draft, (2010), 1 vol.

Fib Model Code 2010, 1st complete draft, (2010), 2 vol.

Fortney, P., Rassati, G., and Shahrooz, B. (2008). Investigation on effect of transverse reinforcement on performance of diagonally reinforced coupling beams. ACI Structural Journal, 105(6).

Galano, L., Vignoli, A.; (2000). Seismic behavior of short coupling beams with different reinforcement layouts, ACI Structural Journal, 97(6), pp 876-885.

Gong, B., Shahrooz, B. M.; (2001). Concrete-Steel Composite Coupling Beams. II: Subassembly Testing and Design Verification. Journal of Structural Engineering, ASCE. 127(6), pp 632-638.

Gong, B., Shahrooz, B. M.; (2001). Steel-concrete composite coupling beams – behavior and design. Engineering Structures, pp 1480-1490.

Guedes, J., Pegon, P., Pinto, A.V.; (1994). A fibre/timoshenko beam element in CASTEM 2000. Special Publication Nr. I.94.31, European Commission, JRC, Ispra (VA), Italy.

Guedes, J., Pinto, A.V., P. Pegon, P.; (2011). Non-Linear Shear Model for R/C Piers. Joint Research Centre, European Commission.

Harries, K. A., 1995, Seismic Design and Retrofit of Coupled Walls Using Structural Steel, Ph.D. Thesis, McGill University, 229 pp.

Heger, J., Norbert, W., Curbach Hegger, J., Will, N., Bruckermann, O., Voss, S.; (2006). Load–bearing behaviour and simulation of textile reinforced concrete. Materials and Structures, 39(8), pp 765-776.

Hillerborg, A.; (1985). The theoretical basis of a method to determine the fracture energy GF of concrete. Materials and Structures, 18 (4), pp 291-296.

Hung, C.C.; (2010). Computational and hybrid simulation of high performance fiber reinforced concrete coupled wall systems. PhD. Dissertation, University of Michigan, Ann Arbor, MI, 191 pp.

Irwin, G.; (1950). Fracture. In Handbuch der Physik 6, pp 551–590.

Jang, S.K., Hong, S.G.; (2004). The shear strength of rc coupling beams with plastic hinges using strut-and-tie model. 13th WCEE.

Jun, P., Mechtcherine, V.; (2010). Behaviour of strain-hardening cement-based composites (SHCCs) under monotonic and cyclic tensile loading. Part 1: Experimental investigations. Cement Concr. Compos., 32.

Kachanov, L.M.; (1986). Introduction to continuum damage mechanics. Martinus Nijhoff Publishers, Dordrecht, Netherlands.

Kesner, K.E., Billington, S.L., Douglas, K.S.; (2003). Cyclic response of highly ductile fiber-reinforced cement-based composites ACI Materials Journal. 10(5), pp 381-390.

Krajcinovic, D.; (1984). Continuum damage mechanics. Appl. Mech. Rev., Vol. 37, pp 1-6.

Lam, W.Y., Su, R.K., Pam, H.J.; (2004). Seismic performance of plate reinforced composite coupling beams. 13th WCEE.

Larrinaga, P., San-José, P.J.T., García, P. J.T., Garmendia, L., Díez, J.; (2010). Experimental study of the flexural behaviour of low performance rc beams strengthened with textile reinforced mortar. International RILEM Conference on Material Science, pp 235 – 244.

Lataste, J.F., Behloul, M., Breysse, D.; (2008). Characterisation of fibres distribution in a steel fibre reinforced concrete with electrical resistivity measurements. NDT & E International, 41(8), pp 638-647.

Lemaitre J.A.; (1996). A course on damage mechanics. Springer-Verlag.

Lequesne, R.; (2011). Behavior and design of high-performance fiber-reinforced concrete coupling beams and coupled-wall systems. Ph.D. Thesis, University of Michigan, USA. 298 pp.

Li, V.C., Mishra, D.K., Naaman, A.E., Wight, J. K. LaFave, J. M., Wu, H., Inada, Y.; (1994). On the shear behavior of engineered cementitious composites Advanced Cement Based Materials, 1(3): pp 142-149.

Li, V.C.; (2002). Reflections on research and development of engineered cementitious composites (ECC). JCI Workshop on Ductile Fiber Reinforced Cementitious Composites (DFRCC).

Magri, A.; (2012). Advanced cementitious composites for structural retrofitting. Ph.D. Thesis, Politecnico di Milano, Italy. 244 pp.

Maringoni, S., Mostosi, Meda, S., Riva, A.; (2011). Rinforzo a taglio di travi in C.A. mediante incamiciature in calcestruzzo ad elevate prestazioni. Aicap 2011.

Martinola, G., Meda. A., Plizzari, G.A., Rinaldi, Z.; (2010). Strengthening and repair of RC beams with fiber reinforced concrete, Cement & Concrete Composites, 32, pp 731-739.

Mazars, J., Kotronis, P., Ragueneau, F., Casaux, G.; (2006). Using multifiber beams to account for shear and torsion - Application to concrete structural elements. Computer Methods in Applied Mechanics and Engineering, 195, pp 7264-7281.

Mazars, J.; (1984). Application de la Mechanique de l'Endommagement au Comportement non Lineaire et a la Rupture du Beton de Structure. These de Doctorate d'Etat, L.M.T., Universite Paris, France.

Mechtcherine, V.; (2012). Towards a durability framework for structural elements and structures made of or strengthened with high-performance fibre-reinforced composites. Construction and Building Materials, 31, pp 94-104.

Meda, A., Rinaldi, Z., Martinola, G., Plizzari, G.A.; (2007). Strengthening of r/c beams with high performance fiber reinforced cementitious composites. HPFRCC 5 - High pererformance fiber reinforced cemntitious composites.

Mihaescu, A., Tudor, D., Ciuhandu, G., Ianca, S.; (1990). Research on the repair and strengthening of coupling beams in coupled shear walls damaged after earthquakes. Proceeding of the 9th ECEE, Moscow.

Moudarres, F. R., Coull, A.; (1986). Stiffening of linked shear walls. Journal of Engineering and Mechanics, 112, pp 223-237.

Naaman A.E., Shah. S.P.; (1979). Fracture and Multiple Cracking of Cementitious Composites. In S.W. Freiman, editor, Fracture Mechanics applied to Brittle Materials. Proceedings of the 11th National Symposium on Fracture Mechanics ASTM, pp 183–201.

Naaman, A., Reinhardt, H.; (2006). Proposed classification of hpfrc composites based on their tensile response. Materials and Structures, 39(5), pp 547–555.

Naish, D., Fry, A., Klemencic, R., Wallace, J.; (2013). Reinforced concrete coupling beams—part I: Testing. ACI Structural Journal, pp 1057-1066.

Naish, D., Fry, A., Klemencic, R., Wallace, J.; (2013). Reinforced concrete coupling beams—part II: modeling. ACI Structural Journal, pp 1067-1076.

Naish, D., Fry, J. A., Klemencic, R., Wallace, J.; (2009). Reinforced concrete link beams: alternative details for improved constructability. Report to Charles Pankow Foundation. UCLA-SGEL, pp 103.

Naish, D., Fry, J. A., Klemencic, R., Wallace, J.; (2009). Experimental evaluation and analytical modeling of aci 318-05/08 reinforced concrete coupling beams subjected to reversed cyclic loading. Report to Charles Pankow Foundation. UCLA-SGEL, pp 122.

Nollet, M.J., Chaallal, O.; (2002). Efficiency concept for upgrading the lateral stiffness of reinforced concrete wall systems. Structural design of tall buildings, 11, pp 15-34;

Ozyurt, N., Mason, T.O., Shah, S.P.; (2006). Non destructive monitoring of fiber orientation using AC-IS: an industrial scale application. Cem. Concr. Res. 36, pp 1653–1660.

Ozyurt, N., Woo, L.Y., Mason, T.O. and Shah, S.P.; (2006) Monitoring fiber dispersion in fiber reinforced cementitious materials: comparison of AC Impedance Spectroscopy and Image Analysis. ACI Materials Journal, 103 (5), pp 340-347

Paparoni, M.; (1972). Model studies of coupling beams. Proceedings of the international Conference on Tall Concrete and Masonry Buildings, pp 871-881.

Park, R., Paulay, T.; (1975). Reinforced concrete structures. John Wiley & Sons, New York, NY, 746 pp.

Park, R., Priestley, M.J.N., Gill, W.D.; (1982). Ductility of square confined concrete columns. Journal of the Structural Division, ASCE, Vol. 108, No. 4, pp. 929-950.

Park, W.S., Yun, H.D., Chung, J.-Y., Kim, Y.-C.; (2005). Experimental studies on seismic behavior of steel coupling beams. Structural Engineering and Mechanics, 20(6), pp 695-712.

Park, W.S., Yun, H.D.; (2011). Seismic performance of strain-hardening cementitious composite coupling beams with different reinforcement details. Composites: Part B. doi 10.1016/j.compositesb.2011.04.049

Paulay, T. (1969), The coupling of shear walls. PhD Dissertation, University of Canterbury, Christchurch, New Zealand, 435 pp.

Paulay, T., Binney, J. R.; (1974). Diagonally reinforced coupling beams of shear walls. Shear in Reinforced Concrete, SP-42, American Concrete Institute, Detroit, MI, 2, pp 579-598.

Paulay, T.; (1971). Coupling beams of reinforced concrete shear walls. Journal of the Structural Division, ASCE, 97 (ST3), pp 843-861.

Peled, A, Bentur, A.; (2003). Fabric structure and its reinforcing efficiency in textile reinforced cement composites. Composites. Part A 34, pp 107-118.

Peled, A., Zhu, D., Mobasher, B.; (2012). Impact behavior of 3D fabric reinforced cementitious composites. High Performance Fiber Reinforced Cement Composites 6 RILEM State of the Art Reports, 2, pp 543-550.

Proceedings of the International Symposium on Ultra High Performance Concrete; (2004). Kassel, Germany, 884 pp.

Riyazi M., Esfahani M. R., Mohammadi H.; (2007). Behavior of coupling beams strengthened with carbon fiber reinforced polymer sheets. IJE Transactions B: Applications; 20(1).

Romualdi, J.P, Batson, G.B.; (1964). Tensile strength of concrete affected by uniformly distributed and closely spaced short lengths of wire reinforcement. ACI Journal, 61(6), pp 657–672.

Shah, S. P., Rangan, B. V. (1971). Fiber reinforced concrete properties. ACI Journal, 68(2), pp 126-135

Shin, S.K., Kim, K., Lim, Y.M.; (2011). Strengthening effects of DFRCC layers applied to RC flexural members" Cement and Concrete Composites, 33: pp 328-333.

Soroushian, P., Lee, C.D,; (1990). Distribution and orientation of fibers in steel fiber reinforced concrete. ACI Mat. J., 87 pp 433-439.

Spini, A.; (2013). Uso di compositi cementizi avanzati per il ripristino/adeguamento di travi di collegamento in calcestruzzo armato. MSc thesis, Politecnico di Milano, Italy 291 pp.

Stahli P, Custer R, van Mier JGM (2008) On flow properties, fibre distribution, fibre orientation and flexural behaviour of FRC. Materials and Structures, 41(1), pp 189–196.

Stroeven, P. and Shah, S.P.; (1978). Use of radiography-image analysis for steel fiber reinforced concrete. in Testing and Test Methods of Fiber Cement Composites, R.N. Swamy, ed. Construction Press, Lancaster, pp 345-353.

Su R.K.L., Zhu Y.; (2005). Experimental and numerical studies of external steel plate strengthened reinforced concrete coupling beams. Engineering Structures, 27(10), pp 1537-1550.

Subedi, N.K.; (1991). RC-Coupled shear wall structures. I: Analysis of coupling beams. Journal of Structural Engineering, ASCE, 117(3), pp 667-680.

Subedi, N.K.; (1991). RC coupled shear wall structures. II: ultimate strength calculations. J. Struct. Eng., 117(3), pp 681–698.

Tassios, T.P., Moretti, M., Bezas, A.; (1996). On the behavior and ductility of reinforced concrete coupling beams of shear walls, ACI Structural Journal, 93(6), pp 711-720.

Teshigawara, M., Sugaya, K., Kato, M., Matsushima, Y.; (1998b). Seismic Test on 12-Storeys Coupled Shear Wall with Flange Walls," Structural Engineering World Wide 1998 – Proceedings, Paper Number T-186-4, Elsevier Science Ltd., 7 pp.

Timoshenko, S. Goodier, J. N.; (1951). Theory of elasticity – McGraw-Hill.

Toniolo, G., Di Prisco, M.; (2010). Cemento armato. Calcolo agli stati limite. Zanichelli.

Triantafillou, T. and Papanicolau, C.; (2005). Textile reinforced mortars (TRM) versus fiber reinforced polymers (FRP) as strengthening materials of concrete structures. FRPRCS7 pp 99-118.

Tudor, D.F., Ciuhandu, G.C.; (1992). Design principles concerning the strengthening of coupling beams. Proceeding of the 10th Earthquake Engineering World Conference, Rotterdam, pp 5127-5130.

UNI EN 12350-2 (2009). Testing fresh concrete Part 2: Slump-test. 12 pp.

UNI EN 12350-9 (2010). Testing fresh concrete Part 2: Part 9: Self-compacting concrete - V-funnel test. 12 pp.

UNI EN 12390-1(2000). Testing hardened concrete — Part 1: Shape, dimensions and other requirements for specimens and moulds. 14 pp.

UNI EN ISO 15630-1 (2010). Acciaio per calcestruzzo armato e calcestruzzo armato precompresso - Metodi di prova - Parte 1: Barre, rotoli e fili per calcestruzzo armato.

Van Damme, S., Franchois, A., De Zutter, D. and Taerwe, L.; (2009). Nondestructive determination of the steel fiber content in concrete slabs with an open-ended coaxial probe. IEEE Transactions on Geoscience and Remote Sensing, 42(11), pp 2511 – 2521.

Vandewalle, L, et al., (2003). Final recommendation of RILEM TC 162-TDF: Test and design methods for steel fibre reinforced concrete sigma-epsilon-design method. Materials and Structures, 36(262), pp 560-567.

Weiland, S., Ortlepp, R., Curbach, M.; (2006). Strengthening of predeformed slabs with textile reinforced concrete. In Proc. Second international congress FIB, RILEM publications SARL.

Wiberg, A.; (2003). Strengthening of concrete beams using cementitious carbon fibre composites. PhD Thesis, Royal Institute of Technology, Sweeden, 151 pp.

Yun H.D., Kim, S.W., Jeon, E., Park, W.S., Lee, Y.T.; (2008). Effects of fibre-reinforced cement composites' ductility on the seismic performance of short coupling beams. Magazine of Concrete Research, 60(3), pp 223 –233.

Yun H.D., Yang I.S., Kim, S.W., Jeon, E., Choi, C.S., Fukuyama, H.; (2007). Mechanical properties of high performance hybrid fiber-reinforced cementitious composites (HPHFRCCs). Magazine of Concrete Research, 59(4), pp 257–271.

Zani, G.; (2013). High performance cementitious composites for sustainable roofing panels. PhD Thesis, Politecnico di Milano, Italy. 167 pp.

Zhao, Z.Z., Kwan, A.K.H., He, X.G.; (2004). Nonlinear finite element analysis of deep reinforced concrete coupling beams. Engineering Structures. 26, pp 13–25.